

Ultra-high resolution observations of selected blazars

INAUGURAL-DISSERTATION

zur

Erlangung des Doktorgrades
der Mathematisch-Naturwissenschaftlichen Fakultät
der Universität zu Köln



vorgelegt von

Jeffrey Adam Hodgson
aus Melbourne, Australien

Köln 2014

Berichterstatter: Prof. Dr. Andreas Eckart
Prof. Dr. Anton Zensus

Tag der letzten mündlichen Prüfung: 27. Januar 2015

Abstract

Active Galactic Nuclei are the luminous centres of active galaxies that produce powerful relativistic jets from central super massive black holes (SMBH). When these jets are oriented towards the observer's line-of-sight, they become very bright, very variable and very energetic. These sources are known as blazars and Very Long Baseline Interferometry (VLBI) provides a direct means of observing into the heart of these objects. VLBI performed at 3 mm with the Global mm-VLBI Array (GMVA) and 7 mm VLBI performed with the Very Long Baseline Array (VLBA), allows some of the highest angular resolution images of blazars to be produced. In this thesis, we present the first results of an ongoing monitoring program of blazars known to emit at γ -ray energies.

The physical processes that produce these jets and the γ -ray emission are still not well known. The jets are thought to be produced by converting gravitational energy around the black hole into relativistic particles that are accelerated away at near the speed of light. However, the exact mechanisms for this and the role that magnetic fields play is not fully clear. Similarly, γ -rays have been long known to have been emitted from blazars and that their production is often related to the up-scattering of synchrotron radiation from the jet. However, the origin of seed photons for the up-scattering (either from within the jet itself or from an external photon field) and the location of the γ -ray emission regions has remained inconclusive. In this thesis, we aim to describe the likely location of γ -ray emission in jets, the physical structure of blazar jets, the location of the VLBI features relative to the origin of the jet and the nature of the magnetic field, both of the VLBI scale jet and in the region where the jet is produced.

We present five sources that have been monitored at 3 mm using the GMVA from 2008 until 2012. These sources have been analysed with near-in-time 7 mm maps from the Very Long Baseline Array (VLBA), γ -ray light curves from the Fermi/LAT space telescope and cm to mm-wave total-intensity light curves. In one source, OJ 287, the source has additionally been analysed with monthly imaging at 7 mm with the VLBA and near-in-time 2 cm VLBI maps. We use these resources to analyse high angular resolution structural and spectral changes and see if they correlate with flaring (both radio and γ -ray) activity and with VLBI component ejections. By spectrally decomposing sources, we can determine the spatially resolved magnetic field structure in the jets at the highest yet performed resolutions and at frequencies that are near or above the turnover frequency for synchrotron self-absorption (SSA). We compute the magnetic field estimates from SSA theory and by assuming equipartition between magnetic fields and relativistic particle energies.

All sources analysed exhibit downstream quasi-stationary features which sometimes exhibit higher brightness temperatures and flux density variability than the VLBI “core”, which we interpret as being recollimation or oblique shocks. We find that γ -ray flaring, mm-wave radio flaring and changes in opacity from optically thick to optically thin, is in many cases consistent with component ejections past both the VLBI “core” and these quasi-stationary downstream features. We find decreasing apparent brightness temperatures and Doppler factors as a function of increased “core” separation, which is interpreted as consistent with a slowly accelerating jet over the de-projected inner ~ 10 -20 pc. Assuming equipartition between magnetic energy and relativistic particle energy, the magnetic field strengths within the jets at these scales are, on average, between $B \sim 0.3 - 0.9$ G, with the highest strengths found within the VLBI “core”. From the observed gradient in magnetic field strengths, we can place the mm-wave “core” ~ 1 -3 pc downstream of the base of the jet. Additionally, we estimate the the magnetic field is $B_{\text{apex}} \sim 3000 - 18000$ G at the base of the jet. We computed theoretical estimates based on jet production under magnetically arrested disks (MAD) and find our estimates to be consistent.

In the BL Lac source OJ 287, we included monthly 7 mm and near-in-time 2 cm VLBA maps to provide full kinematics and increased spectral coverage. Following a previously reported radical change in inner-jet PA of $\sim 100^\circ$, we find unusually discrepant PAs compared with the previous jet direction, that follow very different trajectories. The source exhibits a downstream quasi-stationary feature that at times has higher brightness temperatures than the “core”. The source also exhibited a large change in apparent component speeds as compared with previous epochs, which we propose could be due to changes in jet pressure causing changes in the location of downstream recollimation or oblique shocks and hence their line-of-sight viewing angle. The addition of 2 cm VLBA data allows for a comparison of magnetic fields derived from SSA and equipartition. The magnetic field estimates are consistent within 20%, with $B_{\text{SSA}} \geq 1.6$ G and $B_{\text{equi}} \geq 1.2$ G in the “core” and $B_{\text{SSA}} \leq 0.4$ G and $B_{\text{equi}} \leq 0.3$ G in the stationary feature. Gamma-ray emission appears to originate in the “core” and the stationary feature. The decrease in magnetic field strengths places the mm-wave “core” downstream of the jet base by ≤ 6 pc and likely outside of the BLR. This, combined with the results in other sources are consistent with γ -rays being produced in the vicinity of the VLBI “core” or in further downstream stationary features, which are likely over a parsec downstream of the central black hole, favouring the scenario of photons being up-scattered within the relativistic jet.

Zusammenfassung

Die Kerne aktiver Galaxien (engl. Active Galactic Nuclei; AGN) befinden sich im Zentrum besonders leuchtkräftiger Galaxien. Diese AGN erzeugen starke relativistische Plasmaströme (Jets), die von einem massiven schwarzen Loch im Zentrum der Galaxie ausgehen. Wenn diese Jets in Richtung des Beobachters zeigen, erscheinen sie auf Grund relativistischer Effekte besonders hell, variabel und schnell. Solche auf den Beobachter ausgerichteten AGN-Jets werden Blazare genannt. Mittels der sogenannten Radiointerferometrie auf sehr langen Basislinien (engl. Very Long Baseline Interferometry; VLBI) lassen sich diese Galaxienkerne und ihre Jets im Detail und mit größtmöglicher Auflösung untersuchen. VLBI Beobachtungen bei einer Wellenlänge von 3 mm mit dem Global Millimeter VLBI Array (GMVA) und bei 7 mm Wellenlänge mit dem Very Long Baseline Array (VLBA) liefern höchstauflösende Radiokarten. In dieser Dissertation werden diesbezüglich neue Ergebnisse aus einem laufenden Blazar-Überwachungsprogramm vorgestellt, wobei die Auswahl der Objekte sich auf Quellen beschränkt, die besonders hell im Gamma-Strahlungsbereich des elektromagnetischen Spektrums sind, auf sogenannte Gamma-ray Blazare.

Die physikalischen Prozesse, die Jets und deren Gamma-Strahlung erzeugen, sind noch nicht gut verstanden. Die Jets werden wahrscheinlich durch Konversion von Gravitationsenergie im Umfeld schwarzer Löcher mit hochrelativistischen Teilchen aufgeladen und auf nahezu Lichtgeschwindigkeit beschleunigt. Die Details dieses Mechanismus und die Rolle, die das Magnetfeld dabei spielt, sind jedoch noch nicht vollständig geklärt. Die schon seit längerem bekannte Emission von Gamma-Strahlung in Blazaren wird durch inverse Compton Streuung der Synchrotronphotonen aus dem Radiojet in den Gamma-Bereich erklärt. Der genaue Ursprung der, für die Streuung notwendigen Saat-Photonen (entweder direkt aus dem Jet oder aus einem äußeren Photonenfeld), und die genaue räumliche Lokalisierung des Gamma-Emissionsgebietes ist noch unklar.

Die vorliegende Arbeit zielt darauf ab, den möglichen Ursprung der Gamma-Emissionsgebiete innerhalb der Blazar-Jets, deren physikalische Struktur, sowie die Position der VLBI Komponenten relativ zum Jetursprung, zu bestimmen. Auch wird versucht das Magnetfeld im Jet, auf VLBI Skalen und an der Basis einzugrenzen.

In dieser Arbeit werden 5 Radioquellen, die mit dem GMVA bei 3 mm Wellenlänge

zwischen 2008 und 2012 regelmäßig beobachtet wurden, vorgestellt. Die Datenanalyse bezieht auch zeitnahe 7 mm VLBA-Karten, Gammalichtkurven des Fermi/LAT Satelliten, sowie Radiolichtkurven aus dem cm- bis mm-Wellenlängenbereich mit ein. Für eine dieser Radioquelle, OJ287, wurden sogar 7 mm VLBA Karten, die mit monatlicher Kadenz gemessen wurden, sowie zeitnahe VLBI Karten bei 2 cm Wellenlänge mit berücksichtigt. Diese Daten werden benutzt, um Struktur und Spektral-Variationen mit hoher Winkelauflösung zu erfassen, und um diese Variationen mit Flussdichteausbrüchen (sowohl im Radio- als auch im Gamma-Bereich) und VLBI Komponentenauswürfen zu korrelieren. Durch spektrale Dekomposition der beobachteten Quellen kann man die Magnetfeldstruktur in den Jets bei Frequenzen in der Nähe, oder oberhalb der durch Synchrotron-Selbstabsorption (SSA) bestimmten Turnover-Frequenz, mit höchster Auflösung bestimmen. Dabei wird die Stärke des Magnetfeldes im Rahmen der Theorie der Synchrotron-Selbstabsorption, und durch Annahme von Energiegleichverteilung zwischen Magnetfeldern und relativistischen Teilchen, abgeschätzt.

Alle untersuchten Quellen haben stromabwärtig gelegene, quasi-stationäre Jetkomponenten, die manchmal sogar höhere Strahlungstemperaturen und eine stärkere Flussdichtevervariabilität als der eigentliche VLBI-Kern zeigen. Diese Komponenten werden als Rekollimations-Stoßwellen oder schiefe Schocks interpretiert. Gammastrahlungs-Ausbrüche, mm-radio Flares und der Übergang von optisch dicker zu optische dünner Emission, scheinen in vielen Fällen mit Auswürfen von Jetkomponenten aus dem VLBI Kern, oder mit der Passage einer Jet-Komponente durch ein quasi-stationäres Gebiet, zusammen zu hängen. Ein weiterer Befund ist die Abnahme der scheinbaren Strahlungstemperaturen und des Doppler-Faktors mit zunehmendem Kernabstand. Dies ist konsistent mit der Annahme langsamer Jetbeschleunigung innerhalb von 10-20 pc deprojiziertem Kernabstand. Äquipartition zwischen magnetischer Energie und Energie in relativistischen Teilchen vorausgesetzt, berechnet sich die Magnetfeldstärke in diesem Gebiet zu durchschnittlich $B \sim 0.3 - 0.9 \text{ G}$, mit den höheren Werten innerhalb des VLBI-Kernes. Aus dem beobachteten Gradienten der Magnetfeldstärke leitet sich die Entfernung der Jetbasis vom stromabwärtig gelegenen VLBI-Kern zu $\sim 1-3 \text{ pc}$ ab. Die Magnetfeldstärke an der Jetbasis wird zu $B_{\text{base}} \sim 3000 - 18000 \text{ G}$ abgeschätzt, was in Übereinstimmung mit Vorhersagen erscheint, in denen Jets durch magnetisch arretierte Akkretionsscheiben (magnetically arrested discs; MAD) erzeugt werden.

Für das BL Lac Objekt OJ287 wurden monatlich gemessene 7 mm Karten und zeitnahe 2 cm VLBA Karten verwendet, um eine umfassendere Kinematik und

vergrößerte spektrale Abdeckung zu erhalten. In Übereinstimmung mit publizierten radikalen Änderungen des Positionswinkels des inneren Jets um PA of $\sim 100^\circ$, werden auch hier Positionswinkel gefunden, die um $\sim 60^\circ$ von der vor-maligen Jetrichtung abweichen. Im Jet von OJ 287 gibt es ein stromabwärts gelegenes quasi-stationäres Gebiet, daß bei manchen Epochen eine höhere Strahlungstemperatur aufweist, als der VLBI-Kern. Verglichen mit früheren Beobachtungen, zeigt die Quelle ausserdem starke Variationen in den gemessenen scheinbaren Geschwindigkeiten ihrer Jetkomponenten. Dies könnte durch Druckänderungen im Jet erklärt werden, da der innere Druck die Lage der stromabwärtig gelegenen Rekollimations-Schocks, bzw. die Orientierung der schiefen Schocks, relative zum Beobachter beeinflußt. Die Hinzunahme der 2 cm VLBA Daten, ermöglicht einen Vergleich der aus Äquipartition und Synchrotron-Selbstabsorption abgeleiteten Magnetfeldstärken. Diese stimmen innerhalb von 20 % miteinander überein, wobei man für den VLBI-Kern $B_{\text{SSA}} \geq 1.6 \text{ G}$ and $B_{\text{equi}} \geq 1.2 \text{ G}$ erhält, und für die stationäre Jetkomponente $B_{\text{SSA}} \leq 0.4 \text{ G}$ and $B_{\text{equi}} \leq 0.3 \text{ G}$. Die Gammastrahlung scheint ihren Ursprung sowohl im Kern, also auch in der stationären Jetkomponente zu haben. Mittels der gemessenen Abnahme des Magnetfeldes entlang des Jets, berechnet man, daß der mm-VLBI Kern $\leq 6 \text{ pc}$ stromabwärts vom eigentlichen Jetursprung gelegen ist, also außerhalb der Broad Line Region (BLR). Dies, zusammen mit den Ergebnissen für die anderen Quellen ist konsistent mit der Auffassung, daß die Gamma-Strahlung in der Nachbarschaft des VLBI-Kernes und/oder in weiter stromabwärts gelegenen stationären Komponenten, also in Regionen, die einige Parsek vom schwarzen Loch entfernt sind, erzeugt wird. Damit wird das Model der Gammastrahlungs-Erzeugung durch Hoch-Streuung der Photonen *innerhalb* des Jets favorisiert.

Declaration of Authorship

I, Jeffrey Hodgson, declare that this thesis titled, 'Ultra high resolution observations of Gamma-ray blazars' and the work presented in it are my own. I confirm that:

- This work was done wholly or mainly while in candidature for a research degree at this University.
- Where any part of this thesis has previously been submitted for a degree or any other qualification at this University or any other institution, this has been clearly stated.
- Where I have consulted the published work of others, this is always clearly attributed.
- Where I have quoted from the work of others, the source is always given. With the exception of such quotations, this thesis is entirely my own work.
- I have acknowledged all main sources of help.
- Where the thesis is based on work done by myself jointly with others, I have made clear exactly what was done by others and what I have contributed myself.

Signed: _____

Date: _____

Acknowledgements

I wish to take this opportunity to thank Prof. Dr. Anton Zensus and the International Max-Planck Research School (IMPRS), without who's support, funding and guidance, I would not have completed my doctorate. I would also like to thank the members of my thesis committee, Dr. Thomas Krichbaum, Prof. Eduardo Ros, Prof. Andreas Eckart and Dr. Richard Porcas who's direction and guidance have helped immensely.

Within the VLBI group, I have had the pleasure of working with and learning from some of the greatest minds in the field. In addition to those mentioned previously, I would like to thank Doctors Tuomas Savolainen, Alessandra Bertarini, Uwe Bach, Manolis Angelakis, Helge Rottmann, Andrei Lobanov, Alan Roy and Walter Alef, who have all helped me in my technical and scientific understanding.

I would like to extend a particular thanks to Prof. Alan Marscher and Prof. Svetlana Jorstad, who took me in for a month in Boston and gave me a huge boost in my scientific development.

I must also thank my office mates Florent, Dhanya, Ioannis and Bindu, as well as my fellow VLBI group students Vassilis and Bia for putting up with me and my bad jokes over the years. A special thanks to the Friday night regulars, Richard, Ian, Paulo, Olaf, and many others for keeping me entertained and sane during my time here. And to Raluca, who without your patience, caring, and putting up with my late nights, I could not have imagined completing this thesis.

And a final, particularly special thanks to my supervisor, Thomas Krichbaum, whose infectious enthusiasm for science always made him a great pleasure to work with. His great depth of knowledge, scientific understanding and always approachable personality has allowed me to grow into the astronomer I have become.

Contents

Abstract	iv
Zusammenfassung	vi
Declaration of Authorship	ix
Acknowledgements	x
List of Figures	xvi
List of Tables	xix
1 Introduction	1
1.1 A Brief History of Radio Astronomy	2
1.1.1 Significant Discoveries in Radio Astronomy	7
1.1.2 Famous Telescopes	10
1.2 Interferometry	11
1.3 Very Long Baseline Interferometry	13
1.3.0.1 Other VLBI Applications	16
1.3.1 A Brief History of mm-VLBI	17
1.3.2 The Global mm-VLBI Array	20
1.4 Motivations for mm-VLBI	21
2 Imaging, Calibrating and Data Acquisition	23
2.1 Imaging in Reverse	24
2.1.1 The Final VLBI Image	24
2.1.2 The Dirty Image	24
2.1.3 The Fourier Transform	25
2.1.4 The uv Plane and the Beam	30
2.1.5 Flux Density and Source Brightness	32
2.1.6 Convolution and Deconvolution	32
2.1.6.1 The Point Spread Function	34
2.1.6.2 Aperture Synthesis	35
2.1.7 The CLEAN algorithm	35
2.1.8 Self-Calibration	37
2.1.8.1 Closure Quantities	38
2.1.9 uv-Tapering	39

2.1.10	Amplitude Self-Calibration	39
2.1.11	Model-Fitting	40
2.2	Calibration	40
2.2.1	Phase Calibration	42
2.2.1.1	Delay	42
2.2.1.2	Rate	43
2.2.1.3	Fringe Fitting	43
2.2.1.4	Manual Phase Calibration	44
2.2.1.5	Global Fringe-fit	45
2.2.2	Amplitude Calibration	45
2.2.2.1	System Noise and the SEFD	46
2.2.2.2	System Temperature	46
2.2.2.3	Opacity	47
2.2.3	Polarisation Calibration	47
2.3	Correlation	48
2.3.1	The correlation function and visibilities	50
2.3.2	Types of Correlators	52
2.3.3	Coherence Time and Averaging	52
2.4	Sampling and Recording	53
2.4.1	Bit-Rate	53
2.4.2	Recording Rate and the Nyquist Frequency	54
2.4.3	Sampling, Bandwidth and Sensitivity	54
2.5	Radio Telescopes	55
2.5.1	The Antenna Pattern	55
2.5.2	Detection	56
2.5.3	Effective Aperture and Efficiency	57
2.5.4	Surface Efficiency	58
2.5.5	Receivers	58
2.6	Summary	59
3	Scientific Background	60
3.1	The Radio Sky	61
3.2	The Anatomy of a Radio Galaxy	61
3.2.1	FRI and FRII	63
3.3	Quasars, Blazars and AGN Unification	64
3.4	Relativistic Effects	66
3.4.1	Superluminal motion	66
3.4.2	Doppler Beaming, Time Dilation and Length Contraction	68
3.5	The Thermal Spectrum and Planck's Law	69
3.5.1	Synchrotron Emission	72
3.5.2	Synchrotron Self-absorption	73
3.5.3	Compton Scattering	74
3.5.3.1	X-rays or Gamma-rays	75
3.6	Black Holes	75
3.7	How and Why Are Jets Formed?	76
3.8	Shocks in Jets and Jet Propagation	79
3.9	Historical γ -ray Observations.	82

3.9.1	Early Gamma-ray Observatories	82
3.9.2	The EGRET era	82
3.9.3	The Fermi/LAT era	85
4	A Global 3 mm VLBI survey of Fermi/LAT detected γ-ray blazars.	88
4.1	Motivations and Context	89
4.1.1	Previous Surveys	90
4.1.1.1	BU-VLBA 43 GHz Monitoring	91
4.2	Observations	94
4.2.1	Sample Selection	94
4.2.2	86 GHz GMVA	94
4.2.3	43 GHz	96
4.2.4	Total-Intensity Measurements	96
4.2.4.1	Radio	96
4.2.4.2	Gamma-rays	97
4.2.4.3	LAT Data Reduction	97
4.3	Analysis	98
4.3.1	“Core” Identification	98
4.3.2	Morphology, Spectral Properties and Component Identifi- cation	98
4.3.2.1	Quasi-Stationary Features	99
4.3.2.2	Travelling Components	99
4.3.3	Kinematics	99
4.3.4	Trailing Components	100
4.3.5	Flaring Activity and Ejection Relations	100
4.3.6	Magnetic Fields	100
4.3.6.1	Magnetic Field from SSA	101
4.3.6.2	Magnetic Field from Equipartition	102
4.3.7	Distance to SMBH	103
4.3.8	Location of γ -ray Emitting Regions	104
4.3.9	Magnetic Field in the Broad-Line Region and the Central Engine	105
4.3.10	Imaging Errors and Error Propagation	105
4.4	Results	107
4.4.1	Flux Accuracy and Source Compactness	107
4.4.2	0716+714	109
4.4.2.1	Introduction	109
4.4.2.2	Core Identification	109
4.4.2.3	Morphology	110
4.4.2.4	Spectral Properties	112
4.4.2.5	Kinematics	113
4.4.2.6	Light Curves and Ejection Relations	114
4.4.2.7	Magnetic Fields and Distance to Jet Base	115
4.4.3	0836+710	117
4.4.3.1	Introduction	117
4.4.3.2	Core Identification	117
4.4.3.3	Morphology	118

4.4.3.4	Spectral Properties	119
4.4.3.5	Kinematics	120
4.4.3.6	Light-Curves and Ejection Relations	121
4.4.3.7	Magnetic Fields	122
4.4.3.8	Distance to Black Hole and Magnetic Field Estimates	122
4.4.4	3C 273	124
4.4.4.1	Introduction	124
4.4.4.2	Core Identification	124
4.4.4.3	Morphology	125
4.4.4.4	Spectral Properties	128
4.4.4.5	Kinematics	128
4.4.4.6	Light-Curves and Ejection Relations	130
4.4.4.7	Magnetic Fields	131
4.4.4.8	Distance to Black Hole and Magnetic Field Estimates	131
4.4.4.9	Location of γ -ray emitting regions	131
4.4.5	BL Lacertae	133
4.4.5.1	Introduction	133
4.4.5.2	Core Identification	133
4.4.5.3	Morphology	134
4.4.5.4	Spectral Properties	137
4.4.5.5	Kinematics	137
4.4.5.6	Light-Curves and Ejection Relations	139
4.4.5.7	Magnetic Fields	140
4.4.5.8	Distance to Black Hole and Magnetic Field Estimates	140
4.5	Discussion	140
4.5.1	Morphology	141
4.5.2	Kinematics	142
4.5.2.1	Spectral Properties	143
4.5.3	Ejection Relations	145
4.5.4	Magnetic Fields	146
4.5.4.1	Distance to the Jet Base and B-field at Jet Base	151
4.5.4.2	Apparant Brightness Temperature	153
4.5.5	Equipartition Doppler Factor	155
4.6	Summary	156
5	OJ287	160
5.1	Introduction	160
5.2	Observations and Data Analysis	161
5.2.1	GMVA Observations	161
5.2.2	VLBA Observations at 15 and 43 GHz	162
5.2.3	Long-term Total Intensity Lightcurves	163
5.3	Results	164
5.3.1	Morphology	164
5.3.2	Stationary Features and "Core" Identification	165
5.3.3	Moving Component Identification and Kinematics	167
5.3.4	Position Angle and Trajectories	168
5.3.5	Light-Curves and Spectral Properties	170

5.3.5.1	Total Intensity Radio	170
5.3.5.2	VLBI Component Flux Density Variability	170
5.3.5.3	Spectral Decomposition	173
5.3.5.4	Gamma-Rays	174
5.4	Analysis	174
5.4.1	Component Speeds and Doppler Factor	174
5.4.2	Magnetic Fields	175
5.5	Discussion and Interpretation	178
5.5.1	Jet opening angle	178
5.5.2	Gamma-Component Ejection Relations	178
5.5.2.1	Flaring Activity Within Stationary Feature	179
5.5.3	Physical Nature of the “Core” and Stationary Feature	180
5.5.4	Magnetic fields	181
5.5.5	Magnetic field strength in the BLR and at the SMBH	182
5.5.6	Location of γ -ray Emission	184
5.5.7	Apparent Speeds and “Jet-Wobbling”	185
5.5.7.1	Large PA changes	185
5.6	Summary	187
6	Conclusions and Future Perspectives	194
A	Appendix A - Derived Magnetic Field Tables	199
B	Appendix B - Modelfits	204
B.1	0716+714	204
B.2	0836+710	207
B.3	3C 273	210
B.4	BL Lac	214
C	Appendix C - OJ 287 Modelfits	217
	References	226
	Erklärung	241
	Lebenslauf	242

List of Figures

1.1	The first radio image	4
1.2	The discovery of the spiral structure of the Milky Way	5
1.3	The structure of an AGN	6
1.4	Radio map of Tycho's supernova	7
1.5	Superimposed image of Centaurus A	9
1.6	The first confirmed superluminal motion	10
1.7	Global mm-array in 1985	12
1.8	Sketch of an interferometer	13
1.9	First trans-Atlantic 7 mm maps of 3C 84	14
1.10	7 mm to optical resolution comparison	16
1.11	The first 3 mm observations.	17
1.12	Early 100 GHz maps	18
1.13	Global mm-array VLBI Array map.	20
2.1	Final VLBI map	24
2.2	Dirty VLBI map	25
2.3	Dirty residuals	26
2.4	FFT of a cat and a duck	28
2.5	Inverse FFT with amplitudes switched.	28
2.6	FFT high-pass filtered	29
2.7	FFT Low-pass filtered	29
2.8	The uv-plane of OJ 287	30
2.9	OJ 287 with short baselines removed.	31
2.10	OJ 287 with long baselines removed.	31
2.11	Almost perfect Point Spread Function.	34
2.12	Non-perfect Point Spread Function.	35
2.13	Initial CLEANing	36
2.14	Placing windows for CLEANing	37
2.15	Early radplot.	39
2.16	Final AIPS Calibration.	41
2.17	AIPS Initial Plot	42
2.18	AIPS Manual Phase Cal	44
2.19	AIPS Fringe Fitting.	45
2.20	Polarisation diagram.	48
2.21	Geometric delay sketch	50
2.22	Correlation sketch	51
2.23	1,2 and 3-bit quantisation of a sinusoid.	53
2.24	Sketch of the beam pattern of a radio telescope	56

2.25 Sketch of the radio telescope optics	57
2.26 VLBI Signal Path	59
3.1 AGN Distribution in Northern sky	61
3.2 ATCA, Cent A and Moon composite image	62
3.3 Annotated VLA image of Cygnus A	63
3.4 Zooming in on Cygnus A	64
3.5 AGN	65
3.6 Sketch of superluminal motion	67
3.7 Sketch of an SED	70
3.8 SED of OJ 287	71
3.9 Sketch of synchrotron emission	72
3.10 Sketch of inverse-Compton scattering	74
3.11 Sketch of the structure of accretion flow	77
3.12 Shock-in-jet schematic	79
3.13 Jet simulation	80
3.14 Schematic of recollimation shock formation	82
3.15 LAT Diagram	86
4.1 Typical Core-Jet Morphology	91
4.2 γ -ray emitting region sketch	104
4.3 VLBI map 2009.35 - 0716+714	110
4.4 VLBI map 2009.86 - 0716+714	111
4.5 VLBI map 2010.36 - 0716+714	111
4.6 VLBI map 2011.35 - 0716+714	111
4.7 VLBI map 2011.77 - 0716+714	112
4.8 VLBI map 2012.38 - 0716+714	112
4.9 Spectral Index Evolution 0716	113
4.10 Component separation 0716	113
4.11 Light-Curves 0716+714	114
4.12 VLBI map 2009.86 - 0836+710	118
4.13 VLBI map 2010.36 - 0836+710	118
4.14 VLBI map 2011.35 - 0836+710	119
4.15 VLBI map 2011.77 - 0836+710	119
4.16 VLBI map 2012.46 - 0836+710	119
4.17 Spectral Index Evolution 0836	120
4.18 Component separation 0836	120
4.19 Light-Curves 0836+710	121
4.20 VLBI map 2008.78 - 3C 273	126
4.21 VLBI map 2009.35 - 3C 273	126
4.22 VLBI map 2009.86 - 3C 273	126
4.23 VLBI map 2010.36 - 3C 273	127
4.24 VLBI map 2011.35 - 3C 273	127
4.25 VLBI map 2012.38 - 3C 273	127
4.26 Spectral Index Evolution 3C 273	128
4.27 Component separation 3C 273	128
4.28 Light-Curves 3C 273	130

4.29 VLBI map 2009.35 - BL Lacertae	134
4.30 VLBI map 2009.86 - BL Lacertae	135
4.31 VLBI map 2010.36 - BL Lacertae	135
4.32 VLBI map 2011.35 - BL Lacertae	136
4.33 VLBI map 2012.38 - BL Lacertae	136
4.34 Spectral Index Evolution BL Lacertae	137
4.35 Kinematics for BL Lac	138
4.36 Light-Curves BL Lac	139
4.37 Extended structure of 0716+714	141
4.38 All spectral indices	144
4.39 All B-fields (SSA)	147
4.40 All B-fields (equi)	150
4.41 Binned B-fields (equi)	151
4.42 Histogram of brightness temperatures as a function of "core" separation	153
4.43 All equipartition brightness temperatures	155
4.44 Histogram of equipartition Doppler factor as a function of "core" separation	156
5.1 OJ 287 Natural beam maps at 15, 43 and 86 GHz	163
5.2 Super-resolved maps of OJ 287 at 15, 43 and 86 GHz.	163
5.3 All 7 mm model-fits of OJ 287,	164
5.4 Multi-frequency light-curves in OJ 287	166
5.5 Evolution of PA in OJ 287	167
5.6 Component trajectories in OJ 287	168
5.7 Previous jet direction of OJ 287	169
5.8 Spectral decomposition of OJ 287	171
5.9 Evolution of α in OJ 287	172
5.10 Apparant component speeds as a function of "core" ejection time in OJ 287	172
5.11 Sketch of large PA change interpretation.	186
5.12 3 mm maps of OJ 287 (1)	190
5.13 3 mm maps of OJ 287 (2)	191
5.14 3 mm maps of OJ 287 (3)	192
5.15 3 mm maps of OJ 287 (4)	193

List of Tables

1.1	Overview of stations used in global 3 mm VLBI observations	21
4.1	Survey overview	95
4.2	Survey overview	95
4.3	Survey overview	101
4.4	Source Compactness	108
4.5	0716 Single Dish	109
4.6	0716 Averaged Values	109
4.7	0716 Kinematics	114
4.8	0716 B-field Derived Properties	116
4.9	0836 Single Dish	117
4.10	0836 Averaged Values	117
4.11	0836 Kinematics	121
4.12	0836 B-field Derived Properties.	123
4.13	3C 273 Single Dish	124
4.14	3C 273 Averaged Values	124
4.15	3C 273 Kinematics	129
4.16	3C 273 B-field Derived Properties.	132
4.17	BL Lac parameter overview	133
4.18	BL Lac Averaged Values	133
4.19	BL Lac Kinematics	138
4.20	Variability of β_{app}	142
4.21	Averages on limits on B-fields.	148
4.22	Average distances to jet base and magnetic field estimates.	152
5.1	Overview of VLBI observations	161
5.2	Overview of stations used in global 3 mm VLBI observations	162
5.3	Overview of radio and γ flares	173
5.4	Table of fitted components and derived properties	175
5.5	Current and historical component ejections.	176
5.6	Computed spectral indices for component C and S	176
5.7	Table of derived values from SSA and equipartition	177
5.8	Stationary feature γ -ray relations.	180
5.9	Average properties in “Core” and stationary feature.	182
A.1	0716+714 B-fields	200
A.2	0836+710 B-fields	201
A.3	3C 273 B-fields	202

A.4	BL Lac B-fields	203
B.1	Table of model-fit parameters	204
B.1	Table of model-fit parameters	205
B.1	Table of model-fit parameters	206
B.2	Table of model-fit parameters	207
B.2	Table of model-fit parameters	208
B.3	Table of model-fit parameters	210
B.3	Table of model-fit parameters	211
B.3	Table of model-fit parameters	212
B.3	Table of model-fit parameters	213
B.4	Table of model-fit parameters	214
B.4	Table of model-fit parameters	215
B.4	Table of model-fit parameters	216
C.1	Table of model-fit parameters	217
C.1	Table of model-fit parameters	218
C.1	Table of model-fit parameters	219
C.1	Table of model-fit parameters	220
C.1	Table of model-fit parameters	221
C.1	Table of model-fit parameters	222
C.1	Table of model-fit parameters	223
C.1	Table of model-fit parameters	224
C.1	Table of model-fit parameters	225

Chapter 1

Introduction

Blazars are a form of Active Galactic Nuclei (AGN) where relativistic plasma flows known as jets - formed in processes not yet fully understood - are directed almost exactly towards us here on Earth (Fig. 1.3). They are the brightest, most energetic objects in the known universe, giving astronomers and physicists access to the universe's most extreme laboratories. The processes that produce these jets are at the boundaries of our knowledge, where relativity - the study of the large - and quantum physics - the study of the very small - come together. Their understanding requires peering into the hearts of these incredible objects at the highest possible resolutions and at all accessible wavelengths. Very Long Baseline Interferometry (VLBI) is an observational technique allowing radio telescopes at very large distances to function as one large telescope equivalent to the distance between them - so called aperture synthesis. Operating at the highest frequencies allows us to peer in at ever higher and higher resolutions. The Global mm-VLBI Array (GMVA) is the highest frequency and hence highest resolution telescope capable of producing high fidelity astronomical images. Other telescopes such as the Event Horizon Telescope and the orbiting antenna RadioAstron can achieve higher angular resolutions, but their imaging capabilities are currently limited. Using the GMVA, we can explore the motion, magnetic fields and emission processes of blazars in a unique and groundbreaking way. In this thesis, we use the GMVA to explore the connection between the physics at the highest angular resolution with the highest energy physics in one of the universe's most extreme environments.

There are many excellent textbooks (e.g. [Taylor et al. 2008](#)) and other resources

describing radio astronomy, AGN science and astronomy in general. This chapter is my distilling of these sources, combined with my own experiences and notes from lectures given by respected radio astronomers such as Phil Diamond, Cormac Reynolds, Tuomos Savolainen and Rick Perley, many of whom have personally aided substantially in my studies.

1.1 A Brief History of Radio Astronomy

Astronomy,¹ according to the Oxford English Dictionary, is defined as:

The branch of science which deals with celestial objects, space, and the physical universe as a whole.

And then continues:

In ancient times, observation of the sun, moon, stars, and planets formed the basis of timekeeping and navigation. Astronomy was greatly furthered by the invention of the telescope, but modern observations are made in all parts of the spectrum, including X-ray and radio frequencies, using terrestrial and orbiting instruments and space probes.

Astronomy for millenia was confined to the world of what can be seen with the naked eye. Even for hundreds of years after the first use of telescopes on celestial objects by Galileo, astronomy was confined to the optical spectrum. It was not until the behaviour of electromagnetic fields were first derived by James Clerk Maxwell in the 19th century that we could begin exploring beyond the boundaries of the optical. His famous equations (Maxwell 1865):

$$\nabla \cdot \mathbf{D} = \rho$$

$$\nabla \cdot \mathbf{B} = 0$$

$$\nabla \times \mathbf{E} = -\frac{\partial \mathbf{B}}{\partial t}$$

$$\nabla \times \mathbf{H} = \mathbf{J} + \frac{\partial \mathbf{D}}{\partial t}$$

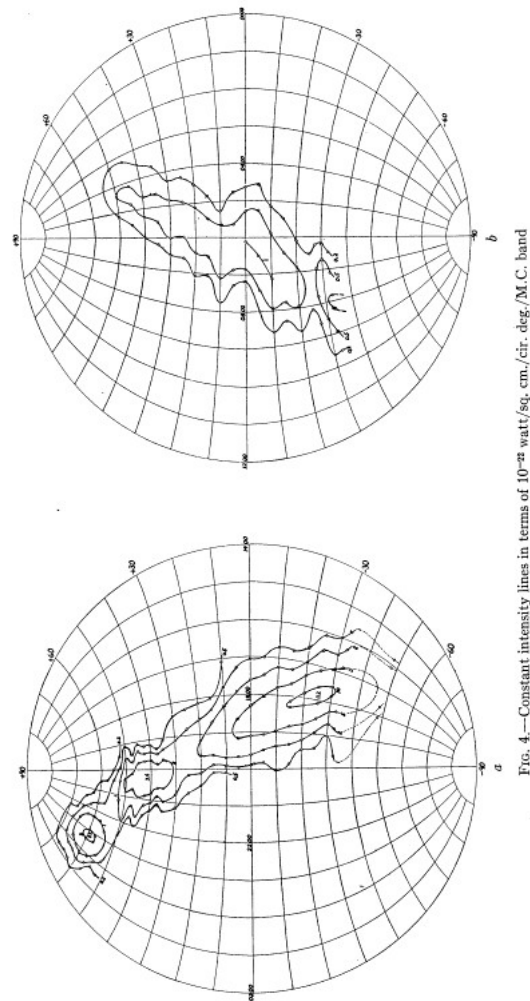
¹This section relies heavily on the excellent NRAO history website, available at http://www.nrao.edu/whatisra/hist_prehist.shtml

where D is the electric flux density, B is the magnetic flux density, E is the electric field and H is the magnetic field. These equations describe the entire behaviour of electromagnetic fields. He showed that two like charges (e.g. two North magnetic poles) attract whilst two unlike charges (e.g. a north and south magnetic pole) repel. He showed that the range of the force would drop off as an inverse square law. And most importantly for our purposes, he showed that a current could be induced in a wire with a varying magnetic field and conversely showed that a current in a wire could produce a magnetic field. Visible light, it turned out, was merely a small part of a much broader electromagnetic spectrum. Electromagnetic waves could be of longer wavelength (radio, infra-red) or shorter (X-rays, γ -rays), opening a whole new world to observe and explore.

The unit of frequency for electromagnetic waves is the Hertz (Hz) named after Heinrich Hertz, the physicist who first generated and detected radio waves, posthumously published after his time as the director of the Physics Institute in Bonn, Germany ([Hertz 1894](#)). He used a coil to generate a high voltage spark between two electrodes, which produced radio waves that were themselves detected by two narrowly separated coils. The properties he derived were consistent with the predictions of Maxwell's equations. Sadly, Hertz died at the age of 36 and it took others to progress his work.

Thomas Edison had proposed to detect radio waves from the sun ([Hey 1973](#)), a feat that was first unsuccessfully attempted and properly documented by [Willing & Scheiner \(1896\)](#). It was then attempted (also unsuccessfully) by Sir Oliver Lodge, likely due to a lack of sensitivity and interference ([Lodge 1900](#)). The lack of success in detecting the Sun was wrongly attributed to atmospheric absorption of radio waves, and French physicist Charles Nordman (1900) attempted to overcome this by performing experiments at high altitude, also unsuccessfully. Perhaps unluckily though, as he performed his experiments during a solar minimum.

It was not until 1932, when Karl G. Jansky (after whom the unit for radio flux density is named), serendipitously discovered a faint steady hiss of unknown origin in the course of his duties for Bell Labs ([Jansky 1979](#)). After noticing that the location of the peak in the signal was coming from the center of the Milky Way, he realised that he had discovered radio emission from it. Unfortunately, he was



© American Astronomical Society • Provided by the NASA Astrophysics Data System

FIGURE 1.1: The first radio image of the Milky Way published by [Reber \(1944\)](#)

not able to continue his work in astronomy and it was not until Grote Reber that the field of radio astronomy was truly born.

Building a parabolic dish for use in astronomy in his backyard using his own funds and time, he produced the first radio map of the Milky Way (Fig. 1.1) and discovered radio sources in Cygnus and Cassiopeia ([Reber 1944](#)). Development of radio astronomy was once again delayed, this time by World War 2. Reber continued building radio telescopes however, first in Hawaii and finally in Tasmania, where he died in 2002.

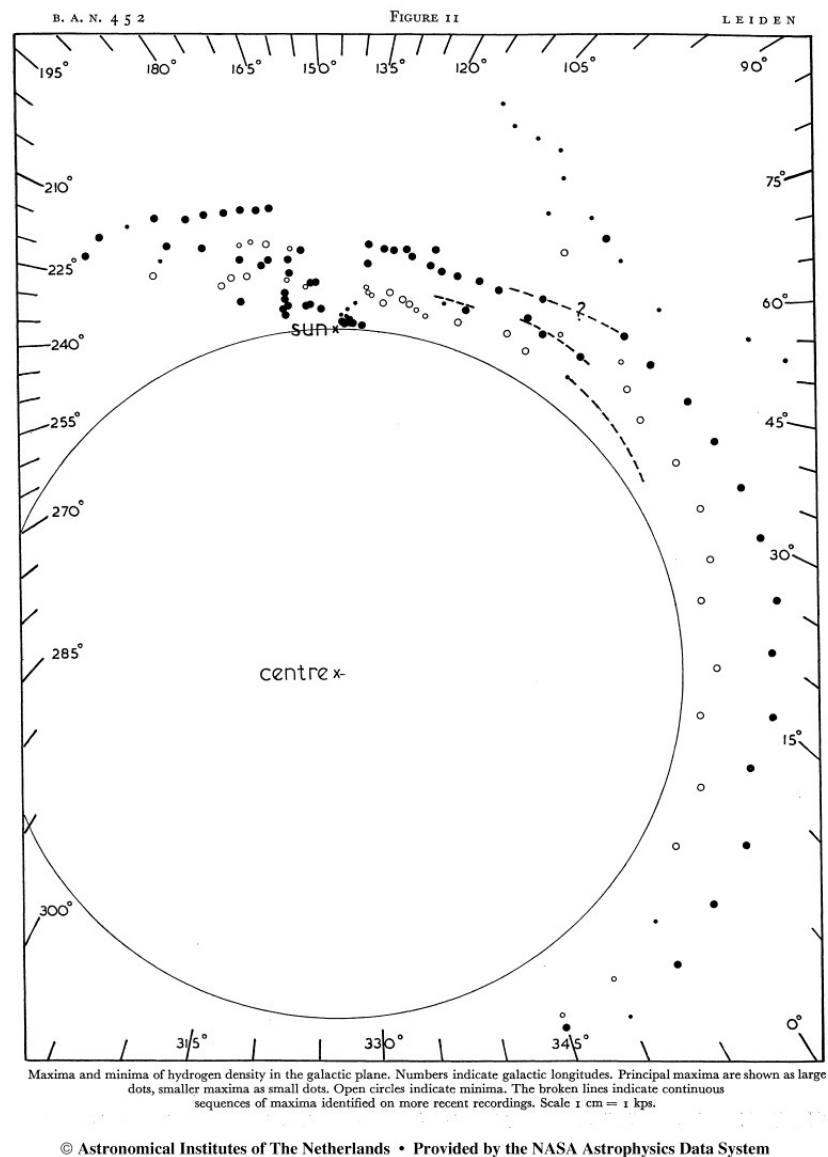


FIGURE 1.2: The discovery of the Milky Way's spiral structure by (Muller & Oort 1951)

Although the Second World War halted the development of radio astronomy, it did have some unexpected benefits. Several independent Commonwealth astronomers discovered radio emission from the Sun that interfered with their radar systems (e.g. Hey 1946). These discoveries spurred the development of better and more sensitive radio equipment and led to many highly qualified radio experts with little to do after the conclusion of the war.

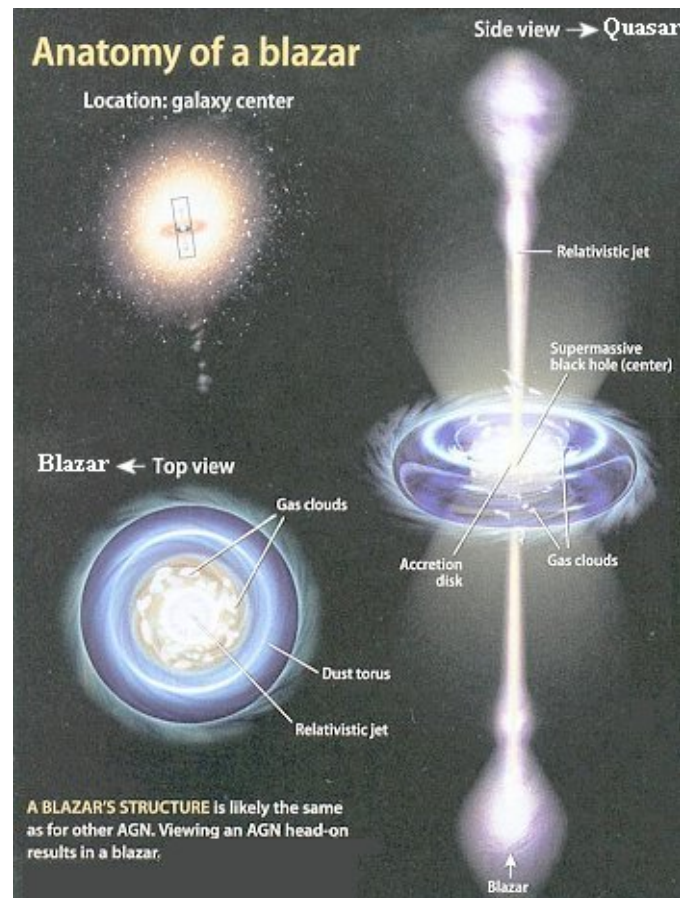


FIGURE 1.3: A sketch of Active Galactic Nuclei (AGN) from [Darling \(2012\)](#). An AGN is thought to be a super-massive black-hole (SMBH) surrounded by gas falling into it via an accretion disk. Whilst most of this gas will be lost to the SMBH, some of it is converted into massively powerful relativistic jets. When observed at large angles, the sources appear as radio galaxies, when we observe them at a small angle to the line-of-sight, they are BL Lacs or quasars and when they are observed at a small angle and are highly flux density variable, they are known as blazars.

Soon after WW2 finished, Dutch astronomer H.C. van de Hulst predicted the existence of the 21 cm hyperfine transition line in the ground state of Hydrogen, the so-called "H I" line ([van de Hulst 1946](#)). These lines were soon detected, first by [Ewen & Purcell \(1951\)](#) and then shortly after by [Muller & Oort \(1951\)](#), leading to the discovery of the spiral structure of the Milky Way ([Oort & Muller 1952](#); [van de Hulst et al. 1954](#)), Fig. 1.2. The field of spectroscopy was born.²

²Spectroscopy in astronomy is where sources either emit or absorb certain frequencies of light. For example, the gas around a star may absorb a very specific shade of yellow light, telling us what the gas is made of.

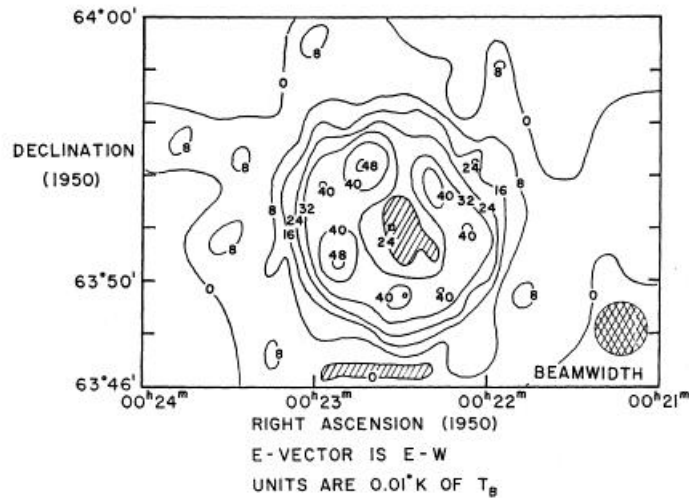


FIGURE 1.4: The first map of Tycho's 1572 supernova ([Dickel 1969](#))

1.1.1 Significant Discoveries in Radio Astronomy

Since its inception, radio astronomy has provided, and continues to provide, profound insights into our universe. In addition to the aforementioned discoveries of the Milky-Way's structure, perhaps the most recent example is the BICEP2 experiment. BICEP2 is a radio telescope in Antarctica designed to detect polarised radio signature from the earliest moments of the universe. This "B-mode" polarisation was detected and if the results hold up to scrutiny, it would confirm one of the major theories that explain the universe's first few nanoseconds after the Big Bang - Cosmic Inflation³ ([BICEP2 Collaboration et al. 2014](#)).

Indeed, it was radio astronomy that provided the first direct evidence of the Big Bang itself. The serendipitous discovery of the faint afterglow of the Big Bang called the Cosmic Microwave Background (CMB) by two Bell Labs engineers, Arno Penzias and Robert Wilson, for which they were awarded the Nobel Prize in 1974, changed how we saw ourselves in the universe. When using the extremely sensitive Horn Antenna in the United States, they identified an excess antenna temperature of 3.5K and attributed it to the CMB, as predicted by [Alpher et al. \(1953\)](#) and [Penzias & Wilson \(1965\)](#).

Another Nobel Prize winning discovery was that of pulsars, by Jocelyn Bell, although it famously went to her supervisor in what is widely regarded as one of

³Cosmic Inflation is the theory that in the very early universe, immediately after the Big Bang, the universe expanded faster than the speed of light.

the biggest travesties in the history of the Nobel Prize. Pulsars are characterised by rapidly repeating “pulses” of radio emission from what are now known to be rapidly rotating neutron stars, similar to the beam of a lighthouse ([Hewish et al. 1968](#)). Some pulsars, known as millisecond pulsars due to their extremely rapid rate of pulsing are extremely stable and can be used for very accurate timing. Astronomers are using this property to attempt the direct detection of gravitational waves, although to date these efforts have been unsuccessful ([Hobbs 2011](#)).

The existence of gravitational waves themselves and the confirmation of Einstein’s General Theory of Relativity (GR) ([Einstein 1916](#)) that they would imply, was also a Nobel Prize winning discovery. In [Taylor & Weisberg \(1989\)](#), it was shown that the slow-down in the pulse period of a binary⁴ pulsar system was exactly as predicted to be due to gravitational wave emission in GR. GR was recently tested to even higher precision by a colleague here at the Max-Planck-Institut fuer Radioastronomie in the binary system J0348+0432 ([Antoniadis et al. 2013](#)).

Supernova remnants were another unexpected discovery in the radio sky. Radio observations by [Hanbury Brown & Hazard \(1952\)](#) found radio emission coming from the Crab Nebula and was found to be the remnants of Tycho’s 1572 supernova and subsequently, maps were made to determine the structure of these remnants, Fig. 1.4 ([Dickel 1969](#)).

The final theme discussed here is the expansive radio emission detected in galaxies, particularly when compared to optical. This can be clearly demonstrated in the spectacular radio/optical/X-ray overlay of the AGN Centaurus A in Fig. 1.5. The radio emission, shown in orange, shows that the galaxy is much larger than it would seem from optical alone. The radio and X-ray emission seen there is caused by jets originating from the center of the galaxy. These jets, when aimed towards our line-of-sight, are called quasars or blazars and form the main topic of this thesis.

When the first high-resolution sequences of images were made of these blazars, a seemingly impossible discovery was made. The motion of plasma features (or “blobs”) emitted from the nuclei of blazars appeared to be moving faster than

⁴A binary is an astrophysical system where two objects are orbiting each other.

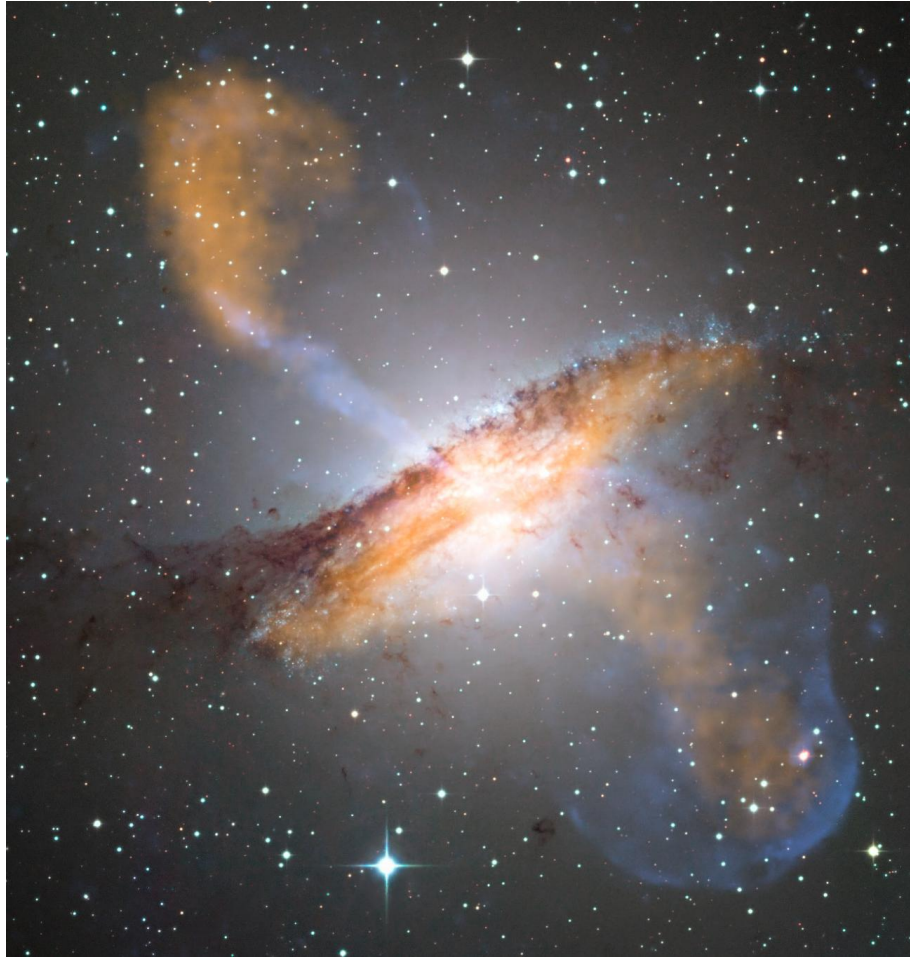


FIGURE 1.5: Radio/optical/X-ray overlay image of the AGN Centaurus A from [ESO \(2009\)](#). Colour composite image of Centaurus A, revealing the lobes and jets emanating from the active galaxy's central black hole. This is a composite of images obtained with three instruments, operating at very different wavelengths. The 870-micron submillimetre data, from LABOCA on APEX, are shown in orange. X-ray data from the Chandra X-ray Observatory are shown in blue. Visible light data from the Wide Field Imager (WFI) on the MPG/ESO 2.2 m telescope located at La Silla, Chile, show the stars and the galaxy's characteristic dust lane in close to "true colour" ([ESO 2009](#)).

the speed of light. An excellent review of early observations was given by [Cohen et al. \(1977\)](#), with the first confirmed case with high quality maps given by [Pearson et al. \(1981\)](#) (Fig. 1.6). This could be explained as an illusion as defined by Einstein's Special Theory of Relativity (SR) ([Einstein 1905](#)). Matter travelling at near light speed is close to catching up with the light it emits, causing us to observe apparent faster-than-light motion ([Blandford et al. 1977](#); [Blandford & Königl 1979](#)). Additionally, relativistic beaming will cause these sources to appear brighter and bendier than they really are (See: Section 3.4).

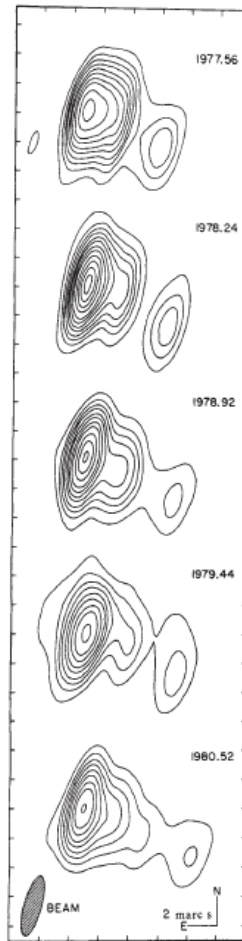


FIGURE 1.6: Although evidence for superluminal motion had been detected earlier, the first high quality VLBI map sequence of the blazar 3C 273B at 10.65 GHz confirmed the phenomenon ([Pearson et al. 1981](#)).

1.1.2 Famous Telescopes

It was around the end of World War 2 that radio astronomy began to be taken seriously by the scientific establishment. The Lovell Telescope at Jodrell Bank Observatory, which was originally built for detecting cosmic rays that were hypothesised to be interfering with radar systems ([Blackett & Lovell 1941](#)), was the first true modern steerable radio telescope. In its early years, it is credited with discovering the first supernova remnants, radio emission from Andromeda and even detecting Sputnik ([Lovell 1968](#)).

One of the worlds most famous radio telescopes, the 65m Parkes Telescope,

was built in Eastern Australia in 1961. It is most famous as the antenna that received live transmissions of the Apollo 11 moon landing, a (somewhat romanticised) story that has been immortalised in the 2000 film, *The Dish*. Its scientific achievements include discovering over half of all known pulsars, interstellar magnetic fields and spacecraft tracking ([Robertson 2010](#)).

Before the construction of the 110m Green Bank Telescope (GBT) in the United States after the earlier telescope collapsed, the largest steerable telescope in the world was the 100m Effelsberg Telescope, near Bonn, Germany. But the largest and arguably most famous radio telescope is the Arecibo Observatory in Puerto Rico, starring in famous movies such as *Goldeneye 007* and *Contact*.

1.2 Interferometry

These large telescopes have a significant limitation in that they have very low angular resolution. Indeed, at an observing wavelength of 21 cm, a telescope such as Effelsberg or the GBT has an angular resolution of ≈ 8 arcminutes, over 16 times lower than the ≈ 0.5 arcminute resolution of the human eye. As a comparison, the angular size of the moon is ≈ 30 arcminutes. One would need a dish of 40 km, in order to achieve the same resolution as the eye. To overcome this limitation, astronomers use a technique known as interferometry. Astronomical interferometry creates a ‘virtual’ telescope that has the angular resolution equivalent to the distance between two telescopes (a “baseline”) (Fig. 1.8). If many telescopes are used, images can be produced using a technique called Rotation Aperture Synthesis. The technique works by “correlating” two or more signals together to form “visibilities”, which can be used to make images of the source. While the technical aspects of Aperture Synthesis will be discussed in future chapters, the scientist who developed the technique, Martin Ryle, jointly won the Nobel Prize with Antony Hewish in 1974 for their efforts.

Inspired by the description of the Fourier transform by [Azad \(2012\)](#), if one imagines that a galaxy you’re observing is a smoothie, a radio interferometer is trying to measure the weights and types of ingredients in that smoothie. Unfortunately, we can only measure some of the ingredients in the smoothie, but given what we can measure, we can make a good guess as to what the actual ingredients are. Once we have that good guess, we can make our own smoothie

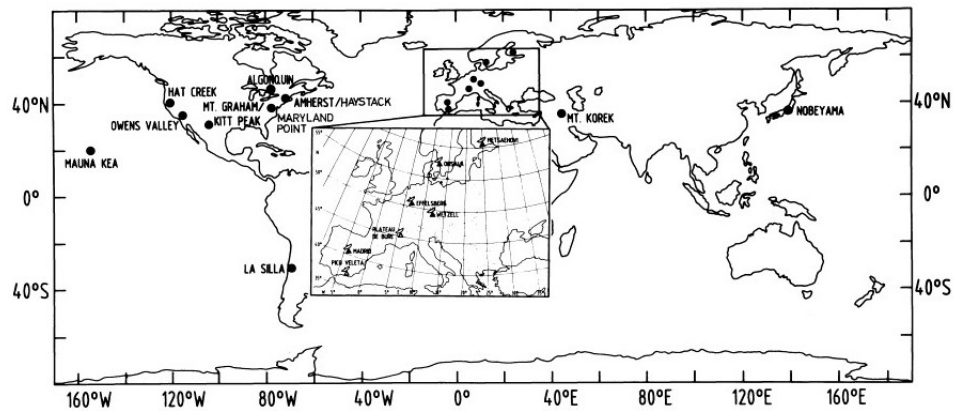


FIGURE 1.7: mm-VLBI capable telescopes in 1985, (Marcaide et al. 1985). A map of mm-wave telescopes currently participating in 3 mm global VLBI is shown in Fig. 1.13

from those ingredients. The more ‘smoothie telescopes’ there are, the more ingredients you can measure and the better the reconstructed smoothie. If you spread the ‘smoothie telescopes’ further apart, we can see the weights required in greater detail, say in milligrams rather than grams. Operating the ‘smoothie telescopes’ at higher frequency yields the same result - but being able to tell colours with better accuracy.

The development of radio interferometry for astronomical use, however, began on the other side of the world in Australia, although there is some disagreement about this, as Ryle & Vonberg (1946) were the first to publish an interferometric experiment. Scientists at the Commonwealth Scientific Industrial Research Organisation (CSIRO) created a sea interferometer that amongst other things detected solar emission and limited the size of Centaurus A to below 8 arc-minutes (Pawsey 1957a,9,9). Ryle & Scheuer (1955) went on to discover the double-lobed structure of Centaurus A, greatly enhancing our knowledge of the extragalactic universe. Perhaps the most prominent Australian astronomer was Joe Pawsey, after whom an astronomical super-computing facility in Perth, Australia is named. This is perhaps ironic as when asked why he did not use computers in the 1950s, he rejected the suggestion as it was much faster to compute the necessary maths by hand rather than use a computer.

There are many examples of interferometers today. Probably the most famous is the Jansky Very Large Array (JVLA), in large part due to its appearance in the movie *Contact*. Other well used interferometers include the Australia Telescope Compact Array (ATCA) in Narrabri, Australia, the Westerbork Telescope in the

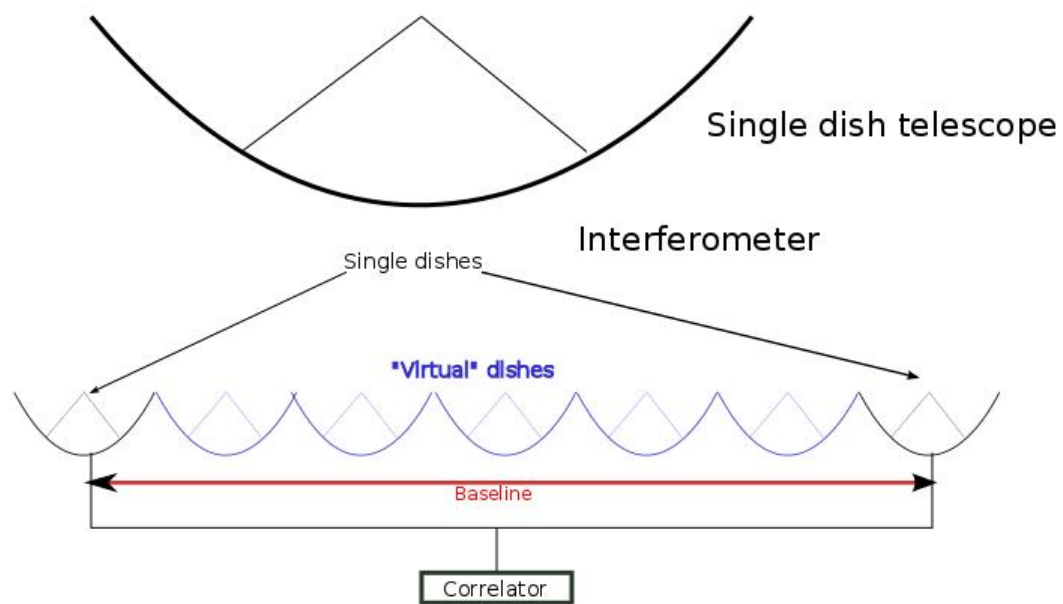


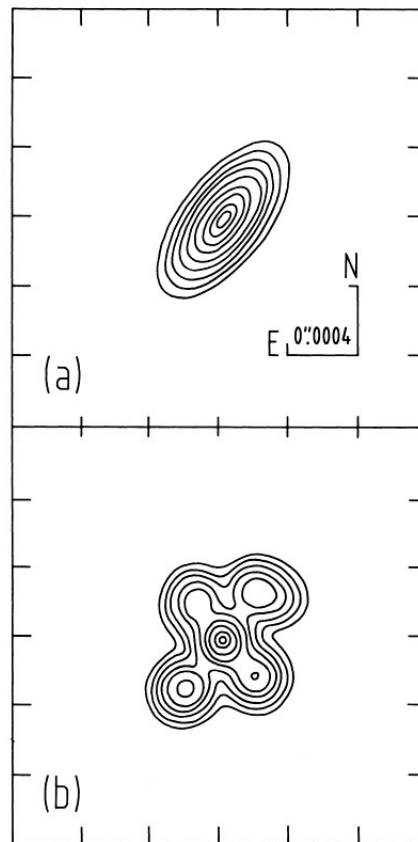
FIGURE 1.8: A simple sketch demonstrating the differences between a single dish radio telescope and an interferometer. The interferometer creates a “virtual” telescope equivalent to a single dish as large in size as distance between them. This is done by “correlating” the signals of these two telescopes. The distance between the two telescopes is known as the baseline.

Netherlands, the Plateau de Bure Telescope in France and the Atacama Large Millimeter Array (ALMA) in Chile.

1.3 Very Long Baseline Interferometry

The discovery of superluminal motion (Fig. 1.6) was only possible using a technique known as Very Long Baseline Interferometry (VLBI). VLBI is identical to a standard interferometer that has antennas connected with wires, except that data are recorded locally with accurate timing (usually from a hydrogen maser) and often has continental or inter-continental baselines. We are moving the ‘smoothie telescopes’ further apart. The data is then transported to a central location to be correlated. An exception to this is the development of eVLBI, where experiments are correlated in near-real-time over the internet ([Rushton et al. 2007](#)). Excellent reviews of the history of VLBI are given by [Clark \(2003\)](#); [Kellermann & Moran \(2001\)](#) and [Kellermann & Cohen \(1988\)](#), a summary of which will only be briefly discussed here.

164

J. M. Marcaide et al.**Figure 3**

Models of the core of 3C84 at 7mm wavelength

© ESO • Provided by the NASA Astrophysics Data System

FIGURE 1.9: First trans-Atlantic 7 mm VLBI maps of 3C 84 from [Marcaide et al. \(1985\)](#).

The first simple (intensity only) non-connected VLBI experiment was performed on Jupiter by [Smith et al. \(1965\)](#). The first true non-connected and correlated VLBI experiment was performed two years later by [Brotten et al. \(1967\)](#), with the detection of 3C 345 on a 3074 km baseline in Canada. The first US VLBI experiments followed shortly after, with detections between the Green Bank Telescope (GBT) and the Maryland Point Station ([Bare et al. 1967](#)). The original GBT collapsed in 1988, and a new 100 m telescope was completed in 2000. An order of magnitude resolution improvement over the US VLBI experiments was then forthcoming with the first trans-Atlantic baseline detected in 1968 between the

old GBT, Haystack and the Onsala Space Observatory in Sweden ([Kellermann & Moran 2001](#)). VLBI experiments were soon planned and successfully completed between the US and the former USSR in late 1969, a collaboration that would continue far into the future.

After these successful early experiments, centrally coordinated arrays consisting of very different telescopes began to develop. Probably the most well known of these is the European VLBI Network (EVN), formed in 1980 and which despite the name includes antennas as far away as East Asia (e.g. [Graham & Matveenko 1984](#)). Within the UK, there is the Multi-Element Radio Linked Interferometer Network (MERLIN) (e.g. [Bridle et al. 1981](#)) and in Australia there are two arrays, the Long Baseline Array (LBA) (e.g. [Frater 1984](#)) and the larger TANAMI array (e.g. [Ojha et al. 2010](#)). Other arrays include the Korean VLBI Network (KVN) (e.g. [Jung et al. 2012](#)) and the Japanese VLBI Exploration of Radio Astronomy (VERA) (e.g. [Kawaguchi et al. 2000](#)). Additionally, there is one VLBI array that was specifically designed and built for the purpose - the Very Long Baseline Array (VLBA) in the United States ([Napier et al. 1994](#)). The VLBA can be combined with the GBT, JVLA and compatible European telescopes (depending on the frequency) to form the High Sensitivity Array (HSA). At 7 and 3 mm wavelengths, this is known as the Global mm-VLBI Array (GMVA).

One must stress that everything else being equal, resolution increases with frequency. As radio has much longer wavelengths, they should have much lower resolution than optical or higher frequencies telescopes. As interferometry can overcome this, operating the highest frequency interferometers will result in the highest angular resolutions. Currently, the highest frequency observed at in VLBI is at 1 mm or 230 GHz, using the Event Horizon Telescope (EHT) ([Doeleman et al. 2008](#)). With global 3 mm-VLBI, resolution of up-to 50 *microarcseconds* can be achieved, equivalent to observing a smartphone on the moon.

Although outside of the scope of this thesis, another way to increase the resolution of VLBI arrays is to increase the baselines into space. This has been done three times, firstly with a satellite as part of the Tracking and Data Relay Satellite System (TDRSS) ([Linfield et al. 1990](#)), secondly with the Japanese VSOP-I/II programs ([Hirabayashi 1998](#); [Tsuboi 2008](#)) and thirdly with the current and ongoing Russian program, RadioAstron, although both were only at cm wavelengths ([Kardashev et al. 2013](#)).

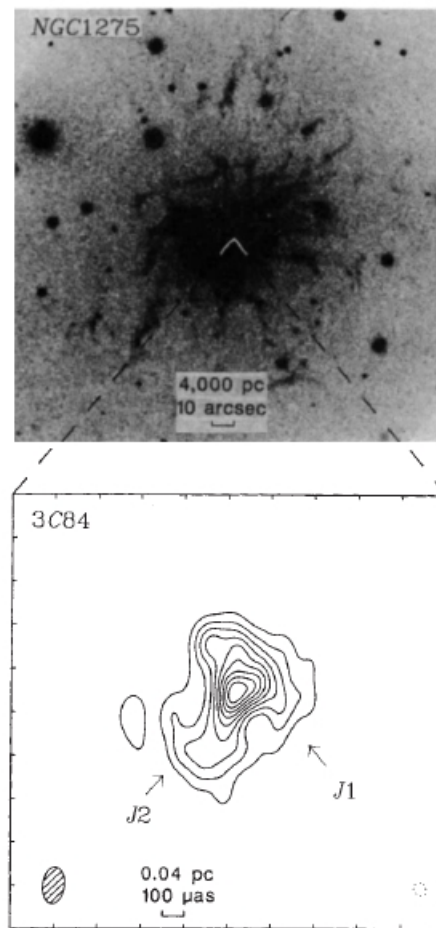


Fig. 1 A narrow band H α photograph²¹ of the galaxy NGC1275 and a hybrid map of the galaxy's nuclear region at 7 mm. North is up and east to the left. The total flux density in the mapped region is 6.9 Jy. The contours are at $-10, 10, 20, 30, 40, 50, 60, 70, 80$ and 90% of the peak brightness of 1.2 Jy per beam area, equivalent to $\sim 5 \times 10^{10}$ K. The 50% contour of the restoring beam with a FWHM size of $100 \times 170 \mu\text{as}$ and a position angle of -7° is shown as the striped ellipse in the lower left corner. The tick marks are separated by $200 \mu\text{as}$.

FIGURE 1.10: A figure from [Bartel et al. \(1988\)](#) showing the increase in resolution possible due to 7 mm VLBI.

1.3.0.1 Other VLBI Applications

Although also outside of the scope of this thesis, VLBI can be used for many other varied and interesting topics. It can be used in the study of astrometry, where VLBI is used to determine the sky positions of astronomical sources and their movements (if any). The main aim of this is to tie the terrestrial reference frame to the inertial celestial reference frame. A good overview of the topic is given by [Bartel \(2003\)](#) and [Ros \(2005\)](#).

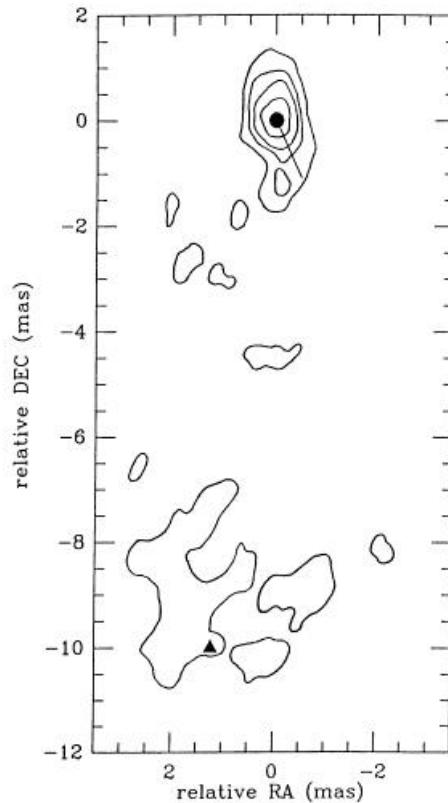


FIGURE 1.11: 22 GHz map with jet position angle overlaid from 3 mm Gaussian model-fits, ([Backer et al. 1987](#)).

A related but scientifically very different field is geodetic VLBI. This can be thought of VLBI in reverse, where we assume knowledge of the location of sources use this to determine the location of the *antennas*. This has many practical applications such as measuring the movement of tectonic plates and polar motion ([Schuh & Behrend 2012](#)). A final use for VLBI is spacecraft tracking. A famous example of this was the use of VLBI to track the descent of the Huygens probe into the atmosphere of Saturn's moon Titan ([Pogrebenko et al. 2004](#)).

1.3.1 A Brief History of mm-VLBI

Millimeter-VLBI extends our widely spaced 'smoothie telescopes' to higher frequencies for the highest possible detail. The first VLBI observations at 3 mm (or 80-100 GHz)⁵ were performed between the Owens Valley Radio Observatory (OVRO) and the Hat Creek Radio Observatory (HCRO) in October 1981 ([Readhead et al. 1983](#); [Backer 1984](#)), although sensitivity was poor. Soon after,

⁵The use of frequencies and wavelengths are used interchangeably (e.g. 86 GHz/3 mm and 43 GHz/7 mm)

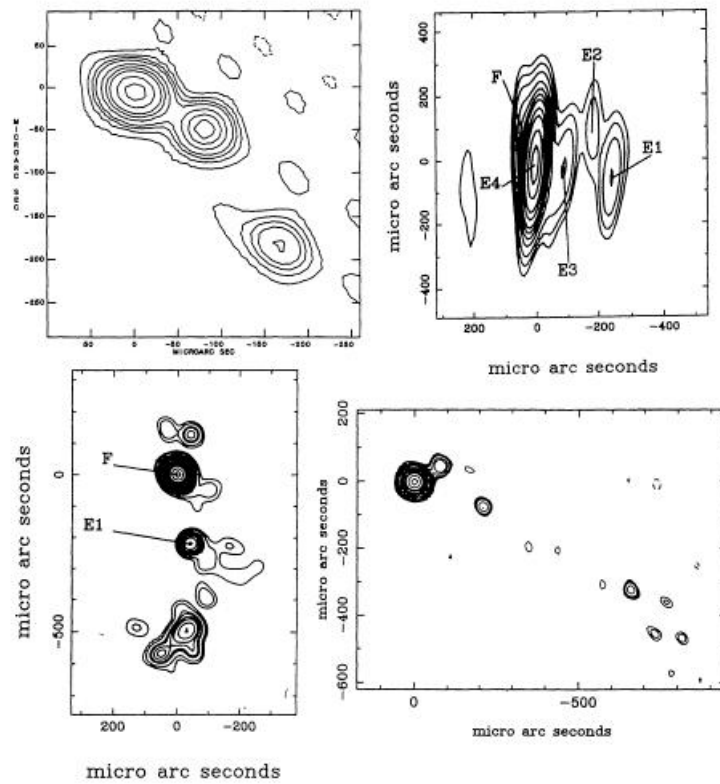


FIGURE 1.12: 100 GHz maps of (from top left to bottom right) 3C 446, 3C 273, 3C 84 and 3C 354 (Baath & Booth 1991)

trans-Atlantic baselines were detected on 3C 84 at 7 mm (Marcaide et al. 1985; Dhawan et al. 1986) (see Fig. 1.9,1.7). 7 mm observations were subsequently performed regularly, with perhaps the most significant early research presented by Bartel et al. (1988). The first observations at 1 mm/230 GHz were performed by Padin et al. (1990) on 3C 273, yielding a size measurement of less than 0.5 mas.

By 1987, 3 mm observations of 3C 84 could be interpreted with the aid of Gaussian model-fits and lower frequency maps, (Fig. 1.11), finding offsets from the lower frequency images (Backer et al. 1987). Generally, 7 mm observations were easier to perform in these earlier days as they could more easily be accommodated by existing VLBI networks. 3 mm observations for many years had to be performed ad-hoc with many telescopes lacking the necessary VLBI equipment (Baath 1994).

Despite these advances, it was not until the late 1980s that sensitive 3 mm observations on inter-continental baselines could reliably be performed (Baath &

Booth 1991). These early images (Fig. 1.12) were for the first time approaching the quality of maps that can routinely be performed today. Subsequent analysis of 3C 273 showed that there were significant differences in the jet direction between 100 GHz and lower frequencies (Baath et al. 1991). Further observations showed that the inner regions of blazars were more curved than at lower frequencies (Baath et al. 1992). An important early 3 mm survey paper was Rantakyro et al. (1998), which found likely two source groupings of either misaligned jets with parsec scale features and aligned sources with straight jets and small changes in Position Angles. Observations of 3C 446, finding it mostly unresolved at these frequencies, followed (Lerner et al. 1993)

By now, mm-VLBI observations were becoming largely routine. By 1995, mm capable stations organised into what became known as the Coordinated Millimeter VLBI Array (CMVA) (Rogers et al. 1995), with significant early results including size estimates on the black hole at the center of the Milky Way by Doeleman et al. (1995); Krichbaum et al. (1998). The CMVA as of 1998 consisted of Effelsberg, Metsahovi, Pico Veleta, Plateau de Bure, Onsala, Sest (decommissioned), Haystack, Quabbin (decommissioned), OVRO, the Berkley Hat Creek Interferometer (now known as the Allen Telescope Array - ATA) and the 12 m dish at Kitt Peak. (Krichbaum 1996). By the late 90s, more VLBA antennas had joined, including Los Alamos, Fort Davis and North Liberty (Krichbaum et al. 1999). In 2002, Plateau de Bure could be used as if it were one single dish (in a process known as array phasing), greatly improving sensitivity of the global VLBI array (Alef et al. 2003).

Early source surveys at 3 mm were performed by Lonsdale et al. (1998) and Lobanov et al. (2000), but were severely limited by sensitivity. With the addition of four more VLBA antennas, the CMVA was succeeded by the Global mm-VLBI Array (GMVA⁶) (Agudo et al. 2007c). The array remained largely unchanged with a twice yearly observing schedule until the addition of the Yebes telescope in Spain since 2012 and the Korean VLBI Network (KVN) and the GBT which is currently in testing. (Hodgson et al. 2014).

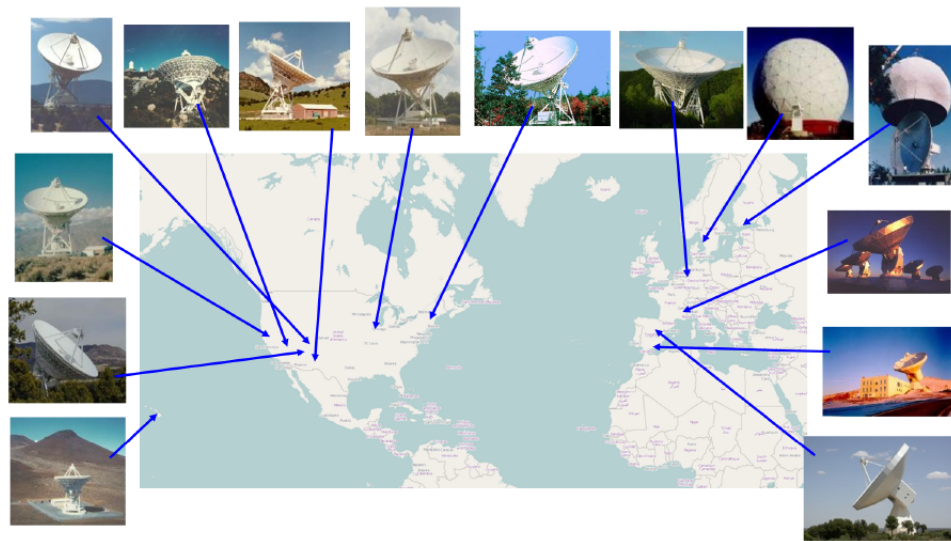


FIGURE 1.13: Telescopes participating in the Global mm-VLBI array (GMVA) as of November 2014. Other telescopes such as the three stations of the Korean VLBI Network (KVN), the Green Bank Telescope (GBT) in the USA and the Noto telescope in Italy (at 7 mm) participate on a best effort basis.

1.3.2 The Global mm-VLBI Array

The GMVA is an array currently consisting of 13 stations spread over the United States and Europe and since October 2011 with Yebes regularly participating in a best effort capacity. It comprises six European stations: Effelsberg (Ef), Onsala (On), Pico Veleta (Pv), Plateau de Bure (PdB), Metsähovi (Mh) and Yebes (Yb) since 2011 and the 8 stations of the Very Long Baseline Array (VLBA) equipped with 3 mm receivers. In May 2012, the Korean VLBI Network (KVN) successfully performed test observations between it and some European stations and may join the GMVA in the future. The station characteristics are summarised in Table 1.1. An angular resolution of up to 40 microarcseconds is achieved, though 50-70 microarcseconds is more typical. The GMVA will also complement the scientific output and interpretation of future space VLBI observations (e.g. RadioAstron at 5 and 22 GHz) and of future 1 mm VLBI (Event Horizon Telescope).

With the additional sensitivity of the GMVA over the CMVA, much interesting science has been performed. The complicated and highly variable inner structure of AGN has consistently been a topic of interest. The jets in the sources ‘swing’ and ‘wobble’ and are highly flux variable, often with corresponding Gamma-ray activity (Agudo et al. 2007a; Giroletti et al. 2008; Schulz et al. 2013;

⁶<http://www.mpifr-bonn.mpg.de/div/vlbi/globalmm/>

TABLE 1.1: Overview of stations used in global 3 mm VLBI observations

Station	Country	Effective Diameter (m)	Typical SEFD (Jy)
Effelsberg	Germany	80	1100
Plateau de Bure	France	34	500
Pico Veleta	Spain	30	700
Onsala	Sweden	20	5500
Metsähovi	Finland	14	17500
VLBA (x8)	United States	25	2000
Yebes	Spain	40	1700*

[Molina et al. 2014](#)). In addition to continuum experiments, spectral line observations have been performed with SiO maser emission detected around AGB stars ([Colomer et al. 2009](#)). In the future as recording rates increase and telescopes improve, sensitivity will become over greater, allowing far fainter sources and structures to be detected and imaged than ever before.

1.4 Motivations for mm-VLBI

To conclude the chapter, we discuss the motivations for doing mm-VLBI more broadly, as these are the motivations behind this thesis. The primary motivation is high angular and spatial resolution. 3 mm VLBI with the GMVA provides the highest resolution images with the highest fidelity of any telescope in the world today. In the future, 1 mm VLBI (with the Event Horizon Telescope (EHT)), will surpass this, but currently the EHT lacks imaging capability and sensitivity. It also is currently scheduled ad-hoc and is not an open-access instrument to which anyone can apply, like the GMVA.

The concepts introduced will be explored in detail in future sections, but a general overview is given here. Beyond simple resolution arguments, the strongest scientific argument is opacity, which vanishes towards shorter wavelengths (Section 3.5). One can think of opacity as your ability to see through something. For example, a clear sky at night has very low opacity, but if there are some small, wispy clouds, the opacity will increase. If the sky is overcast, you will see nothing and hence have very high opacity. However, if you observe the sky at radio

wavelengths, you can “see through” the clouds. Similarly, in AGN, the vast majority of emission is due to Synchrotron radiation (Section 3.5.1) and at lower frequencies, this emission is self-absorbed (Section 3.5.2) - or highly opaque. We are able to “look through” the clouds of synchrotron emission at the highest possible resolutions and often able to calculate magnetic fields too (Section 4.3.6). These abilities provide to us a unique opportunity to understand the processes that power blazars - the highest energy laboratory in the universe.

Chapter 2

Imaging, Calibrating and Data Acquisition

VLBI is challenging. There are many excellent resources available describing the process from detection at the telescope through to final imaging, including Synthesis Imaging In Radio Astronomy II ([Taylor et al. 2008](#)) as well as many excellent online resources (e.g. [VERA \(VLBA\)](#), [NRAO \(VLBA\)](#), [ITN \(EVN\)](#), [Argelander](#)). Here, we will attempt a different method by beginning with the final VLBI map and explaining how we arrived at it. We will also attempt to describe this non-mathematically where possible, but providing references for more in-depth explanation.

2.1 Imaging in Reverse

2.1.1 The Final VLBI Image

As this thesis is devoted to 3 mm VLBI, we will begin by presenting a final 3 mm VLBI map of the blazar OJ287 from the May 2010 GMVA session in Fig. 2.1. This is a typical blazar image, with a bright “core” and the jet extending away from it. The “core” is typically (but not always) the brightest, most compact component in the image. It is considered to be the most upstream visible component of a relativistic jet, a small distance upstream of central black hole. All imaging performed here is using the Caltech DIFMAP package (Shepherd et al. 1994) although other packages such as CASA, MIRIAD and AIPS can be used.

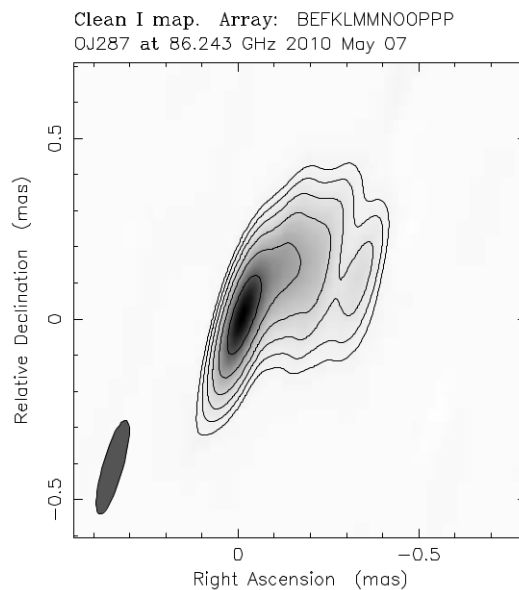


FIGURE 2.1: The final VLBI map of OJ287 after all calibration and processing has been applied. Contours at -1%, 1%, 2%, 4%, 8%, 16% 32% and 64%.

2.1.2 The Dirty Image

When you first load your data into DIFMAP, what you will first see is the “dirty image”, such as in Fig. 2.2. The “dirty image” looks almost nothing like the final map. In Fig. 2.3, we see the residuals, which are the difference between areas of high and low flux in the map. We can see in Fig. 2.3 that the greatest difference in flux is located at the “phase center” at position (0,0), which is likely where most of the flux is located. The process of imaging uses our discretion to determine where we believe that flux *should* be. A feature one may notice

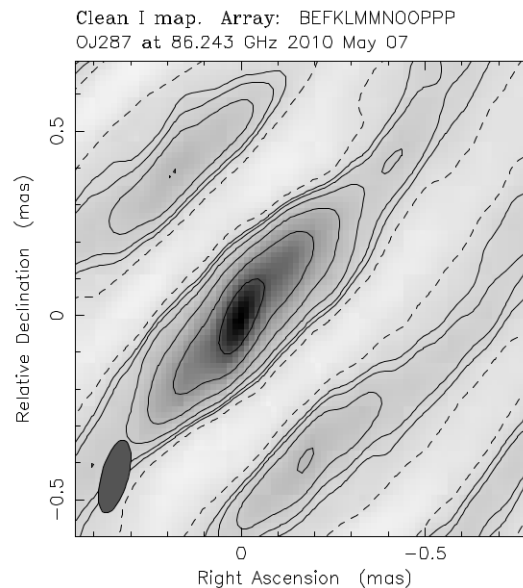


FIGURE 2.2: The “dirty image” of OJ287 after all calibration has been applied, but only an initial starting model. Contours at -1%, 1%, 2%, 4%, 8%, 16%, 32% and 64%.

in Fig. 2.2 is its symmetrical nature, with flux going above and below the central region. This happens because the image is an incomplete inverse Fourier transform of the output of the correlator. To get from the “dirty image” to the final map, we must go through a process known as *deconvolution* (Section 2.1.7).

2.1.3 The Fourier Transform

Any signal can be described by the addition of a large number of sine waves. The frequency and amplitudes of these sine-waves are what make up the Fourier transform (FT). Using the smoothie analogy from Chapter 1, as inspired by [Azad \(2012\)](#):

- What does the Fourier Transform do? Given a smoothie, it finds the recipe.
- How? Run the smoothie through filters to extract each ingredient.
- Why? Recipes are easier to analyse, compare, and modify than the smoothie itself.
- How do we get the smoothie back? Blend the ingredients.

So, the recipe is the FT of the smoothie. As described in the Introduction, in a radio interferometer, we are measuring the *ingredients* of the smoothie. The

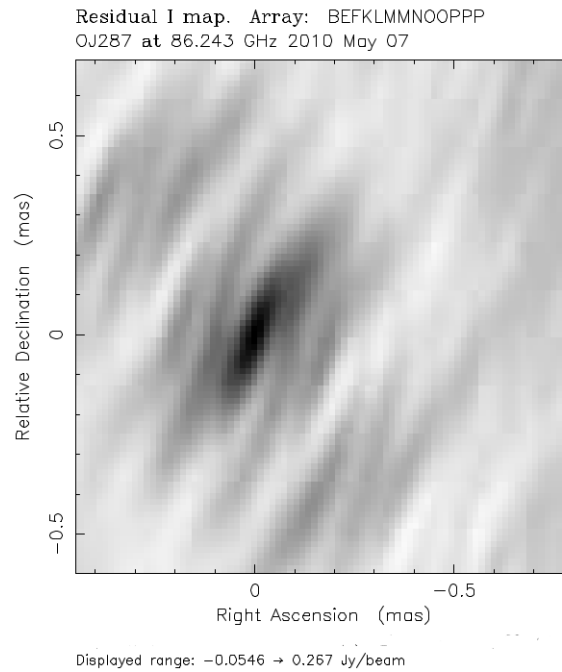


FIGURE 2.3: The “dirty residuals” of OJ 287 after all calibration has been applied, but no initial imaging. The dark region near (0,0) is where most of the flux is located.

problem is that we cannot measure all the ingredients accurately. Trying to make a reasonable guess at what the real smoothie would be like given our limited knowledge of the ingredients is called *deconvolution*. The details of Fourier transforms can be found in many other resources, such as thefouriertransform.com. On computers, the FT is approximated using the *Fast Fourier Transform* (FFT) and the acronym FFT is often used to refer to a Fourier Transform. An important point to keep in mind is that the Fourier Transform has two components, the *amplitude* and the *phase*. You can think of the amplitudes as being the amount of ingredients you need but the phases tell you what *kind* of ingredients to put in.

To give a feeling for how the FT and its image effect each other, I have included some examples from University of York. A simple picture of a cat, a duck and their FFTs are given in Fig. 2.4. There are a few features to note here. The first is that the larger scale details are represented near the center and the finer details closer to the edges of the FFT. The second is that the ‘angles’ of the image are rotated 90° in the FFT. This is more noticeable in the FFT of the cat, where the back of the cat is lopsided but which is rotated in the FFT. In the next example Fig. 2.5, the amplitudes of the FFTs have been switched but the phases kept. We can see that doing this has very little effect on the final image. It is the

kind of ingredients that matter, rather than the amount - the phases provide the most important information in an FFT. The amplitudes tell you how bright a pixel is, the phases tell you where the pixel should be put. This means that in a VLBI experiment, the phases carries most of the information.

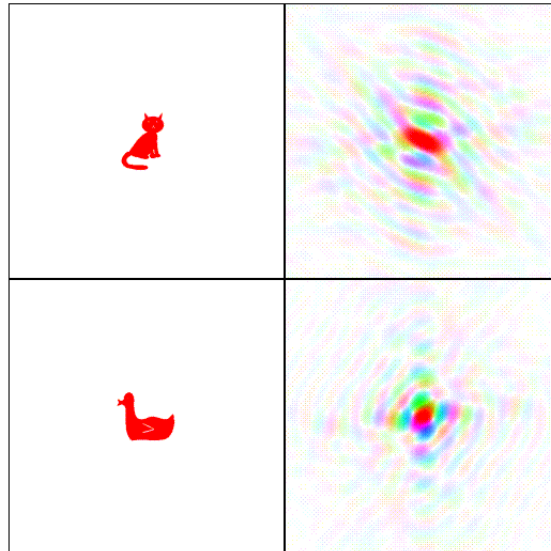


FIGURE 2.4: A cat, a duck and their Fourier Transforms. Note that the large scale structures are located represented near the center of the FFT. The finer details are represented closer to the edges of the FFT. The Fourier Transform can be thought of as the ingredients of the image.

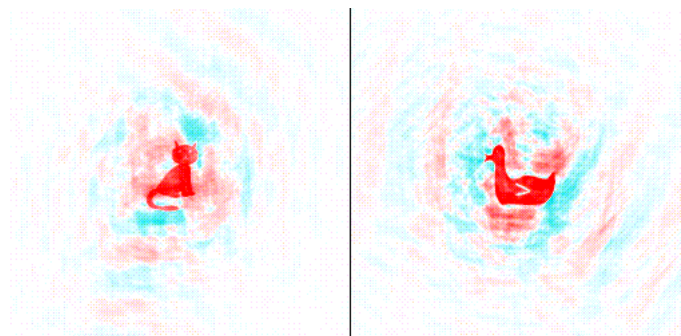


FIGURE 2.5: In this example, the amplitudes of the two FFTs are switched, but the phases are kept. We can see that the amplitudes make very little difference to the final image. The phases are where most of the information is.

In Fig. 2.4, we see that the fine details were encoded in the edges of the FFT. In the next examples, we will see what happens when we remove certain areas from the FFT. In Fig. 2.6, the central area of the FFT has been removed, corresponding with the “larger-scale” details. You can see that in the inverted image, the outline of the duck is still visible as well as features such as the eye, beak and the wing, but the internal details are gone. In the next example, Fig. 2.7, we have done the opposite, removing the outer regions of the FFT. Now we can see that the duck is just a blurry outline, but all the fine details are still there. In both images, you can see ‘ripples’ emanating. These are known as *sidelobes* and not real. They are very important as they are a side-effect of having an undersampled FT.

This occurs in radio interferometry. We are sampling the *Fourier Transform* of the source, but only a limited amount of it. At low frequencies and short baselines, we measure the blurry edges of a source and other extended structures, but at higher frequencies and with longer baselines, we can see finer details and structures. To get a full picture of a source, it is necessary to get both.

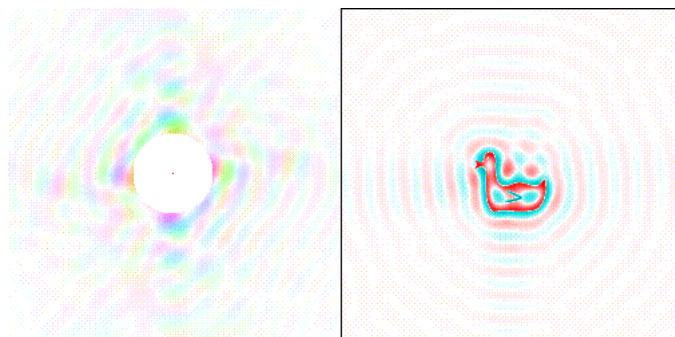


FIGURE 2.6: In this example, the low information about the larger structures has been removed. Finer details such as the outline of the duck, the eye, the beak and the wing are visible, but the internals are gone.

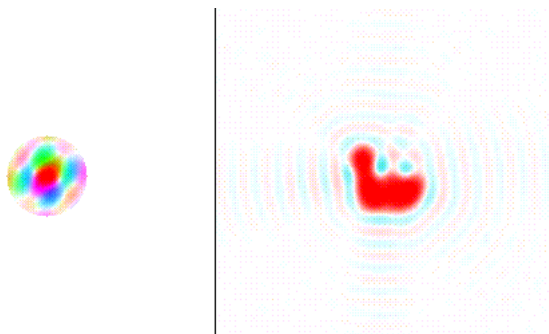


FIGURE 2.7: In this example, finer detailed information is removed. Now we can only see a blurry outline of the duck.

2.1.4 The uv Plane and the Beam

The radio interferometric equivalent of the Fourier Transform of the image is known as the *uv-plane*. Radio astronomers commonly speak of *uv-coverage*, which is a way of describing how well the uv plane is sampled. So, better uv-coverage, means better sampling the FT of the source - the better we can measure the galaxy smoothie's ingredients. Each point in the uv-plane is called a **visibility** and is the output of the *correlator*. Another way of thinking of uv-coverage is to imagine that you are at the source, looking at earth. The uv-plane would then be the positions of the telescopes as you see them *from the source*.

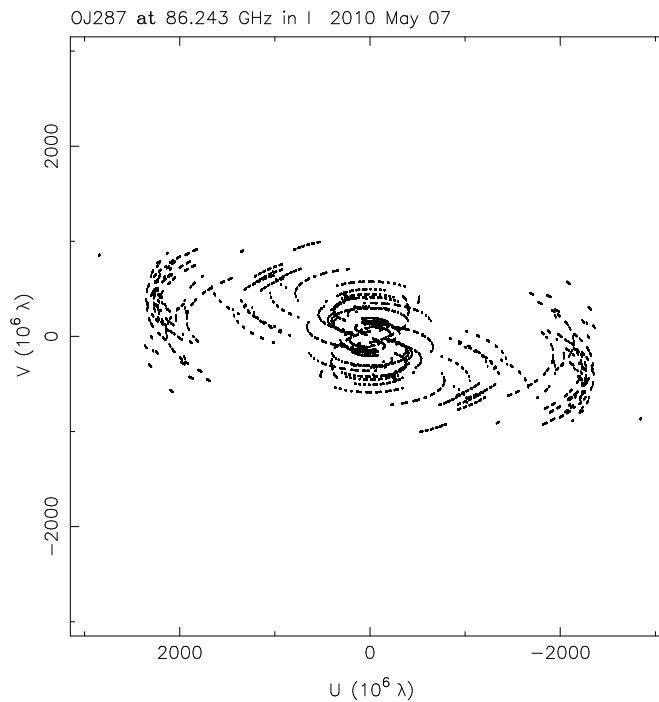


FIGURE 2.8: The uv-plane of the May 2010 observations of OJ287.

In Fig. 2.8, we see the uv-coverage of the May 2010 observation of OJ287. If you look on the axes, you will see that the units are given in millions of wavelengths¹. This is because the resolution is actually a function of how many *wavelengths* can fit between two stations. It should now be clear why increasing the separation between stations and increasing the frequency increases the resolution. If we move the telescopes further apart, we can fit in more wavelengths. If we

¹The unit for wavelength is λ and is usually expressed in meters.

increase the frequency, the individual wavelengths become shorter and hence we can fit more wavelengths in this way too.

If one looks in the bottom left corner of Fig. 2.1, we see the ‘beam’, which can be thought of as what the telescope can see at any given time. The smaller the beam, the higher the resolution. In Fig. 2.8, we can see that there are more points spread out along the horizontal direction, leading to a more “vertical” beam in Fig. 2.1.

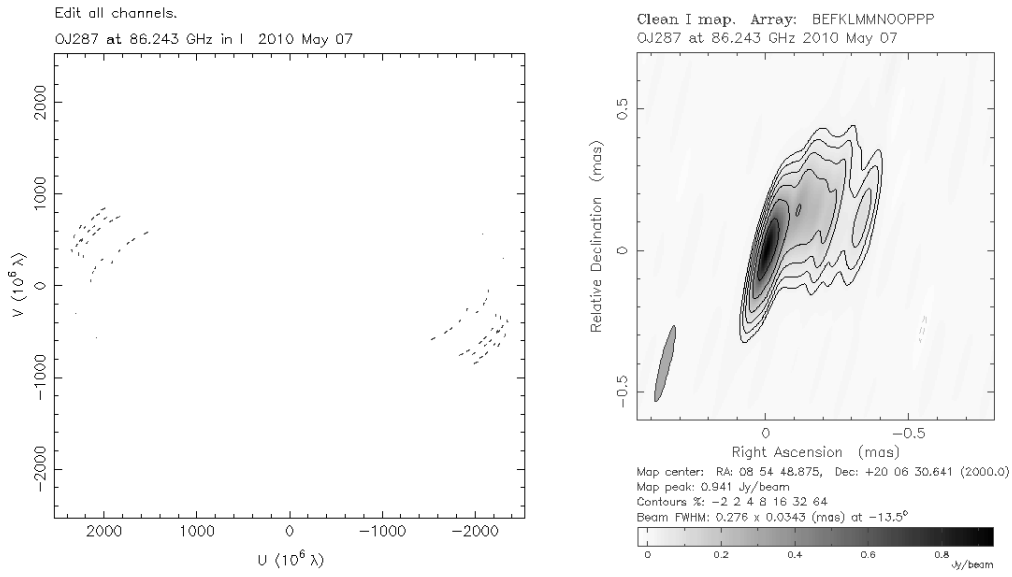


FIGURE 2.9: uv-plot and image of OJ 287 with short baselines removed.

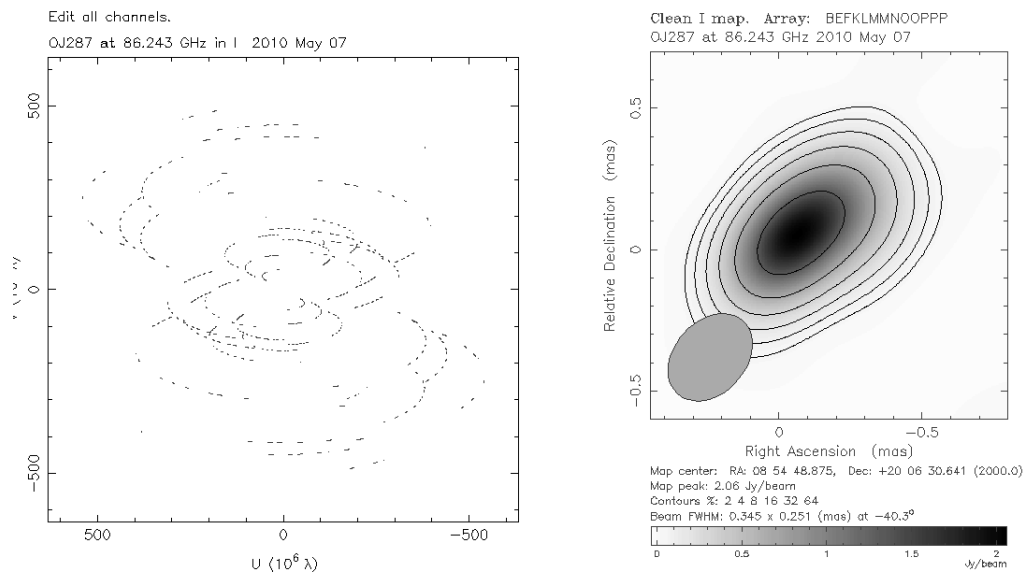


FIGURE 2.10: uv-plot and image of OJ 287 with long baselines removed.

In Figs. 2.9 and 2.10, we can see the effects of removing uv information on the final image. In Fig. 2.10, the effect of removing long baselines is dramatic. The beam now is much larger and the image resembles a large unresolved ‘blob’. In Fig. 2.9, the beam is slightly narrower but the image looks remarkably similar to Fig. 2.1, especially given that almost two thirds of the data has been removed. One may believe that short baselines are not important as Fig. 2.9 looks similar to the original image in Fig. 2.1, but has more jagged edges. As will become clear in the next sections, these short baselines are very important for calibration as they are generally much more sensitive to extended structure and are commonly more reliable due to higher redundancy². Additionally, if there are extended structures that are larger than the beam, they may not be detected at all - a problem known as *resolving out*.

2.1.5 Flux Density and Source Brightness

Before discussing the finer points of the uv-plane, we should review what is actually being detected and displayed in the image. Radio signals are impressively weak, with detections being over a *billion-billion-billion* times weaker than a TV transmission. When radio astronomers talk about how bright a source is, they are usually referring to the *flux density* - the total brightness of the source given its size on the sky. The flux density of radio sources is often extremely small and radio astronomers use a non-SI unit to describe it - the Jansky (Jy):

$$1 \text{ Jy} = 1 \times 10^{-26} \text{ Wm}^{-2} \text{ Hz}^{-1}, \quad (2.1)$$

which is an impressively small amount of energy to detect. Even more impressive is that many modern telescopes can detect to the milli-Jy or even *micro*-Jy level. It is important to reiterate that the brightness is *independent* of distance and only a measure of what we detect at the telescope.

2.1.6 Convolution and Deconvolution

The relationship between how many antennas are observing and the final image via the uv-plane should now be clear. This does not explain, however, why the “dirty image” in Fig. 2.2 looks so different from the final image in Fig. 2.1 when

²In this context, higher redundancy means that if there are many similar baselines, we would expect them to measure similar information. If they do, we can be more confident that what they are measuring is correct.

both should be the inverse FT of the same underlying data. The reason is that any image we make is the *convolution* of the uv information and the “dirty beam”. Returning to the smoothie analogy, we remember that we only have a guess at the ingredients of the smoothie and that we try to improve our guess. This was called *deconvolution*, and is our attempt to disentangle the uv information from the “dirty beam”. So:

$$\text{Best guess smoothie} = \text{Real smoothie} * \text{dirty beam}$$

Where ‘*’ is the symbol for convolution. The “dirty beam” exists because our FT is under-sampled. Remember that the beam can be thought of as what the telescope can see at any given time. Each dish has its own beam, and these are combined to form the *synthesised beam*³.

The definition of a convolution is difficult, with a good mathematical description of it in ([Acadamy 2014](#)). For our purposes, the most important point is that a convolution is the same as a multiplication in the uv-plane/Fourier space and a multiplication is much easier to deal with than a convolution. So:

$$\text{Best guess smoothie} = \text{Real smoothie} * \text{dirty beam}$$

FT

$$\text{Best guess ingredients} = \text{Real ingredients} \times \text{dirty beam}$$

We want to minimise the effects of the dirty beam, so that we get closer to the real ingredients. In order to do this, we can constrain the guess on the real ingredients by making some assumptions. For example, we know that all values must be positive (i.e. negative ingredients are impossible), that the sky is mostly blank (ingredients won’t be floating around behind it) and that sources are mostly smooth (i.e. it will not drastically change over small distances).

To create a better map, we are attempting to interpolate and extrapolate the gaps between the uv samples.

³The VLBA has (almost) identical dishes and hence almost identical beams, leading to a much better synthesised and hence dirty beam.

2.1.6.1 The Point Spread Function

If we had an almost perfectly sampled uv plane, the beam would resemble an almost perfect *Point Spread Function* or PSF. **The PSF is the Fourier Transform of the uv -plane.** In Figs. 2.1, 2.9 and 2.10, we can see that features in the final image are shaped by the beam. It comes as no surprise that having a beam that is more circular will produce better looking images, which would require antennas to be arranged in a circular way, which is difficult in the real world.

This almost perfect PSF/beam would look something like Fig. 2.11. Notice how the PSF peaks in the center and smoothly drops off. In a telescope beam, this means we would be most sensitive here and if we know how the beam is *shaped*, we can reconstruct the final image with great confidence. Unfortunately, in VLBI the beamshape is the superposition of the beams of many different dishes/antennas, hence it is not always well known. In this case, the PSF/beam might look similar to Fig. 2.12. Notice the outside of the center of the beam, there are large ‘ripples’ around the beam. These are known as *sidelobes* and can make your image look very ugly. These “ripples” can be clearly seen in the duck and cat examples in Figs. 2.6 and 2.7 and are a direct consequence of an undersampled FT. This is also extremely evident in the dirty map in Fig. 2.2, where although the map is still brightest in the center, there are bright bands emanating from it. These are sidelobes and should not be confused with real structure.

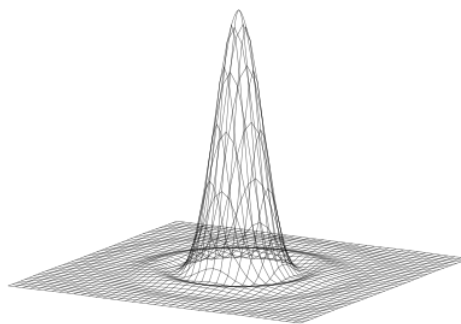


FIGURE 2.11: An example of an almost perfect Point Spread Function from [Wikipedia](#).

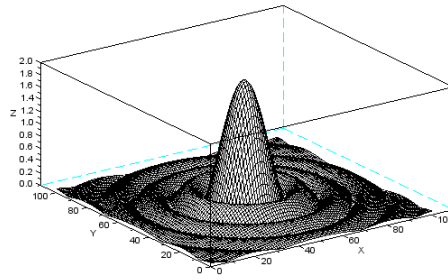


FIGURE 2.12: A non-perfect Point Spread Function from [Lessons Learned](#). Notice the large ‘ripples’ from around the center.

2.1.6.2 Aperture Synthesis

It has been previously stated that the uv-plane can be thought of as the view of the antennas from the source. The Earth is not stationary and rotates on its axis every day, hence the antennas would appear to move, if viewed from the source. Hence, we can fill in more of the uv-plane using *Aperture Synthesis*. With clever scheduling of telescopes, many sources can be interwoven to improve uv-coverage using this method. This is visible in Fig. 2.8, where there are obvious “tracks” in the uv-plane. This is due to the rotation of the Earth. The gaps in the “tracks” are due to the array observing other sources.

2.1.7 The CLEAN algorithm

The most widely used method of deconvolution is the CLEAN algorithm, first developed by [Högbom \(1974\)](#) although this has been extended and modified since then. The method works by approximating the dirty image with a series of point sources⁴. Generally, although not necessarily, we put “windows” where we think emission should be. Within these “windows”, the peak pixel is found and a slightly scaled version of the PSF (typically less than 20 percent) is subtracted from the peak. New point sources represent the flux subtracted from the peak pixel. This process is iteratively performed and is stopped when the residuals (e.g. 2.3) are near zero.) The point sources are then convolved with an estimate of the central peak of the PSF, the residuals are added back to the point sources and a final image is produced.

⁴These point sources are delta function which are themselves a Gaussian that it is zero everywhere except at 0.

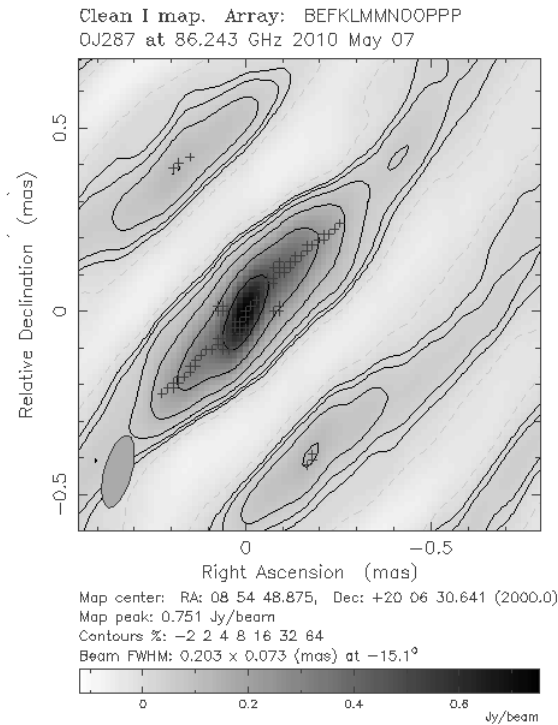


FIGURE 2.13: An initial CLEAN run over the data with no windows. The (hard to see) grey crosses are the point sources representing the source.

In practice, using DIFMAP, we can perform this in either the image or residual planes. Taking our dirty residuals from Fig. 2.3, we put windows in regions where we believe emission should be, which is often easier to do in the residual plane. However, with 3 mm VLBI, the sidelobes can be very bad, so it is preferable to CLEAN in the image plane as well, to check the source structure. Using windows can be dangerous as the window placement is *subjective*. It is often a good idea to image with lower frequency or earlier maps as guidance.

In our example, after the data is loaded into DIFMAP, a first initial CLEAN is performed to create a starting model in Fig. 2.13. The data looks very bad, with emission in all directions with very bad sidelobes. However, we know from 7 mm images as part of the [BU-VLBA-BLAZAR Monitoring Program](#) that the emission is brightest in the south-west and emanates north-easterly from there, so we position our windows accordingly in Fig. 2.14. We proceed until the residuals look almost smooth. When this is done, we perform amplitude *self-calibration*.

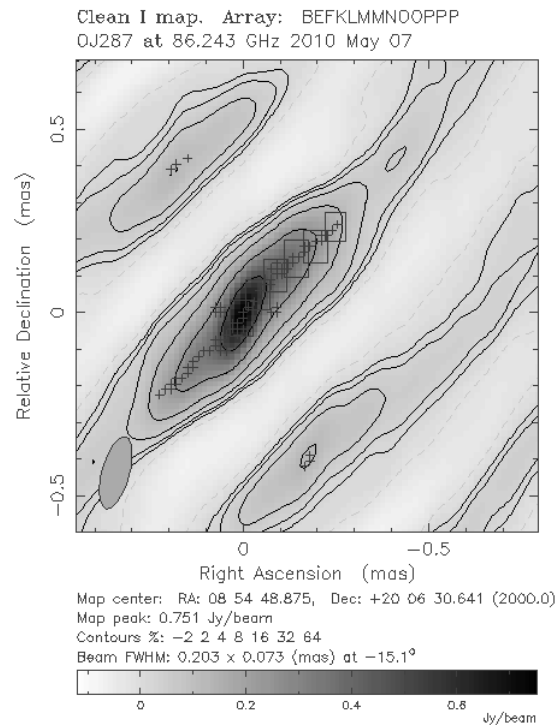


FIGURE 2.14: Same as Fig. 2.13, but with windows where we think emission is.

2.1.8 Self-Calibration

Self-calibration is the process of minimising the difference between observed visibilities and a plausible model of the source structure, usually a CLEAN model but also could be a Gaussian model-fit (see Section 2.1.11). This section relies heavily on the lectures by [Cornwell & Fomalont \(1999\)](#). It can be performed in phase and in amplitude and like CLEAN is performed iteratively, often in conjunction with CLEAN. It works as such:

- 1. Create a CLEAN (or other method) model of the source;
- 2. FT the model to produce visibilities;
- 3. Fit the data to the model visibilities in amplitude and phase.
- 4. Using the fitted data, CLEAN some more
- 5. When you think the model looks good, you're finished. If the model is not good, return to step 1. A good way to check if you're done is to look in the residuals. It should appear noise-like with no features resembling the beam.

Self-calibration works because the system is overdetermined and works better when there are more elements in the image. A concept fundamental to self-calibration is that of closure quantities.

2.1.8.1 Closure Quantities

Closure phases and amplitudes are an observable property of interferometers containing at least 3 stations for phase or 4 stations for amplitude. [Jennison \(1958\)](#) showed that closed loops of baselines are free of element related errors. This means that the noise terms can be cancelled out. Thus, following [Cornwell & Fomalont \(1999\)](#), [Cotton \(1979\)](#) and [Readhead et al. \(1980\)](#):

- 1. Create a CLEAN (or other method) model of the source;
- 2. Compute all independent closure phases and then use the initial CLEAN model to estimate the true phases from the observed closure phases.
- 3. Produce a new CLEAN model from observed amplitudes and newly predicted phases.
- 4. Return to step 2 until satisfied.

Thus, phase self-calibration, which uses the closure phases, is free of instrumental effects. Phase self-calibration is always performed alongside CLEAN. Amplitude self-calibration is used more narrowly and should not be used until the flux in the model reaches that of the data. Failing to do this can lead to large errors in amplitudes. To check if the model amplitudes match well with the data, we can inspect this in, [Fig. 2.15](#): This plots all visibilities as a function of uv-distance. uv-distance is the number of wavelengths between two stations on a given baseline. We can see here that the model (in blue) does not fit the data very well, so more CLEANing and phase self-calibration is required before we attempt amplitude self-calibration.

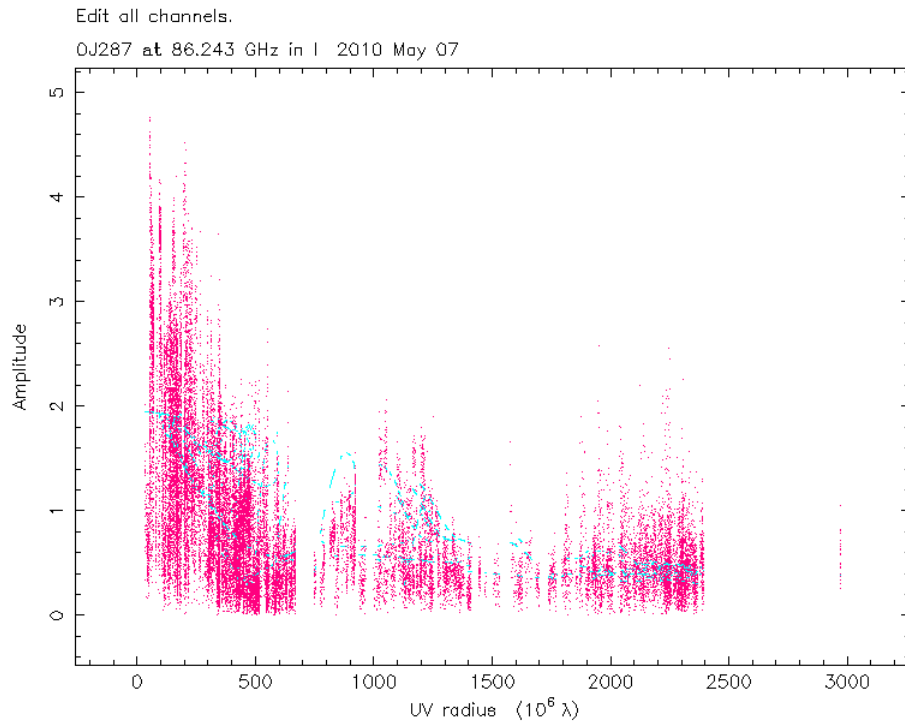


FIGURE 2.15: Radplot after initial windowing, CLEANing and phase self-calibration. Radplot displays visibility amplitude as a function of uv-distance. The visibilities are pink and the model in blue. Note how the model amplitudes does not fit the data well, particularly in middle uv-spacings. This indicates that further CLEANing and phase self-calibration is required.

2.1.9 uv-Tapering

The small beam-size of 3 mm VLBI leads to the possibility that emission could be ‘resolved out’. We can try to mitigate against this by applying a uv-taper. A uv-taper weighs down long baselines thereby increasing the weighting of shorter baselines. This has the practical effect of increasing the beamsize and sensitivity of the array towards low brightness features and extended emission.

2.1.10 Amplitude Self-Calibration

The process of CLEANing and phase self-calibrating is continued until CLEAN is no longer reporting that it is removing significant amounts of flux off the peak pixel, finding additional flux by expanding windows has been exhausted and the model amplitudes match well with the visibilities in ‘radplot’. When this happens, we can proceed with *amplitude self-calibration*. Caution must be

exercised here as this “locks in” changes made to the image during the initial CLEANing and phase self-calibration steps.

This process is continued iteratively, reducing the time averaging at each step by approximately half until the time averaging is 0. At this stage, it is often a good idea to perform a ‘deep’ CLEAN by setting the number of iterations high (perhaps 500) and CLEANing without windows. Once the image is fully self-calibrated, it is important to do a round of CLEANing with no windowing.

2.1.11 Model-Fitting

Though CLEAN algorithms can be used to produce realistic looking maps, it is sometimes more convenient to represent the data in the form of Gaussian components, allowing for easier analysis. The process of representing the data with Gaussian components is known as *Model-Fitting* and can be performed in DIFMAP. Typically, the model-fitting process is performed on the final self-calibrated and CLEANed uv-data-set. We can determine the goodness-of-fit by determining the reduced chi-squared ($\frac{1}{n-1}\chi^2$). This is performed by maximising the likelihood that the model represents the data. In a model with n data points and f free-parameters, this can be determined with:

$$\chi^2 = \sum_{i=1}^n \left(\frac{V(u_i, v_i) - F(u_i, v_i; a_1, \dots, a_M)}{\sigma_i} \right)^2 \quad (2.2)$$

Where σ is the standard deviation, V is the observed distribution and F is the predicted distribution. Thus, it can be seen that as the closer the reduced- χ^2 value is to one, the better the quality of the fit.

2.2 Calibration

Now that we know how to image a data-set, we can now investigate how to produce this calibrated data from the raw data outputted from the correlator. Most calibration is performed in AIPS, although some calibrations are applied at the correlator stage. Almost all VLBI calibration is performed using the Astronomical Image Processing System or AIPS.

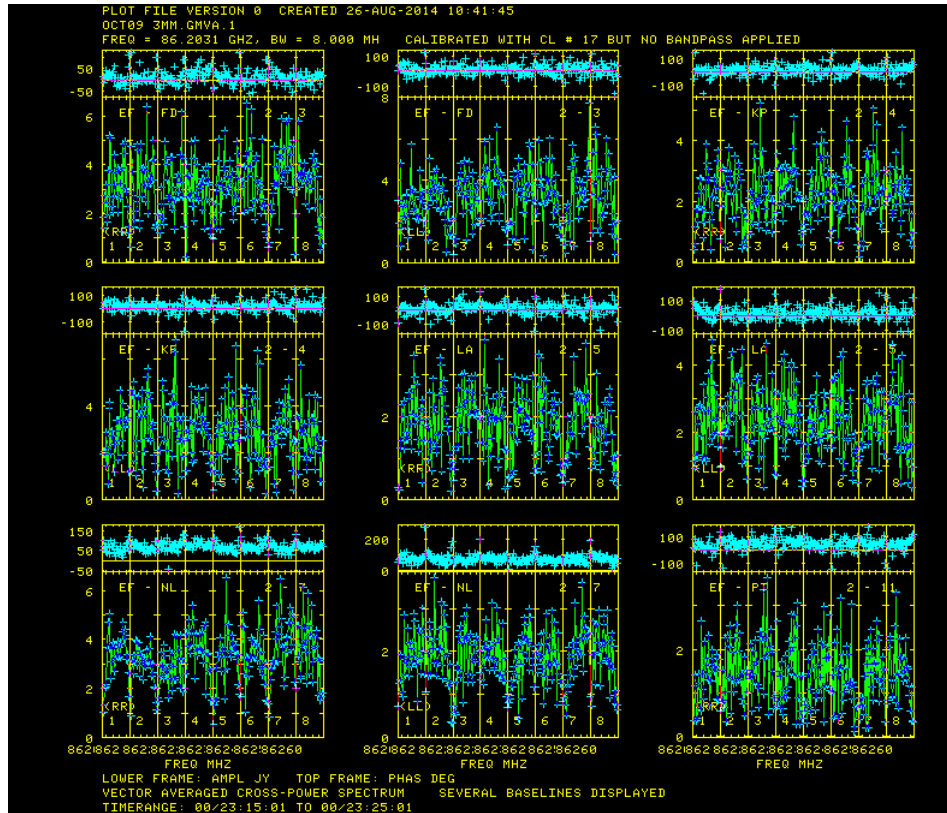


FIGURE 2.16: Final calibrated AIPS dataset. Phases (top panel) are all aligned and fluxes are corrected showing amplitudes of 2-3 Jy.

An example of a fully calibrated data-set that is ready for export is given in Fig. 2.16. Each plot contains in the top panel, the phases and in the bottom, the amplitudes. The phases should be flat across the frequency band and the amplitudes should have units that seem reasonable (although this is more easily checked in DIFMAP). Each plot is subdivided into 8 intermediate frequencies, or IFs. This should be checked in all polarisations, including LL (left-left), RR (right-right), RL (right-left) and LR (left-right), for circularly polarised feeds. If linear polarised feeds are used, the polarisations will be XX, YY, XY and YX. The cross-polarisations (RL/LR and XY/YX) are important for producing polarisation images and should be flat also.

Broadly, there are two categories of calibration; *a priori* calibration and *phase* calibration which uses a technique called *Fringe Fitting*. It is not important in which order the calibrations are applied apart from corrections applied directly after data-loading. This section relies heavily on Taylor et al. (2008).

2.2.1 Phase Calibration

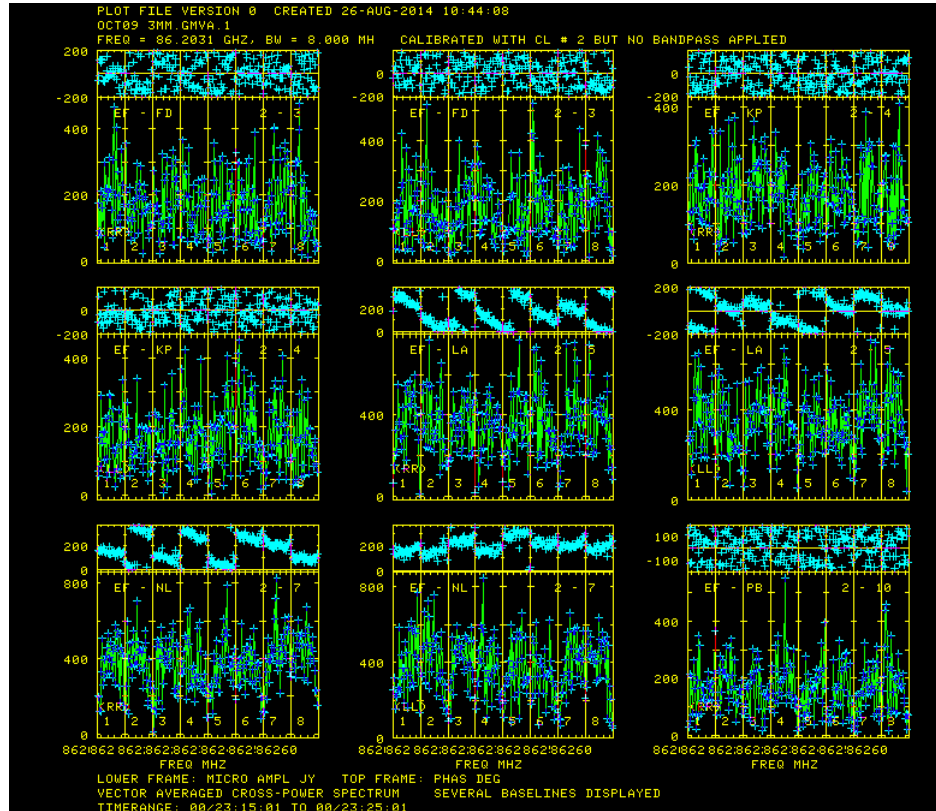


FIGURE 2.17: Possm plot before any calibrations are applied.

The phases seen in Fig. 2.16 are a function of $frequency \times delay$. The rate and delay are terms that come up frequently in VLBI analysis and an understanding of what they are and how they effect data quality are important.

2.2.1.1 Delay

When we speak of the *delay*, we must consider how an interferometer works. Light from the source arrives at one antenna with a *delay* relative to the other antenna. Whilst these delays are mostly taken into account at the correlator, some errors remain. Because the instrumental phase is $frequency \times delay$ and the IFs are made up of channels with different frequencies, errors should exhibit themselves as a slope in the phases of a *possm* plot.

There are two delays that must be solved for: single-band delay and multi-band delay. The single-band delay corrects the delay in a single IF. The multi-band delay is solving for frequency dependence of the single-band delay and hence

combines the single-band delay over all IFs.

2.2.1.2 Rate

We cannot expect that the errors in delay stay constant with time in a VLBI experiment. The change of the phase with time is known as the *fringe rate* and not accounting for it can limit the sensitivity of the experiment. Similarly, the change in delay with time is known as the *delay rate*. Time dependent changes are typically due to atmosphere and drifts in local timing standards. This is usually less of a problem for connected interferometers (e.g. VLA/ATCA) as these errors are correlated for each antenna and can be removed with self-calibration. This will obviously not be the case with VLBI and hence must be accounted for to maximise the quality of the experiment.

2.2.1.3 Fringe Fitting

The process that removes residual errors in delay and rate is known as *fringe-fitting*. Fringe-fitting is a conceptually simple process that begins with Fourier Transforming the amplitudes and phase as a function of frequency into a function of delay and rate. The position of the peak amplitude in this FT is the error in any given scan and the delays and rates are corrected against a reference antenna. The absolute value of the offset in delay and rate from zero is not important, but that the *relative* offsets between different antennas and the reference antenna are zero.

There are two kinds of fringe-fit. The first is a baseline fringe-fit, where only two stations are used and hence each baseline is independently fitted for delay and rate. The second is the *global fringe-fit*, where all baselines are used to estimate the antenna delays and rates (and hence phases) relative to a reference antenna ([Schwab & Cotton 1983](#)). The global fringe-fit also uses the closure quantities for rate, delay and phase.

2.2.1.4 Manual Phase Calibration

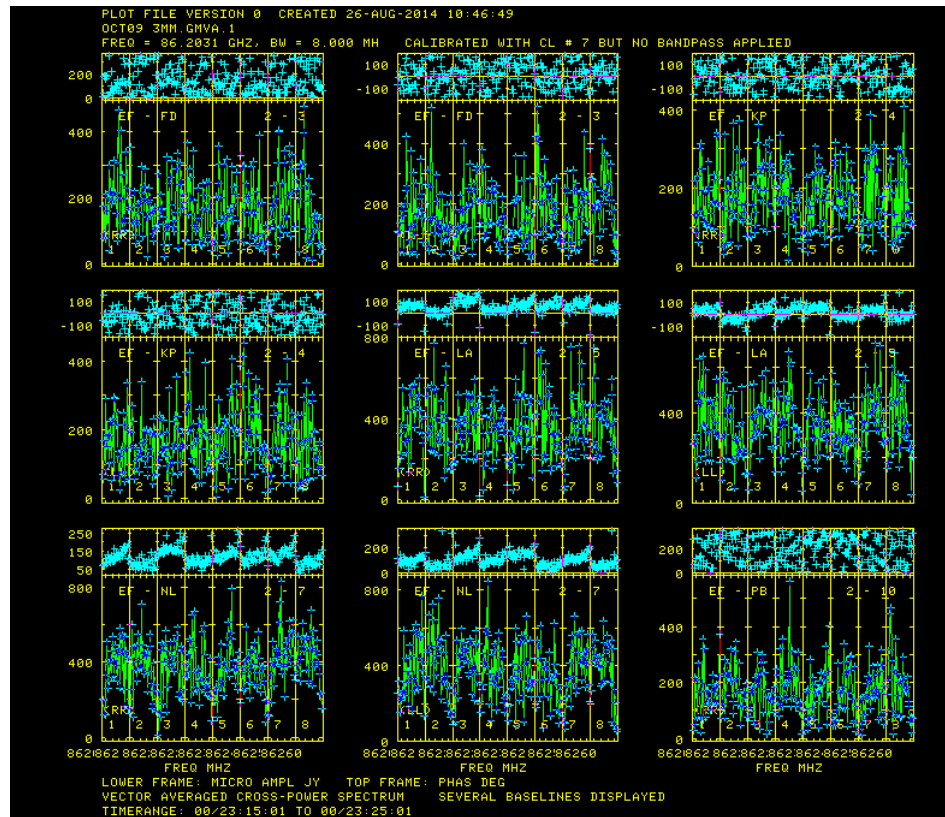


FIGURE 2.18: Possum plot after Manual Phase Calibration in AIPS. Note how the phases are now flat *within* the IFs.

After loading the raw data into AIPS, the IFs will appear unaligned as in Fig. 2.17 as each of these IFs has partially independent phases and delays. The manual phase calibration is the process that “flattens” out the phases of the IFs, taking into account most instrumental effects. This is calibrating the single-band delay. Essentially, the manual phase-cal step ensures that all baselines have their delays and phases relatively close to each other in preparation for the global fringe-fit (rates are set to zero). The technique entails fringe-fitting a small section of data on a bright source and then applying the solutions to the whole experiment under the assumption that instrumental delays and phase offsets between IFs do not vary significantly over the course of an experiment. At this stage, all delays in the IFs are also set to the same value. A more in-depth explanation of the process is given in Chapter 3.

2.2.1.5 Global Fringe-fit

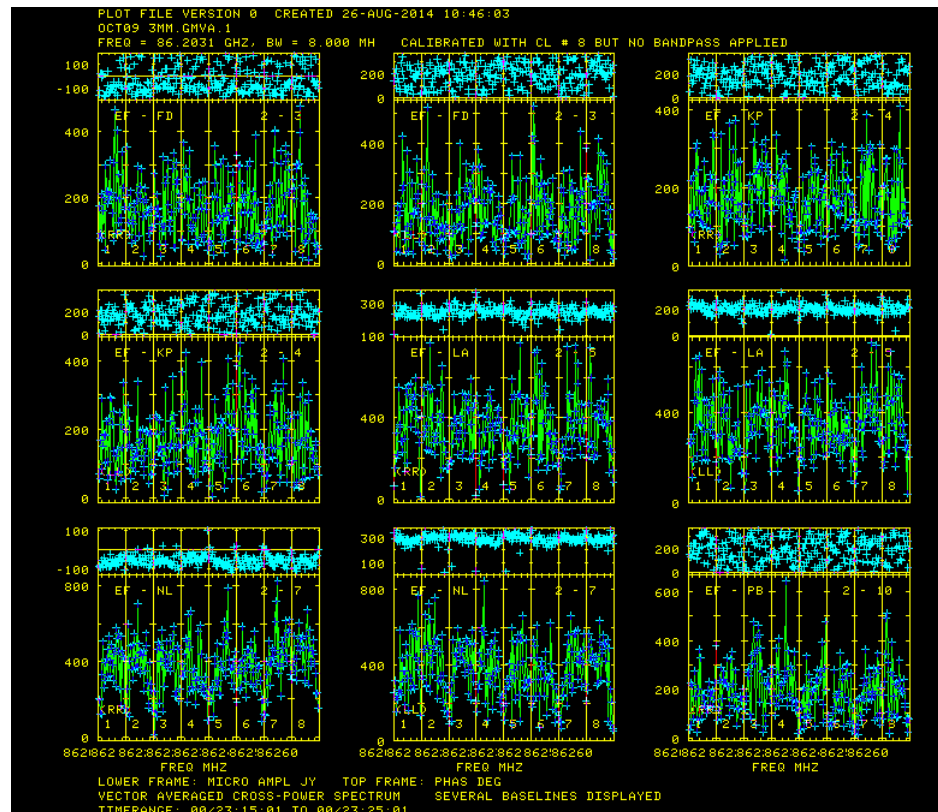


FIGURE 2.19: Possm plot after Fringe-Fitting in AIPS. Note how the phases are now flat *across* the LFs, as compared with Fig. 2.18

Once the manual phase-cal has been performed and the delays and residual phase offsets are fairly close to each other on all baselines, we can proceed and perform a global fringe-fit. The aim of the global fringe-fit is to produce as many solutions as possible. In theory, this should be easy. Simply find the peak in the delay/rate plane and shift all scans accordingly.

2.2.2 Amplitude Calibration

With connected element interferometers, calibrating amplitudes is much simpler, as their resolutions are much lower than in VLBI, many sources are strong, unresolved and do not vary on short time-scales. This means that if we know the source flux ahead of time, we can correct for atmospheric and instrumental amplitude errors against a source model.

Unfortunately, in mm-VLBI there are no standard source calibrators because sources compact enough to be detected with VLBI tend to vary very rapidly in flux. In order to circumvent this, the sensitivity must be measured at individual stations. In practice, this means that tables of *System Temperatures* (T_{sys}) and *gain curves* are recorded at the antennas and then distributed to the PI for calibration. Additionally, in mm-VLBI experiments, the atmosphere can play a significant role in amplitude errors and *opacity* (τ , Section 2.2.2.4) values are also distributed to the PI.

2.2.2.1 System Noise and the SEFD

In a radio telescope, usually the noise dominates over the signal that you are trying to measure. A convenient measure of the system noise is the *System Equivalent Flux Density* (SEFD). The SEFD is a measure of how strong a source must be in order to double the power output of the telescope due to noise alone. The SEFD is defined as:

$$\text{SEFD} = \frac{T_{\text{sys}}}{G} \text{ Jy} \quad (2.3)$$

Where T_{sys} is the System Temperature in K and G is the gain in (K/Jy) .

2.2.2.2 System Temperature

The system temperature (T_{sys}) measured in Kelvin, is a measure of the noise in the system from various sources, such as the receiver itself, the ground, interference and the (otherwise blank) sky. Clearly, all these variables can change rapidly, so they must be measured continuously. The most common way to measure this is to inject noise of a constant and known temperature at the point the radio waves are detected (the receiver). The T_{sys} can then be calculated with:

$$T_{\text{sys}} = \frac{T_{\text{cal}} P_{\text{cal-off}}}{P_{\text{cal-on}} P_{\text{cal-off}}} \quad (2.4)$$

Where $P_{\text{cal-on}}$ and $P_{\text{cal-off}}$ are the measured power (in Watts) with the noise cal on and off respectively. However, before continuing, we should discuss why we use *temperatures* for measuring noise and signal strengths.

While *black-body radiation* will be covered in greater detail in Chapter 4, it is important to know that it is a representation of radio *brightness*. It is the temperature that an ideal black-body radiator (e.g. the Sun is a black-body radiator) would have to be in order to be the *brightness* that we observe. For example, the brightest regions of Fig. 2.1 have a very high brightness temperature because they are very bright and come from a very small region at a great distance. Hence, the system temperature is the equivalent temperature of the system. A typical system temperature at a telescope such as Effelsberg or Pico Veleta at 3 mm may be 100-150 K.

2.2.2.3 Opacity

Radio waves are absorbed by the atmosphere and at mm wavelengths, this effect is particularly important. The amount of radio radiation that is not absorbed and makes it to the telescope is known as the *opacity* or τ . That is to say that if τ is 0, no emission is absorbed and we see the source perfectly. In practice, only a space based telescope will have no opacity, but we can correct for the effects of opacity using the following equation:

$$T_{\text{sys}} = T_{\text{antenna}} + T_{\text{atmosphere}}(1 - e^{-\tau/\sin(\text{elevation})}) \quad (2.5)$$

2.2.3 Polarisation Calibration

Incoming radio waves at the receiver are very low energy and treated as waves. In Fig. 2.20 we see an incoming wave has an oscillating electric field that induces voltage oscillations in a conductor. These oscillations are known as the polarisation and if you have a pair of crossed wires, called a *dipole*, this can be detected. However, in most telescopes, the orientation of the dipole towards the sky changes as the telescope tracks sources. The parallactic angle correction simply 'rotates' the dipole so that the orientation is the same at all times. This should be done very early in the reduction process, prior to fringe fitting.

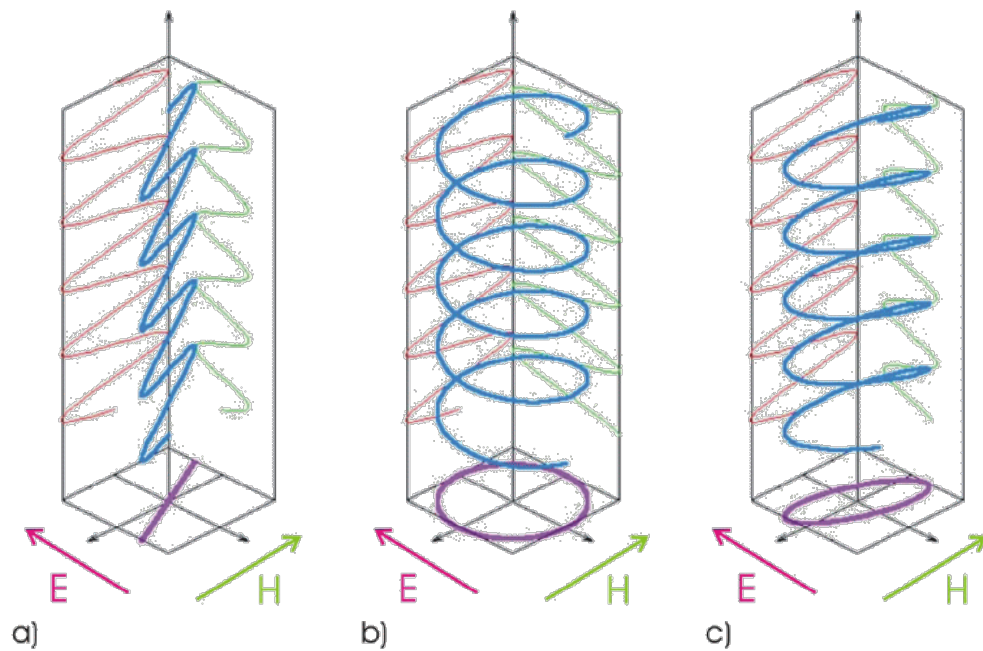


FIGURE 2.20: A sketch of oscillating radio waves or polarisation from HarzOptics GmbH. In panel a) linear polarisation b) circular polarisation c) elliptical polarisation. E is the electric field and H is the magnetic field. The cross at the bottom can be thought of the dipole antenna that detects the radio waves.

It is the correlations between the two dipoles that allows us to extract polarisation information. It is common to observe in left (LCP) and right (RCP) handed circular polarisation, giving four correlations. RR, LL, RL and LR. RR and LL are the single polarisations. RL and LR are the *cross polarisations* and is where the polarisation information is found. In Fig. 2.16, we can see that we are only seeing the LL and RR correlations. We need the phases to be flat in the cross-polarisations as well, requiring calibration similar to that of the manual phase-calibration step. Unfortunately, the detection of polarisation is not perfect and there is a significant effect known as *leakage*, where some voltages in one wire leaks into the other. To correct for this, we need to determine the so-called *D-terms*, which describe the cross-talk between the two orthogonal polarisation directions.

2.3 Correlation

The data that you input into AIPS is the output of the *correlator*. At it's most simple, a correlator simply takes two digital representations of voltages and multiplies them together, however as one may expect, it's far more complicated

than that.

The source we are looking at is so distant that we assume that any waves we receive from it are parallel. What this means, is that any telescope should detect an identical signal except with a *delay* equivalent to the speed of light and the distance between the two telescopes. A simplified version of this situation is shown in Fig. 2.21. This delay, known as the *geometric delay* is easily computed with:

$$\tau = \frac{b}{c} \sin \theta \quad (2.6)$$

Where b is the baseline length vector, c is the speed of light and θ is the angle to the source. At the correlator, this delay is added to the signals using the *correlator model*. The correlator model at its most simple is a model of the locations of the telescopes, although these locations must be known to a very accurate degree. Typically, the correlator models can be accurate to within centimetres. Modern correlators do far more these days, however, with them taking into account relativistic corrections of the earth's orbit, path delays at telescope. However, these models are not perfectly accurate and any residual errors are corrected for during the fringe-fit process (e.g. in *fring* in AIPS).

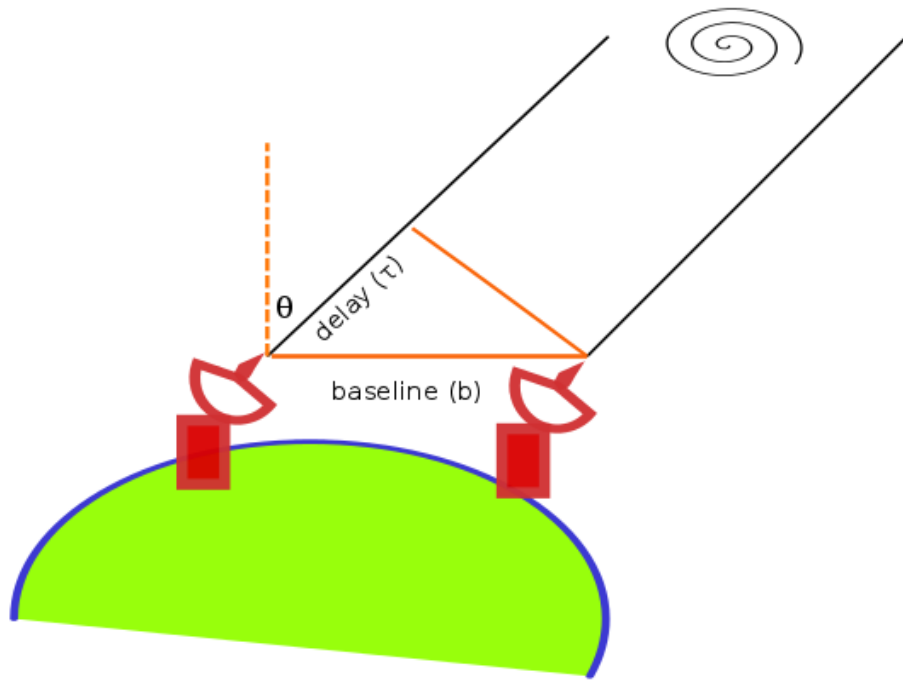


FIGURE 2.21: Incoming waves from a distant source appear as parallel wavefronts. Each telescope receives the same signal but with a *geometric delay*. This delay is accounted for at the correlator. The process of correlation finds where the delay occurs and multiplies the signals together.

2.3.1 The correlation function and visibilities

If you have two similar signals, one can compute the *correlation function* to determine when or where the signals are most similar. In the case of radio astronomy, we wish to determine when they are most similar.

In Fig. 2.22, we can see two signals, red and blue. When they are multiplied together, they create a correlation amplitude or *fringe*, shown in green. Essentially, the correlation function slides the two signals against each other and where the fringe strength is maximum, the two signals are most correlated.

When this is found, this is known as the *visibility function* and for the correlation between two voltages V_1 and V_2 , it is given by:

$$\text{Visibility} = \langle V_1 \cdot V_2^* \rangle = V_0^2 \cos(2\pi\omega\tau) \quad (2.7)$$

Where ω is the frequency and τ is the geometric delay.

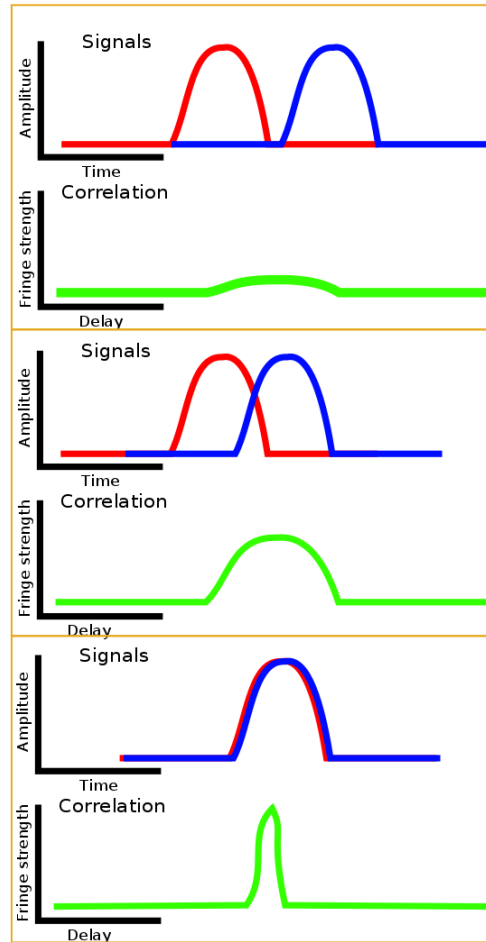


FIGURE 2.22: As the two signals (red and blue) are slid against each other, where the fringe amplitude is maximum, the two signals are most alike or most highly correlated. In the case of radio astronomy, we are attempting to find the *time* where the two signals are most highly correlated as this corresponds to the geometric delay between the two.

For each scan, the visibility function (or just a *visibility* in VLBI parlance) is computed. Each visibility that is computed corresponds to a single point on the uv-plane in Fig. 2.8. The correlation function is FT of the sky brightness distribution, thus the visibilities are proportional to the cross-correlation function.

The more visibilities, the more points on the uv-plane and the better quality image at the end.

2.3.2 Types of Correlators

Whilst conceptually simple, correlators are massively computationally expensive. There are two broad categories of correlator, XF (or lag) correlators and FX correlators, such as the DiFX correlator used at the MPIfR. Remember that the uv-plane is the *Fourier Transform* of the actual source structure, so the output of the correlator must be in *Fourier* or “frequency” space.

The XF or lag correlator works in the way described in Fig. 2.22. It is so called as the correlation is performed first (X) and then Fourier Transformed (F) into output visibilities. The signals are shifted against each other by a certain amount known as the *lag*. The larger the lag, the larger the amount the signals are shifted against each other. It is generally preferable to reduce the size of the lag as large values become increasingly computationally expensive. This form of correlator was until recently the most common form.

Today however, the FX correlator is prevalent with the DiFX software correlator being probably the most commonly used (Deller et al. 2011). In an FX correlator, the data is first Fourier Transformed and the peak of the correlation function is found in frequency space, which is also the form in which the data are written out in.

2.3.3 Coherence Time and Averaging

The coherence time can be thought of as the amount of time that we can confidently predict the state a sine-wave will be in. In practice, this means that we cannot average longer than the time it takes for the phases to rotate 180 degrees. In a correlator, in order to make the signal easier to detected, the data is averaged in time, but in mm-VLBI the coherence time can be a significant problem, with the coherence time frequently being little more than a few tens of seconds. The averaging time in the correlator must be carefully selected so that the signal strength is maximised while ensuring that data is not lost due to averaging longer than the coherence time.

2.4 Sampling and Recording

In order for the data to be correlated, the data must be sampled, digitised and recorded. The sampling and digitisation is performed using the *backend* and then recorded on *Hard-Disk recorders*.

At its most simple, a radio telescope of any kind is detecting sinusoidal electric waves, which are detected as sinusoidal voltages, V . These voltages must be recorded in such a way that a computer can then read them. In modern VLBI backend systems, the signal is digitised in high quality but recorded at lower qualities. Typically in this context, when we refer to 'quality' we are referring to the bit rate.

2.4.1 Bit-Rate

Computers operate in the digital domain, implying that any external analog signal must be *quantised*. When a signal is recorded, the *bit-rate* refers to how many steps of amplitude is being recorded. The number of steps that can be encoded is 2^{bitrate} , so 2 bits gives 4 amplitude steps and 4 bits gives 16 amplitude steps and so on. In a modern backend such as the DBBC, the signal is *sampled* at 10 bit resolution but is *recorded* at 2 bit resolution.

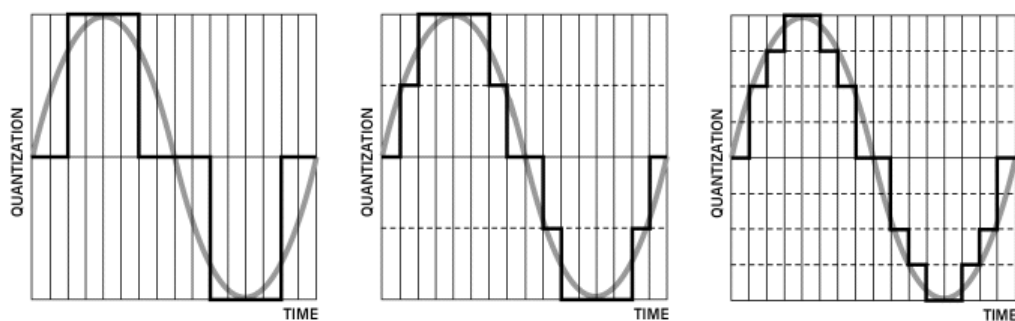


FIGURE 2.23: In this sketch from [Soundcloud](#), we can see how the number of bits effects the quality of the sinusoid's digital representation. From left to right, 1 bit, 2 bits and 3 bits.

2.4.2 Recording Rate and the Nyquist Frequency

A concept that is related to the bit-rate is the *sampling rate*, which is how frequently the signal is sampled. In order for a signal to be completely reconstructed, the signal must be sampled at least twice as fast as the highest frequency in the signal. This frequency is known as the *Nyquist Frequency*. Luckily in a radio telescope, we know very precisely the frequency of the sinusoid to be sampled. Hence, most astronomical data recording is recorded at or near Nyquist so as to maximise the amount of data that can be stored in a given amount of hard-disk space.

2.4.3 Sampling, Bandwidth and Sensitivity

An important consideration when determining the bit-rate is the *sensitivity*, defined as a measure of the weakest source that can be detected. If a perfectly sampled sinusoid has a sensitivity of 100 %, one bit recording will have only 64 %. 2 bit recording however recovers 81% of the sensitivity and 3 bit 88%. As can be seen, adding more bits leads to the law of diminishing returns. The sensitivity of a two element interferometer (stations a and b) is given by:

$$\text{Sensitivity} = \Delta S_{ab} = \frac{1}{\eta_s} \sqrt{\frac{\text{SEFD}_a \text{SEFD}_b}{2\Delta\nu t_{av}}} \quad (2.8)$$

Where SEFD are the System Equivalent Flux Densities of the stations, η_s is the system efficiency factor (which takes into account various losses in the electronics etc.), t_{av} is the averaging time at the correlator and $\Delta\nu$ is the bandwidth. The bandwidth can be thought of as the difference between the highest and lowest frequency observed. For example, in a 3 mm observation, we commonly refer to this also as an 86 GHz observation, however in reality, only the *center frequency* may be this. If an experiment has 512 MHz of bandwidth with a center frequency of 86 GHz, the frequencies between 85.75 GHz and 86.25 GHz are being observed.

Hence, we can see that in most situations, increasing the bandwidth rather than the bit-rate is preferable for increasing sensitivity.

2.5 Radio Telescopes

The first step in the long process of creating a radio interferometric image is detecting the radio waves at the radio telescope. We already know that the telescope detects induced voltages on a dipole from incoming polarised radio magnetic fields which are then detected in digital backends. The process of taking the signal at the dipole is however complicated and summarised here.

2.5.1 The Antenna Pattern

Most antennas are not omnidirectional, which is to say that they do not have an equal *response* in all directions - they point better in a particular direction. In Fig. [2.24](#) we can see how this directionality effects how and where the antenna is sensitive. The area between the two lines denoting the Full-Width-Half-Maximum (FWHM) is properly known as the primary lobe, but is better known as the telescope *beam*. The resolution(θ_{res}) of the antenna is given by:

$$\theta_{\text{res}} = 1.22 \frac{\lambda}{D}, \quad (2.9)$$

where λ is the observing wavelength, D is the diameter of the telescope and 1.22 is the taper function.

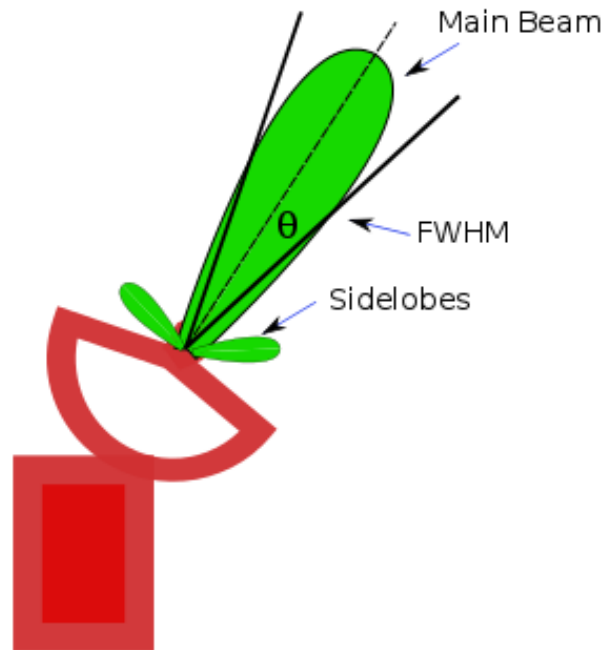


FIGURE 2.24: Sketch of the beam-shape of a radio telescope. The Full-Width-Half-Maximum (FWHM) is the .

2.5.2 Detection

Before being detected by the dipole, the radio waves are (in almost all telescopes) reflected and concentrated - the famous 'dish' of radio astronomy. In Fig. 2.25, we see that the dish takes a large area of radio waves and concentrates it into a small area. This is a lens, in the same way an optical telescope. There are many varied forms of dishes, but most reflect the waves into the *primary focus*. The waves are either detected there directly or reflected again into a *secondary focus* and detected there. For more information on this, see Section 3.5.

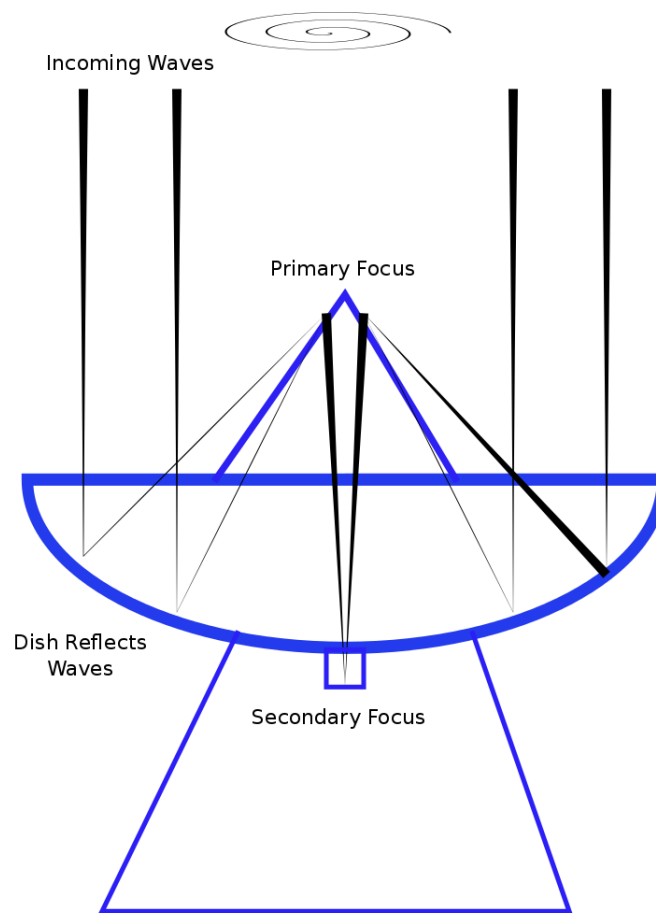


FIGURE 2.25: Sketch of the optics of a radio telescope. Incoming radio waves are reflected and concentrated in the primary focus. They are either detected there or reflected again to a secondary focus where the detection is performed instead.

2.5.3 Effective Aperture and Efficiency

The characteristics of the main beam and sidelobes, the accuracy of the surface of the dish and many other things contribute to the *efficiency* of the telescope. Generally, engineers try to get efficiency as close to 1 (perfect efficiency) as possible. Related to the concept of efficiency is *gain*. The gain and SEFD are related to how well the telescope can take a faint signal and amplify it. The *effective aperture* is jargon for how much of the telescope's surface area can be used for collecting radio waves. It is simply the ratio of the physical area of the dish to the *effective or usable area* of the dish.

2.5.4 Surface Efficiency

As one may expect, radio telescopes are not perfect reflectors. They have defects in the surface during construction. Ambient temperature changes can cause the shape of the dish to change slightly. Wind and gravity can do the same. The measure of these imperfections is known as the *surface efficiency*. At high frequencies the surface needs to be very accurate in order to make detections. As an example, for observing at 86 GHz, the surface must be correct to within 175 *microns* for a surface efficiency of 70%. This feat is sometimes achieved by using *adaptive optics*, where the surface is deformed deliberately to account for atmospheric errors. The gain (G) can be computed with the Ruze formula:

$$G = G_0 e^{(-4\pi\delta/\lambda)^2}, \quad (2.10)$$

where G_0 is the gain of a perfect reflector, δ is the (random) rms surface error and λ is the wavelength in the same units as the rms surface error.

2.5.5 Receivers

After the radio waves have been reflected and collected, they must be detected with the *receiver*. Typically, it consists of a feedhorn or waveguide that channels the reflected radio waves onto the dipoles. These are typically single-feed, but it is increasingly common to have two or more feedhorns in the receiver. The feedhorns themselves are often corrugated in order to reduce surface impedance.

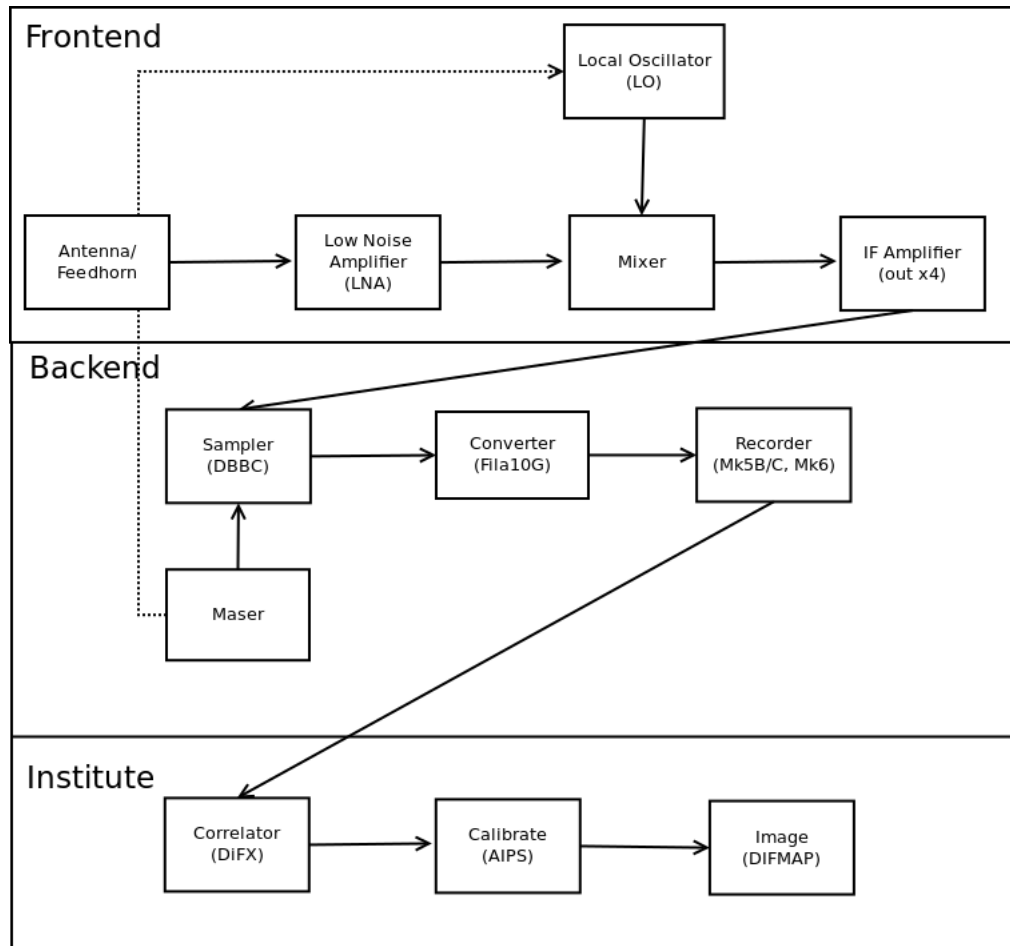


FIGURE 2.26: An overview of the signal path in a typical *digital* VLBI system.

2.6 Summary

This is just a high-level overview of the day-to-day operations in VLBI astronomy. The only way to learn how to perform these tasks properly is to reduce and analyse real data.

In the next chapter, we will overview the scientific background of this thesis.

Chapter 3

Scientific Background

The sources of interest of this thesis are Active Galactic Nuclei or AGN, which are the most continuously luminous objects in the known universe. Specifically, we are investigating the form of AGN where we are looking 'down the jet' - a source type known as a blazar. What causes blazars to be so luminous? Why do they behave so weirdly? What is the bigger context of these amazing objects? How and where are γ -rays produced? In this chapter, we hope to explore the state of knowledge in reasonable detail and demonstrate how high frequency VLBI can shed light on these questions.

3.1 The Radio Sky

There have been many surveys of the radio sky at various frequencies, with probably the best known being the NRAO VLA Sky Survey (NVSS) at 1.4 GHz (Condon et al. 1998). These surveys have shown that the sky is dominated by discrete sources which are approximately uniformly distributed with a slight excess towards the galactic center. Outside of the galactic plane, there is no preferred direction of sources.

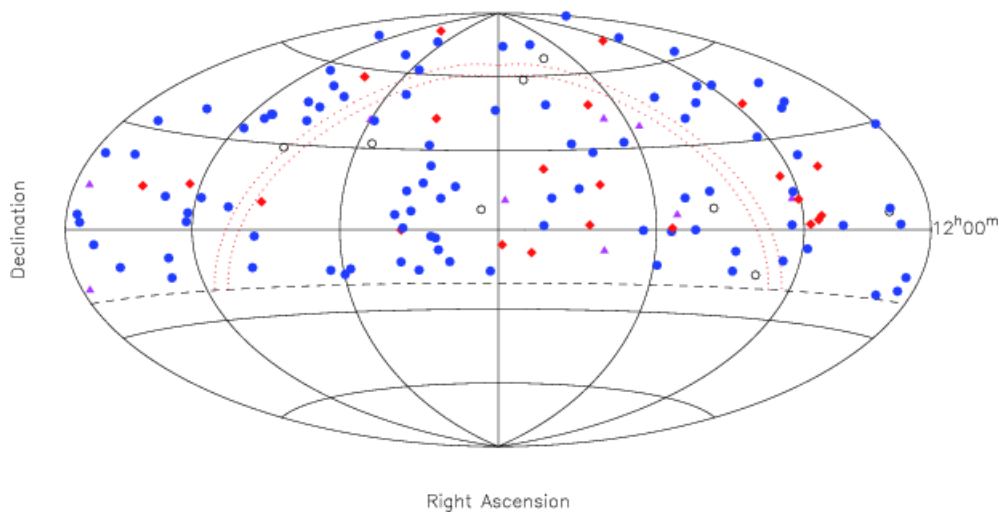


FIGURE 3.1: Distribution of 133 AGN in the Northern sky from Arshakian et al. (2006). Filled circles are quasars, diamonds are BL Lacs and triangles are radio galaxies.

There are many sources that emit at radio wavelengths including pulsars, supernova remnants, star forming regions, the galactic center and radio galaxies, including quasars and blazars.

3.2 The Anatomy of a Radio Galaxy

Radio galaxies are immense objects, the scale of which most people cannot fathom, especially when viewed at radio wavelengths. In Fig. 3.2, Centaurus A is overlayed on the sky with ATCA and the full moon for scale. We can see that it is over 200 times bigger than the moon, despite being *12 million light years* away.



FIGURE 3.2: Composite image of Cent A with ATCA and the moon for scale.

CSIRO

Another very famous radio galaxy is Cygnus A and in Fig. 3.3, a 6 cm VLA image has been annotated. In the center is the so called “core”, where jets are thought to originate. It is presumed that a Super Massive Black Hole (SMBH) resides within this unresolved nucleus, powering processes that are not fully understood. The jets continue in a very collimated fashion until they hit the surrounding Inter-Galactic Medium (IGM), where a bow-shock forms. This creates bright lobes with hot-spots and a back-flow. To give a sense of scale, the distance from the “core” to the radio lobes is approximately 160 000 light years.

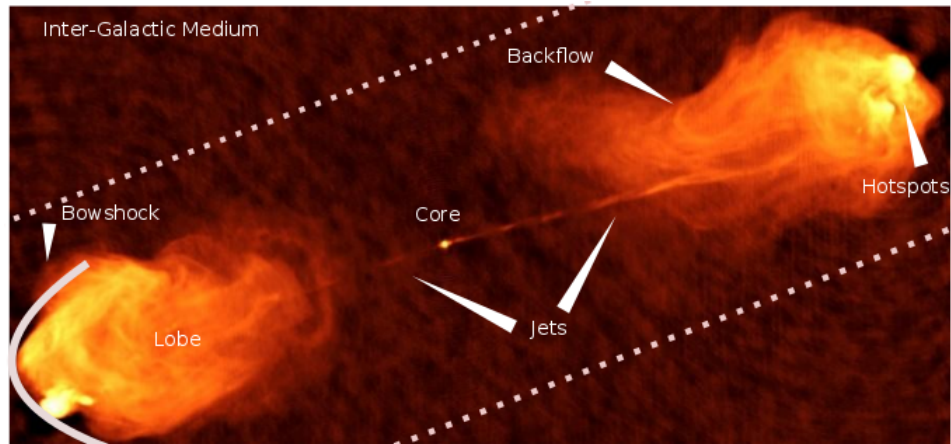


FIGURE 3.3: Annotated 6 cm VLA image of the radio galaxy Cygnus A. NRAO

The jets are remarkably straight, given the likely turbulent local environment.

As we increase baseline lengths and frequency, we can peer further into these ‘core’ regions, as can be seen in Fig. 3.4. As we zoom in, we can resolve more detail around the “core” and the jets that emanate from it. The “core” itself is normally characterised by a *flat spectrum* - that is that the “core” emits at almost the same amplitude across all frequencies.

From the ‘core’, many components get ejected, with a range of different sizes and properties. Their origins are a mystery that high resolution VLBI studies can possibly resolve. The morphology on large scales is dominated by the local environment. Jets are often found in galaxy clusters, and as galaxies move through the Inter-Cluster-Medium, the jets can distort and bend, leading to the two broad categories of radio galaxies - FRI and FRII

3.2.1 FRI and FRII

(Fanaroff & Riley 1974) introduced the Fanaroff-Riley dichotomy that us still in use today. Fanaroff-Riley I (FRI) galaxies are characterised by double sided jets and diffuse lobes. They tend to be *limb darkened* and less luminous when compared with Fanaroff-Riley II (FRII) sources. Correspondingly, they have lower jet speeds, with the jet fading out and dissipating before reaching the lobes. Following from their lower speeds and luminosities, they also tend to be more effected by their environments. They also have no (or very weak) optical emission lines. FRII galaxies are similarly characterised with double-sided jets, though they are more collimated than FRIs and terminate in bright hot-spots. Their jets are edge

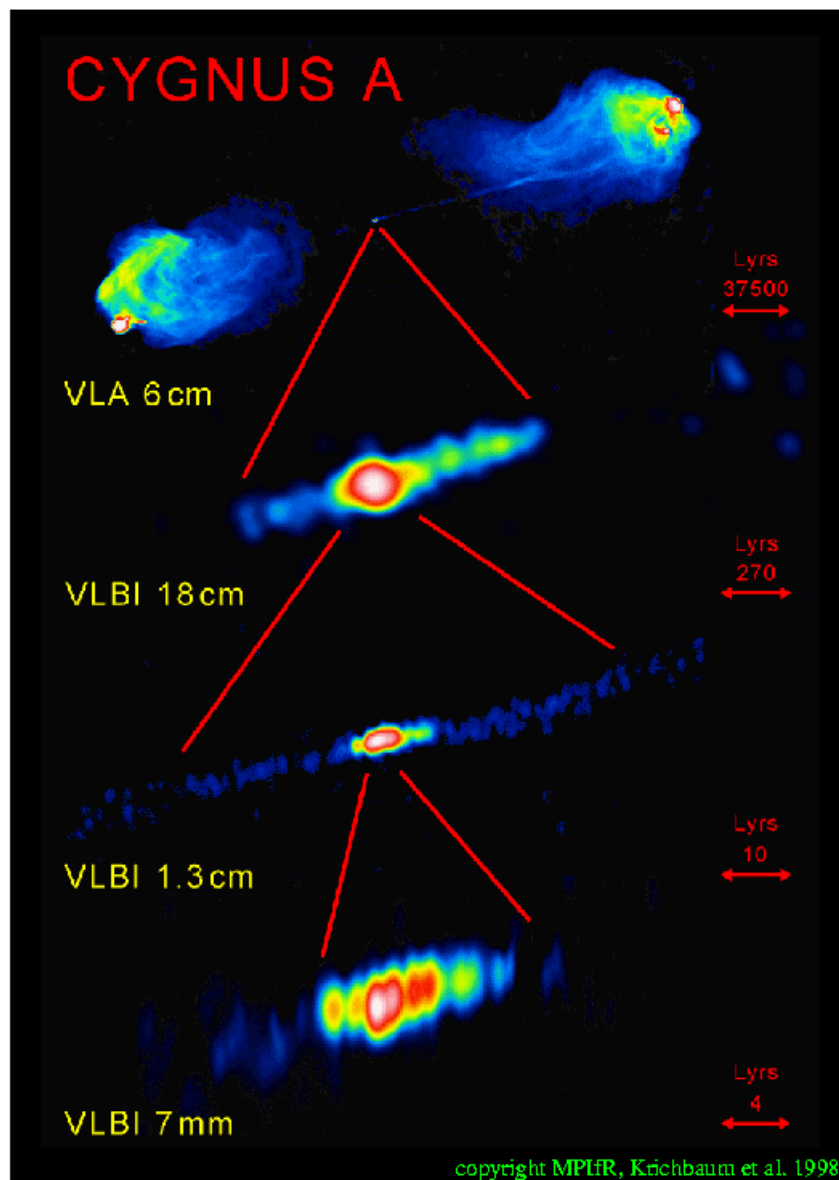


FIGURE 3.4: An example of the resolving power of VLBI on Cygnus A, from Thomas Krichbaum at MPLfR

brightened, more collimated, faster and more luminous with strong optical emission lines .

3.3 Quasars, Blazars and AGN Unification

The first Active Galactic Nuclei (AGN) activity was detected in NGC 1068 over a century ago, though their full significance was not realised at the time (Fath 1909). Less than a decade later, the first jet was detected in M87, though once

again its extragalactic nature was not known (Curtis 1918). Quasars were first observed in radio frequencies in the late 1950's by Baade & Minkowski (1954), with the first observations performed on Cygnus A. Using early interferometers they determined that these 'Quasi-Stellar Objects' (from where the term quasar is derived) were of very small angular extent - looking optically like stars (Schmidt 1963)¹. Schmidt (1963) defined a quasar as being characterised by its star-like appearance and flat emission line spectra. Complications with identifying radio sources with optical counterparts delayed the first redshift determination until 1963, when the quasar 3C 273, and found to have a redshift of 0.158 (Schmidt 1963), and the subsequent realisation that redshifted spectral lines were due to their cosmological origins.

However, it later transpired that these quasars were merely one form of AGN.

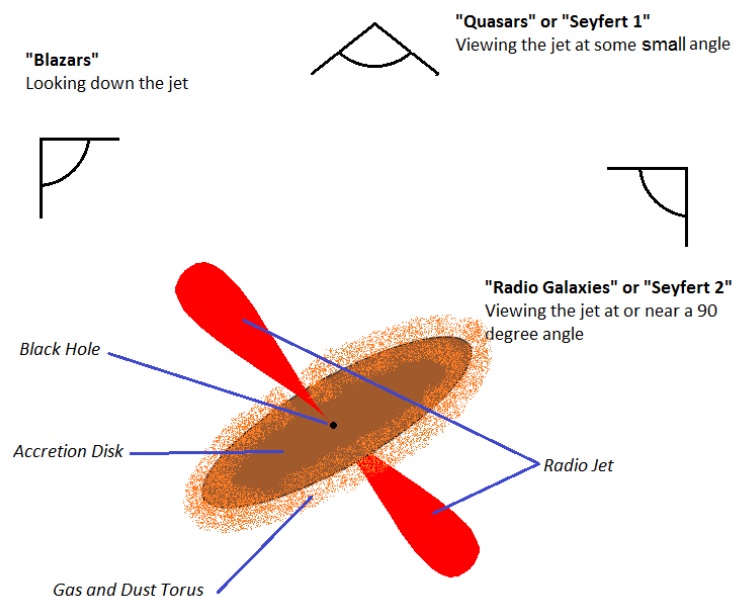


FIGURE 3.5: A simplified diagram explaining the broad differences in the categories of AGN. Also a diagram of the features of AGN.

Quasars (or QSOs), then, are defined as highly powerful AGN, with approximately 10 percent being "radio loud", while Seyfert galaxies are spiral galaxies that have quasar like AGN. BL Lacs are like QSOs but tend to be less distant and with no optical emission lines. Optically Violently Variable objects are similar to BL Lacs but with broad emission lines. Blazars are the combined population of QSOs and BL Lac sources that are particularly active and variable.

¹The term quasar was actually first coined by Hong-Yee Chiu in Physics Today in 1964.

Blandford & Rees (1971) noted that variability of these sources meant that they would be of order light days across, if stationary. They suggested that the radiation was produced by synchrotron emission and that it was relativistically beamed forward. Hence, the increased variability was directly caused by this relativistic beaming with the observed variations being compressed in time. Indeed, the idea of relativistic boosting as an astrophysical phenomenon had been raised earlier by Woltjer (1964). It was suggested that blazars were the case of looking “down” the jet. Quasars are being viewed at small angle to the jet and radio galaxies edge on. Hence, the changes in variability are likely due to variations in Doppler boosting due to smaller angles to the line-of-sight (see Section 3.4.1). Statistical analysis of AGN by Orr & Browne (1982) gave strong evidence for the model - and it is now accepted by most astronomers. The unification model is described in detail by Urry & Padovani (1995). Fig. 3.5 shows a simplified diagram of the AGN unification scheme.

3.4 Relativistic Effects

One of the most striking features of AGN and particularly in blazars are relativistic effects. As matter approaches the speed of light, one can think of it as catching up to its own wave-fronts, causing many strange effects. The most striking of these effects are superluminal motion, Doppler boosting and time dilation. These sections are largely based off (Rybicki & Lightman 1979, and references therein).

3.4.1 Superluminal motion

Apparent Superluminal motion is the effect of components appearing to travel faster than the speed of light. It is not a real effect but an optical illusion.

At time t_0 , the orange object in Fig. 3.6 emits photon 1 in the direction of the observer. At time $t = 2$, the orange object has moved a tangential distance:

$$r = v \cos \theta \Delta t, \quad (3.1)$$

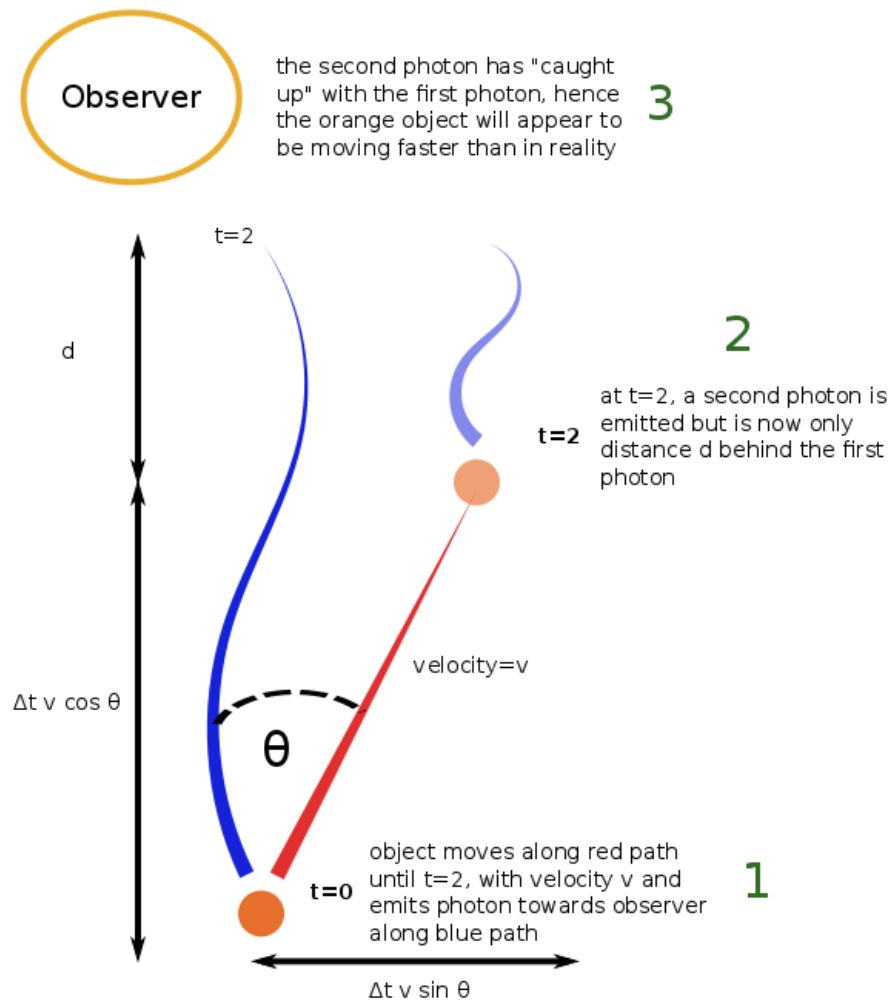


FIGURE 3.6: A sketch describing the basics of apparent superluminal motion.

where Δt is the time taken to get from $t = 0$ to $t = 2$. At $t = 2$, when the second photon is emitted, it is trailing the first photon by only:

$$d = c\Delta t - v \cos \theta \Delta t, \quad (3.2)$$

the time taken for the photon to travel distance d will be:

$$t_d = \frac{d}{c} = \Delta t(1 - \beta \cos \theta), \quad (3.3)$$

where $\beta = v/c$, or the speed as fraction of the speed of light. It should be clear that the closer β is to 1 (i.e. v is closer to c) and the smaller the angle to the line-of-sight, the more pronounced is the effect. The distance apparently travelled

on the plane of the sky in the time taken to get from $t=0$ to $t=2$ is then:

$$d_{\text{sky}} = v \sin \theta \Delta t, \quad (3.4)$$

and the apparent velocity on the sky is:

$$v_{\text{app}} = \frac{v \sin \theta}{1 - \beta \cos \theta}, \quad (3.5)$$

hence, the observed velocity v_{app} is a function of the intrinsic speed (β) and the viewing angle (θ)

Unfortunately, the viewing angle can be difficult to directly determine. However, we can find the angle where the apparent velocity v_{app} is maximised by taking the derivative with respect to θ and solving for 0.

$$\frac{d\beta_{\text{app}}}{d\theta} = \frac{\beta(\cos \theta_m - \beta)}{(1 - \beta \cos \theta_m)^2} = 0, \quad (3.6)$$

which can be solved for 0 with:

$$\cos \theta_m = \beta, \quad (3.7)$$

and also with:

$$\sin \theta_m = \frac{1}{\Gamma}, \quad (3.8)$$

where Γ is the Lorentz factor:

$$\Gamma = \frac{1}{\sqrt{1 - \beta^2}}, \quad (3.9)$$

and since superluminal motion can only be observed when the intrinsic speed β_{int} is higher than some minimum value, we can also compute:

$$\beta_{\text{app,max}} = \frac{\beta_{\text{int}} \sin \theta}{1 - \beta_{\text{int}} \cos \theta} = \beta_{\text{int}} \Gamma. \quad (3.10)$$

3.4.2 Doppler Beaming, Time Dilation and Length Contraction

As we saw in the previous paragraph, the photon emitting particles are catching up with the photons they are emitting, leading to apparent superluminal motion. This means that we observe photons being received faster than they were being emitted. This has two additional effects, the first being *time dilation*, where changes appear faster than they happen:

$$t_{\text{obs}} = \frac{t_{\text{emitted}}}{D}, \quad (3.11)$$

where D is the *Doppler Factor*:

$$D = \frac{1}{\Gamma(1 - \beta \cos \theta)}, \quad (3.12)$$

this will also effect the *frequency* of the observed emission:

$$\nu_{obs} = \nu_{emitted} D, \quad (3.13)$$

following from this, it also means that things appear *smaller* than they are in an effect known as *relativistic length contraction*. The solid angle (Ω) subtended is modified as:

$$\Omega_{obs} = \frac{\Omega_{emitted}}{D^2} \quad (3.14)$$

This also means that sources appear 'bendier' than they really are. Finally, the observed flux density (S) is boosted:

$$S_{obs} = D^{3+\alpha} S_{emitted} \quad (3.15)$$

Where α is the spectral index defined as $S \propto \nu^\alpha$. Stationary jet features are boosted $S_{obs} = D^{2+\alpha} S_{emitted}$. A flat spectrum source would hence be boosted by $S_{obs} = D^3 S_{emitted}$.

3.5 The Thermal Spectrum and Planck's Law

We know that AGN emit radiation across a broad range of wavelengths, from radio at long wavelengths to Gamma-rays at short. Despite knowing that the sources are *not* black-body radiators, radio astronomers frequently describe a source by a temperature that is equivalent to the temperature that a black-body radiator would have. This is the *brightness temperature*. The thermal spectrum tells us how much of a source's flux density is expended at a given frequency. Hence, when astronomers speak of a *flat* (emitting equally across all frequencies), *inverted* (flux density increasing with frequency) or *steep* (flux density decreasing with frequency) spectra, they are talking about the shape of a graph of received flux density and frequency, a sketch of which is provided in Fig. 3.7. This graph is known as a *Spectral Energy Distribution* or SED and its shape can tell us much about the processes that produce the emission. The thermal spectrum is given by *Planck's Law* from which one can compute a

brightness (B) as a function of temperature (T) and wavelength (λ):

$$B(\lambda, T) = \frac{2hc^2}{\lambda^5} \frac{1}{e^{\frac{hc}{\lambda kT}} - 1} \quad (3.16)$$

Where h is Planck's constant, c is the speed of light and k is Boltzmann's constant. Essentially, this is saying that entire spectrum is divided into h/λ sized packets of energy. This is known as *quantisation* and is what quantum theory derives from. However, radio waves are very low energy and are more easily described as a wave rather than as packets of energy. The previous equation can be approximated for long wavelengths using the Rayleigh-Jeans relation:

$$B(\lambda, T) = \frac{2ckT}{\lambda^4} \quad (3.17)$$

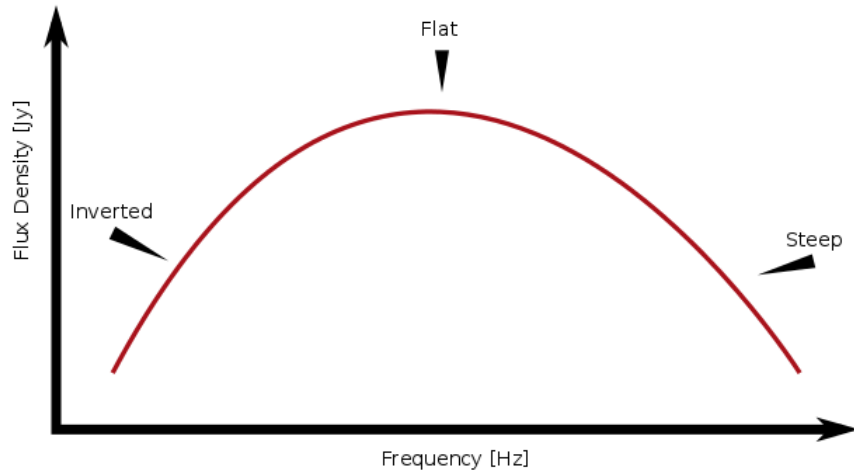


FIGURE 3.7: Spectral Energy Distribution (SED) sketch, showing the jargon commonly used to describe the spectrum of a source.

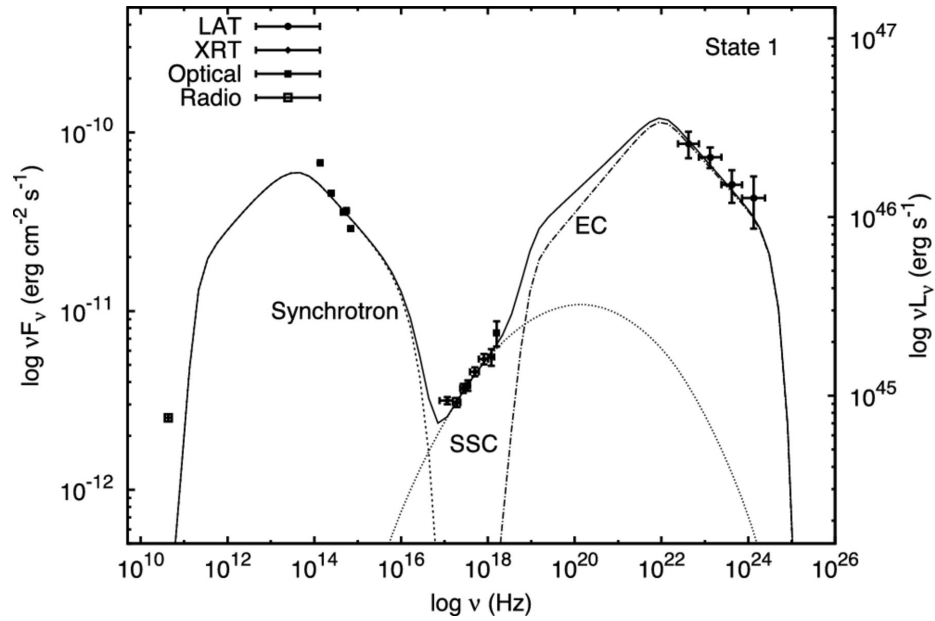


FIGURE 3.8: Spectral Energy Distribution (SED) of OJ287 from [Kushwaha et al. \(2013\)](#), showing the three main emission mechanisms modelled to fit the observed spectrum.

But how is the emission actually produced? The spectral properties of relativistic jets was first described by [Blandford & Königl \(1979\)](#), and was expanded to include high energy emissions (such as γ and X-rays) by [Konigl \(1981\)](#). In Fig. 3.8, we see the SED of the blazar OJ287 by [Kushwaha et al. \(2013\)](#), which has been modelled to include several emission processes. These processes are Synchrotron at low energies, and with Synchrotron-Self-Compton (SSC) and External Compton (EC) at higher energies.

3.5.1 Synchrotron Emission

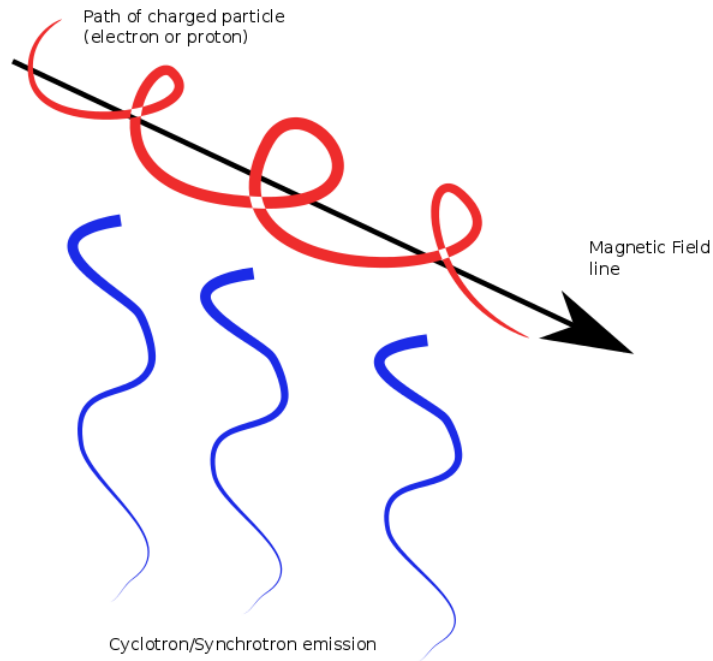


FIGURE 3.9: Highly relativistic charged particles gyrating around magnetic field lines gives rise to Synchrotron emission.

Synchrotron Emission is relativistic cyclotron emission, originating from charged particles (likely electrons) gyrating at high speeds around magnetic field lines. The mathematical description of highly accelerated electrons was first published by [Schwinger \(1949\)](#) and was soon suggested as a way of explaining the radio emission of jets (or “radio stars” as they were known) ([Alfvén & Herlofson 1950](#)). In the relativistic case, the acceleration vector is constantly changing, making the emission highly directional and beamed. This is why at radio wavelengths, blazars are often much brighter than quasars or radio galaxies. An additional side-effect is that synchrotron emission is also highly polarised, with polarisation perpendicular to the magnetic field lines. Probably the most comprehensive overview of the topic is given by [Begelman et al. \(1984\)](#) and also in [Rybicki & Lightman \(1979\)](#). The intensity of synchrotron radiation at any given angle, θ is given by:

$$I(\theta) = \frac{e^2}{16\pi^2 c^2 \epsilon_0} a^2 \sin^2 \theta, \quad (3.18)$$

where e is the charge of an electron, ϵ_0 is the emissivity of free space and a is the acceleration vector in ms^{-1} . We know from electromagnetism that the radius

electrons will have while travelling in a magnetic field with:

$$r = \frac{m_e v}{eB}, \quad (3.19)$$

where m_e is the mass of the electron in kg , v is the velocity in ms^{-1} and B is the magnetic field strength in G . But in the relativistic case, this changes to:

$$r = \frac{m_e v}{eB \sqrt{1 - (v/c)^2}}, \quad (3.20)$$

where $1/\sqrt{1 - (v/c)^2}$ is the *Lorentz factor* (Γ). As the velocity becomes closer to the speed of light, the larger the Lorentz factor and the more significant are the relativistic effects. When you take the average over many electrons travelling at near the speed of light, a power-law relation is yielded. Unless energy is re-injected into the system, the gyrating electrons will lose energy. Also, stronger magnetic fields cause electrons to radiate at higher frequencies and hence lose energy faster. The *turnover frequency* is the point where synchrotron emission is maximised and can be found with:

$$\nu_t = 2.8 \times 10^6 B \Gamma^2, \quad (3.21)$$

with the *spectral index*, α , which describes the slope of the SED given by:

$$P(\nu) \propto \nu^\alpha, \alpha = \frac{p-1}{2}, \quad (3.22)$$

where p is the power law index of the energy distribution of emitting electrons. Typical values for α are ≈ 2.5 in the below the turnover frequency (synchrotron self-absorbed) and ≈ -0.7 above it.

3.5.2 Synchrotron Self-absorption

Any process that can emit radiation can also absorb it. When this happens with synchrotron radiation, it is known as *Synchrotron Self-Absorption*. At low frequencies, one might think that flux densities could increase without limit, so long as energy is being injected. However, once the energies are high enough, the high-energy gyrating electrons get absorbed by low energy photons. This is particularly common in AGN, as they are very compact with high synchrotron electron densities - causing these regions at lower frequencies to become *optically thick*. When the electron densities become sufficiently low, or energy is

being dissipated fast enough, it is said the source is *optically thin* - the region above the turnover frequency and a unique observational aspect of mm-VLBI.

3.5.3 Compton Scattering

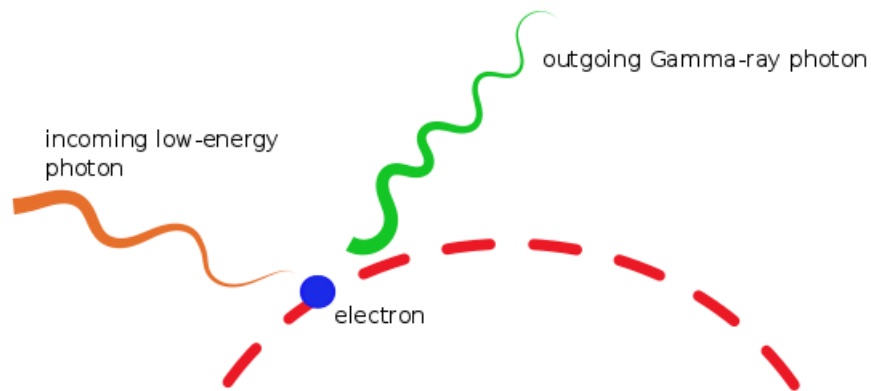


FIGURE 3.10: Inverse Compton Scattering is the process where incoming low-energy photons interact with high energy electrons, leading to high energy photon production - including Gamma-rays.

Compton scattering, first discovered by its namesake [Compton \(1923\)](#), or more specifically for our causes, *inverse Compton scattering* is the process where incoming low-energy photons interact with high energy electrons to produce outgoing high energy photons. This is the preferred model for explaining the production of γ -rays in AGN. The important question is the source of the seed low-energy photons. Are the seed photons from synchrotron photons already within the plasma (synchrotron self-Compton or SSC), ([Marscher & Gear 1985](#)) or do the photons originate externally (external Compton or EC, [Dermer & Schlickeiser 1993](#)). There are many sources for these external photons, including from the accretion disk, the broad-line-region (BLR) or even from the jet itself.

In order to discriminate between these models, there are several observational clues. The first is that γ -ray luminosities must be comparable to that of synchrotron luminosities in the SSC scenario. For sources emitting at TeV energies, this would require synchrotron energies extending to the X-ray band ([Sikora et al. 1994](#)). If a spectral break would be observed, this would suggest external seed photons. Additionally, if γ -rays are produced in close proximity to external X-ray photons from the BLR or accretion disk, the γ -rays should be absorbed by the

X-rays and hence X-ray luminosities should be comparable to the γ -ray luminosities (Ghisellini & Madau 1996).

See section 3.9 for an overview of the history of γ -ray observations and observational support for the competing models.

3.5.3.1 X-rays or Gamma-rays

In astronomical jargon, there is no well defined limit between X-rays and γ -rays, but typically, X-rays are considered to be produced by atomic or thermal processes (e.g. from the BLR or accretion disk) and γ -rays at similar energies by non-thermal processes (e.g. synchrotron emission). At energies above 1 Mega electron Volt (MeV), all particles are considered γ -rays (Thompson 2008). Although X-rays are not discussed in this thesis, they are also an important frequency band for the study of AGN. A good review of the current state of X-ray studies is given by Boeck (2012).

3.6 Black Holes

The idea of a black hole has its origins in Einstein's General Theory of Relativity (Einstein 1916). Objects with mass curve and bend "spacetime", the 4-dimensional construct that houses our entire universe. Schwarzschild (1916) first described how spacetime behaves around a point mass and from this, derived the gravitational radius (R_g):

$$R_g = \frac{Gm}{c^2}, \quad (3.23)$$

where G is the gravitational constant ($G = 6.67 \times 10^{-11} \text{m}^3 \text{kg}^{-1} \text{s}^{-2}$) and m is the mass of the central object in kg. For any mass, a radius exists where no light can escape, this is the famous *Schwarzschild Radius* R_s or *Event Horizon*:

$$R_g = \frac{2Gm}{c^2} \quad (3.24)$$

As an example, the Earth would need have a radius of slightly less than a cm - about the size of a pea - in order to become a black hole. For this reason, objects need to have very large masses in order to collapse under their own gravitational force. In addition to this, Kerr (1963) showed that rotating matter

and by extension, a rotating black hole, effects spacetime. defining the *Kerr parameter*:

$$a = \frac{cJ}{Gm^2} \quad (3.25)$$

Where J is the angular moment. This value, a , varying from -1 (maximally counter-rotating), 0 (non-rotating) to 1 (maximally rotating) is one of the fundamental observational parameters of black holes. The detection of BH spin has attracted considerable levels of research and is considered to be an important parameter is the formation of jets and even general galactic properties. The spin of a black-hole is related to the *Innermost Stable Circular Orbit* or ISCO. While a BH is itself not directly visible, the ISCO is, with a ring-like structure expected to be observable due to emission from the counter-jet (Dexter et al. 2012). The size of this ring should vary between $1 R_g$ (maximally rotating), $6 R_g$ (non-rotating) and $9 R_g$ (counter-rotating) (Bardeen et al. 1972). Measurements of size of the jet base in M87 yielded a size of $R = 5.2 R_g$ corresponding to $a > 0.2$ (Doeleman et al. 2008,0; Dolence et al. 2012). Recent studies suggest that black hole spins may be very important in the formation of jets and in explaining the observed blazar population distributions (e.g. Gardner & Done 2014).

3.7 How and Why Are Jets Formed?

Jet's are surprisingly common in the universe and are found where there is matter falling onto a compact central object. Not only are jets formed around the SMBH in large galaxies, but in pulsars (Lyubarsky & Eichler 2001), collapsing stars possibly causing Gamma-ray bursts (MacFadyen & Woosley 1999) or even in star formation (Hartigan et al. 1995). The question then arises, how are these jets formed? Is the physics the same in stars, pulsars and AGN? If not, are the jets powered by converting rotational BH energy into jet power? Are magnetic fields important?

What occurs at the base of the jet directly influences the effects we see downstream, particularly visible in blazars. It is important to note that the jets are very likely 'formed' off the accretion disk, as in Fig. 3.11 from Donea & Biermann (2002). The inflowing thin accretion disk is entrained as a hot corona that is then sent along the outer jet or 'sheath'. Material that penetrates the base of the jet (at R_{jet}) would by send through the central part of the jet or 'spine'.

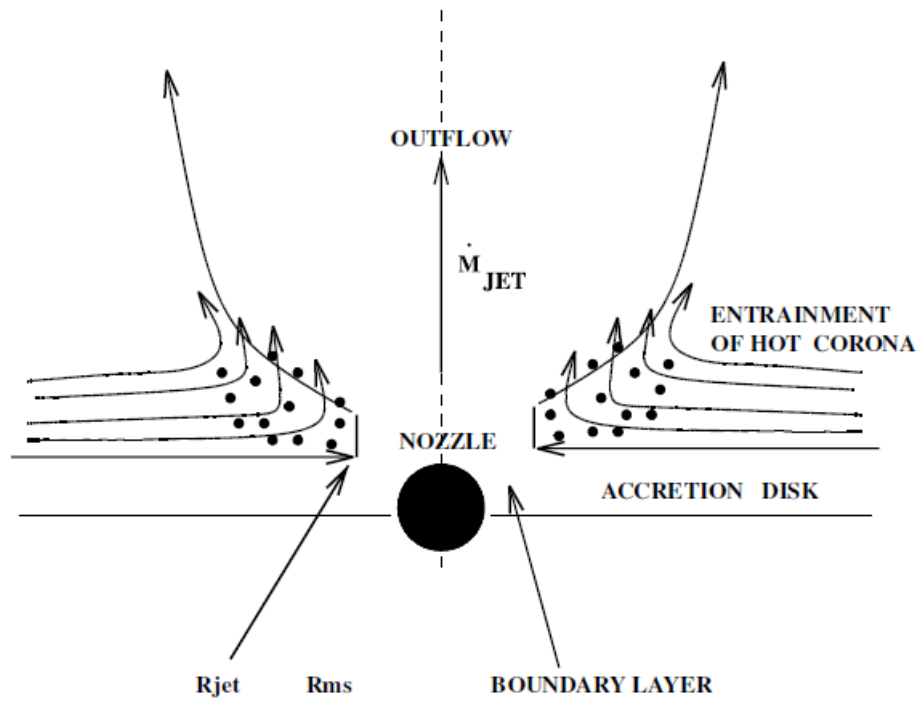


FIGURE 3.11: A sketch from [Donea & Biermann \(2002\)](#) describing the supposed accretion flow at the base of AGN jets. The corona is entrained in such a way as to create an envelope of hot gas. The footpoint of the jet, R_{jet} is outside of the edge of the accretion disk and the further in Innermost Stable Circular Orbit, R_{ms} (ISCO).

Simply put, angular momentum must be lost in order for material to accrete onto the central SMBH. Outflows are the most obvious way to help remove angular momentum from the accretion disk. [Sikora et al. \(2005\)](#) showed that jets must be powered by extracting energy as Poynting flux² from the accretion disk. That we see bipolar jets in almost any source that exhibits jets at all strongly suggests that there is a common axis of rotation, with simulations supporting this view ([McKinney et al. 2012](#)). The exact method of this conversion is not known, but there are two main contenders for the formation of jets, *Disk-launched (BP)* and *BH-launched (BZ)* or possibly a combination of both ([Xie et al. 2012](#)).

Magnetic fields are very important in both the BP and BZ models, and would be anchored at different points in the accretion disk as BHs cannot intrinsically produce a magnetic field themselves. As the disk rotates, the magnetic field lines would become twisted and break, leading to open field lines. These open field

²The Poynting Flux is the energy flux of a propagating electromagnetic wave. For more information, see [Wolfram](#)

lines could then accelerate material off the disk. But perhaps the biggest circumstantial evidence for magnetic fields being involved is that magnetic fields are necessary to collimate the jets.

Under the BZ or Blandford-Znajak model, jet power is extracted from BH spin, specifically by having the BH magnetosphere³ anchored to the accretion flow, allowing the conversion of BH rotational energy into jet Poynting flux. Amongst the first evidence found suggesting the BZ model was found by [Wilms et al. \(2001\)](#), where the modelling of emission lines in the Seyfert I galaxy MCG-6-30-15 was found to *'be best explained by the extraction and dissipation of rotational energy from a spinning black hole by magnetic fields connecting the black hole or plunging region to the disk'*. They also suggested that the field strength was of order $10^4 G$ at the base of the jet. This was subsequently modelled and simulated numerically by [Koide et al. \(2002\)](#), which showed the process is stable and plausible although failed to explain how the plasma could be propagated relativistically.

Simulations, observations and theoretical development continued apace. The apparent detection of helical magnetic fields in 3C 273 by [Asada et al. \(2002\)](#) using Faraday Rotation and polarisation observations, suggested that this was due to the winding up of the initial magnetic field at the accretion disk. Simulations by [Hujeirat et al. \(2003\)](#) refined the configuration of the jet and disk, taking into account effects such as frame dragging and [Koide \(2004\)](#) continued their earlier work by showing that magnetic flux tubes are twisted into the shape of screws to propel plasma around the black hole relativistically.

Numerical simulations by [McKinney & Gammie \(2004\)](#) compared their results with analytical models (such as the BZ model) and found that the numerical models agree best with the BZ model. Soon after, [McKinney \(2005\)](#) included more realistic accretion disks in their models as previously they had been assumed to be infinitely thin, whilst still concluding that only the BZ mechanism could produce the relativistic jets seen in AGN.

However, while the BZ process seems likely to power or at least dominate jet production in high-mass AGN, in lower mass systems, such as black-hole X-Ray binaries it may be that the BP process dominates. In particular, a recent study by [Díaz](#)

³A magnetosphere is simply a magnetic sphere around a central object. For example, the Earth's magnetic field is a magnetosphere.

Trigo et al. (2013) showed significant *hadronic* matter in the candidate X-Ray binary 4U 1630-47. This is important as the plasma itself can be *leptonic* (consisting of electrons and positrons), or *hadronic* (consisting of protons). It seems that disk powered (BP) jets will consist of more hadronic matter than BH powered (BZ) jets, because in BP jets the accretion disk is more directly launched into the jet. In AGN, it is thought the jets consist of electrons and positrons, with for example, circular polarisation detected in blazars suggesting radiating particles extending to very low energies which can only be produced by Faraday conversion, requiring leptonic matter (Wardle et al. 1998; Homan & Lister 2006). The exact relationship between the two is an area of active research, but current evidence seems to suggest that BZ processes dominate at higher masses and BP processes dominate at lower masses.

3.8 Shocks in Jets and Jet Propagation

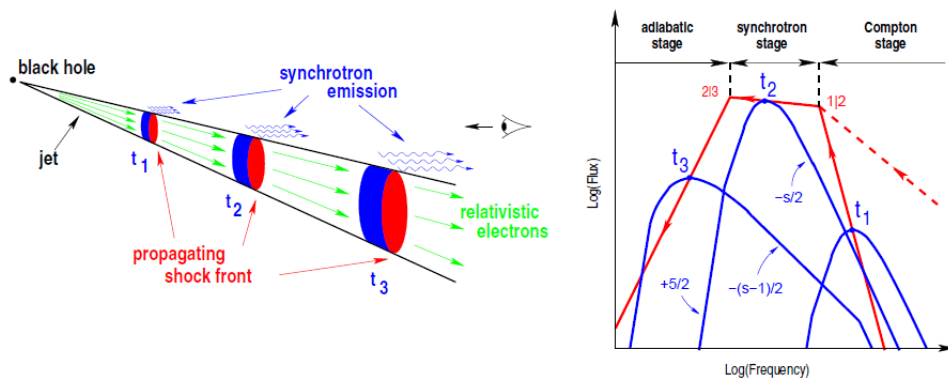


FIGURE 3.12: The shock-in-jet model from Türler (2011) where a propagating shock front causes spectral changes and flaring within an AGN jet.

Once the jet plasma has been launched it then propagates into the external medium and McKinney (2006) included propagation into the external medium in simulations of jet formation. Relativistic shocks travelling down jets have long been proposed as the explanation for the superluminal ‘blobs’ seen in most quasars and blazars (Blandford & Rees 1978; Marscher & Travis 1996). The most favoured model is the “shock-in-jet” model (Blandford & Rees 1978; Marscher & Gear 1985; Türler 2011). The original shock-in-jet of Marscher & Gear (1985) model was used to describe the spectral behaviour of 3C 273, where the turnover

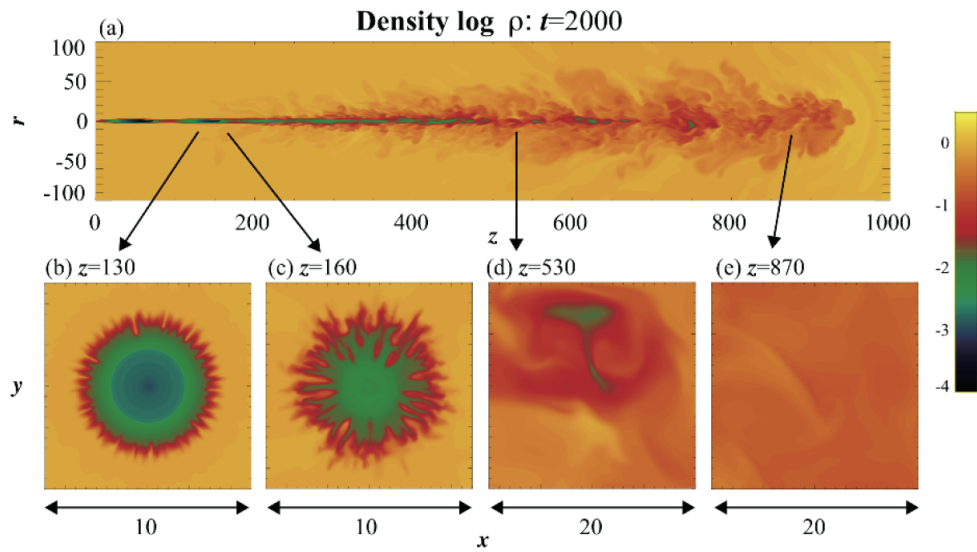


FIGURE 3.13: 2d snapshot of a 3D simulation of a relativistic jet propagating through an external medium from [Matsumoto & Masada \(2013a\)](#). The region below 200 on the z axis is of most interest to us, with two recollimation shocks forming (the tighter regions of the collimated jet).

frequency for synchrotron self absorption shifted from higher to lower frequencies. The model described an adiabatically expanding, Compton and Synchrotron cooled propagating perturbation of plasma crossing a shock-front, as seen in Fig. 3.12. As the shocks evolve, they proceed through an adiabatic, synchrotron and then Compton stage. Where the peak frequency occurs tells us what stage of evolution the shock is in.

The jet, however, is not fastest at the base, but in fact accelerates (and collimates) with increasing separation from the base of the jet by converting relativistic particle energies into bulk kinetic energies with magnetic fields expected to be highly involved, especially in collimating ([Bogovalov & Tsinganos 2005](#); [Schinzel 2011](#)). The propagation has also been simulated numerically, with the creation of many kinds of shocks predicted. In general, there are three kinds of shocks; internal, external and termination shocks. The external shocks are the are bow/forward shocks which accelerate ambient gas and termination shocks are terminal Mach/reverse shocks where the jet itself ends ([Smart et al. 1984](#); [Mizuta et al. 2004](#)).

Closer to the central engine, there are the previously mentioned propagating perturbations which are thought to be caused by changes in the flow at the

jet base and then stationary or slowly moving recollimation shocks. The “hot-spots” along the jets are thought to be recollimation shocks, caused by the overpressure of the jets relative to the external medium. The first simulations were performed by [Norman et al. \(1982\)](#), which showed that:

...such (supersonic jet) beams propagate efficiently at Mach numbers greater than about six, and that the beam is decelerated at the working surface by a Mach-disk shock front which is in general much stronger than the bow shock running ahead of the jet. Waves and instabilities on the jet boundary generally perturb the beam, which is itself stable, and it is noted that perturbations set up oblique internal shock waves in the beam with a regular spacing of 1-2 jet diameters, independent of beam Mach number.

Early work on the re-confinement or *recollimation* of jets was performed by [Sanders \(1983\)](#) although magnetic fields were not considered. They showed that a rapidly expanding jet will eventually come into equilibrium with the external medium and that when this happens, the re-confinement is accompanied by conical shocks that heat the jet, causing it to re-expand as a free jet and that this can happen multiple times. The theoretical background was codified further by [Daly & Marscher \(1988\)](#), which explained how the formation of shocks depended critically on the decrease in external pressure and the initial Lorentz factor of the jet flow. They also provided an excellent diagram of how these shocks are formed which can be seen in Fig. 3.14.

Many theoretical, observational and simulation advances have been made since then, culminating in recent simulations by [Perucho \(2013\)](#), [Fromm et al. \(2012\)](#), [Matsumoto & Masada \(2013b\)](#) and others perhaps crucially including magnetic fields. [Fromm et al. \(2012\)](#) showed that the interactions between travelling shocks and standing recollimation shocks could produce the kind of phenomena that is observed in blazars with VLBI. [Perucho \(2013\)](#) showed how under certain pressure conditions helical patterns within jets can be formed through various kinds of internal instabilities while [Matsumoto & Masada \(2013b\)](#) investigated the nature of instabilities within jets, apparently excluding Kelvin-Helmholtz instabilities as a destabilising mechanism.

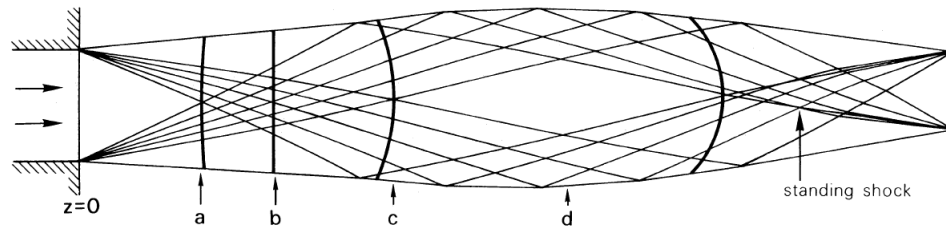


FIGURE 3.14: An illustration of a flow pattern creating a recollimation (standing) shock from [Daly & Marscher \(1988\)](#) where the external pressure is less than half the initial jet pressure (at $z = 0$). The shock is formed due to the crossing of characteristics in downstream regions.

3.9 Historical γ -ray Observations.

3.9.1 Early Gamma-ray Observatories

The first early γ -ray satellites were the NASA Small Astronomy Satellite SAS-2 ([Knif-fen et al. 1973](#)), launched in 1972 and the European Space Agency's Cos-B satellite, launched in 1975 ([Bignami et al. 1975a](#)). Both were built with spark chamber detectors, making SAS-2 sensitive to γ -rays between 20 MeV and 1 GeV , and Cos-B sensitive between 30 MeV and 10 GeV . While both were primarily used for detection of galactic emission ([Stecker et al. 1974](#); [Bignami et al. 1975b](#); [Stecker 1977](#)), they also detected emission from pulsars ([Kanbach et al. 1977](#); [Thompson et al. 1975](#)) and AGN ([Swanenburg et al. 1978](#); [Moffat et al. 1983](#); [Lau & Young 1985](#); [Young & Yu 1988](#)).

3.9.2 The EGRET era

The Energetic Gamma Ray Experiment Telescope (EGRET) on board the Compton Gamma Ray Observatory (CGRO) was the first γ -ray observatory that could be used properly for the study of extra-galactic γ -ray sources. It was launched in 1991 as part of NASA's "Great Observatories" program and de-orbited in 2000 after one of its gyroscopes failed ([Kanbach et al. 1988](#); [Ahmed et al. 2001](#)). EGRET was capable of detecting γ -rays between the energies 20 MeV and 30 GeV , had a peak effective area of 1500 cm^2 at 500 MeV , an energy resolution of 15% of the Full-width-half-maximum (FWHM) and timing accuracy of better than 100μ as ([Thompson 2008](#)). It used a spark chamber to measure the direction of the incoming γ -ray, like previous designs, and a calorimeter to determine its energy. The design is similar to that of the later Fermi/LAT instrument, of which

more details can be found in Section 3.9.3. A thorough review of science performed with EGRET can be found in [Thompson \(2008\)](#). Over the course of its operational life, it detected 67 blazars, of which the majority were flat spectrum radio quasars (FSRQs), with the remainder being BL Lacs ([Mukherjee 2001](#)).

The first detection of γ -ray emission in an AGN from EGRET was reported by [Hartman et al. \(1992\)](#) of 3C 279, which was a surprise as it was expected to be 3C 273. They found that the γ -ray flux density was much higher than at earlier times, making it the most luminous γ -ray source yet detected. Soon after, the first γ -rays from a BL Lac were reported ([Lin et al. 1992](#)). A review of early results is presented by [Fichtel et al. \(1993\)](#), which also reported the detection of γ -rays from pulsars, bursts and galactic diffuse emission. Gamma-rays were subsequently detected in the OVV quasar 3C454.3 ([Hartman et al. 1993](#)), the BL Lac 0235+164 ([Hunter et al. 1993b](#)), the quasars 0528+134 and 1633+382 ([Hunter et al. 1993a](#); [Mattox et al. 1993](#)), which found variability on the time-scale of a few days and evidence for the Doppler boosting of emission.

By 1994, continued observations of AGN with EGRET had revealed that blazars exhibited highly variable γ -ray flux densities, and a lack of evidence of γ -ray absorption due to pair-production ([Thompson et al. 1993](#); [Sikora et al. 1994](#)). [Sikora et al. \(1994\)](#) interpreted these findings as the γ -ray emission originating from the inner parts of relativistic jets that are near to our line-of-sight. They favoured a model of γ -ray production invoking a single population of relativistic electrons accelerated by a disturbance (Synchrotron Self-Compton or SSC), rather than being due to some ambient radiation field (External Compton or EC). However, they noted that the detection of TeV γ -rays in the source Mkn 421 ([Punch et al. 1992](#)) may require an ambient photon field. They proposed that the detection of a well-defined spectral break between the X-ray and γ -ray bands would imply this scenario, as the synchrotron luminosity must lower than the γ -ray luminosity. The TeV emission could be explained if the synchrotron component extended into the X-rays, but relevant X-ray observations were not available at the time.

Multi-wavelength observations of the quasar 3C 273 appeared to support the view that γ -rays are produced through SSC mechanisms rather than EC ([Maraschi et al. 1994](#)) and soon later by [George et al. \(1994\)](#) in PKS 1502+106. [Lichti et al. \(1995\)](#) showed tentative evidence for two or more populations of relativistic

electrons in 3C 273. Also, due to the prominent emission seen in the optical and UV, suggested that the X-rays and γ -rays are produced in optically thin regions, by the inverse Compton scattering of ambient synchrotron photons and/or photons from the disk corona.

[Macomb et al. \(1995\)](#) returned to the TeV emitting source Mkn 421, which was found to be flaring in May 1994. Simultaneous observations were performed across the entire spectrum. They concluded that the flare was most likely caused by the sudden excitation of a single population of electrons, consistent with SSC emission, although they could not rule out the EC scenario. [Grandi et al. \(1996\)](#) showed that it was unlikely that the X-ray emission in 3C 279 was due to external seed photons as they could exclude the seed photons being in the optical.

A review of the state of research in 1996 was published by [Ghisellini & Madau \(1996\)](#). They concluded that the inverse Compton process and relativistic beaming almost certainly produces the γ -ray emission. They found it unlikely that external seed photons from the accretion disk or the broad-line region (BLR) would be important as the γ -rays would likely be absorbed by the X-rays and lead to comparable γ -ray and X-ray luminosities, which is not observed. They hence reversed the argument to estimate that the γ -ray emitting region must be at least $\sim 3 \times 10^{16} \text{ cm}$ (but still only $\sim 0.01 \text{ pc}$) away from the central engine in order for the X-ray luminosities *not* to be comparable to that of the γ -rays.

By this stage, evidence seemed to be pointing strongly towards SSC production of γ -rays at some distance from the central engine. However, [Mukherjee et al. \(1999\)](#) modelled the spectral energy distribution (SED) of the blazar PKS 0528+134 and found that multi-component models including both SSC and EC models were required to adequately explain the shape of the SED. Indeed, the same source had previously been shown to correlations between radio flux densities, γ -ray flux densities and jet component ejections ([Krichbaum et al. 1998](#)). It also appeared that during flare states, the high energy emission was dominated by EC processes while the γ -ray emission was dominated by SSC processes at low states.

After this breakthrough, many sources were modelled to include both EC and SSC components, including BL Lacertae ([Böttcher & Bloom 2000](#)) and 3C 279 ([Hartman et al. 2001](#)). Not all sources fit into this picture though, with MrK 501

being well modelled with only SSC contributions (Petry et al. 2000). Ghisellini et al. (1998) applied both combined SED/EC models and pure SSC models to 51 sources with similar SEDs from the EGRET catalog and found that most blazar SEDs can be adequately modelled by both. This led to the so-called blazar sequence of high frequency peaked BL Lac objects (HBLs) → low frequency peaked BL Lac object (LBLs) → high frequency peaked flat-spectrum radio quasars (HPQs) → low frequency peaked flat-spectrum radio quasars (LPQs). They suggested that the changes between the classes may be due to the EC processes increasingly dominating over SSC processes. That is to say, the role of broad emission-line radiation is more important in the production of γ -rays in LPQs than in HBLs. Later studies also tended to confirm that view (e.g. Zhang et al. 2005; Gao et al. 2011).

By this time, regular monitoring of blazars using VLBI was producing high cadence data-sets with extremely high angular resolution. Jorstad et al. (2001), using high cadence monitoring of blazars using 7 mm VLBI, showed that γ -ray flares were occurring at similar times to component ejections. This suggested that the site of γ -ray emission could be occurring parsecs downstream from the central engine. This raised the question of how EC processes could be involved in γ -ray production so far from the BLR and accretion disks. Also contributing to this problem is the fact that most sources detected at TeV energies are HBLs. This requires extremely high Lorentz factors, which does not agree with observations (e.g. Marscher 1999; Krawczynski et al. 2002). A possible solution to this dilemma was proposed by Georganopoulos & Kazanas (2003), where they proposed that TeV emission is produced in a decelerating flow far downstream from the central engine.

Unfortunately, the telescope had to be de-orbited in 2000 and it was not until the launch of the new Fermi/LAT telescope in 2008 that observations could continue.

3.9.3 The Fermi/LAT era

In 2008, almost eight years after EGRET was de-orbited, a new γ -ray telescope, called the *Fermi Gamma-ray Space Telescope* was launched. The telescope was launched by the National Aeronautical and Space Administration (NASA) in June 2008 into a low Earth orbit. On board the satellite are two detectors:

1. GLAST Burst Monitor (GBM) and;
2. Large Area Telescope (LAT)

The GBM is an instrument designed to detect sudden γ -ray flares (Meegan et al. 2007). The LAT (Fig. 3.15), however, is the instrument most relevant for our purposes and is described in detail by Atwood et al. (2009). The LAT detects γ -ray photons by pair-converting a γ -ray photon into an electron-positron pair through a high-Z foil. The resulting shower is detected with high precision calorimeters. A calorimeter is a device for measuring the heat of chemical reactions. These calorimeters detect the relative arrival times of electron-positron pairs with great accuracy, allowing the LAT to achieve a very good resolution of between 0.15° and 3.5° , depending on the energy band. The LAT can observe between 100 MeV and over 10 GeV. The LAT can view the entire sky within two orbits, or about 6 hours. A good video describing the operation of the LAT can be found [here](#).

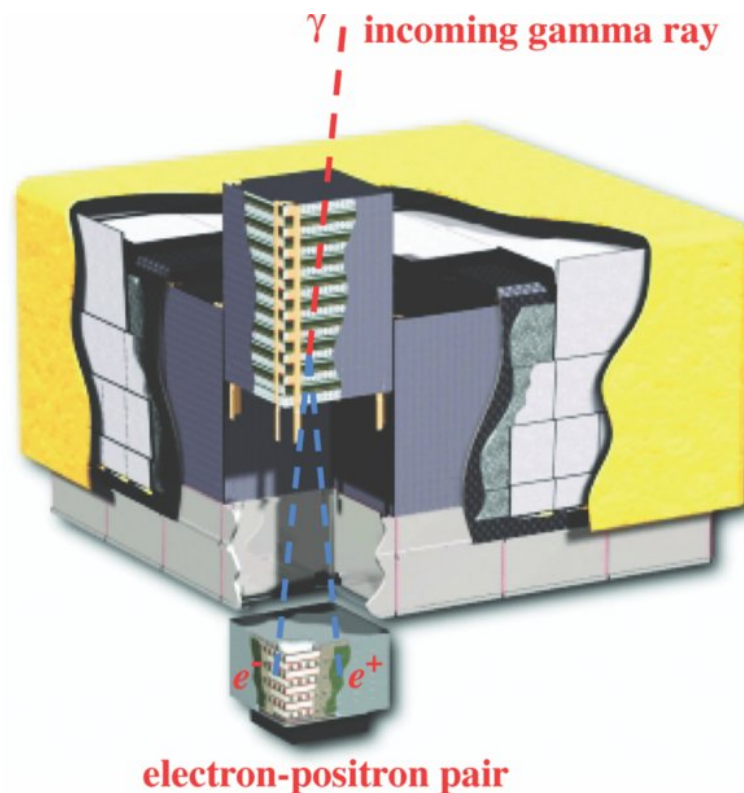


FIGURE 3.15: Schematic of the Large Area Telescope aboard the Fermi Gamma-ray Space Telescope.

With the launch of Fermi/LAT, Abdo et al. (2010) suggested a revision to the blazar sequence first proposed by Ghisellini et al. (1998). Under this scheme, the sequence becomes FSRQs \rightarrow LBLs \rightarrow Intermediate peaked BL Lac IBLs \rightarrow HBLs,

with decreasing importance of external radiation fields. Indeed, some argue that all γ -ray emission is dominated by the EC process in FSRQs (Cao & Bai 2008; Liu et al. 2008). Gao et al. (2011) used the Fermi/LAT sample to determine that the ratio between the external radiation and the internal magnetic field energy depends on the Lorentz factor.

Abdo et al. (2011) showed that in the BL Lac 3C 66A could have its SED fully explained through SSC processes and did not require an external radiation field. However, they did need to include EC processes to explain the optical variability, once again suggesting that in all sources, both processes are at work. Indeed, in the famous BL Lac OJ287 which is studied in detail in Chapter 5, Kushwaha et al. (2013) found that both SSC and EC processes were required to model the SED. They also placed the emission region many parsecs downstream, consistent with VLBI results (Agudo et al. 2011).

Another significant area of investigation with the γ -ray telescopes is the composition of jets. Are they leptonic (electrons and positrons) or hadronic (protons)? While not deeply reviewed here, most results from SED modelling suggest that jets are leptonic matter. However, there are outliers, including the QSO AO 0235+164 which do not fit into the leptonic matter models. This suggests that although most jets may be leptonic, it increasingly seems that it may not exclusively be the case (e.g. Böttcher et al. 2013, and references therein).

The current state of research seems to suggest that γ -rays are produced through both the SSC and EC process, but the exact location of the site of γ -ray production remains elusive. VLBI results suggest that γ -ray production is *mostly* produced parsecs downstream, but there is much evidence to suggest that γ -rays produced near the central engine and/or the BLR are also possible. Both scenarios likely occur. How these findings fit into the different observed classes of blazars and the importance of magnetic fields are an active area of research.

Chapter 4

A Global 3 mm VLBI survey of Fermi/LAT detected γ -ray blazars.

The primary focus of this thesis is to provide an analysis of an ongoing 4 year long campaign to monitor γ -ray bright blazars using the *Global mm-VLBI Array* (GMVA). Unlike previous surveys at 3 mm, which were *detection* surveys, this is a systematic survey, aiming to monitor sources and determine their properties over time. In total, 26 sources were observed over the 4 years that we are analysing here. In this chapter, we concentrate on five sources that were regularly observed over the 4 years of observations. Although many other sources have been observed, we selected these sources for further analysis as they were regularly observed and exhibited interesting behaviour such as flaring during this period. An overview of these sources and their basic properties is given in Table. [4.2](#). Additionally, the source OJ287 is examined in greater detail in Chapter 5.

4.1 Motivations and Context

The goal of VLBI monitoring programs can be summarised thus: (i) how relativistic flows from black holes are produced; (ii) how these flows are collimated and accelerated; (iii) what is the relationship between the kinematics and component trajectories and flaring activity at other wavebands (e.g. γ -rays and X-rays); (iv) the nature of stationary and propagating shocks within jets and (v) the role that magnetic fields play in all of these areas of investigation. This thesis is the first analysis of an ongoing 3 mm/86 GHz VLBI monitoring program of γ -ray bright blazars.

Prior to this survey and still ongoing, was a program of monthly monitoring γ -ray bright blazars using the Very Long Baseline Array (VLBA), known as the BU-VLBA Blazar Monitoring Program. Most sources observed as part of this program exhibit ejections from the VLBI “core” every few months, corresponding to large mm-wave radio and γ -ray flares. Additionally, sources exhibit large degrees of superluminal motion, jet “wobbling” and sub-parsec scale quasi-stationary features. An overview of previous results is given in Section [4.1.1.1](#).

Complimentary to the BU-VLBA Blazar Monitoring Program is the Monitoring Of Jets in Active galactic nuclei with VLBA Experiments (MOJAVE) 15 GHz/2 cm monitoring program. The MOJAVE program has observed over 100 quasars and blazars at parsec scale resolution since 1994, producing a statistically complete sample of the kinematic and polarisation properties and evolution of AGN.

One of the primary drivers in beginning this monitoring program is determining the site of γ -ray production within AGN jets. If we can know where in the jets γ -rays are produced, we can begin to understand the mechanism of their production (see Chapter 3). 3 mm global VLBI with the Global mm-VLBI Array can help achieve these goals by providing direct imaging at sub-parsec scales of regions thought to be very close to the γ -ray production regions. Additionally, emission due to synchrotron self-absorption begins to become optically thin in the mm-wavebands, allowing us to not only probe at the highest resolutions but also in a regime that is not obscured by optically thick emission.

In this chapter, we will present 3 and 7 mm maps of 5 γ -ray blazars, comparing and contrasting their differences and similarities. We will perform spectral

decompositions in tandem with single-dish light curves from the FGAMMA and SMA monitoring programs, in order to determine limits on how the strength of the magnetic field changes down the jet (Section 4.3.6.1 and Section 4.3.6.2). By determining this, we can estimate distance between the mm-wave “core” and the central super-massive black-hole (SMBH) (Section 4.3.7) and estimate the magnetic field strength both there and within the broad-line region (BLR).

In Chapter 5, we analyse the blazar OJ287 in greater detail, adding full kinematics from 7 mm BU-VLBA monitoring, spectral information from 15 GHz MOJAVE monitoring, single-dish light curves of the FGAMMA program and γ -ray light curves from Fermi/LAT. This allows us to locate the site of γ -ray emission, investigate the sub-parsec morphological behaviour and magnetic field configuration in a way that has never been previously performed.

4.1.1 Previous Surveys

Several detection surveys of sources at 3 mm were performed with the GMVA’s precursor; the CMVA or *Coordinated mm-VLBI Array* (Beasley et al. 1997; Lonsdale et al. 1998; Rantakyro et al. 1998; Lobanov et al. 2000). Unfortunately, the sensitivity of the array was lacking with only 44 sources detected and only 24 of these sources imaged out of a total of 124 sources observed (Lee et al. 2008). During the transition from the CMVA to the GMVA a new survey of bright 3 mm sources begun with the aim of increasing the number of sources available for observations with the GMVA. This work, which was the primary focus of Lee (2007), provides much of the context of this thesis. In total, 90 sources were imaged during this campaign for a total of 110 sources including previous surveys. However, of additional relevance for this thesis are the ongoing systematic surveys of quasars and blazars by the 43 GHz BU-VLBA-BLAZAR program.

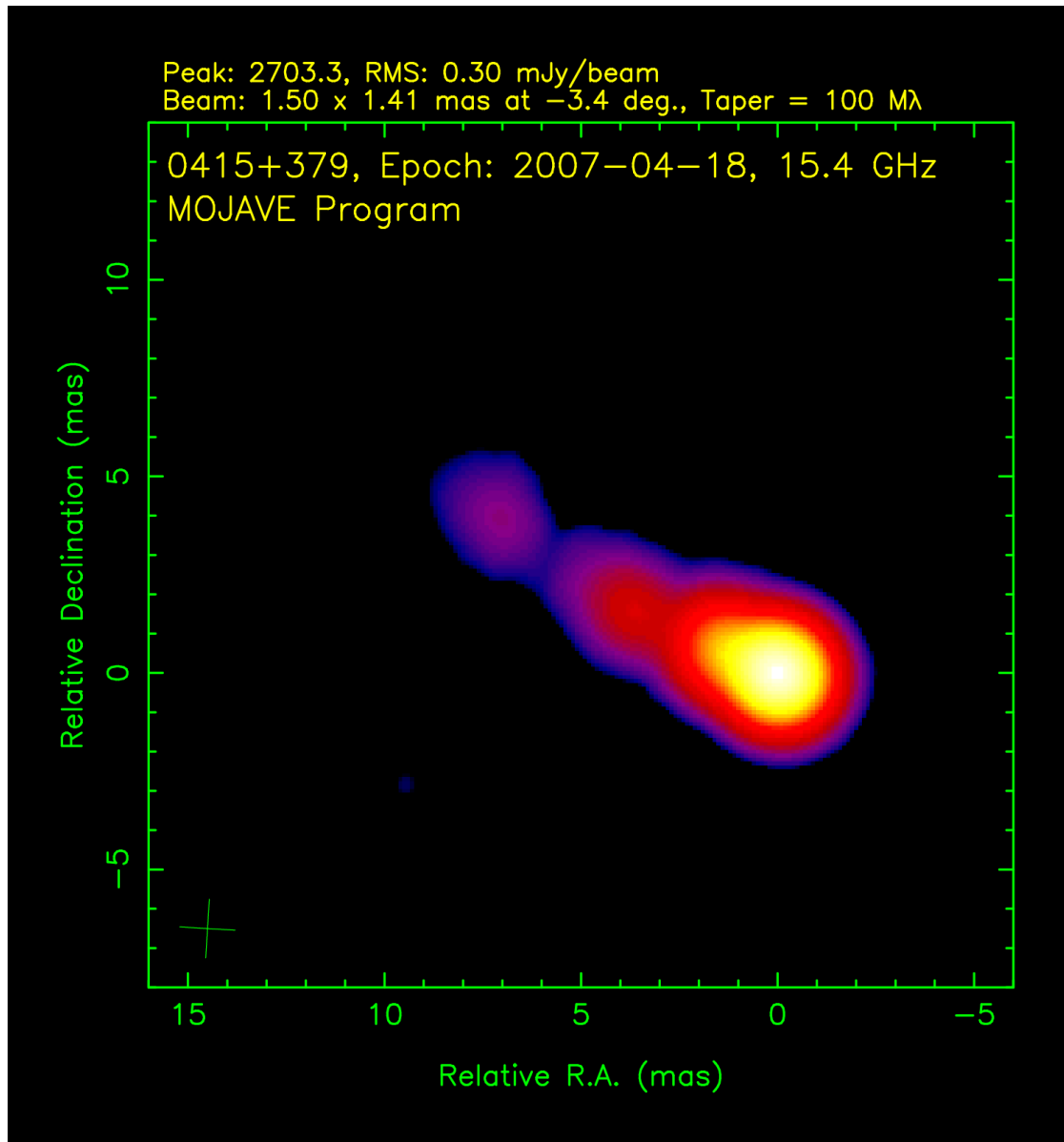


FIGURE 4.1: An example of typical “core”-jet morphology, of 3C 111. The bright component to the south-west is the “core” and the jet is extending away from there (Lister & Homan 2005).

4.1.1.1 BU-VLBA 43 GHz Monitoring

The first incarnation of the BU-VLBA 43 GHz monitoring of γ -ray bright blazars was performed between November 1993 and July 1997 (Jorstad et al. 2001). They found that higher apparent superluminal motions were higher in γ -ray blazars compared with the standard AGN population. Additionally, they found a positive correlation between VLBI “core” flux and γ -ray flux suggesting that more generally that component ejections should correlate with γ -ray flares. Unfortunately, due to the lack of cadence in γ -ray light-curves and VLBI monitoring,

they were not able to conclusively show this. Nevertheless, they found it very likely that both radio and γ -ray flaring events originate from the same site and that this site is not co-spatial with the SMBH.

A follow-up to this work was published by [Jorstad et al. \(2005\)](#), this time including polarisation maps and an emphasis on kinematics. They reported that at 7 mm, structural changes can occur on the scale of weeks to months and even more rapidly in polarisation. They reported that components ejected from the “core” tend to accelerate away from it, although sometimes local decelerations were detected. This was interpreted as being a combination of intrinsic component acceleration and velocity changes due to components moving into and out of our line-of-sight. Component ejections were found to be faster in quasars than in BL Lacs, suggesting a difference in how disturbances are created. Approximately 11% of components detected were interpreted as trailing shocks or features (see Section [4.3.4](#)). In addition to higher component speeds, estimated viewing angles, opening angles and Doppler factors were higher in quasars than BL Lacs, albeit with some overlap. They found a relationship between the opening angles and the Lorentz factor, which lead them to suggest that the external medium has approximately 1/3 the pressure of the internal jet pressure. In some sources, changes in the Electric Vector Position Angle (EVPA) underwent rotations a large distance away from the “core”, which was interpreted as being due to interactions with gas clouds probably due to the external medium. Brightness temperatures were found to be lower through direct measurements than when derived from equipartition (see Section [4.3.6.2](#)), suggesting magnetic dominance of the jets, on average.

In [Jorstad et al. \(2007\)](#), the emphasis was again on polarimetry, with 15 AGN analysed with quasi-simultaneous linear single-dish polarisation measurements at 1 mm, 3 mm and at optical. They found that objects with low variability of polarisation in the “core” were both radio galaxies and quasars with low optical polarisation. Sources with intermediate variability of polarisation included all BL Lac sources and quasars where the EVPA is close to the jet direction and that these sources are all very relativistic. Sources exhibiting high levels of variable polarisation included optically violent variable (OVV) blazars and OJ 287 (which is a BL Lac). They interpreted the polarisation variability as due to weak shock waves propagating down jets with turbulent magnetic fields and that these shocks lie at oblique angles to the jet axis.

Additionally, many single-source papers have been published, and these are referenced accordingly in the introductions to the relevant sources.

4.2 Observations

Table 4.1 displays an overview of all sources that were observed as part of the γ -ray monitoring program from 2008.78 until 2012.38. In total, there are 26 sources that were observed at various times over the course of observations. The sample consists of 19 Flat-Spectrum-Radio-Quasars (FSRQ), 6 BL Lacs and 1 Radio Galaxy. In the next two chapters, we focus on five sources in Table 4.2. In Chapter 5, the BL Lac source OJ 287 is examined in greater detail.

4.2.1 Sample Selection

The sample selection is broadly similar to that described in [Jorstad et al. \(2005\)](#), which is adapted here:

1. The sources should be bright, ≤ 0.5 Jy, and polarised, $\leq 3\%$, at submillimeter wavelengths.
2. The size of the sample and brightness of sources should allow us to perform GMVA observations at a single 24 hr epoch, with sufficient (u, v) coverage to produce total and polarised intensity images at 86 GHz with high dynamic range.
3. The sample should contain sources with resolved radio structure from different subclasses of AGNs for which variability in the jet flow can be expected on timescales of 6 months to a year.
4. The sources should be convenient for monitoring in the Northern Hemisphere, and their coordinates should cover the whole range of right ascensions.

4.2.2 86 GHz GMVA

Data were observed during the period 2008.78-2012.35 using the Global mm-VLBI Array (GMVA) (see Section 1.3.2), with data acquisition and analysis described in Chapter 2 and an overview of the VLBI data path in a modern digital system shown in Fig. 2.26. CLEAN maps were produced using the Caltec DIFMAP package as described in Chapter 2 ([Shepherd et al. 1994](#)). Data were fringe-fitted and calibrated using standard procedures in AIPS for high frequency VLBI

Source	J2000	T	z	E1	E2	E3	E4	E5	E6	E7
0133+476	0136+475	Q	0.859 (3)					x		
0235+164	0238+162	Q	0.940 (1)	x		x			x	
3C 84	0319+413	B	0.017 (3)					x		x
CTA 26	0336-019	Q	0.852 (3)						x	x
NRAO 150	0359+506	Q	1.520 (5)				x	x		x
3C 111	0418+213	R	0.048 (4)		x	x	x	x	x	x
0420-014	0423-012	Q	0.915 (2)	x	x	x	x	x	x	x
0528+134	0530+133	Q	2.070 (2)	x	x	x	x	x	x	x
0716+714	0722+712	B	>0.3 (2)		x	x	x	x	x	x
0827+243	0830+241	Q	0.941 (2)	x	x	x	x	x	x	x
0836+710	0841+705	Q	2.218 (1)			x	x	x	x	x
OJ 287	0854+201	B	0.306 (2)	x	x	x	x	x	x	x
0954+658	0958+653	B	0.899 (3)							x
3C 273	1229+023	Q	0.158 (3)	x	x	x	x	x		x
3C 279	1256-055	Q	0.536 (3)		x		x	x		x
1502+106	1504+103	Q	1.838 (3)		x		x	x	x	
1510-089	1512-090	Q	0.360 (3)	x	x		x	x	x	x
1611+343	1613+341	Q	1.400 (3)	x	x					
1633+38	1635+381	Q	1.813 (3)	x	x		x	x	x	x
3C 345	1642+395	Q	0.593 (3)	x	x	x	x	x	x	x
NRAO 530	1733-130	Q	1.037 (3)	x	x					
1749+096	1751+094	B	0.322 (3)	x		x				
BL Lac	2202+421	B	0.0686 (3)		x	x	x	x	x	x
3C 446	2225-046	Q	1.404 (3)	x	x	x	x	x	x	x
3C 454.3	2255+161	Q	0.859 (3)	x	x	x	x	x	x	x
CTA 102	2232+114	Q	1.037 (3)	x	x	x	x	x	x	x

TABLE 4.1: An overview of sources observed and analysed. Type B: BL Lac, Q: FSRQ, R: Radio Galaxy. (1: [Linfoord et al. 2012](#)), (2: [Healey et al. 2008](#)), (3: [Lister et al. 2011](#)), (4: [Hewitt & Burbidge 1991](#)), (5: [Agudo et al. 2007b](#)). E1: 2008.78; E2: 2009.35; E3: 2009.86; E4: 2010.36; E5: 2011.35; E6: 2011.78; E7: 2012.38.

Source	Coord.	Type	z	D_L (Gpc)	(pc/mas)	Max. β_{app}^1
0716+714	0716+714	B	> 0.3	> 1.5	> 4.5	18.0 ± 4.1
4C +71	0836+710	Q	2.218	17.96	8.408	21.1 ± 0.8^2
OJ 287	0854+202	B	0.3056	1.60	4.551	18.0 ± 4.1
3C 273	1229+023	Q	0.1584	0.762	2.755	12.2 ± 0.6
3C 345	1641+399	Q	0.593	3.520	6.725	23.9 ± 1.1
BL Lac	2202+422	B	0.0686	0.311	1.321	9.0 ± 0.5
3C 454.3	2251+158	Q	0.859	5.55	7.786	24.8 ± 2.5

TABLE 4.2: An overview of sources observed and analysed. Type B: BL Lac, Q: QSO. ¹ Maximum Doppler factor from [Jorstad et al. \(2005\)](#). ² from [Lister et al. \(2013\)](#).

data reduction (e.g. [Jorstad et al. 2005](#)) with extended procedures written in ParselTongue as described by [Marfí-Vidal et al. \(2012\)](#). Within AIPS, amplitudes were corrected for sky opacity, system temperatures, gain-elevation curves and then averaged over all IFs to increase SNR. Calibration was performed on the brightest sources and scans within the experiment. Relative flux accuracy of VLBI measurements as compared with F-GAMMA (section 2.3.2) and VLA/EVLA

fluxes is within 5 percent. Data were correlated at the Max-Planck-Institut für Radioastronomie in Bonn, Germany.

4.2.3 43 GHz

Complimenting GMVA observations are near-in-time observations from the use of 43 GHz VLBA data from the VLBA-BU-BLAZAR Monitoring Program [VLBA-BU](#), funded by NASA through the Fermi Guest Investigator Program. The VLBA is an instrument of the National Radio Astronomy Observatory. The National Radio Astronomy Observatory is a facility of the National Science Foundation operated by Associated Universities, Inc. The data were reduced using similar methods described in this thesis and also described by [Jorstad et al. \(2005\)](#).

4.2.4 Total-Intensity Measurements

4.2.4.1 Radio

We make use of single-dish measurements at (1) 15 GHz/2 cm, (2) 32 GHz/9 mm, (3) 43 GHz/7 mm, (4) 86 GHz/3 mm and (5) 225 GHz/1 mm. The 15-86 GHz radio light curves have been obtained within the framework of a *Fermi*-GST related monitoring program of γ -ray blazars (F-GAMMA program, Fuhrmann et al. 2007, Angelakis et al. 2008, Fuhrmann et al. 2014). The millimetre observations are closely coordinated with the more general flux monitoring conducted by IRAM, and data from both programs are included in this paper. The overall frequency range spans from 2.64 GHz to 142 GHz using the Effelsberg 100-m and IRAM 30-m telescopes. The 225 GHz (1.3 mm) flux density data was obtained at the Submillimeter Array (SMA) near the summit of Mauna Kea (Hawaii). The sources in this thesis were included in an ongoing monitoring program at the SMA to determine the flux densities of compact extragalactic radio sources that can be used as calibrators at mm wavelengths ([Gurwell et al. 2007](#)). Observations of available potential calibrators are from time to time observed for 3 to 5 minutes, and the measured source signal strength calibrated against known standards, typically solar system objects (Titan, Uranus, Neptune, or Callisto). Data from this program are updated regularly and are available at the SMA website.

The Effelsberg measurements were conducted with the secondary focus heterodyne receivers at 2.64, 4.85, 8.35, 10.45, 14.60, 23.05, 32.00 and 43.00 GHz.

The observations were performed quasi-simultaneously with cross-scans, that is slewing over the source position, in azimuth and elevation direction with adaptive number of sub-scans for reaching the desired sensitivity (for details, see Fuhrmann et al. 2008; Angelakis et al. 2008). Consequently, pointing off-set correction, gain correction, atmospheric opacity correction and sensitivity correction have been applied to the data. The IRAM 30-m observations were carried out with calibrated cross-scans using the ‘ABCD’ SIS (until March 2009) and new EMIR horizontal and vertical polarisation receivers operating at 86.2 and 142.3 GHz. The opacity corrected intensities were converted into the standard temperature scale and finally corrected for small remaining pointing offsets and systematic gain-elevation effects. The conversion to the standard flux density scale was done using the instantaneous conversion factors derived from frequently observed primary (Mars, Uranus) and secondary (W3(OH), K3-50A, NGC 7027) calibrators.

4.2.4.2 Gamma-rays

4.2.4.3 LAT Data Reduction

LAT data were analysed using the standard ScienceTools (software version v9.32.5) and instrument response function P7REP_SOURCE. Photons in the source event class were selected for the analysis. A region of interest of 10° in radius was analysed, centred at the position of the γ -ray source, using a maximum-likelihood algorithm (Mattox et al. 1996). In the model for the γ -ray emission from the region, we included all the 23 sources of the 2FGL catalog (Nolan et al. 2012) within 10° with their model parameters fixed to their catalogue values except for sources within the 5° ROI which are kept free.

Source variability is investigated by producing the light curves ($E > 100$ MeV) by likelihood analysis with time bins of 7- and 30-days. The weekly and monthly binned light curves of the source at $E > 100$ MeV were produced by modelling the spectra over each bin by a simple power law ($N(E) = N_0 E^{-P}$, N_0 : normalisation factor, and P : power law index). For this analysis, we used the unbinned maximum-likelihood algorithm¹ (Mattox et al. 1996). The analysis performed here is very similar to that reported in Rani et al. (2013), to which we refer for details.

¹http://fermi.gsfc.nasa.gov/ssc/data/analysis/scitools/likelihood_tutorial.html

In some cases, light-curves analysed in this way were not available, and publicly available light-curves from the FERMI collaboration website were used.

4.3 Analysis

4.3.1 “Core” Identification

A critical part of VLBI analysis is “core” identification, as it is required in order to perform kinematic analysis. The VLBI “core” is assumed to be the most upstream visible component in a VLBI image and is assumed to be stationary. The “core” is typically identified on the basis of i) morphology, ii) small size, higher flux densities and correspondingly higher brightness temperatures than downstream components iii) an optically thick (inverted) or flat spectrum and iv) increased levels of flux density variations. At wavelengths lower than at millimetre, the “core” is often relatively easy to identify, as it is usually the brightest component by far. However, at high frequencies, this can sometimes be difficult, as the sub-parsec scale structure can include quasi-stationary features that are sometimes brighter and more compact than the “core” ([Jorstad et al. 2005](#)). Nevertheless, based on the criteria listed above, it has been always possible to confidently identify the “core” in our VLBI maps. When this is done, we apply the label C1.

4.3.2 Morphology, Spectral Properties and Component Identification

At mm wavelengths, the parsec scale morphology is dominated by stationary features and both fast and slow travelling components ([Jorstad et al. 2005](#)). Components are cross-identified between frequencies under the assumption that their properties such as flux, core-separation, size, the position angle (PA) are not significantly different and the change between frequencies occurs in a systematic way (e.g. steep spectrum in travelling components). For each component, we have two spectral points (at 43 and 86 GHz). While we need at least 3 spectral points to compute a spectrum, we can derive useful information about the source properties by comparing against total intensity measurements. A component is subsequently identified by the observing frequency (e.g. a component identified as $X2$ on a 86 GHz map will be labelled $X2_{86}$ in tables and in the text).

Typically, one assumes that the jet contains a power-law distribution of electrons of $N(E) = N_0 E^{-p}$, where E is the energy and p is the power law index (Kellermann 1966).

4.3.2.1 Quasi-Stationary Features

As discussed in Section 4.3.1, there can be other components that can be brighter or more compact than the “core”. These features tend to be either quasi-stationary or slowly moving. We identify stationary components when a fit to their motion does not allow for a realistic estimated “core” ejection date to be computed (e.g. Fig. 4.10). Stationary features that are not the “core” are labelled C2, C3 and so on, with increasing “core” separation.

4.3.2.2 Travelling Components

Travelling components are generally fainter and larger than stationary components and are labelled X1, X2 and so on. Higher values imply a more recent detection date. The trajectories of travelling components can help distinguish the VLBI “core” from downstream stationary features.

4.3.3 Kinematics

In the sources analysed here, the motion of components can be measured relative to some reference point. This is taken as the component labelled C1. This is the “core”, and all motions are measured relative to this. Of particular interest to us, is the inner-jet (< 1 mas) region. Component speeds are measured in mas/year, but are converted into β_{app} and used to derive properties of the source, as described in Section 3.4.1. Identification of travelling components can be difficult with the present and rather low observational cadence. Travelling components can often be resolved into several components, particularly at 3 mm, making speed determinations difficult. Where possible, an estimated “core” ejection time t_0 is computed by linearly extrapolating the trajectories back to the reference point. When components can be resolved into sub-components, a central location is taken with the errors derived from the average position of the sub-components. The emphasis in this thesis is on the spectral

properties and the physical properties we can derive from that. While kinematics are computed, they will in the future be combined with high-cadence 7 mm and 2 cm VLBI monitoring, which should yield even more reliable results.

4.3.4 Trailing Components

A common feature in high frequency VLBI maps of blazars are trailing components, studied in detail by [Agudo et al. \(2001\)](#) and adapted here. Trailing components appear to be ejected from a main travelling component, and travel $\sim\sqrt{2}$ slower than the main travelling component.

4.3.5 Flaring Activity and Ejection Relations

In this thesis, we are analysing two forms of flaring activity; radio and γ -ray. For each source, the radio and γ -ray light-curves are over-plotted. If flaring activity occurs at a similar time to component ejections and flare peaks, we can estimate the distance between the emitting regions. For example, if the γ -ray flare precedes a component ejection time t_0 by a few days, we can say that the γ -rays are emitted upstream of the “core”.

4.3.6 Magnetic Fields

As VLBI at 3 mm allows observations at or above the turnover frequency for synchrotron radiation, it allows for a novel approach for deriving estimates of the magnetic field in blazars. Although at least three spectral points are required to derive a spectrum (and determine with confidence the turnover frequency), the combined use of 3 and 7 mm VLBI maps allows for limits to be computed for the magnetic field as a function of distance down the jet. In the future, the addition of 1 mm and 2 cm MOJAVE data will allow us to determine the turnover frequency more robustly. The inclusion of 15 GHz MOJAVE data is performed on OJ287 in Chapter 5. For this analysis, only components that could be fitted to a single, non-delta component at both frequencies were used. Typically, the “core” is taken to be the component labelled C1.

4.3.6.1 Magnetic Field from SSA

Usually, the “core” is expected to have a flat to slightly inverted spectrum (flux density increasing with frequency), whilst travelling components are expected to have a steeper spectrum (flux density increasing with decreasing frequency). To derive an estimate on the magnetic field, we require the spectral index of optically thin emission (α) the turnover frequency (ν_m) and turnover flux density (S_m). A single epoch was analysed in this manner in CTA 102 by [Fromm et al. \(2013b\)](#), but we expand to determine ν_m or limits on it in individual components over time. Using the approach of ([Lobanov & Zensus 1999](#)) and using fitted components to derive fluxes and sizes ([Marscher 1983](#); [Bach et al. 2005](#)):

$$B_{\text{SSA}} = 10^{-5} b(\alpha) \frac{\theta_m^4 \nu_m^5 \delta^{2-\alpha}}{S_m^2 (1+z)} \text{ Gauss}, \quad (4.1)$$

where $b(\alpha)$ is a parameter between 1.8 and 3.8 for optically thin emission (see Table 4.3, adapted from [Marscher 1983](#)), and θ_m is the FWHM of the component in mas and δ is the Doppler factor ([Bach et al. 2005](#)). The power of $2 - \alpha$ is added because stationary features (including the “core”) are steady-state rather than evolving in time and a factor of δ is lost. Additionally, a compression factor, κ must be taken into account ([Cawthorne 2006](#)):

$$\kappa = \frac{\Gamma \beta_{\text{int}} \sin \theta_0 (8\beta^2 \sin^2 \theta_0 - \Gamma^{-2})^{1/2}}{(1 - \beta^2 \cos^2 \theta_0)^{1/2}} \quad (4.2)$$

In epochs where ν_m is detected, errors on the turnover frequency are taken as ± 20 GHz. In other epochs, lower limits were computed when ν_m was above 86 GHz and upper limits when ν_m was below 15 GHz. The results of this analysis are given in Tables A.1-A.4. The values in this table are *uncorrected* by the Doppler factor.

α	b
-0.25	1.8
-0.50	3.2
-0.75	3.6
-1.00	3.8

TABLE 4.3: Dimensionless parameters of the spectral index α , adapted from [Marscher \(1983\)](#).

4.3.6.2 Magnetic Field from Equipartition

An alternative method to estimate of the magnetic field strength is via equipartition arguments. The jet emission is said to be in equipartition when relativistic particle and magnetic energies are equal. If we assume that the jet is in equipartition, we can compute minimum magnetic field strengths, energies and luminosities. An equipartition ‘critical size’ can be calculated (Scott & Readhead 1977; Gujosa & Daly 1996, e.g.):

$$\theta_{\text{crit}} = \left[\frac{\left[\frac{8\pi F(\alpha)}{(1 \times 10^{-5})b(\alpha)} \right]^2}{\nu_m^{17} D_L S_m^8 (1+z)^9} \right]^{7+4\alpha/17} \quad (\text{mas}) \quad (4.3)$$

Where S_m and ν_m are the turnover fluxes and frequencies respectively, α is the spectral index, $F(\alpha)$ is a scaling factor from Scott & Readhead (1977). If the observed size in the source (scaled by a factor of 1.6 Marscher 1977) is less than this ‘critical size’ it implies a particle dominated jet, and a larger size implies a magnetically dominated jet. If we assume equipartition between relativistic particles and magnetic fields, we can estimate the Doppler factor:

$$\delta_{\text{equi}} = \left(\frac{U_{\text{rel}}}{U_{\text{mag}}} \right)^{1/(7+4\alpha)} \quad (4.4)$$

Where U_{rel} and U_{mag} are the energy densities of relativistic particles and magnetic fields respectively:

$$U_{\text{rel}} = \frac{F}{D_L (\theta_m^9 \nu_m^7 S_m^4 (1+z)^7)} \cdot \delta^{-(5+4\alpha)} \quad (4.5)$$

$$U_{\text{mag}} = \frac{\delta^2 B_{\text{SSA}}^2}{8\pi} \quad (4.6)$$

We can also compute the brightness temperature:

$$T_B = 1.22 \times 10^{12} \frac{S_m}{\theta_{\text{obs}}^2 \nu_m^2} \cdot \frac{\delta}{1+z} \quad (\text{K}), \quad (4.7)$$

the equipartition brightness temperature can be compared against the brightness temperature derived from standard means. If they are not equal, it could imply a jet that is not in equipartition. An estimate of the minimum magnetic field strength can hence be calculated from (Bach et al. 2005):

$$B_{\text{equi}} = 5.37 \times 10^{12} (S_m \nu_m D_L^2 R^{-3})^{-2/7} \delta^{(2-2\alpha)/7} \quad (\text{G}), \quad (4.8)$$

where D_L is the luminosity distance and R is the linear radius of the emitting region in cm. The magnetic field must also be corrected by the compression factor κ , described in Section 4.3.6.1.

4.3.7 Distance to SMBH

The relativistic jet model was first proposed to explain the variability of non-thermal emission in quasars and blazars (Blandford & Rees 1978; Blandford & Königl 1979). As Marscher et al. (1992) puts it:

The jet is assumed to be generated at some point R_0 , beyond which it flows at a constant Lorentz factor Γ (at speed βc), confined to a cone of constant opening half-angle ϕ .

If the jet is confined only by its own inertia, the jet density will decrease as $1/r^2$, where r is the radial distance from the jet apex. If the magnetic field is parallel to the jet (toroidal), the magnetic field will decrease as $B_{\parallel} \propto r^{-2}$, when it is perpendicular (poloidal) $B_{\perp} \propto r^{-1}$. This can be re-expressed (e.g. Gujosa & Daly 1996):

$$B \propto (1/r)^n \quad (4.9)$$

Where n is an exponent for poloidal ($n=1$) or toroidal ($n=2$) magnetic field configurations. We can compute an estimate of the distance from the “core” to the jet apex with the ratio of magnetic fields and the separation between the “core” (C) and downstream components (S):

$$\frac{B_{C1}}{B_{C2}} = \sqrt[n]{\frac{r_{\text{apex}} + \Delta r_{C2}}{r_{\text{apex}}}} \quad (4.10)$$

Where r_{apex} is the distance to the black hole in mas, Δr_{C2} is the separation between the “core” and stationary feature. Rearranging, we get:

$$r_{\text{apex}} = \frac{\Delta r_{C2}}{(B_{C1}/B_{C2})^n - 1} \quad (4.11)$$

Recent work by Gabuzda et al. (2014) and Zamaninasab et al. (2014) suggests that toroidal ($n=1$) magnetic exist in AGN, although any other configuration could plausibly exist.

An important caveat is that this technique can only be used when the magnetic field is weaker downstream than it is upstream. This problem is more acute

here, as we can only determine limits, we only have two spectral points from 7 mm and 3 mm. In our case, we can only compute limits when the upper limit of an upstream component is higher than the lower limit of a downstream component. This means that derived values must be upper limits, as the difference in magnetic field strengths can only increase and not decrease.

4.3.8 Location of γ -ray Emitting Regions

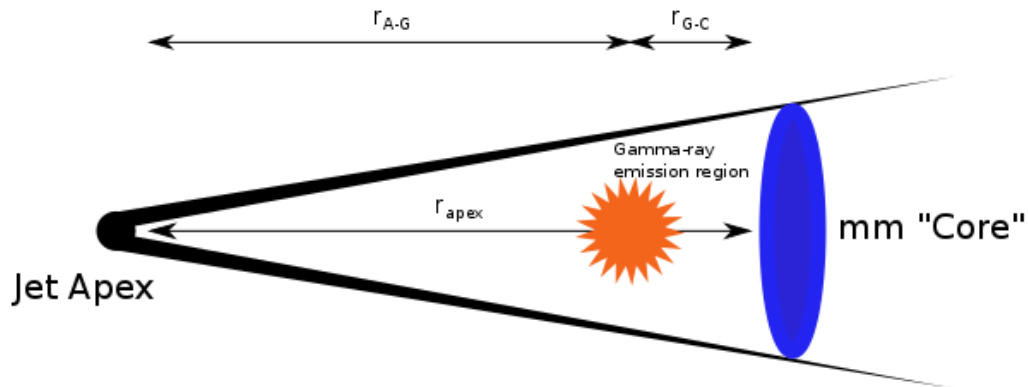


FIGURE 4.2: A sketch the location of γ -ray emission region. The γ -ray emission region is located a distance R_{A-G} from the jet apex.

Once the distance to the jet apex is known, we can calculate the distance to the γ -ray emitting regions. Figure 4.2 depicts a stylised sketch of a relativistic jet. The γ -ray emission region is located a distance r_{A-G} from the jet apex. This distance is the difference between the distance to the “core” from the jet apex, r_{apex} and the distance between the “core” and the γ -ray emission region, r_{G-C} .

In Section 4.3.7, we described a method to determine the distance from the “core” to the jet apex, r_{apex} , using the decrease of magnetic field strength down the jet. With this, we can then solve for the distance to the γ -ray emitting region, r_{A-G} , as described above. Recent work by Gabuzda et al. (2014) and Zamaninasab et al. (2014) suggests that toroidal ($n=1$) magnetic plays a more important role in AGN than assumed before. McKinney (2014, private communication), suggests that the value of n could even be lower than 1.

4.3.9 Magnetic Field in the Broad-Line Region and the Central Engine

If we can measure the decrease in magnetic field down the jet and hence find the distance to the central engine, we can extrapolate the values for the magnetic field to other locations. If we re-arrange Equation 4.9, we can solve for the magnetic field $B_{\Delta R}$ at a distance ΔR from the jet apex:

$$B_{\Delta R} = \left[\frac{B_{C1} \times \Delta R_{C1}}{-\Delta R_{C1-\Delta R} + \Delta R_{C1}} \right]^{1/n} \text{ (G)}, \quad (4.12)$$

where B_{C1} is the magnetic field in the “core”, ΔR_{C1} is the distance to the “core” and $\Delta R_{C1-\Delta R}$ is the difference between the “core” and the distance being solved for. In this thesis, we compute magnetic field estimates at $R_{BLR} = 0.05 \text{ pc}$ and $R_{BH} = 5R_G$, where R_G is the gravitational radius of the black hole.

4.3.10 Imaging Errors and Error Propagation

Errors introduced through the measurement systems (receivers, etc), can usually be assumed to be Gaussian in nature. Unfortunately, these simple Gaussian properties break down when propagated with the use of CLEAN, making quantitative computation of errors difficult, although possible (Lee 2007; Schinzel 2011). Jorstad et al. (2005) and others estimate errors on Gaussian components with nominal values of 15% on fluxes (20% at 86 GHz), 20% of the beam width on component full-width half maximums (FWHM) and core-separations and 5° for the position angle (PA). These values arise due to the gridding in the map. However, the errors on Gaussian components can be found more formally using the methods of Fomalont (1999) and Lobanov (2005), and as adapted from (Section 4.1.3 Schinzel 2011). First, one calculates the Signal-to-noise ratio (SNR):

$$SNR = \frac{S_p}{\sigma_p}, \quad (4.13)$$

where S_p is the peak flux density and σ_p is the root-mean-square (rms) noise level of a map. The error on an individual component, σ_c , is thus:

$$\sigma_c = (\sigma_p \sqrt{1 + SNR}) \cdot \sqrt{1 + (S_c^2/S_p^2)}, \quad (4.14)$$

where S_c^2 is the flux density of the component. The limits on component size errors are found by first finding the FWHM limit $FWHM_{lim}$:

$$FWHM_{lim} = \frac{4}{\pi} \sqrt{\pi \ln(2.0) \theta_{beam} \ln(SNR/SNR - 1)}, \quad (4.15)$$

where θ_{beam} is the beam size. This relation is true when $FWHM_{\text{lim}} > FWHM$, otherwise $FWHM_{\text{lim}} = FWHM$. The errors on the component FWHM (σ_{FWHM}) are then:

$$\sigma_{FWHM} = \frac{\theta_p FWHM_{\text{lim}}}{S_p}, \quad (4.16)$$

the errors on the “core” separation (σ_{sep}) are:

$$\sigma_{\text{sep}} = 0.5\sigma_{FWHM}, \quad (4.17)$$

and the errors on the position angle (PA) (σ_{PA}) are:

$$\sigma_{PA} = \arctan(\sigma_{\text{sep}}/\text{sep}). \quad (4.18)$$

Errors are propagated by simulating variables 10 000 times using normally distributed random variables and distributing using Monte-Carlo methods. 1σ errors reported.

4.4 Results

4.4.1 Flux Accuracy and Source Compactness

All maps are corrected against total intensity measurements because absolute fluxes are less important than *relative* fluxes for our analysis. Single dish measurements are interpolated between near-in-time measurements to estimate fluxes on the date of 3 mm observations as fluxes can change rapidly on the scale of days to weeks. The 7 mm receiver at Effelsberg, used for flux monitoring was not available in 2010 and 2011, we use 9 mm data with increased error bars for corrections where 7 mm data were not available. Here, we compute the ratio between total VLBI flux densities and total intensity flux densities, commonly known as source compactness. The source compactness is:

$$C = \frac{S_{\text{VLBI}}}{S_{\text{tot}}}, \quad (4.19)$$

where S_{tot} is the total flux density from single-dish measurements and S_{VLBI} is the total flux density as measured by VLBI model-fits. In the context of VLBI experiments, the source compactness is a measure of how resolved a source is. A completely unresolved source would have a source compactness = 1 (e.g. [Kovalev et al. 2005](#)). With knowledge of how each source is resolved, we can use this as a measure of flux calibration accuracy. The corrected flux density, $S_{\text{VLBI,corr}}$, can be found with the following equation:

$$S_{\text{VLBI,corr}} = S_{\text{VLBI}} \frac{S_{\text{tot}}}{S_{\text{VLBI}}} \langle C \rangle, \quad (4.20)$$

where $\langle C \rangle$ is the average compactness of a source. The results of this analysis are shown in Table 4.4 and for most epochs, the correction is less than 10%. As an additional check, individual components were checked for their spectral indices (e.g. an optically thin component should exhibit a spectral index of $\alpha \sim -0.7$) and results were found to be reasonable.

With the exception of 3C 273, the source compactness is always lower at 3 mm than at 7 mm, implying that sources are more resolved at 3 mm than at 7 mm. This is as expected due to the higher resolution offered by the GMVA at 3 mm compared with the VLBA at 7 mm. 0716+714 ($80 \pm 17\%$), 0836+710 ($73 \pm 8\%$),

Source	ν GHz	E1	E2	E3	E4	E5	E6	E7	Aver
0716+714	43		3.1	2.2	1.5	0.7	1.1	1.3	1.6 ± 0.3
0716+714	86		1.3	2.4	2.4	2.0	2.2	1.6	2.0 ± 0.2
0836+710	43			0.9	1.2	1.1	1.1	1.0	1.1 ± 0.1
0836+710	86			1.9	1.5	1.3	1.7	1.2	1.5 ± 0.1
3C 273	43	1.2	1.5	1.3	1.6	1.2		1.4	1.4 ± 0.1
3C 273	86	4.0	1.0	1.1	1.3	1.2		1.2	1.2 ± 0.4
BL Lac	43		1.2	1.3	1.5	1.0	0.9	1.2	1.2 ± 0.1
BL Lac	86		2.1	1.8	1.3	1.3	1.4	1.8	1.6 ± 0.2

TABLE 4.4: An overview of inverse source compactness. The numbers represent the factor required to scale total VLBI flux densities to that from single-dish measurements. E1: 2008.78; E2: 2009.35; E3: 2009.86; E4: 2010.36; E5: 2011.35; E6: 2011.78; E7: 2012.38.

3C 273² ($86 \pm 10\%$) and BL Lac ($75 \pm 11\%$), all exhibit statistically significant decreases in compactness at 3 mm, compared with 7 mm. This suggests that with the exception of 3C 273, sources are $21 \pm 3\%$ more resolved at 3 mm than at 7 mm.

²The scaling in epoch E1 was not included as the data had large amplitude errors.

4.4.2 0716+714

4.4.2.1 Introduction

0716+714 is known as an extremely rapid intra-day variable (IDV) source (along with PKS 1257-326, examined in Chapter 6) (Wagner et al. 1996). It is also a well studied blazar that exhibits highly variable properties across the electromagnetic spectrum. A multi-wavelength study was performed by Villata et al. (2008) finding correlated variability at optical, radio and γ -ray wavelengths, further corroborated by Fuhrmann et al. (2008) and Rani et al. (2013). As the source has a featureless optical spectrum, its redshift is not well constrained and is taken typically to be $z = 0.3$. A VLBI analysis at lower frequencies by Bach et al. (2005), found that the source had particularly fast components - unusual for a BL Lac object. Jorstad et al. (2005) and Rani et al. (2013) found a stationary feature at approximately 0.1 mas from the VLBI “core” that is also detected with 3 mm VLBI here.

Epoch ₈₆	Epoch ₄₃	$S_{\text{tot},15}$ (Jy)	$S_{\text{tot},43}$ (Jy)	$S_{\text{tot},86}$ (Jy)	$S_{\text{tot},225}$ (Jy)
2009.35	2009.41	1.4 ± 0.05	2.0 ± 0.2	1.2 ± 0.2	0.9 ± 0.1
2009.78	2009.79	1.3 ± 0.02	2.1 ± 0.2	1.4 ± 0.2	1.4 ± 0.1
2010.35	2010.38	2.7 ± 0.05	2.8 ± 0.2	3.3 ± 0.3	2.2 ± 0.2
2011.35	2011.39	2.7 ± 0.05	$3.2^* \pm 0.9$	3.9 ± 0.3	3.0 ± 0.3
2011.77	2011.79	1.5 ± 0.05	$2.5^* \pm 0.8$	3.5 ± 0.6	2.1 ± 0.1
2012.38	2012.40	0.9 ± 0.04	$0.9^* \pm 0.6$	0.9 ± 0.2	1.1 ± 0.2

TABLE 4.5: An overview of 0716+714 total intensity flux densities.* Large gap in 7 mm total-intensity measurements, 9 mm flux density measurement is used.

4.4.2.2 Core Identification

ID	S_{43} (Jy)	S_{86} (Jy)	α	θ_{43} (mas)	θ_{86} (mas)	$T_{B,43}$ ($\times 10^{11}$ K)	$T_{B,86}$ ($\times 10^{11}$ K)
C1	1.76 ± 0.13	1.48 ± 0.10	-0.3 ± 0.2	0.03 ± 0.01	0.02 ± 0.01	15.2 ± 2.2	35.1 ± 5.2
C2	0.41 ± 0.02	0.46 ± 0.03	0.2 ± 0.1	0.01	0.03 ± 0.01	0.5 ± 0.1	1.4 ± 0.2

TABLE 4.6: An overview of 0716+714 averaged values.

In Table 4.6, we can see the averaged quantities for the flux densities, the measured sizes (component FWHMs), spectral indices and brightness temperatures for the two stationary components, C1 and C2. C1 has a significantly higher brightness temperature, smaller size and higher average flux density, although it

has a more inverted spectrum than C2. Additionally, all travelling components move outwards, away from C1. Hence, we conclude that C1 is the “core”. Component C2 is seen at a quasi-stationary position of ~ 0.1 mas from C1 and is identified as a stationary feature. The brightness temperatures in C1 is over $T_B \sim 10^{12}$, suggesting that both are Doppler boosted.

4.4.2.3 Morphology

In Fig. 4.3 - Fig. 4.8, 7 and 3 mm maps are presented. The maps are morphologically similar, with only minor differences between both frequencies, although additional structure is sometimes detected in the 3 mm maps. For example, in Fig. 4.5, a component, C1x, is detected between components C1 and C2. In all epochs, both stationary features and travelling components can be cross-identified between the frequency bands, allowing component speeds to be derived. In the most recent epoch (Fig. 4.8), new components X8 and X9 are detected.

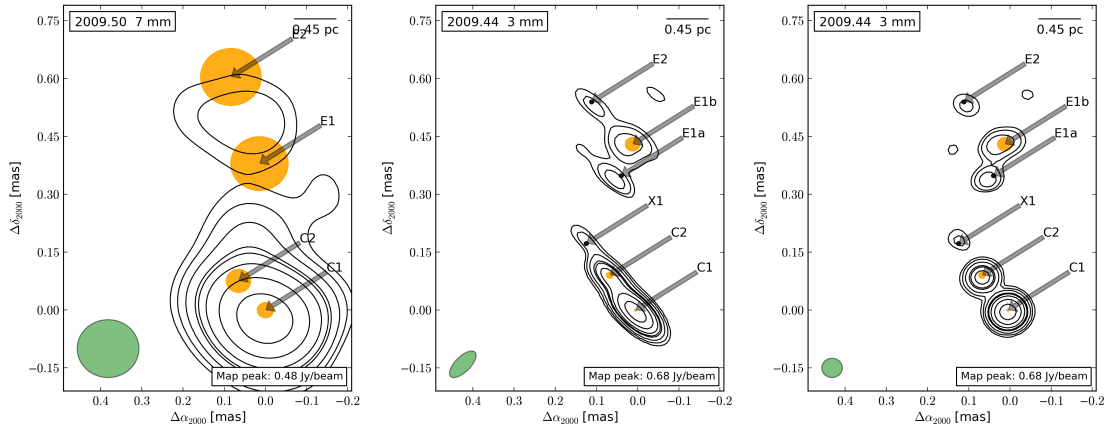


FIGURE 4.3: VLBI map of 0716+714 in 2009.35. Contours: -1, 1, 2, 4, 8, 16, 32, 64%.

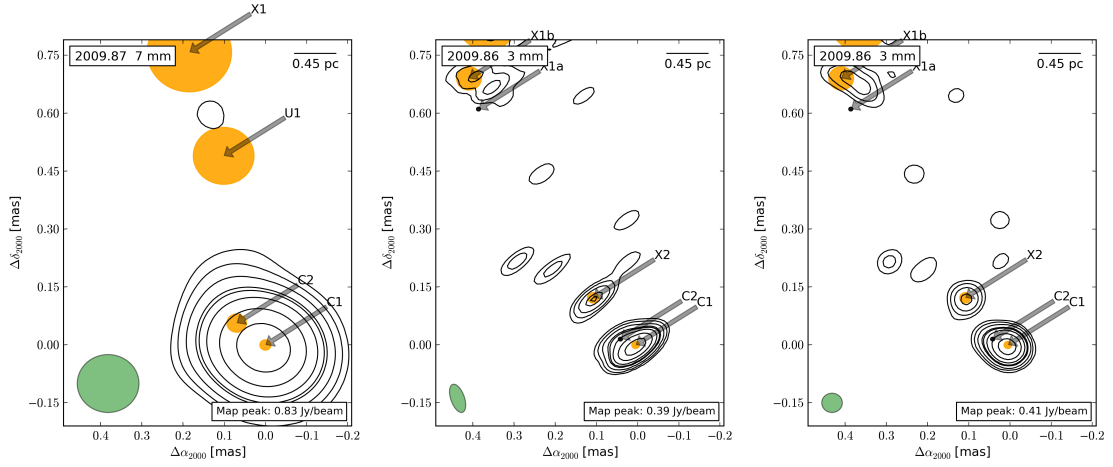


FIGURE 4.4: VLBI map of 0716+714 in 2009.86. Contours: -1, 1, 2, 4, 8, 16, 32, 64%.

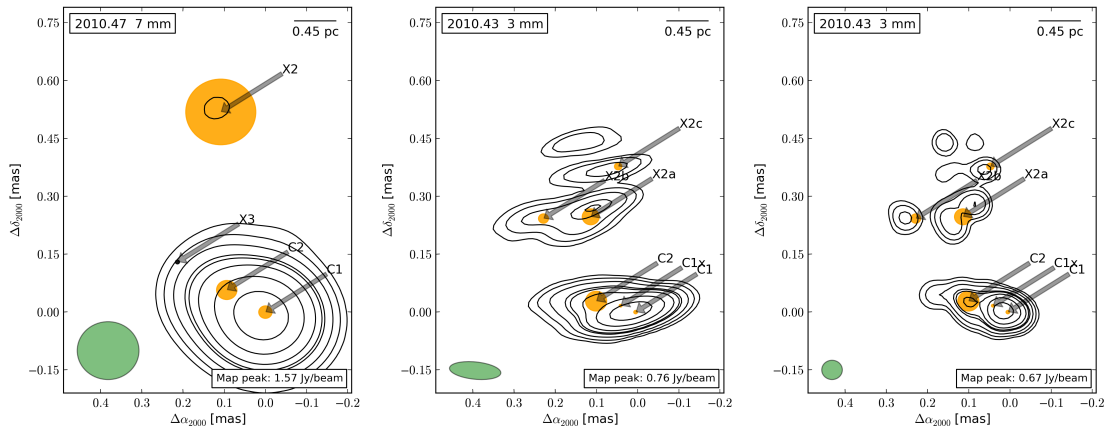


FIGURE 4.5: VLBI map of 0716+714 in 2010.36. Contours: -1, 1, 2, 4, 8, 16, 32, 64%.

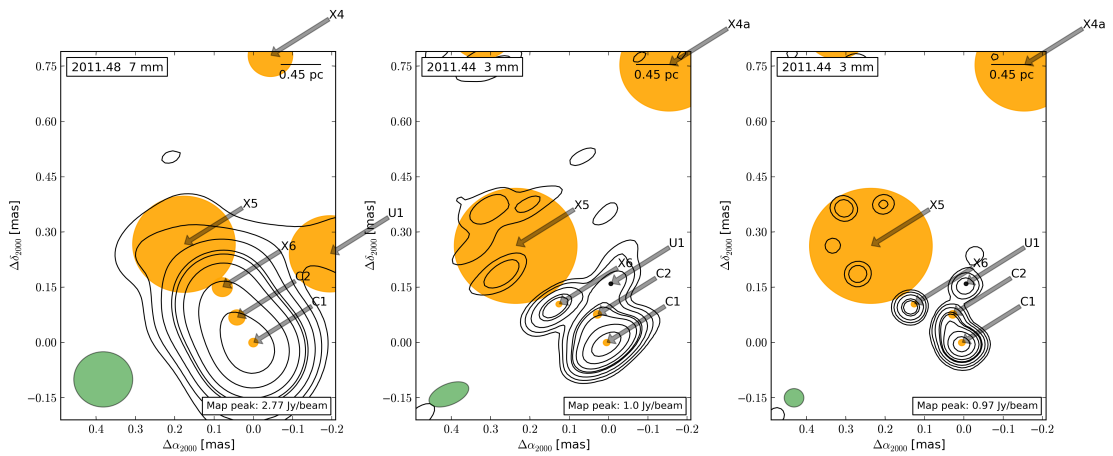


FIGURE 4.6: VLBI map of 0716+714 in 2011.35. Contours: -1, 1, 2, 4, 8, 16, 32, 64%.

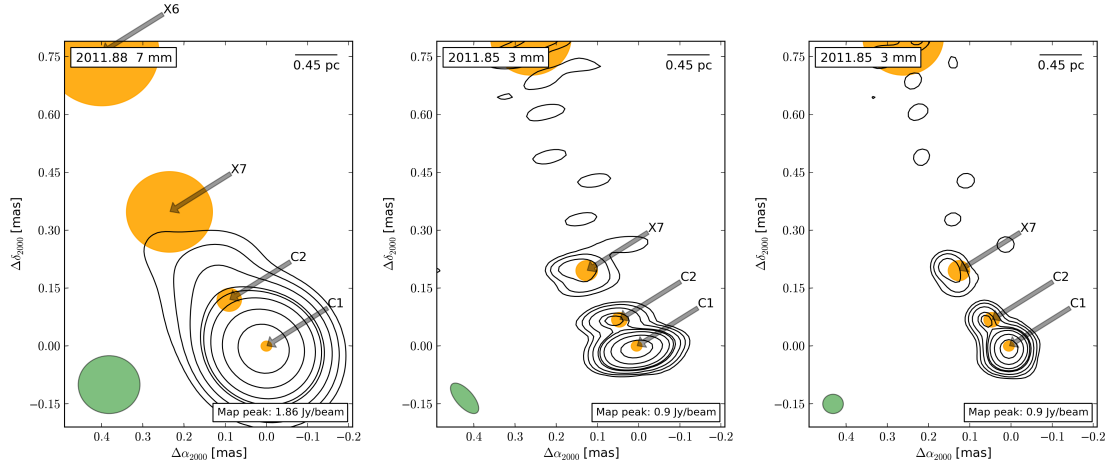


FIGURE 4.7: VLBI map of 0716+714 in 2011.77. Contours: -1, 1, 2, 4, 8, 16, 32, 64%.

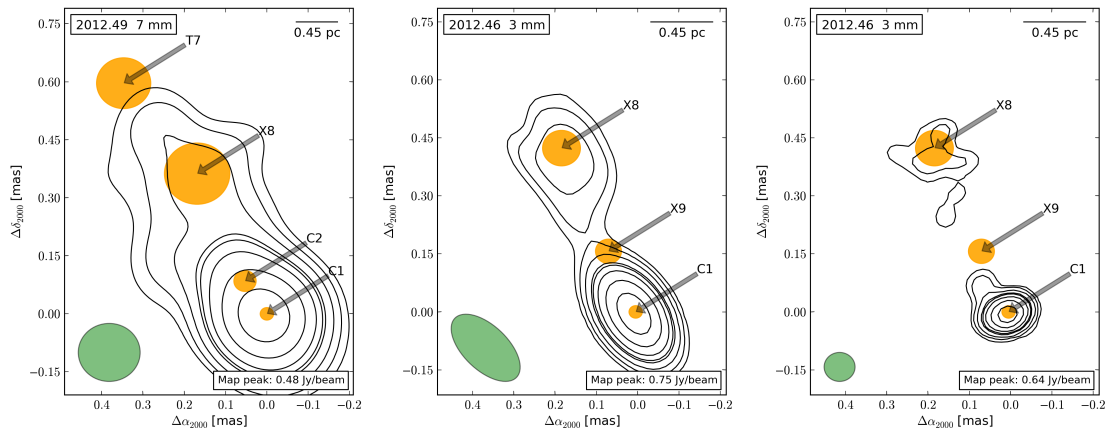
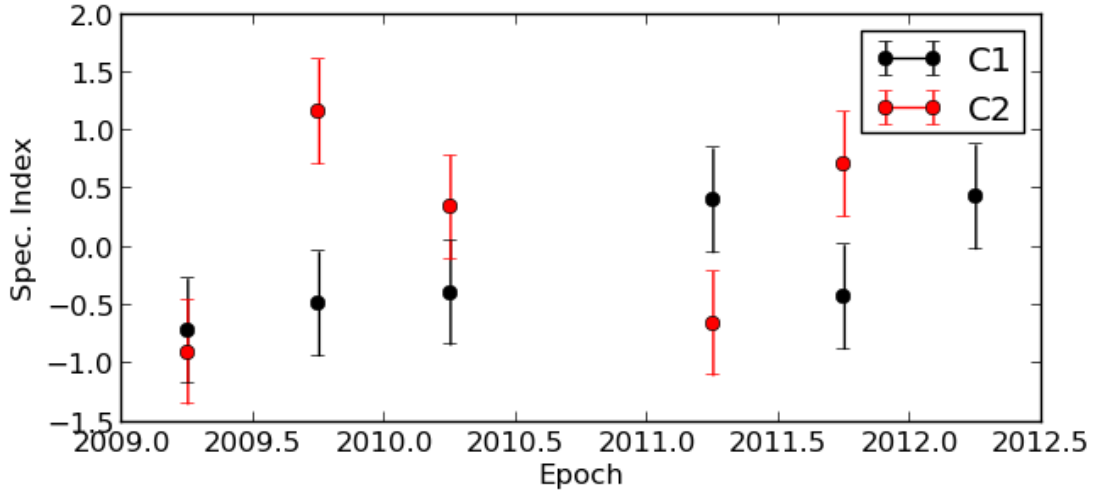


FIGURE 4.8: VLBI map of 0716+714 in 2012.38. Contours: -1, 1, 2, 4, 8, 16, 32, 64%.

4.4.2.4 Spectral Properties

In Fig. 4.9, we observe that both stationary features C1 and C2 show a variable 43-86 GHz spectrum. Component C1 exhibits a steep-to-flat spectrum in most epochs, with $\alpha \sim -0.5$, with the exception of 2011.35 and 2012.38, where it exhibits an optically thick (flux density increasing with frequency) spectrum of $\alpha \sim 0.5$. Component C2 exhibits a rapid change from an optically thin $\alpha \sim -0.8$ to an optically thick $\alpha \sim 1.0$ spectrum between 2009.35 and 2009.86, before returning to an optically thin spectrum $\alpha \sim -0.7$ in 2011.35. In 2011.77, it again exhibits an optically thick spectrum of $\alpha \sim 0.7$. It is remarkable that component C1, despite exhibiting higher flux densities and brightness temperatures does not show an inverted or flat spectrum in most epochs, as is usually expected for the VLBI “core” at longer wavelengths.

FIGURE 4.9: The spectral index evolution of 0716+710, $S \propto \nu^\alpha$

4.4.2.5 Kinematics

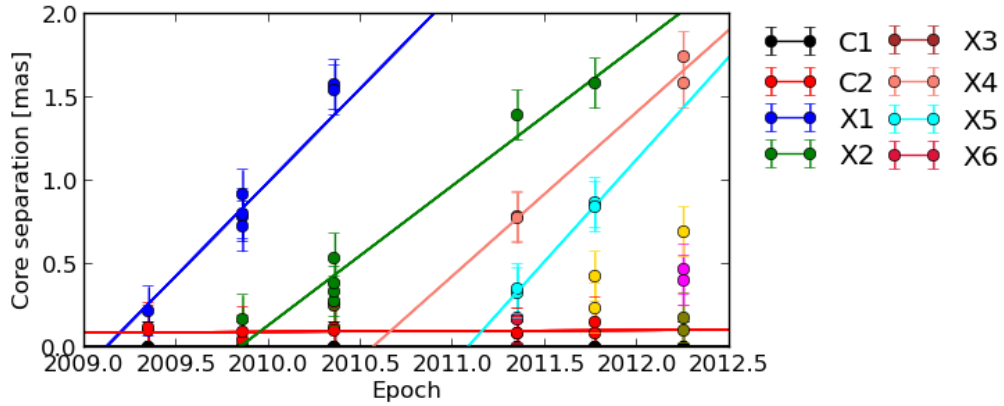


FIGURE 4.10: Component ejections in 0716+710.

The source kinematics for 0716+714, (Fig. 4.10) are difficult to compute robustly, as 0716+714 is a fast source and cadence is low. Some components at 3 mm intermittently appear then disappear, likely due to travelling components being resolved into multiple components, due to the higher resolution at 3 mm, making ejections appear more frequent. For components that could be cross-identified in multiple epochs, their speeds and derived properties are given in Table 4.7. In this table, the proper motion μ is used to compute the apparent superluminal motion, β_{app} . β_{app} is then used to derive the minimum Doppler

factor δ_{\min} , the minimum Lorentz factor Γ_{\min} , the critical angle θ_{crit} and the estimated “core” ejection time, t_0 . No significant difference in component speeds between 3 and 7 mm are detected, and linear fits used components at both frequencies. Derived Lorentz factors are consistent with previous studies (e.g. [Jorstad et al. 2005](#)).

ID	μ (mas/yr)	β_{app}	Γ_{\min}	δ_{\min}	θ_{crit} ($^\circ$)	t_0 (yr)
X1	1.12 ± 0.24	16.7 ± 3.5	18.9 ± 4.1	16.7 ± 4.0	3.4 ± 1.4	2009.10 ± 0.19
X2	0.84 ± 0.16	12.5 ± 2.9	14.2 ± 4.8	12.5 ± 2.7	4.5 ± 1.7	2009.84 ± 0.24
X4	0.98 ± 0.21	14.7 ± 3.9	16.6 ± 4.9	14.7 ± 3.5	3.9 ± 0.4	2010.12 ± 0.26
X5	1.23 ± 0.20	18.4 ± 2.4	20.8 ± 3.2	18.4 ± 2.6	3.1 ± 1.1	2011.24 ± 0.35

TABLE 4.7: An overview of 0716+714 kinematics.

4.4.2.6 Light Curves and Ejection Relations

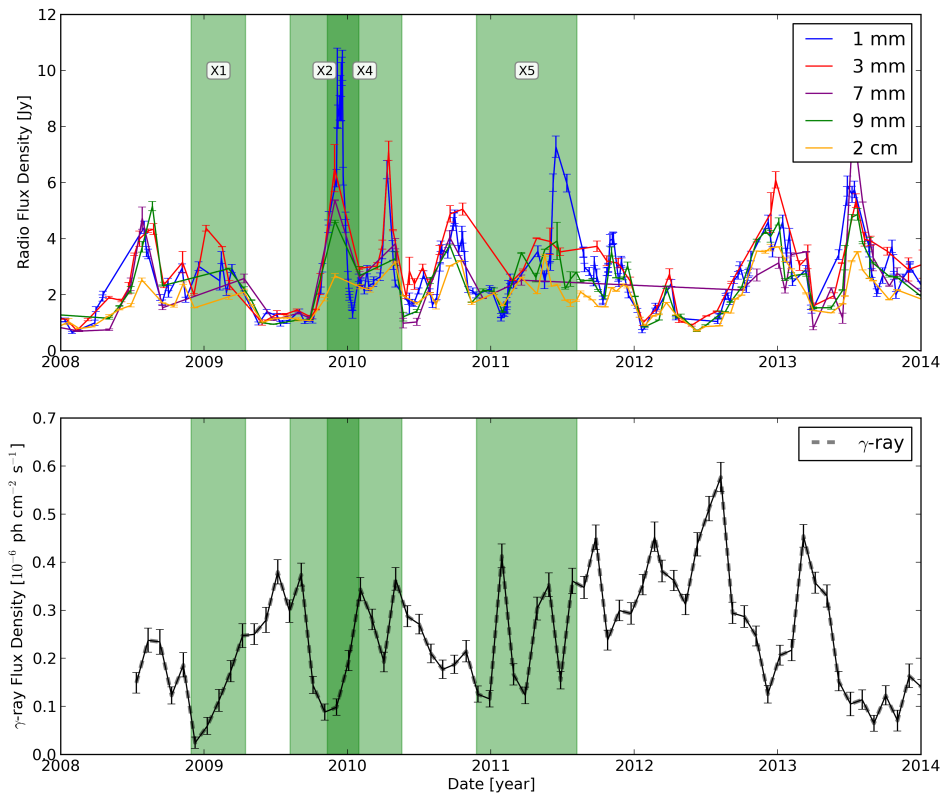


FIGURE 4.11: Radio and γ -ray light-curves from 2008.0-2014.0 in 0716+714. Green shaded areas are estimated “core” ejection times

0716+714 exhibits a high degree of flux variability at both radio and γ -rays and component ejections appear to be associated with this flaring activity. In Fig. 4.11, many bright radio and γ -ray flares are observed and estimated component ejection times are over-plotted in the shaded green area. Between 2010.0 and 2012.0, the γ -ray light-curve exhibits many local maxima which could be regarded as individual flaring events. During this period, several VLBI components were ejected, perhaps explaining the large amount of γ -ray variability. Component X1 is estimated to have been ejected during a radio flare in early 2009, as a γ -ray flare is rising. The most prominent radio flare is in late 2009 to early 2010 and has a large γ -ray flare preceding it in mid 2009. Both components X2 and X4 could be associated with this activity. Similarly, component X5 is estimated to have been ejected near-in-time to a radio flare in mid-2011, coinciding with rapid γ -ray variability. In early 2012, the radio flux density was relatively quiet, although γ -ray activity was still highly variable.

The spectral variability seen in Fig. 4.9 also has possible correlations with ejections and flaring activity. In 2009.86, when the “core” (C1) exhibits $\alpha \sim -0.7$ and a large γ -ray flare, the estimated ejection (t_0) time of component X1 is near in time with the onset of this flare, suggesting that it originates in the “core” region. Similarly, the estimated ejection times of components X2 and X4 coincides with the onset of γ -ray flares and optically thin spectra in the “core” region. Taken together, it appears likely that some part of the γ -ray activity occurs within the VLBI “core” region.

4.4.2.7 Magnetic Fields and Distance to Jet Base

In Table A.1 we summarise some of the derived physical properties of the jet. On average, the magnetic field from synchrotron self-absorption (SSA) is less than 0.18 G in the “core”. In stationary component C2, the magnetic field typically ~ 2 times stronger than in C1. On average, the magnetic field from equipartition, yields a value of ~ 0.6 G in both the “core” and component C2.

There is only one epoch where the lower limit for the magnetic field strength in the “core” was higher than the upper limit downstream. This occurs in 2011.35 where one obtains a lower limit of 1.30 G in the “core” and an upper limit of 0.34 G in component C2. This means the magnetic field has dropped by at

least 76%. In Table 4.8 we summarise the estimated distance to the jet apex and the magnetic fields at various distances, using these numbers. In Table 4.8, n denotes if the calculation assumed toroidal ($n=1$) or poloidal ($n=2$) geometry. The jet base is estimated to be ≤ 4.7 pc upstream of the VLBI “core”, if we assume a toroidal magnetic field geometry. Under this assumption, the magnetic field is estimated to be ≤ 122 G in the broad line region at $R_{\text{BLR}} = 0.05$ pc and ≤ 40576 G at the jet base $R_{\text{apex}} = 5R_G$. The values are very high, but as they are upper limits, the magnetic field strengths could be lower.

ID	n	ΔR_{BH} (mas)	ΔR_{BH} (pc)	B_{BLR} (G)	B_{BH} (G)
2011.35 B_{equi}	1	≤ 0.04	≤ 4.72	≤ 123	$\leq 4 \cdot 10^4$
2011.35 B_{equi}	2	≤ 0.01	≤ 1.07	≤ 5	≤ 200

TABLE 4.8: An overview properties derived from magnetic fields in 0716+714.

4.4.3 0836+710

4.4.3.1 Introduction

With a redshift of $z = 2.218$, 0836+710 is the highest redshift blazar investigated in our sample. [Jorstad et al. \(2005\)](#) reported a faint stationary feature in the jet at approximately 0.2 mas from the “core”, with occasionally moving features in between. They also reported a stationary feature (comprising a complex of two components) at approximately 3 mas from the “core”, first reported by [Krichbaum et al. \(1990\)](#) at 5 GHz. A multi-frequency VLBI analysis by [Perucho et al. \(2012\)](#) suggested that high-frequency observations show only the outer ridge-line of the jet, rather than the full width of the jet. [Jorstad et al. \(2013a\)](#) analysed 0836+710 as part of the BU-VLBA-BLAZAR program and found that γ -ray emission in early and late 2011 was associated with a component ejection.

Epoch ₈₆	Epoch ₄₃	$S_{\text{tot},15}$ (Jy)	$S_{\text{tot},43}$ (Jy)	$S_{\text{tot},86}$ (Jy)	$S_{\text{tot},225}$ (Jy)
2009.86	2009.88	1.6 ± 0.02	$2.5^* \pm 0.2$	2.5 ± 0.2	1.4 ± 0.1
2010.36	2010.38	1.9 ± 0.05	3.6 ± 0.2	2.9 ± 0.3	2.2 ± 0.2
2011.35	2011.39	2.4 ± 0.05	$2.5^* \pm 0.9$	2.2 ± 0.3	0.5 ± 0.3
2011.77	2011.79	2.9 ± 0.05	$2.1^* \pm 0.8$	1.6 ± 0.6	0.5 ± 0.3
2012.38	2012.40	0.9 ± 0.04	$0.9^* \pm 0.6$	0.9 ± 0.2	1.1 ± 0.2

TABLE 4.9: An overview of 0836+710 fluxes.* Large gap in 7 mm single-dish measurements, 9 mm flux measurement is used.

4.4.3.2 Core Identification

ID	S_{43} (Jy)	S_{86} (Jy)	α	θ_{43} (mas)	θ_{86} (mas)	$T_{B,43}$ ($\times 10^{10}$ K)	$T_{B,86}$ ($\times 10^{10}$ K)
C1	1.33 ± 0.23	0.95 ± 0.17	-0.5 ± 0.2	0.10 ± 0.02	0.10 ± 0.02	13.2 ± 2.0	9.8 ± 1.5
C2	0.98 ± 0.14	0.50 ± 0.06	-1.0 ± 0.2	0.05 ± 0.01	0.04 ± 0.01	40.3 ± 6.1	35.8 ± 5.4
C3	0.39 ± 0.12	0.28 ± 0.05	-0.6 ± 0.2	0.05 ± 0.01	0.05 ± 0.01	13.0 ± 2.0	12.4 ± 1.9

TABLE 4.10: An overview of 0836+710 averaged values.

In Table 4.10, we can see the averaged quantities for 0836+710. There are three stationary components, C1, C2 and C3. Components C2 and C3 have higher brightness temperatures than C1, but C1 exhibits a higher flux density. Components, however, are seen travelling away from component C1. As the sources is highly Doppler beamed (e.g. [Jorstad et al. 2005](#)), it is highly unlikely that components C2 or C3 would be a counter-jet. We therefore identify component

C1 as the “core”. Both components C2 and C3 are identified as being quasi-stationary features, as they do not move significantly on the sky in the period of observation. The source also exhibits two more distant stationary features, E1 and E2, at “core” separations of ~ 2.5 and ~ 3.5 mas respectively, consistent with [Krichbaum et al. \(1990\)](#). The spectral indices are all on average optically thin, with C2 exhibiting a particularly steep spectrum of $\alpha = -1.0 \pm 0.2$.

4.4.3.3 Morphology

In Fig. 4.12 - Fig. 4.16, 7 mm and 3 mm maps are presented of 0836+710. As with 0716+714 (Section 4.4.2), the general morphological properties of the 7 mm and 3 mm maps are broadly similar. The 3 mm maps however, reveal much higher levels of detail (e.g. in Fig. 4.15, a component is detected between C1 and C2). Both 7 mm and 3 mm maps exhibit a stationary feature at ~ 0.15 mas. In all epochs, both stationary features and travelling components could be cross-identified between the 43 GHz and 86 GHz, allowing speeds to be derived.

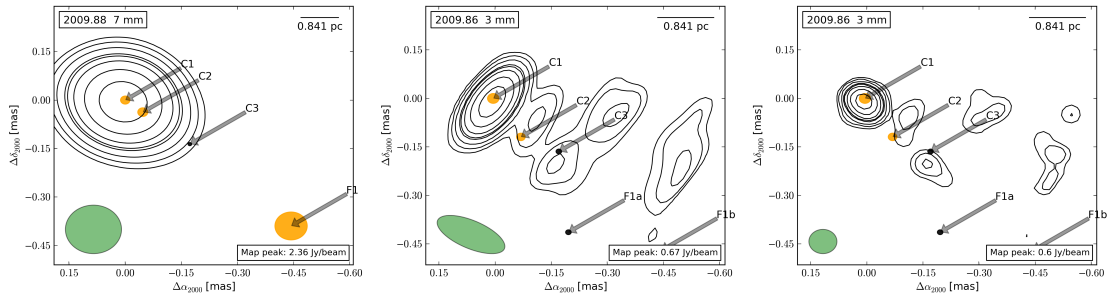


FIGURE 4.12: VLBI map of 0836+710 in 2009.86. Contours: -1, 1, 2, 4, 8, 16, 32, 64%.

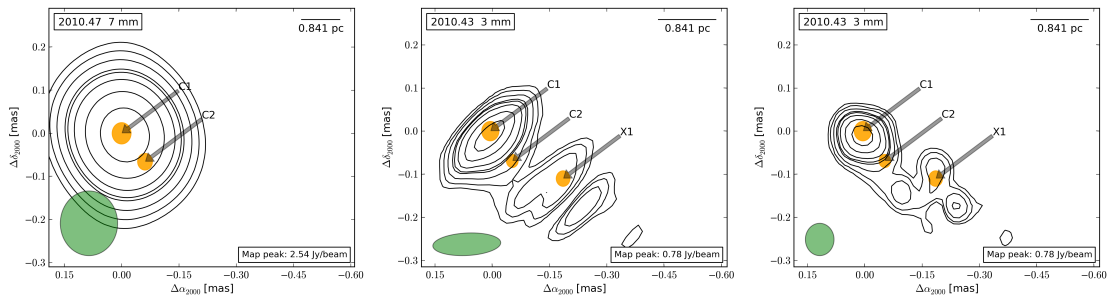


FIGURE 4.13: VLBI map of 0836+710 in 2010.36. Contours: -1, 1, 2, 4, 8, 16, 32, 64%.

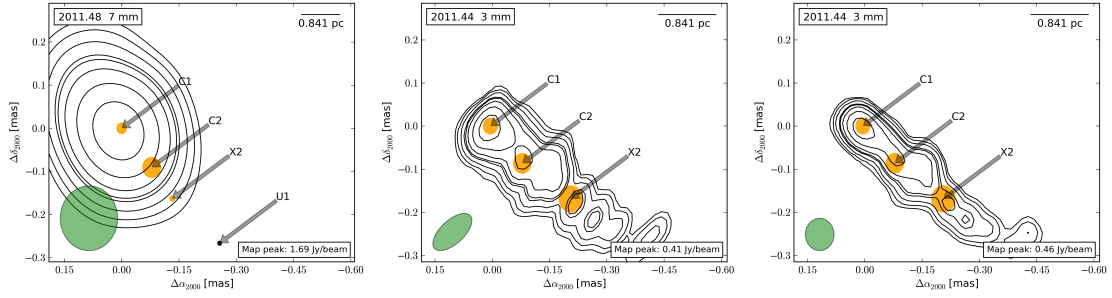


FIGURE 4.14: VLBI map of 0836+710 in 2011.35. Contours: -1, 1, 2, 4, 8, 16, 32, 64%.

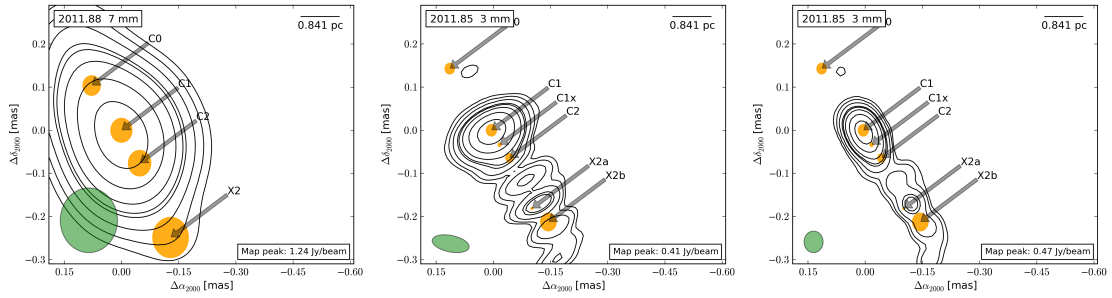


FIGURE 4.15: VLBI map of 0836+710 in 2011.77. Contours: -1, 1, 2, 4, 8, 16, 32, 64%.

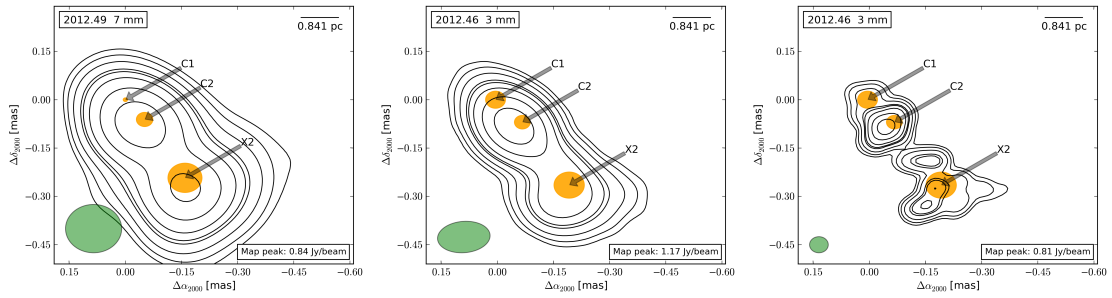


FIGURE 4.16: VLBI map of 0836+710 in 2012.46. Contours: -1, 1, 2, 4, 8, 16, 32, 64%.

4.4.3.4 Spectral Properties

The time evolution of the spectral properties of stationary features can be seen in Fig. 4.17. In the earliest epoch, 2009.78, the “core” exhibits an optically thick spectrum of $\alpha \sim 0.3$, before becoming thin with a spectrum of $\alpha \sim -0.7$ in later epochs. Component C2 is optically thin in 2009.78 with $\alpha \sim -0.7$, but within 6 months has changed to an optically thick spectrum of $\alpha \sim 0.7$, itself 6 months after the “core” had exhibited an optically thick spectrum. In all later epochs, both the “core” and component C2 exhibit optically thin spectra, with the exception of the most recent image in 2012.46 (Fig. 4.16), where C2 exhibits an

optically thick spectrum of $\alpha \sim 0.5$. It is also much brighter than the “core” at this time. Component C3 exhibits an optically thick spectrum of $\alpha \sim 0.7$ until the most recent epochs where it is optically thin ($\alpha \sim -0.7$).

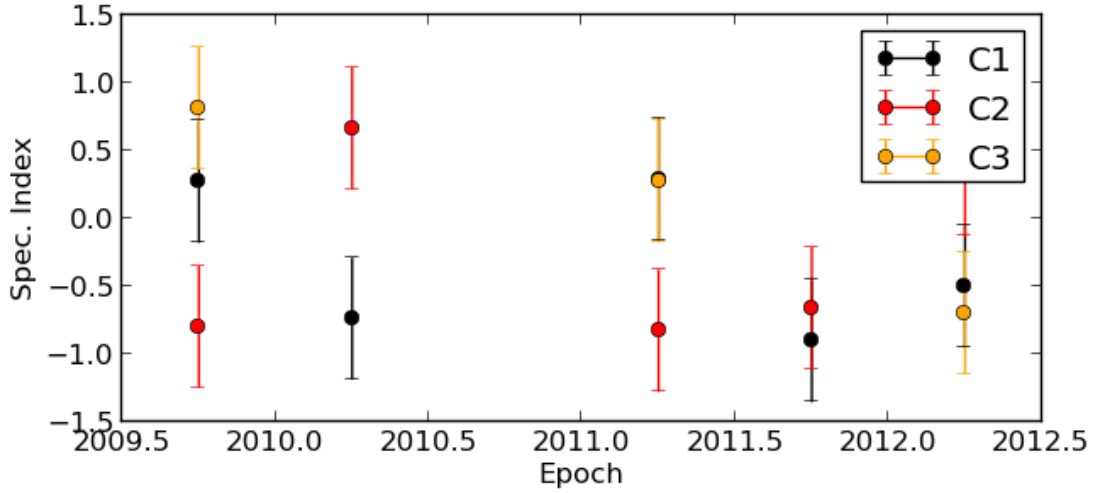


FIGURE 4.17: The spectral index evolution of 0836+710, $S \propto \nu^\alpha$.

4.4.3.5 Kinematics

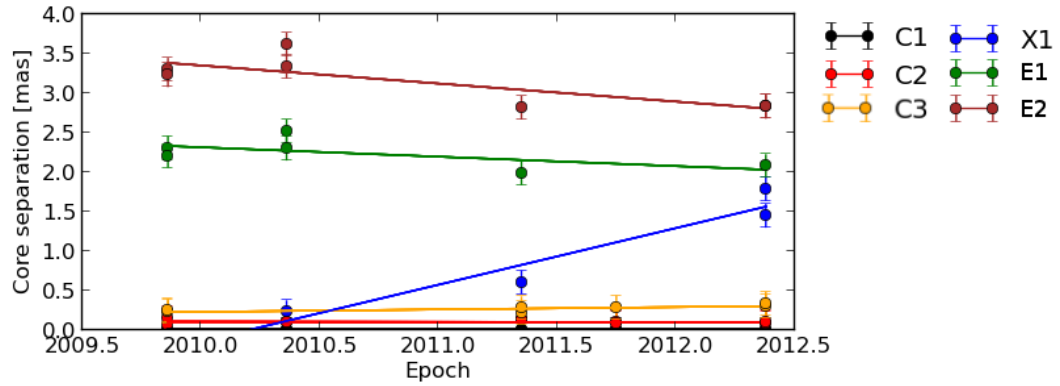


FIGURE 4.18: Component ejections in 0836+710.

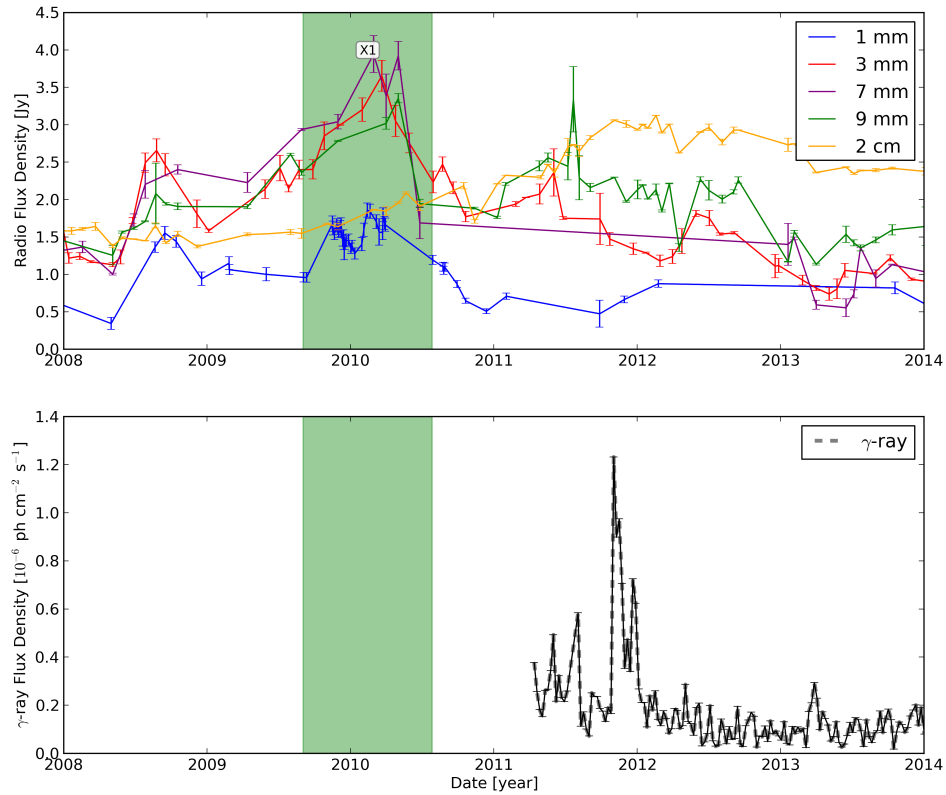
0836+710 exhibits slower motions on the sky than other sources here due to its high redshift, making the kinematics more robust. There is only one travelling component detected, component X1. Although we have only performed a linear fit here, Fig. 4.18 suggests that the component could be accelerating. Our derived kinematic properties in Table 4.11, match closely with those reported

in the literature. Nevertheless, we adopt $\delta \approx 21.3$, $\Gamma \approx 19.8$ and $\theta_0 \approx 2.7^\circ$ from [Jorstad et al. \(2013a\)](#) for further analysis. Two possible stationary features, E1 and E2, are detected at ~ 3 mas “core” separation, although they could be receding and may in fact be travelling components themselves, although stationary features are expected to be at approximately this location ([Krichbaum et al. 1990](#)).

ID	μ (mas/yr)	β_{app}	Γ_{min}	δ_{min}	θ_{crit} ($^\circ$)	t_0 (yr)
X1	0.72 ± 0.26	18.1 ± 8.2	21.1 ± 4.9	18.2 ± 4.0	2.7 ± 1.4	2010.12 ± 0.45

TABLE 4.11: An overview of 0836+710 kinematics.

4.4.3.6 Light-Curves and Ejection Relations

FIGURE 4.19: Radio and γ -ray light-curves from 2008.0-2014.0 in 0836+710.

In Fig. 4.19, we see the radio light curves of 0836+710. The light curves are dominated by a large radio flare peaking in early 2010, coinciding with the estimated

“core” ejection time of component X1. There is a smaller flare in mid 2008, occurring during the rise of the bigger flare. Unfortunately there is no γ -ray data available before early 2011. In 2010.38, the “core” is optically thin, coinciding with the “core” ejection time of component X1.

In the γ -rays, there is a large flare in late 2011 that was preceded by a smaller flare in mid 2011. We note with interest that we see component C1x at 3 mm in Fig. 4.15 (2011.77) while both the “core” and quasi-stationary feature C2 exhibit optically thin spectra. The large γ -ray flare occurs soon after this. Component C2 is also much more luminous than the “core” at this time. If we adopt a speed of $\mu \sim 0.7$ mas/yr for component C1x, it would pass the “core” in ~ 2011.4 , coinciding with the smaller preceding γ -ray flare. This suggests that the second larger γ -ray flare originates in the region of C2 and the smaller preceding flare originates in the “core” region. Additional VLBI data will be required to determine if a component ejection is also coincident with this flaring activity.

4.4.3.7 Magnetic Fields

As in 0716+714, the magnetic fields strength computed from synchrotron self-absorption (SSA) lead to much higher results than when derived from equipartition. The results appear to show a very strong magnetic field in 0836+710, with $B \sim 1 - 2$ G in the “core” region, possibly due to the source being in a flare state for much of the period analysed, also matching the previously known high polarisation in this source (Krichbaum et al. 1990). A single epoch, in 2010.36 with equipartition calculations, allowed estimates to be derived. Interestingly, on average, all components have higher flux densities at 7 mm than at 3 mm, making this source an excellent candidate for full analysis including 2 cm VLBI data.

4.4.3.8 Distance to Black Hole and Magnetic Field Estimates

In one epoch, 2010.36 and from equipartition calculations, we can derive estimates of the distance to the BH and compute estimates on the magnetic field strength. We find that if we assume a toroidal magnetic field, that the magnetic field strength is ≤ 137 G in the BLR and ≤ 70000 G at the jet apex. The base of the

jet is $\sim 1.3 - 2.7$ pc upstream of the mm-wave “core” depending on a toroidal or poloidal magnetic field configuration.

ID	n	ΔR_{BH} (mas)	ΔR_{BH} (pc)	B_{BLR} (G)	B_{BH} (G)
2010.36 $B_{\text{equi}, C1-C2}$	1	≤ 2.65	≤ 214.3	≤ 137	≤ 68868
2010.36 $B_{\text{equi}, C1-C2}$	2	≤ 1.27	≤ 103.2	≤ 8	≤ 182

TABLE 4.12: An overview derived properties from magnetic fields in 0836+710.

4.4.4 3C 273

4.4.4.1 Introduction

The well studied blazar 3C 273 ($z = 0.158$) is one of the most luminous blazars in the sample and the first quasar ever identified. [Jorstad et al. \(2005\)](#) and [Attridge et al. \(2005\)](#) both found that the VLBI “core” was very unpolarised, although downstream components could be very polarised. [Lobanov & Zensus \(2001\)](#) using space-VLBI observations to show a double-helix structure for the first time in the jet of a quasar. The source was analysed by [Krichbaum et al. \(2001\)](#) at mm-wavelengths and component accelerations were detected.

3C 273 has a very complex jet structure and to aid analysis, after fitting the “core” region, a heavy uv-taper was applied and model-fit components were fitted to that, allowing for easier comparisons of jet features between frequency bands.

Epoch ₈₆	Epoch ₄₃	$S_{\text{tot},15}$	$S_{\text{tot},43}$	$S_{\text{tot},86}$	$S_{\text{tot},230}$
2008.78	2008.87	29.9 ± 0.02	16.5 ± 0.2	16.1 ± 0.2	10.1 ± 0.1
2009.44	2009.55	27.8 ± 0.05	24.3 ± 0.2	19.1 ± 0.3	9.3 ± 0.2
2009.78	2009.79	28.6 ± 0.02	$20.1^* \pm 0.2$	18.4 ± 0.2	12.5 ± 0.7
2010.36	2010.38	29.6 ± 0.05	27.3 ± 0.2	16.2 ± 0.3	8.4 ± 0.2
2011.35	2011.39	24.1 ± 0.05	$10.8^* \pm 0.9$	11.3 ± 0.3	5.3 ± 0.3
2012.38	2012.40	16.6 ± 0.04	$10.4^* \pm 0.6$	7.85 ± 0.2	3.9 ± 0.2

TABLE 4.13: An overview of 3C 273 fluxes.* Large gap in 7 mm single-dish measurements, 9 mm flux measurement is used.

4.4.4.2 Core Identification

ID	S_{43} (Jy)	S_{86} (Jy)	α	θ_{43} (mas)	θ_{86} (mas)	$T_{B,43}$ ($\times 10^{11}$ K)	$T_{B,86}$ ($\times 10^{11}$ K)
C1	3.80 ± 0.22	5.03 ± 0.36	0.4 ± 0.1	0.07 ± 0.01	0.08 ± 0.01	1.72 ± 0.26	2.01 ± 0.30
C2	4.09 ± 0.44	3.04 ± 0.28	-0.5 ± 0.2	0.09 ± 0.01	0.11 ± 0.01	4.38 ± 0.71	2.42 ± 0.36

TABLE 4.14: An overview of 3C 273 averaged values.

In Table 4.14, we summarise the averaged quantities for the quasi-stationary components C1 and C2 in 3C 273. Component C2 has the highest brightness temperature, and comparable flux densities and sizes with C1. However, as all components are seen travelling away from C2 and as with all sources in this

sample, the source is highly beamed, which makes interpreting C1 as a counter-jet unlikely. Component C1 is on average optically thick and the component C2 is optically thin, as is normally expected. We therefore conclude that C1 is likely the “core” and C2 is a downstream quasi-stationary feature.

4.4.4.3 Morphology

In Fig. 4.20 - Fig. 4.25, 7 mm maps convolved with a 0.15 mas circular beam, 3 mm maps with a natural beam and 3 mm maps convolved with a 0.05 mas beam are presented. The morphologies between the frequency bands are broadly consistent. In all epochs, many components could be cross-identified between frequency bands. While there are many more details visible in 3 mm CLEAN maps, the UV-taper applied during model-fitting averages out some of these differences, although extended travelling components are still resolved into several sub-components.

In the epoch 2009.44 (Fig. 4.21), we see structure upstream of what is identified as the “core” and then in 2009.77 (Fig. 4.22), we can see an extension downstream of the “core” in both 7 mm and 3 mm maps. There are three possible interpretations: 1) the “core” was misidentified and the upstream component is the “core”; 2) it is an imaging artifact and; 3) there is emission upstream of the VLBI “core”. We consider the first scenario as unlikely, because if this feature is set as the reference point, the location of component C2 would be very different compared with previous epochs, placing component C2 (~ 0.3 mas rather than its usual ~ 0.15 mas). The second option cannot be ruled out, but the feature is seen in both 7 mm and 3 mm maps in a consistent location, relative to other components. This leads us to conclude that the emission is likely real and upstream of the VLBI “core”.

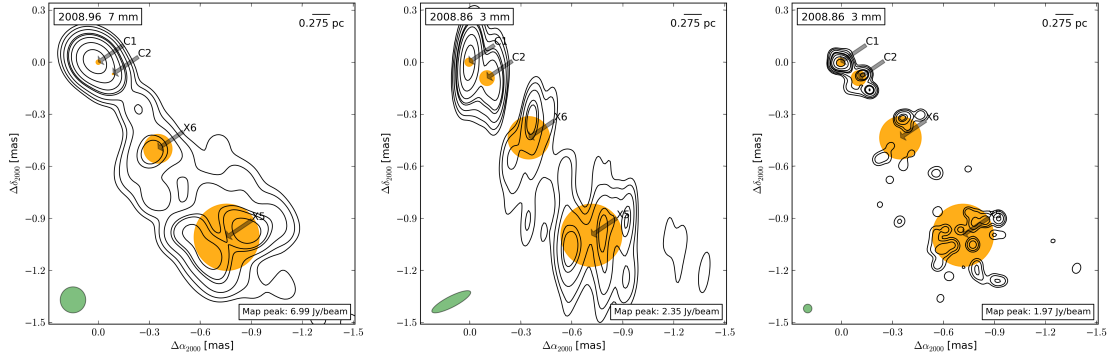


FIGURE 4.20: VLBI map of 3C 273 in 2008.78. Contours: -1, 1, 2, 4, 8, 16, 32, 64%. From left to right is (i) 7 mm map resolved with circular 0.15 mas beam; (ii) natural beam 3 mm map and; (iii) 3 mm map resolved with circular 0.05 mas beam.

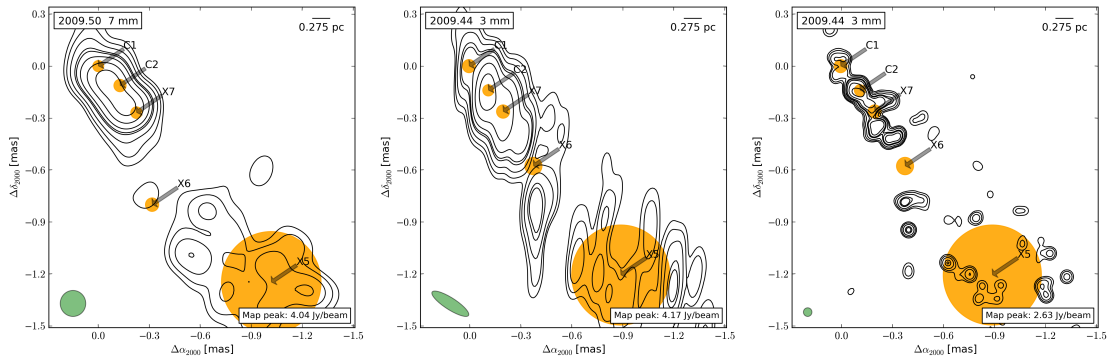


FIGURE 4.21: VLBI map of 3C 273 in 2009.35. Contours: -1, 1, 2, 4, 8, 16, 32, 64%. From left to right is (i) 7 mm map resolved with circular 0.15 mas beam; (ii) natural beam 3 mm map and; (iii) 3 mm map resolved with circular 0.05 mas beam.

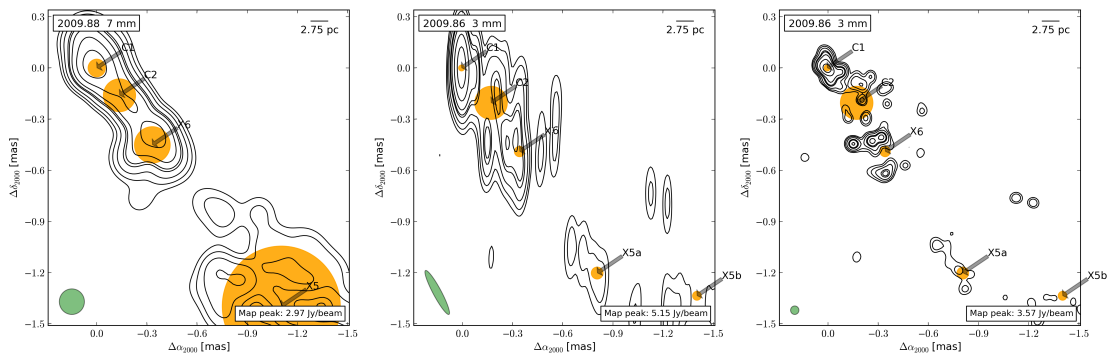


FIGURE 4.22: VLBI map of 3C 273 in 2009.86. Contours: -1, 1, 2, 4, 8, 16, 32, 64%. From left to right is (i) 7 mm map resolved with circular 0.15 mas beam; (ii) natural beam 3 mm map and; (iii) 3 mm map resolved with circular 0.05 mas beam.

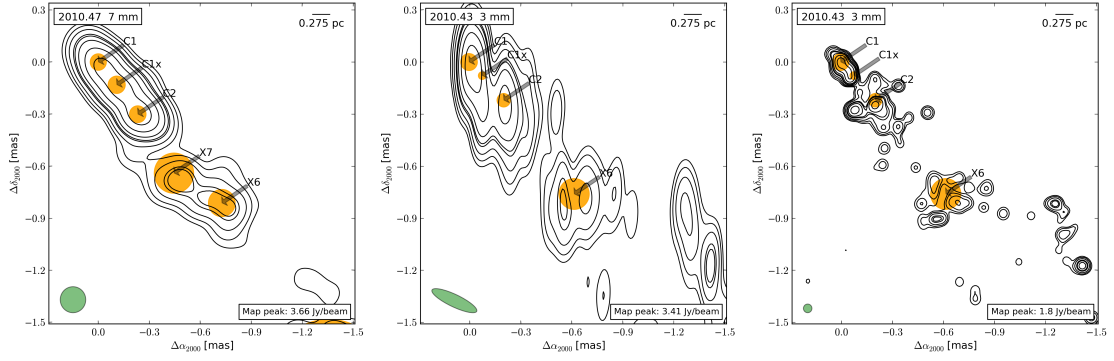


FIGURE 4.23: VLBI map of 3C 273 in 2010.36. Contours: -1, 1, 2, 4, 8, 16, 32, 64%. From left to right is (i) 7 mm map resolved with circular 0.15 mas beam; (ii) natural beam 3 mm map and; (iii) 3 mm map resolved with circular 0.05 mas beam.

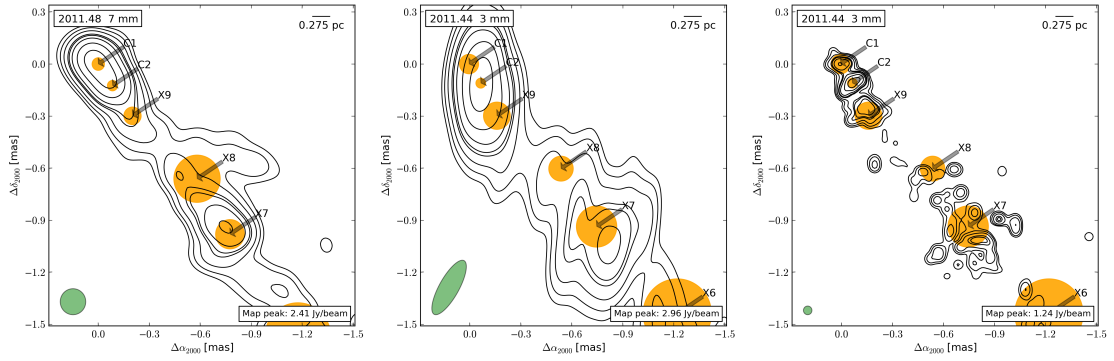


FIGURE 4.24: VLBI map of 3C 273 in 2011.35. Contours: -1, 1, 2, 4, 8, 16, 32, 64%. From left to right is (i) 7 mm map resolved with circular 0.15 mas beam; (ii) natural beam 3 mm map and; (iii) 3 mm map resolved with circular 0.05 mas beam.

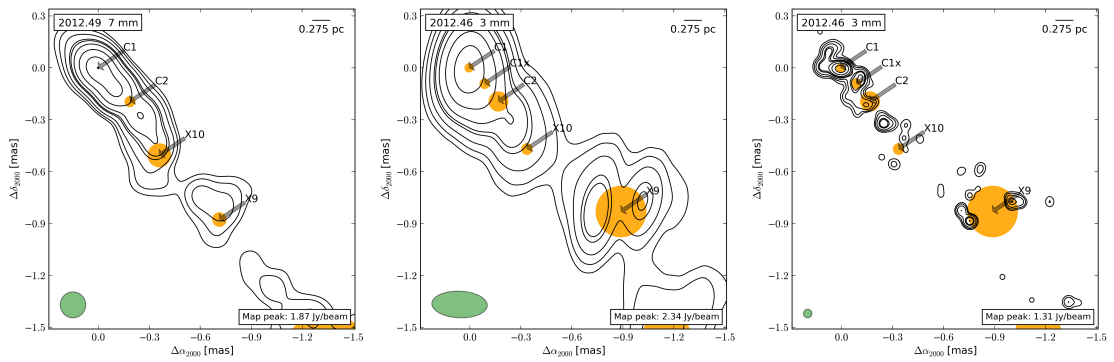


FIGURE 4.25: VLBI map of 3C 273 in 2012.38. Contours: -1, 1, 2, 4, 8, 16, 32, 64%. From left to right is (i) 7 mm map resolved with circular 0.15 mas beam; (ii) natural beam 3 mm map and; (iii) 3 mm map resolved with circular 0.05 mas beam.

4.4.4.4 Spectral Properties

The time evolution of the spectral properties of stationary features in 3C 273 can be seen in Fig. 4.26. The “core” (component C1) exhibits an optically thick spectrum $\alpha \sim 0 - 1$ that rises with frequency, from 2008.79 until the most recent epoch, 2012.49, where it exhibits an optically thin spectrum of $\alpha \sim -0.5$. The quasi-stationary feature C2 exhibits an optically thick spectrum similar to the “core” in 2008.79 and 2009.78, but then exhibits an optically thin spectrum in all subsequent epochs.

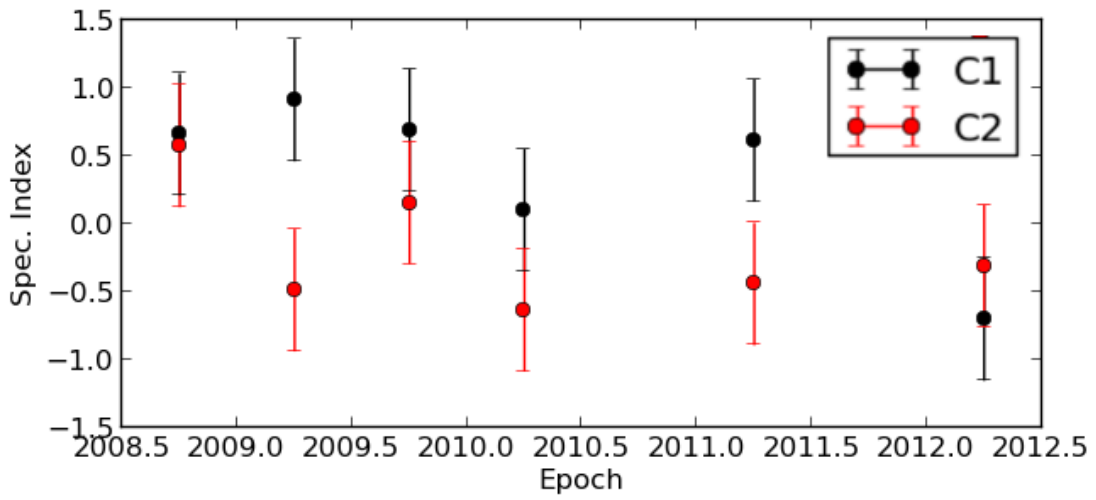


FIGURE 4.26: The spectral index evolution of 3C 273, $S \propto \nu^\alpha$.

4.4.4.5 Kinematics

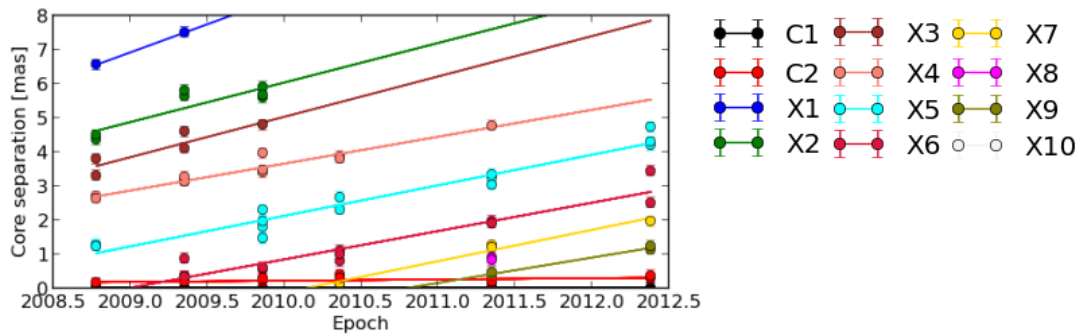


FIGURE 4.27: Component ejections in 3C 273.

In Table 4.15, the kinematics for 3C 273 are summarised and in Fig. 4.27, the “core” separation as a function of time is plotted for each component. Many

travelling components having been resolved into several sub-components. When sub-components were detected, the fit for the component speeds was made using a weighted average over all sub-components. Some components are consistent with being trailing components (see: Section 4.3.4). Components X1 and X2 have almost the same “core” ejection time and X2 is travelling $\sim \sqrt{2}$ the speed of component X1. Similar behaviour was exhibited between components X3 and X4. Component X5 has a “core” ejection time consistent with that of the VLBI component labelled 24 in MOJAVE data (2007.392 ± 0.062) and similar speed ($\beta_{\text{app}} = 7.32 \pm 0.25 c$ (Lister et al. 2013)). The speed of component X7 is consistent with being component C1x in 2010.47 (Fig. 4.23). No significant differences in speeds between 43 GHz and 86 GHz were detected.

The speeds detected are broadly consistent with those reported by Jorstad et al. (2005), but it is interesting that components detected at larger “core” separations (e.g. X1, X2) have higher speeds than those detected earlier and those reported in Jorstad et al. (2005), suggesting acceleration in the jet, consistent with the results of Krichbaum et al. (2001), where the acceleration was interpreted as due to the jet bending into our line-of-sight. The speed of component X1 is comparable with the highest speeds reported of $\beta_{\text{app}} = 14.9 c$, reported by Lister et al. (2013). For further calculations, we adopt the values of $\delta \approx 9.0$, $\Gamma \approx 10.6$ and $\theta_0 \approx 6.1^\circ$ from Jorstad et al. (2005).

ID	μ (mas/yr)	β_{app}	Γ_{min}	δ_{min}	θ_{crit} ($^\circ$)	t_0 (yr)
X1	1.64 ± 0.39	14.3 ± 3.6	15.9 ± 3.4	14.0 ± 3.3	4.1 ± 1.7	2004.84 ± 0.35
X2	1.16 ± 0.42	10.0 ± 3.2	11.1 ± 2.1	9.9 ± 2.2	5.2 ± 2.6	2004.92 ± 0.51
X3	1.18 ± 0.21	10.1 ± 1.8	11.2 ± 1.1	10.0 ± 1.2	5.1 ± 1.6	2005.81 ± 0.32
X4	0.79 ± 0.12	6.8 ± 0.9	7.5 ± 1.8	6.7 ± 0.7	5.9 ± 0.9	2005.65 ± 0.24
X5	0.89 ± 0.13	7.5 ± 0.8	7.8 ± 1.6	7.4 ± 0.9	5.5 ± 0.8	2007.37 ± 0.19
X6	0.83 ± 0.09	7.2 ± 0.9	7.5 ± 1.1	7.3 ± 1.1	5.7 ± 0.6	2009.21 ± 0.24
X7	0.92 ± 0.17	7.8 ± 1.8	8.0 ± 1.8	7.8 ± 1.7	5.4 ± 1.1	2010.28 ± 0.30
X9	0.74 ± 0.41	6.5 ± 2.1	7.3 ± 2.4	6.5 ± 2.6	6.1 ± 2.5	2010.82 ± 0.42

TABLE 4.15: An overview of 3C 273 kinematics.

4.4.4.6 Light-Curves and Ejection Relations

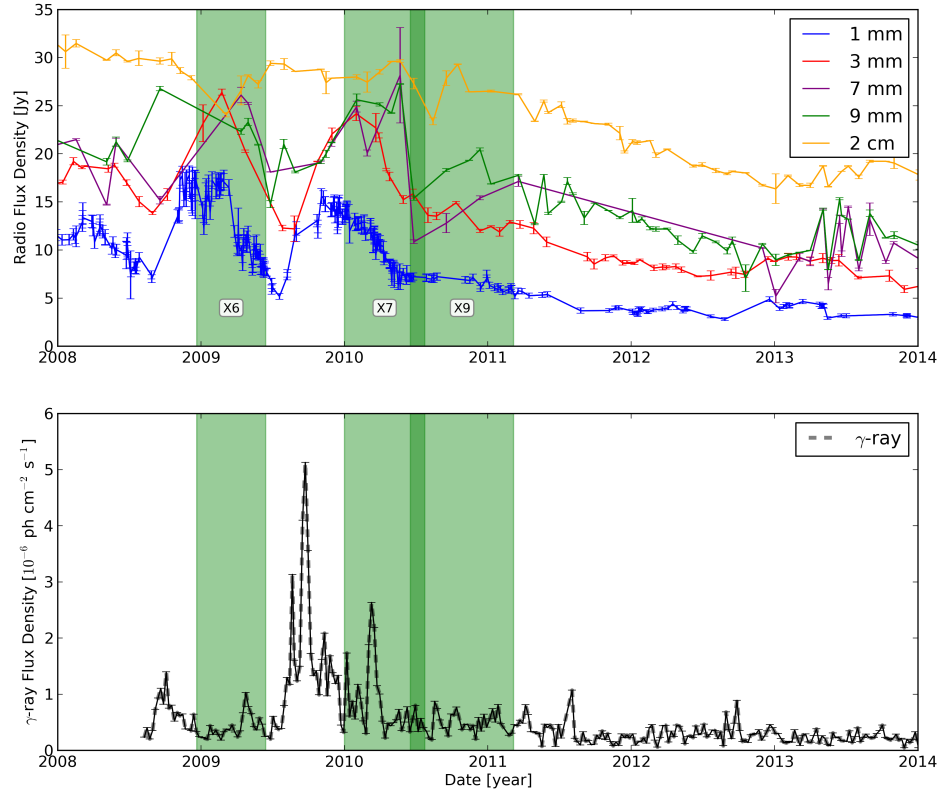


FIGURE 4.28: Radio and γ -ray light-curves from 2008.0-2014.0 in 3C 273.

In Fig. 4.28, we display the radio and γ -ray spectrum from 2008.0 until 2014.0. We can see three radio peaks at mm frequencies, occurring in approximately early 2008, early 2009 and late 2009 to early 2010, with mm flux densities fading until the most recent data. The first flare peaks before we have VLBI or γ -ray data, however. The second, most prominent radio flare, unfortunately peaks between the 2008.78 and 2009.44 epochs. The third radio flare peaks in early 2010, and is once again between observations. There is one prominent γ -ray flare in late 2009, with a smaller flare following it in early 2010. The γ -ray flare precedes the peak of the mm-wave radio peak, but onset at similar times, consistent with behaviour reported by others (e.g. [Valtaoja & Terasranta 1995](#)). After this, there is considerable “flickering” before returning to quiescence in mid 2011.

In 2009.38 (Fig. 4.21), we saw possible emission upstream of the VLBI “core”. In 2009.78 (Fig. 4.22), there is an extension downstream of the VLBI “core”. An

epoch later in 2010.47 (Fig. 4.23), we see a component (C1x) detected between the “core” (C1) and component C2, that was tentatively identified with travelling component X7. The most prominent γ -ray flare peaks near when we see the extension of the “core” downstream in 2009.78. During this time, the “core” exhibits an optically thin spectrum. If component X7 is correctly identified, this strongly suggest that the γ -ray flare originates in the “core” region, due to the passing of component X7.

4.4.4.7 Magnetic Fields

In Table A.3, we see the derived magnetic field estimates for 3C 273. As with the other sources analysed in this chapter, the derived limits on the magnetic field from synchrotron self-absorption (SSA) are much higher than those from equipartition calculations. The magnetic fields derived through both calculations are very strong in comparison with other sources, with occasionally $B_{\text{equi}} \geq 2$ G. On average, upper limits on the magnetic field strength are derived and these limits are higher in the quasi-stationary feature C2.

4.4.4.8 Distance to Black Hole and Magnetic Field Estimates

In 3C 273, several epochs produced limits where we could compute an estimate of how the magnetic field decreases down the jet. The results of this analysis are given in Table 4.16. We can see that there are widely varying estimates of the distance to the black hole and magnetic field strength. It appears that flaring activity in the source can effect the results considerably, particularly on an epoch-to-epoch basis. Assuming a toroidal magnetic field, on average, the equipartition magnetic field is ≤ 1.8 G in the BLR and ≤ 900 G at the jet apex.

4.4.4.9 Location of γ -ray emitting regions

If as described in Section 4.4.4.6, the γ -rays are being produced in the “core” region, we can estimate the location of the “core” from the jet base. SSA calculations would place the “core” within at least 0.5 pc of the central engine,

depending on the magnetic field geometry assumed, but as discussed in Section 4.4.4.7, the SSA calculations may be less reliable than equipartition calculations. Under equipartition, the “core” and hence the γ -ray emitting region, is ≤ 8 pc or ≤ 3 pc, depending on the chosen magnetic field geometry.

ID	n	ΔR_{BH} (mas)	ΔR_{BH} (pc)	B_{BLR} (G)	B_{BH} (G)
2008.78 $B_{\text{equi,C1-X6}}$	1	≤ 0.08	≤ 2.1	≤ 30.9	≤ 9.6
2008.78 $B_{\text{equi,C1-X6}}$	2	≤ 0.01	≤ 0.3	≤ 2.2	≤ 2.8
2008.78 $B_{\text{equi,C2-X6}}$	1	≤ 0.11	≤ 3.1	≤ 21.9	≤ 6.8
2008.78 $B_{\text{equi,C2-X6}}$	2	≤ 0.03	≤ 0.9	≤ 2.5	≤ 3.1
2009.35 $B_{\text{equi,C1-X5}}$	1	≤ 0.31	≤ 8.5	≤ 67.6	≤ 21.1
2009.35 $B_{\text{equi,C1-X5}}$	2	≤ 0.04	≤ 1.2	≤ 3.1	≤ 3.9
2009.35 $B_{\text{SSA,X6-X5}}$	1	≤ 0.2	≤ 5.6	≤ 44.1	≤ 13.7
2009.35 $B_{\text{SSA,X6-X5}}$	2	≤ 0.03	≤ 0.8	≤ 2.5	≤ 3.1
2010.36 $B_{\text{equi,C1-C2}}$	1	≤ 4.11	≤ 113.1	≤ 864.1	≤ 269.4
2010.36 $B_{\text{equi,C1-C2}}$	2	≤ 1.97	≤ 54.2	≤ 20.4	≤ 25.4
AVER $B_{\text{SSA,C1-C2}}$	1	≤ 0.01	≤ 0.5	≤ 2.6	≤ 1306.8
AVER $B_{\text{SSA,C1-C2}}$	2	≤ 0.01	≤ 0.01	≤ 0.5	≤ 10.2
AVER $B_{\text{equi,C1-C2}}$	1	≤ 0.24	≤ 7.9	≤ 1.8	≤ 903.0
AVER $B_{\text{equi,C1-C2}}$	2	≤ 0.09	≤ 3.0	≤ 0.8	≤ 18.5

TABLE 4.16: An overview derived properties from magnetic fields in 3C 273.

4.4.5 BL Lacertae

4.4.5.1 Introduction

BL Lacertae (BL Lac) is the archetypal BL Lac object, after which the source class is named. [Jorstad et al. \(2005\)](#) showed that the inner 0.2 mas of BL Lac is variable, with [Stirling et al. \(2003\)](#) suggested that it exhibits a precessing jet with a ~ 2 yr period. They also reported that component trajectories appear to exhibit relatively straight trajectories near the “core”, becoming more helical only further downstream. Follow up studies by [Mutel & Denn \(2005\)](#) and [Caproni et al. \(2013\)](#) appear to confirm this finding, although the latter found the period to be ~ 12 yr. This was then analysed further by [Cohen et al. \(2014\)](#), which found that the PA to be variable but not periodic. Additionally, they found a quasi-stationary feature at ~ 0.26 mas in 15 GHz maps and conclude that this feature is a recollimation shock.

Epoch ₈₆	Epoch ₄₃	$S_{\text{tot},15}$	$S_{\text{tot},43}$	$S_{\text{tot},86}$	$S_{\text{tot},230}$
2009.35	2009.41	2.7 ± 0.2	3.3 ± 0.2	4.2 ± 0.2	3.2 ± 0.2
2009.77	2009.79	4.3 ± 0.1	4.3 ± 0.3	4.6 ± 0.3	3.2 ± 0.2
2010.35	2010.38	4.2 ± 0.2	$4.3^* \pm 0.6$	4.3 ± 0.3	3.4 ± 0.2
2011.35	2011.38	4.4 ± 0.1	$4.3^* \pm 0.5$	4.5 ± 0.4	3.9 ± 0.2
2011.77	2011.79	4.7 ± 0.4	$5.8^* \pm 0.6$	6.6 ± 0.3	5.5 ± 0.5
2012.38	2012.40	6.1 ± 0.1	$6.4^* \pm 0.6$	6.7 ± 0.3	6.1 ± 0.5

TABLE 4.17: An overview of BL Lac.* Large gap in 7 mm single-dish measurements, 9 mm flux measurement is used..

4.4.5.2 Core Identification

ID	S_{43} (Jy)	S_{86} (Jy)	α	θ_{43} (mas)	θ_{86} (mas)	$T_{B,43}$ ($\times 10^{11}$ K)	$T_{B,86}$ ($\times 10^{11}$ K)
C1	1.91 ± 0.13	1.85 ± 0.14	0 ± 0.2	0.02 ± 0.01	0.02 ± 0.01	31.1 ± 4.7	39.4 ± 5.8
C1a	0.94 ± 0.05	0.90 ± 0.14	0.1 ± 0.2	0.04 ± 0.01	0.02 ± 0.01	5.1 ± 0.8	26.2 ± 3.8
C2	0.83 ± 0.07	0.59 ± 0.02	0.5 ± 0.1	0.07 ± 0.01	0.04 ± 0.01	1.7 ± 0.3	3.0 ± 0.5
C3	0.75 ± 0.10	0.82 ± 0.12	-0.1 ± 0.2	0.08 ± 0.01	0.09 ± 0.01	0.3 ± 0.1	0.3 ± 0.1

TABLE 4.18: An overview of BL Lac averaged values.

In Table 4.18, we present the averaged quantities in BL Lacertae. It comprises three or possibly four quasi-stationary components, C1, C1a, C2 and C3. Component C1 has the highest brightness temperature, a higher average flux density and a smaller average size at all frequencies. As all travelling components are

observed to be travelling away from component C3 and C1 exhibits the highest brightness temperatures, we conclude that C1 is likely the “core”. Other downstream features that are persistently detected in most epochs and are not seen to vary largely in “core” separation are interpreted as quasi-stationary features. All components exhibit spectra consistent with being optically thick, on average.

4.4.5.3 Morphology

We label the inner components C1-C3 with C1 being the northernmost component and reference all observations to the northern-most component C1. Components C1-C3 appear to be stationary and visible in all epochs. In some epochs, a fourth component is detected between C1 and C2, labelled C1a. Structure beyond C3 is defined as extended structure components are labelled accordingly.

No 3 mm observations of BL Lac were performed in 2008.78 and data quality issues forces us to not analyse the source in 2011.77. Consistent with all other sources analysed, the morphology is consistent between 7 mm and 3 mm, with the 3 mm maps showing additional levels of detail owing to the higher resolution.

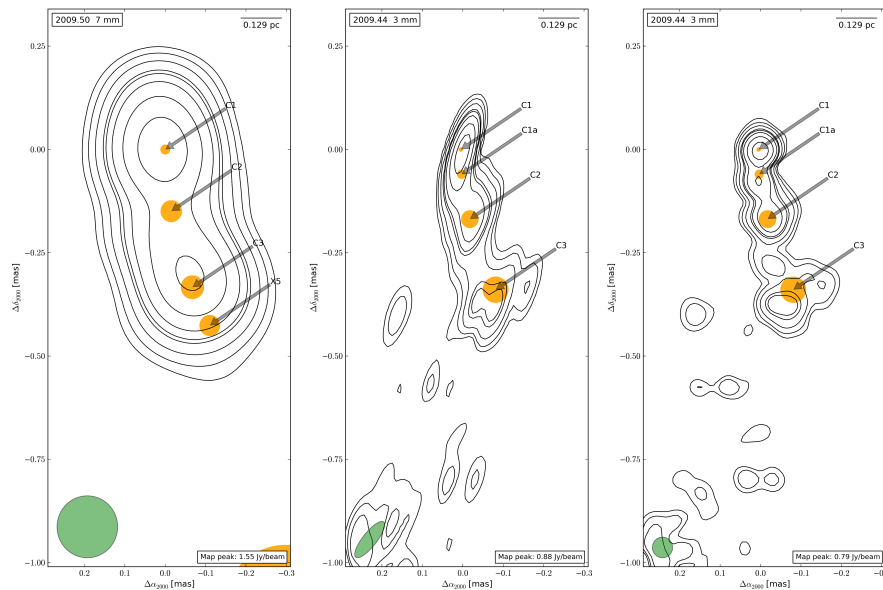


FIGURE 4.29: VLBI map of BL Lacertae in 2009.35. Contours: -1, 1, 2, 4, 8, 16, 32, 64%. From left to right is (i) 7 mm map resolved with circular 0.15 mas beam; (ii) natural beam 3 mm map and; (iii) 3 mm map resolved with circular 0.05 mas beam.

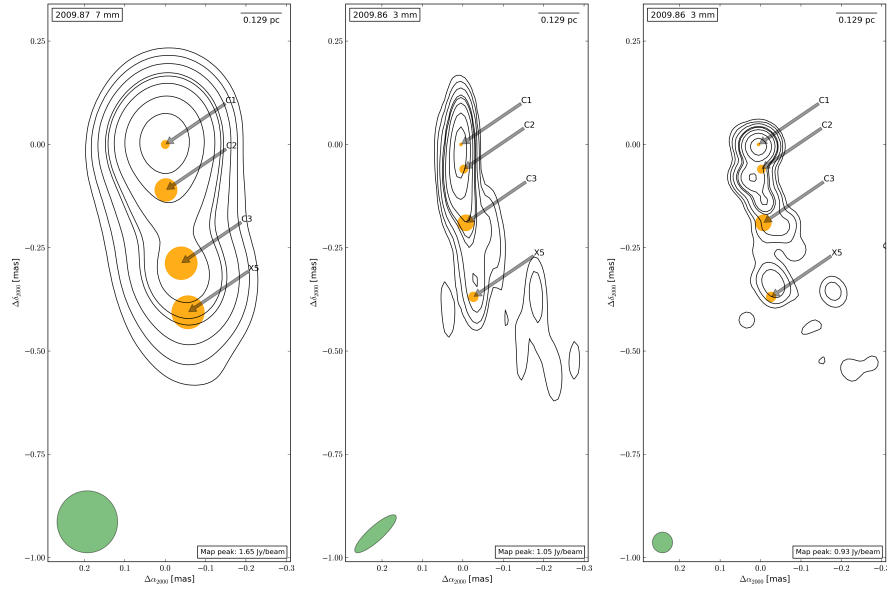


FIGURE 4.30: VLBI map of BL Lacertae in 2009.86. Contours: -1, 1, 2, 4, 8, 16, 32, 64%. From left to right is (i) 7 mm map resolved with circular 0.15 mas beam; (ii) natural beam 3 mm map and; (iii) 3 mm map resolved with circular 0.05 mas beam.

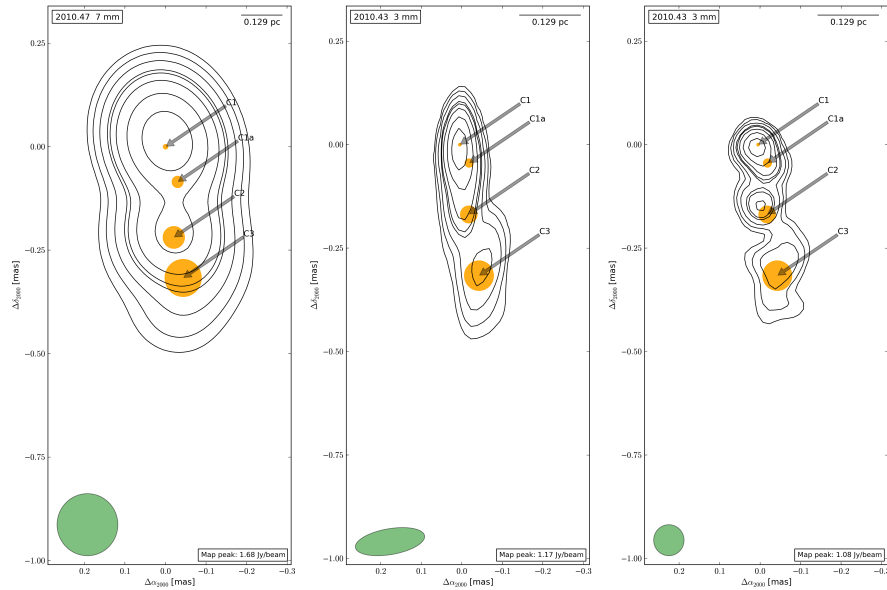


FIGURE 4.31: VLBI map of BL Lacertae in 2010.36. Contours: -1, 1, 2, 4, 8, 16, 32, 64%. From left to right is (i) 7 mm map resolved with circular 0.15 mas beam; (ii) natural beam 3 mm map and; (iii) 3 mm map resolved with circular 0.05 mas beam.

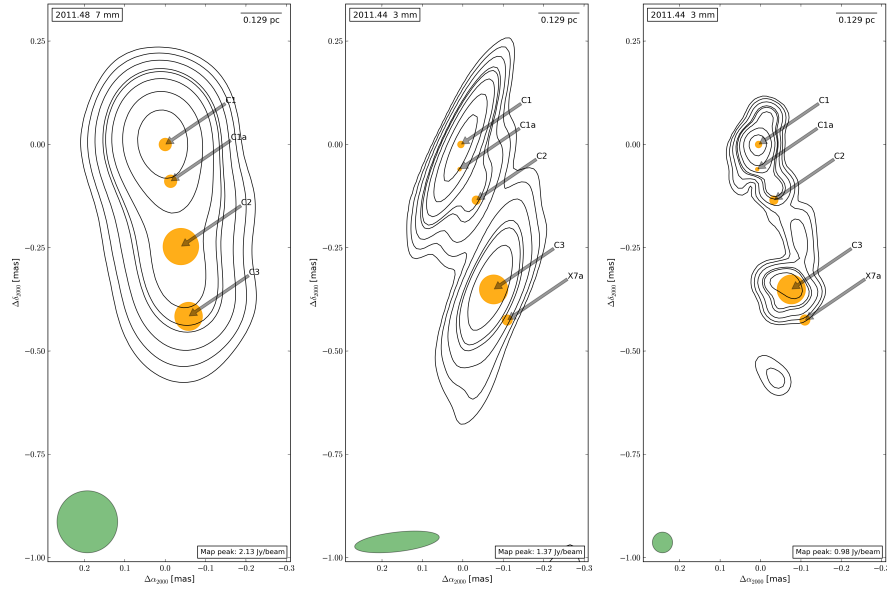


FIGURE 4.32: VLBI map of BL Lacertae in 2011.35. Contours: -1, 1, 2, 4, 8, 16, 32, 64%. From left to right is (i) 7 mm map resolved with circular 0.15 mas beam; (ii) natural beam 3 mm map and; (iii) 3 mm map resolved with circular 0.05 mas beam.

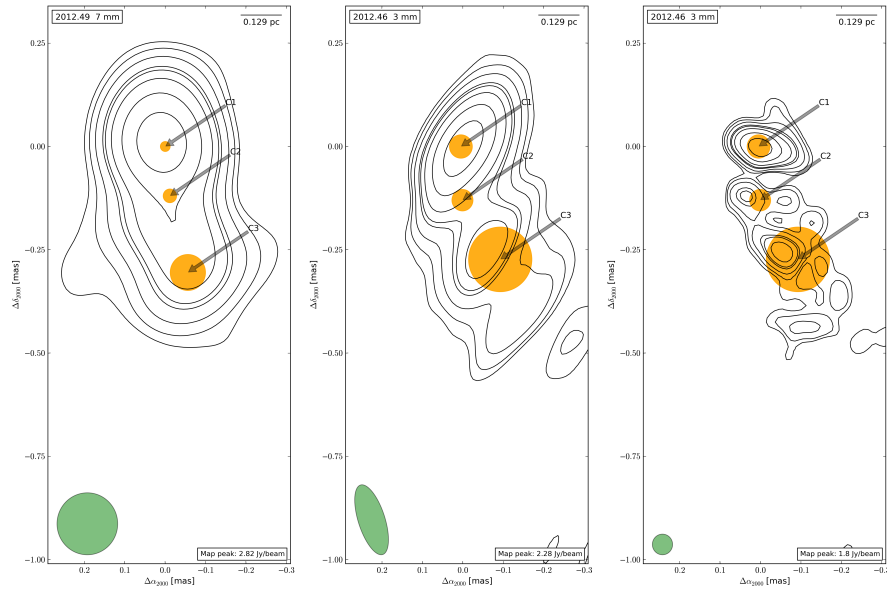


FIGURE 4.33: VLBI map of BL Lacertae in 2012.38. Contours: -1, 1, 2, 4, 8, 16, 32, 64%. From left to right is (i) 7 mm map resolved with circular 0.15 mas beam; (ii) natural beam 3 mm map and; (iii) 3 mm map resolved with circular 0.05 mas beam.

4.4.5.4 Spectral Properties

The evolution of the spectral properties of stationary features can be seen in Fig. 4.34. In 2009.44, both the “core” (C1) and component C2 exhibit an optically thick (flux density rising with frequency) spectrum of $\alpha \sim 0.3$. Approximately 6 months later in 2009.78, the “core” exhibits an optically thin spectrum of $\alpha \sim -0.5$, while C2 continues to exhibit a thick spectrum. On 2010.44, both C1 and C2 exhibit an approximately flat spectrum. In 2011.44, the “core” is has a flat spectrum while C2 now has an optically thin spectrum of $\alpha \sim -0.7$, which it continues to exhibit until 2012.38. Component C3 exhibits an optically thick spectrum in all epochs except for 2009.44 where it exhibits a slightly thin spectrum of $\alpha \sim -0.3$. Component X2 exhibits a steepening (becoming increasingly optically thin) trend with time.

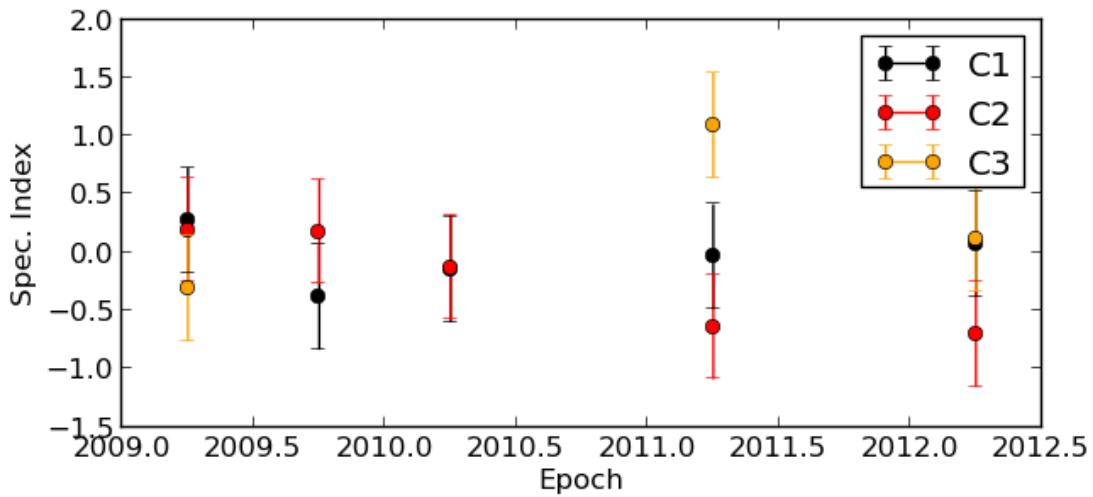


FIGURE 4.34: The spectral index evolution of BL Lac

4.4.5.5 Kinematics

The kinematics derived from this source are shown in Table 4.19 and component “core” separation as a function of time shown in Fig. 4.19. Speeds measured here are consistent with those previously reported, although slower than the highest speeds reported in the MOJAVE sample ($\beta_{\text{app,max}} \approx 9$). For derived quantities, we adopt the values from Jorstad et al. (2005) of $\delta \approx 7.2$, $\Gamma \approx 7.0$ and $\theta_0 \approx 7.7^\circ$.

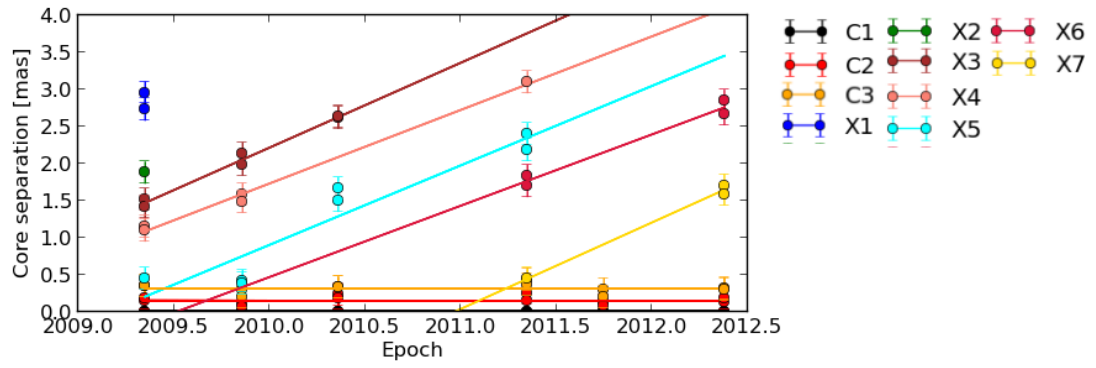


FIGURE 4.35: Fitted components as a function of “core” separation in BL Lacertae.

ID	μ (mas/yr)	β_{app}	Γ	δ	θ_0 ($^\circ$)	t_0 (yr)
X3	1.37 ± 0.27	5.88 ± 1.13	13.4 ± 6.1	6.1 ± 2.5	9.3 ± 2.3	2008.33 ± 0.12
X4	1.10 ± 0.54	4.62 ± 2.10	4.8 ± 0.7	4.8 ± 0.7	11.8 ± 8.8	2008.64 ± 0.31
X5	1.01 ± 0.85	4.20 ± 3.36	4.3 ± 0.6	4.4 ± 0.7	13.0 ± 8.8	2009.25 ± 0.17
X6	1.05 ± 0.21	4.20 ± 0.88	7.9 ± 3.6	4.8 ± 1.8	12.0 ± 3.2	2009.59 ± 0.19
X7	1.16 ± 0.41	4.37 ± 1.48	8.2 ± 3.7	4.8 ± 2.2	11.5 ± 4.2	2011.02 ± 0.34

TABLE 4.19: An overview of BL Lac kinematics.

4.4.5.6 Light-Curves and Ejection Relations

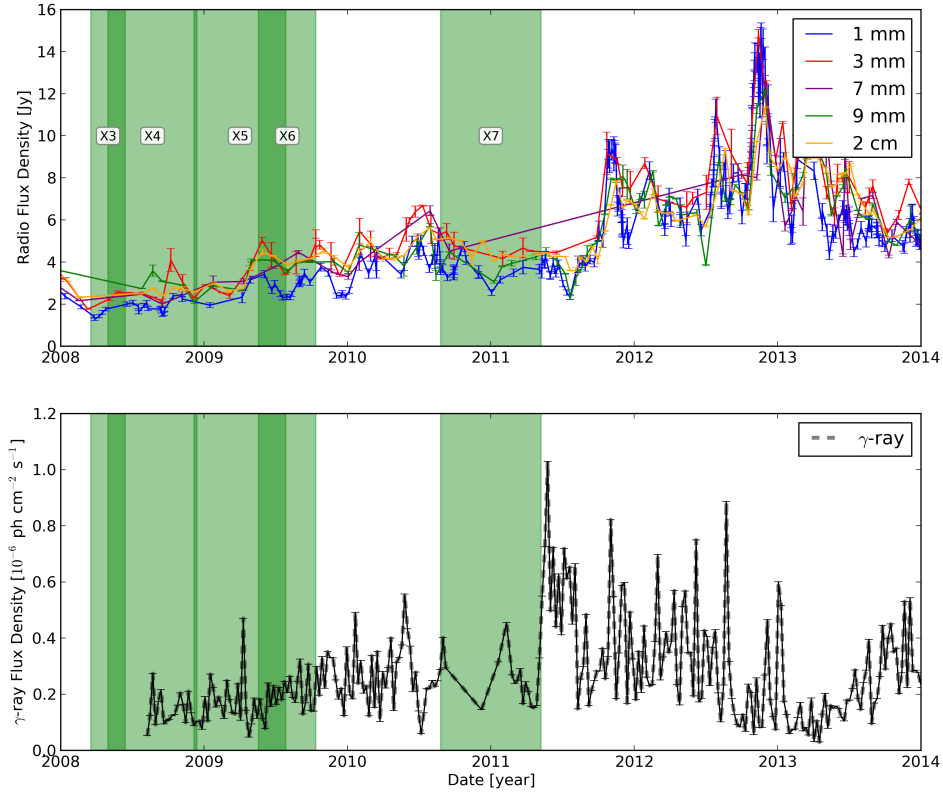


FIGURE 4.36: Radio and γ -ray light-curves from 2008.0-2014.0 in BL Lacertae.

In Fig. 4.36 we see a variable, but slowly rising mm-wave flux density from 2008 until mid 2011, where the fluxes drop to approximately 3 Jy until late 2011 and a large flare begins. During the following period, BL Lac exhibits elevated flux density levels and considerable flaring, culminating in a large peak in late 2012. From then until the most recent data, the flux density was decreasing. The radio light curves are interesting in that the total intensity spectrum stays remarkably flat during the entire flaring period. In γ -rays, there was relatively minor flaring activity until mid-2010, consistent with the radio flaring at this time. Similarly, when the radio flux densities increased dramatically in late 2011, γ -rays did also. After ~ 2011.5 , The γ -rays stayed extremely variable until early 2013, also consistent with the radio light curves.

Concentrating first on the period 2009-2011, there are five radio peaks from i) late 2008, ii) mid 2009; iii) late 2009; iv) early 2010 and v) early-mid 2010. This

period could be considered non-minor, when compared to later activity, but the peak in early-mid 2010 is still ~ 3 times higher than in early 2008. Also, γ -ray flaring occurs at similar times to the later four peaks of the radio flares. There are two component ejections relevant for this period, X5 and X6. Component X5's estimated t_0 time coincides closely with the first radio flare in late 2008.

We note with interest that the “core” exhibits an optically thin spectrum near in time with the estimated “core” ejection time of component X7 and immediately preceding a large γ -ray flare. The “core” ejection time for component X7 coincides with the *onset* of both the γ -ray and radio flares beginning in early 2011. This suggests that the large γ -ray flare of early 2011 originated in the “core” region.

4.4.5.7 Magnetic Fields

In Table A.4, the derived magnetic field estimates in BL Lacertae are presented. On average, upper limits on the equipartition magnetic fields B_{equi} are of the order $B_{\text{equi}} \sim 0.3 - 0.9$ G in the central quasi-stationary features. As with other sources, the magnetic fields derived from synchrotron self absorption (SSA) calculations can often be much stronger and seem to be less reliable without additional spectral information.

4.4.5.8 Distance to Black Hole and Magnetic Field Estimates

As there were no epochs where upper limits in the VLBI “core” were higher than downstream lower limits, we could not compute a minimum magnetic field difference. Hence, no estimates on the distance to the jet base could be determined.

4.5 Discussion

For the discussion of the magnetic fields (Section 4.5.4) and brightness temperatures (Section 4.5.4.2), in addition to the sources analysed previously in this chapter, the BL Lac OJ 287 is included in the analysis.

4.5.1 Morphology

All sources have a consistent sub-parsec structure when compared with 7 mm maps, except with finer details now being visible at 3 mm, suggesting that some sources are at least partially resolved at 3 mm. All sources broadly exhibit the standard “core-jet” morphology expected of blazars (e.g. Zensus et al. 1995). However, all sources analysed here appear to exhibit at least one stationary feature within 0.3 mas of the “core”, unlike other surveys at lower frequencies where only some sources exhibited stationary features (e.g. Jorstad et al. 2005), although this could be due to low sample statistics. Some sources (e.g. BL Lacertae, 0836+710) appear to have two or possibly more stationary features. These stationary features can also frequently exhibit higher flux densities and higher brightness temperatures than the “core” (C1), particularly during flare events, although on average they tend to have lower flux densities and brightness temperatures than in the “core”. The physical nature of these stationary features is discussed in greater detail in Section 5.5.3.

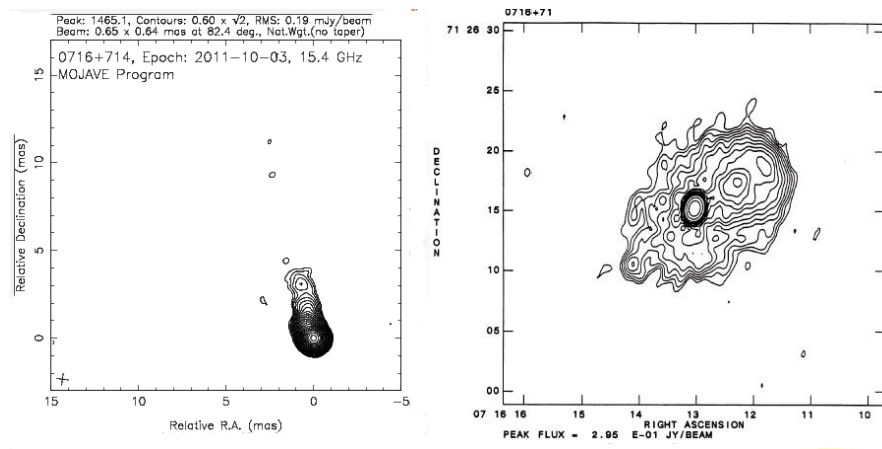


FIGURE 4.37: A comparison of the parsec scale (2 cm, VLBA) and kilo-parsec scale (20 cm, VLA) structure of the BL Lac 0716+714 (Lister et al. 2013; Antonucci et al. 1986).

While the morphology at 3 mm is largely consistent with 7 mm maps, the inner jet region at mm wavelengths is often considerably misaligned with the parsec or kilo-parsec scale jet morphology. For example, in 0716+714, the inner 0.1 mas in 3 mm maps (e.g. Fig. 4.5), compared with Fig. 4.37) has a considerably different position angle (PA) of $65.4^\circ \pm 5^\circ$, compared with component ejections and the parsec scale structure seen in MOJAVE maps, which exhibit PAs of $\sim 15^\circ$ (e.g. Lister et al. 2013) and radically misaligned with the Kpc scale structure (Antonucci et al. 1986). BL Lac and 0836+710 both exhibit misaligned

inner jet features ($\sim 10 - 20^\circ$), although not to the same extent, while 3C 273 is quite well aligned with its parsec scale jet structure ($\leq 10^\circ$). This behaviour has been seen previously, with a bent jet of $\sim 210^\circ$ reported by [Savolainen et al. \(2006\)](#) in the radio-loud quasar PKS2163+141, which was interpreted as being due to an intrinsic helical geometry. BL Lac sources could be more mis-aligned due to the observer seeing inside the helical inner-jet structure (e.g. [Conway & Murphy 1993](#)). Additionally, they suggested that the jet could be distorted by disturbances being externally driven into the jet and that our line-of-sight falls within the opening angle of the helix cone. Such an interpretation could explain the misalignments seen in the sources analysed.

4.5.2 Kinematics

The source kinematics were computed in all sources where components could be cross-identified in multiple epochs. No statistically significant speed difference was detected between 7 mm and 3 mm. All sources exhibit highly relativistic motion, consistent with Doppler boosted emission due to the sources being close to our line-of-sight. All sources exhibit variability in the observed apparent speeds (β_{app}), with the exception of 0836+710 which only had one travelling component detected. In Table 4.20, we see the maximum range of apparent component speeds for each source, but generally fall into the range of $\sim 30 - 50\%$. The highest variability is seen in 3C 273, which has a $45 \pm 27\%$ difference between the fastest and slowest component speed measured. This behaviour is also seen in the BL Lac source OJ287, which is analysed in the next chapter. Such behaviour may be interpreted as being due to components being ejected with different trajectories from the “core”, hence causing components to have different angles to the line-of-sight. This interpretation is discussed in more detail in Section 5.5.7. Alternatively, the variations could be due to changes in pattern speeds (e.g. [Hardee 2003](#)), or a combination of both.

Source	$\Delta\beta_{app}$
0716+714	$32 \pm 17\%$
3C 273	$45 \pm 27\%$
BL Lac	$26 \pm 25\%$

TABLE 4.20: Overview of the maximum difference in β_{app} observed.

4.5.2.1 Spectral Properties

All sources exhibit large degrees of spectral variability in the “core” region and downstream stationary features. That the “core” region can exhibit both an optically thin (flux density decreasing with increasing frequency) and an optically thick (flux density increasing with increasing frequency) is an important result, as it gives suggestions about the physical nature of the VLBI “core”. These periods of optically thin emission within the “core” and stationary features, often coincide with expected component ejection times (e.g. component X7 in 3C 273, discussed in more detail in Section 4.5.3), suggesting that the spectral changes (and γ -ray flaring) are due to interactions between travelling components passing the “core” or stationary feature. In 3C 273, the “core” region is optically thin in most epochs (Fig. 4.26), as is 0716+714 (Fig. 4.9) and 0836+714 (Fig. 4.17), while BL Lac exhibits an optically thin spectra in the “core” in one epoch, although the downstream component C2 is optically thin in later epochs (Fig. 4.34). The average “core” spectral index is $\alpha = 0.10 \pm 0.02$ and the average spectral index in downstream stationary features is $\alpha = -0.34 \pm 0.03$. Interestingly, in the case of 0716+714 and also BL Lacertae (both BL Lacs), the total intensity spectrum is mostly flat, but the spectral decompositions reveals a more complicated substructure.

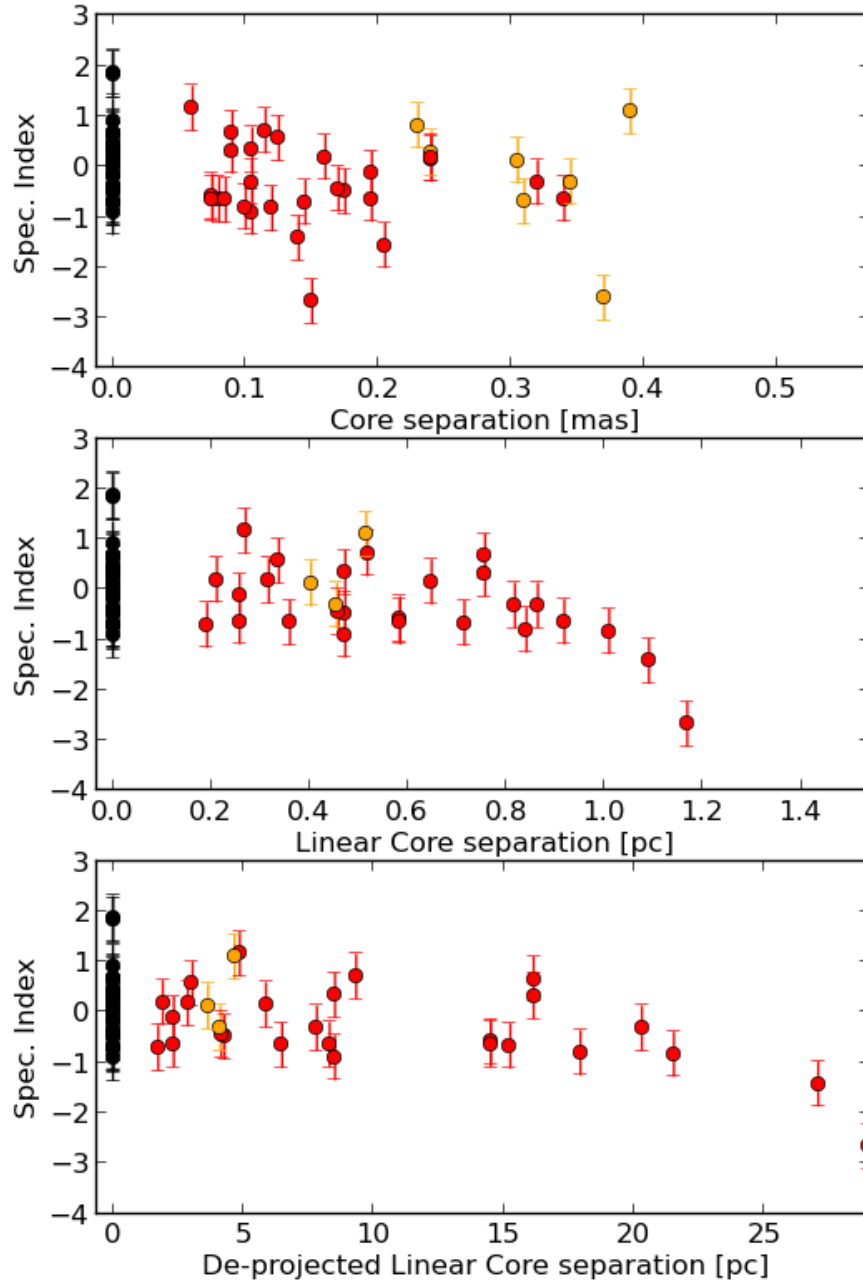


FIGURE 4.38: Spectral indices as a function of distance from the "core". From top to bottom, plots are (i) "core" separation in mas, (ii) projected "core" separation in parsecs and (iii) de-projected "core" separation in parsecs. Black symbols are for the "core" (C1), red and tellow symbols are for other downstream stationary features.

In Fig. 4.38, we can see how the spectral index of stationary features changes as a function of distance from the "core". As we can see, there appears to be a slight trend towards more optically thin spectra as a function of "core" separation. Such a steepening of the spectrum as a function of increased "core" separation could be explained by radiative losses due to synchrotron cooling

(Kardashev 1962), changes in the Lorentz factor down the jet, particle accelerations and decelerations within the jet causing changes in the underlying electron distribution or due to flux being resolved out in components at larger “core” separations. A study of the spectral evolution of the MOJAVE sample was performed by Hovatta et al. (2014). In that study, they found that the overall jet spectra steepen at about a rate of -0.001 to -0.004 per de-projected parsec. Performing a linear fit to all derived spectral indices finds the spectra steepening by -0.0009 ± 0.0004 per de-projected parsec, consistent with the MOJAVE results. Hovatta et al. (2014) concluded that the spectral steepening was most likely due to the evolution of the Lorentz factor or radiative losses, although they could not rule out changes in the underlying electron distribution. The effect being caused by collimation in jets in the MOJAVE sample could not be ruled out, but noted that other studies (e.g. Jorstad et al. 2005; Pushkarev et al. 2009; Clausen-Brown et al. 2013) showed conical jets at parsec scales. As described in Section 4.5.1, many stationary features are seen at sub-parsec scales, which are interpreted as either recollimation or oblique shocks (see: Section 5.5.3). However, if the spectral steepening were due to radiative losses, we would not expect to see jets at parsec or kilo-parsec scales and in all cases, jets are seen at these scales. Therefore, the most likely cause of the spectral steepening would be due to resolution effects, although we cannot rule out collimation or a combination of both.

4.5.3 Ejection Relations

Large radio and γ -ray flares have been seen in all sources analysed here. While ejection relations are discussed in more detail in the appropriate source sections, we nevertheless frequently find that flares can appear to be attributed to downstream stationary features as well as in the “core” region. This behaviour has been observed before (e.g. Agudo et al. 2011), but this is the first time it has been observed in several sources and possibly correlated with spectral variability.

On some occasions, a component can be detected between two stationary features. An example of this is in 3C 273, where a component was detected between the “core” (C1) and the downstream stationary feature (C2) (Fig. 4.23), immediately after the “core” became very bright and immediately before the downstream stationary feature exhibited a very high flux density (Fig. 4.24). Also,

in Fig. 4.21, the downstream component C2 is much brighter than the “core” in the 3 mm map. The backward extrapolated trajectory of component X7, ties in well with being tentatively cross identified with the component C1x and the spectral changes of the inner-jet. This behaviour is evident in all other sources analysed in this chapter and also in OJ 287, analysed in Chapter 5.

When discussing the relationship between radio and γ -ray flares with component ejections, one should be careful to discriminate between flare *onsets* and flare *peaks*. While we often see large time differences in the peaks between radio and γ -ray flares, the onset is often at a very similar time. (e.g. in 3C 273; Fig. 4.28 and BL Lac; Fig. 4.36). These flare onsets are often near in time with estimated “core” ejection times and spectral changes (see: Section 4.5.2.1). In a source such as 0716+714, the correlation between γ -ray variability and component ejections is more tentative, but has been analysed by Rani et al. (2014) and found a possible connection between γ -rays and position angle (PA) variability, suggesting that geometry is important in the appearance of γ -ray flares.

Perhaps most interestingly, component ejections, radio flares and sometimes γ -ray flares appear to be correlated with spectral changes within the “core” or downstream stationary features. As it’s highly unlikely that a stationary feature, such as the “core” or further downstream features could change from being optically thick to optically thin (or visa-verse) within months, we interpret the spectral changes as being due to optically thin travelling components passing optically thick shocked regions. This scenario is discussed in greater detail in Section 5.5.3.

4.5.4 Magnetic Fields

For the first time, the evolution of magnetic fields in jets both spatially and in time, using multiple methods has been investigated. These methods (from synchrotron self absorption (SSA) and equipartition) can then provide us a method to derive an estimated distance between the “core” and the jet base and also an estimate of the magnetic field strength at the jet base. Magnetic field estimates are primarily dependent the turnover frequency (ν_m) observed angular

size (θ_m) and the observed flux density S_m at the turnover frequency (see: Section 4.3.6 for more details).

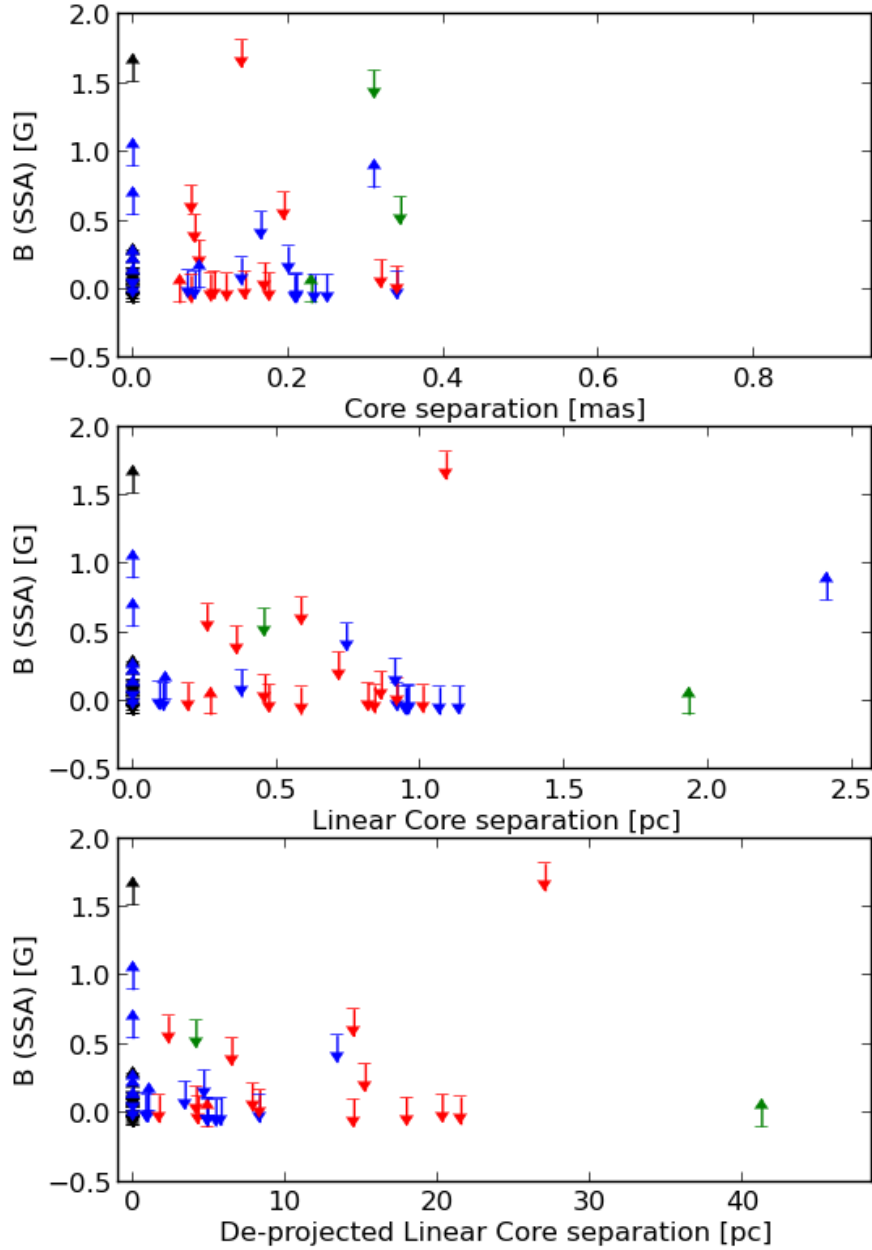


FIGURE 4.39: All magnetic fields as derived from synchrotron self-absorption (SSA) calculations. From top to bottom, plots are (i) “core” separation in mas, (ii) projected “core” separation in parsecs and (iii) de-projected “core” separation in parsecs. Black symbols are C1, red symbols are other C components and blue symbols denote travelling components.

Although we can only derive upper or lower limits on the magnetic field strength, when upper limits are computed, they tend to be consistently higher when derived from SSA. The most likely explanation for this is that the SSA calculations

depend highly on knowledge of the turnover frequency and the size of the emitting region, which is not well known. When the turnover frequency is significantly less than 43 GHz, this leads to large upper limits on the magnetic field strength. At larger “core” separations, it is likely that the component size is underestimated, leading to very large lower limits on the magnetic field strength. In Fig. 4.39, we can see the magnetic fields derived from synchrotron self-absorption. Most of the derived limits are off the plotting scale, but for some components it is still possible to see trends. In the de-projected plot, the magnetic fields are strongest in the “core” region, where there are many lower limits of ~ 0.5 G, consistent with results from equipartition calculations. In order to improve the accuracy of SSA calculations, the addition of lower frequency VLBI was used on the BL Lac OJ287. This analysis is presented in Chapter 5, where significantly improved results from SSA calculations are attained.

r_d (pc)	$B_{\text{equi},>}$ (G)	$B_{\text{equi},<}$ (G)	$B_{\text{SSA},>}$ (G)	$B_{\text{SSA},<}$ (G)
All	0.46	0.60	875	$1 \cdot 10^5$
0	0.91	1.06	0.02	70
$0 < 2$	0.53	1.07	0.02	7
$2 < 4$	0.26	0.41	0.64	292
$4 < 6$	0.49	0.36	0.04	122
$6 < 8$	0.18	-	359	-
$8 < 10$	0.24	0.44	1.6	18.5
$10 < 20$	0.38	1.32	95	$1 \cdot 10^5$
> 20	0.14	0.35	1784	$1 \cdot 10^5$

TABLE 4.21: The average upper and lower limits on the Doppler corrected magnetic field strength as a function of linear de-projected distance from the “core”.

In Table 4.21, the derived magnetic fields have been binned (every two de-projected parsecs until a “core” separation of 10 pc) and the average upper and lower limits computed. The SSA calculations are highly uncertain, with the magnetic field strength in the “core” is between 0.02 and 70 G. For this reason, further discussion of magnetic fields are limited to those derived from equipartition.

On average, the magnetic field strength in the entire jet is between ~ 0.5 and 0.6 G. In Fig. 4.40, we see how the magnetic field derived from equipartition calculations changes as a function of “core” separation. The magnetic field

appears to drop from ~ 1 G to ~ 0.3 G, before an increase to ~ 0.5 G at approximately 5 pc. The magnetic fields appear to further decrease until there is another increase in field strength at ~ 10 pc. Beyond this, the field strengths are lower and likely limited by sensitivity in maps and resolution effects. We can also test the rate at which the magnetic field decreases with increasing “core” separation, by performing a power-law fit, $B \propto r^{-n}$. This yields a value of $n = 0.3 \pm 0.2$, which is consistent with what is expected from simulations and with a toroidal magnetic field configuration (Mckinney, 2014, private communications).

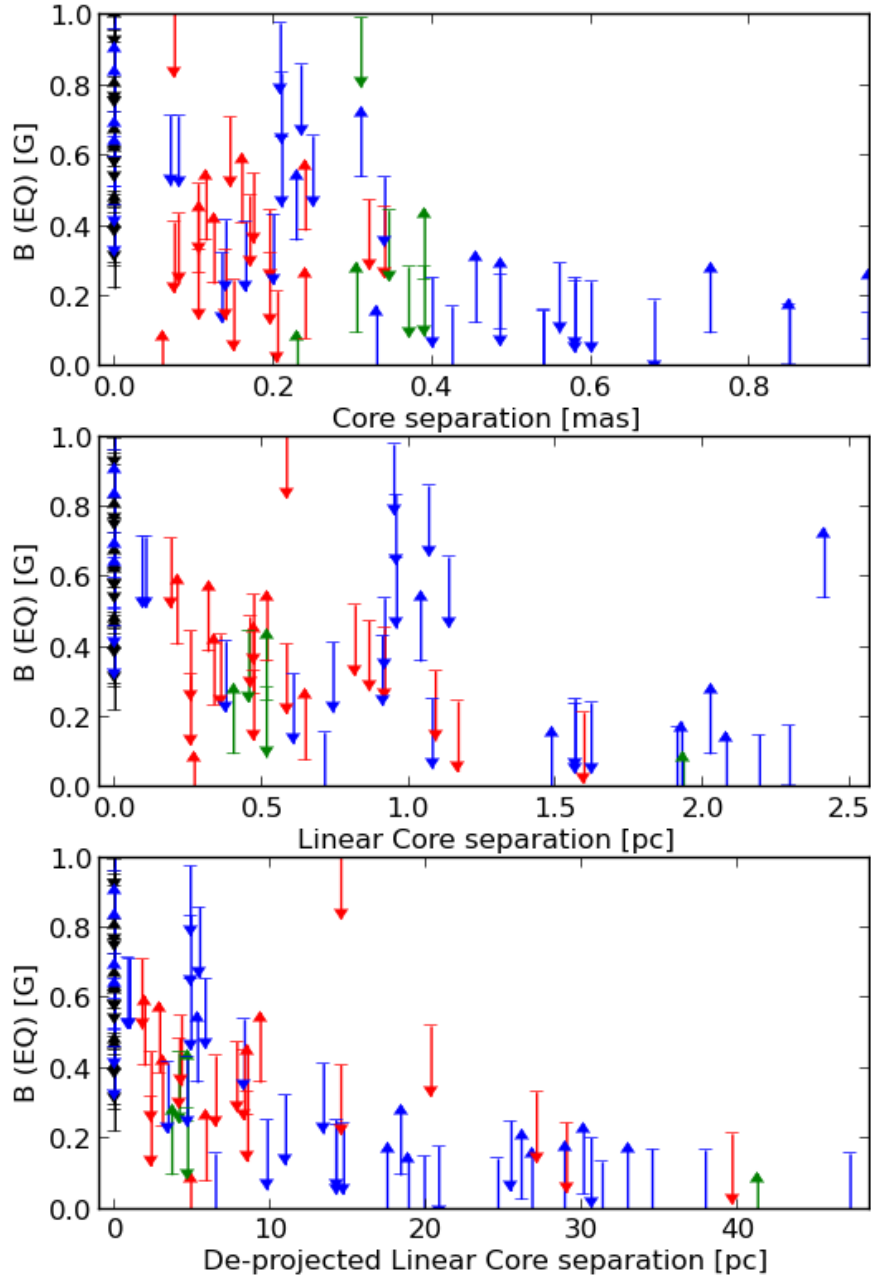


FIGURE 4.40: All magnetic fields as derived from equipartition calculations. From top to bottom, plots are (i) “core” separation in mas, (ii) projected “core” separation in parsecs and (iii) de-projected “core” separation in parsecs. Black symbols are C1, red symbols are other C components and blue symbols denote travelling components.

To better quantify this, the binned field strengths in Table 4.21 are plotted in Fig. 4.41. From this, we find that the Doppler corrected magnetic field strength in the “core” is on average between ~ 0.8 and 1.4 G, which is stronger than the results found via “core-shift” by O’Sullivan & Gabuzda (2009), which on a sample of 6 quasars found magnetic field strengths of 10s to 100s of mG, but consistent with the values found in the MOJAVE sample by Pushkarev et al. (2012), which found

values of ~ 0.9 G in FSRQs and ~ 0.4 G in BL Lacs.

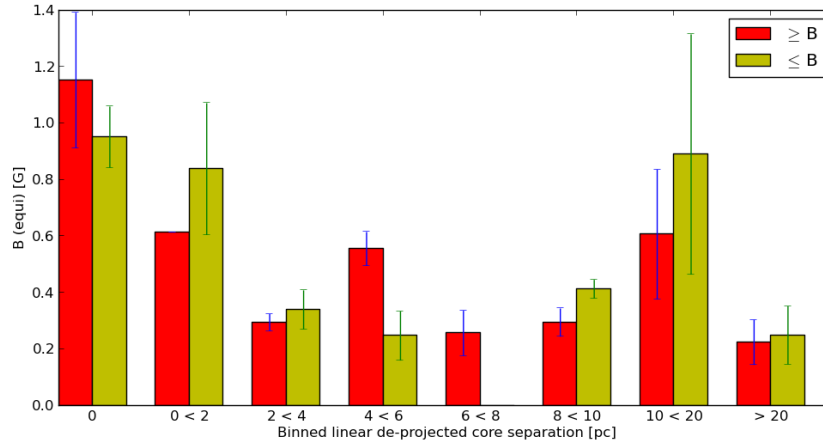


FIGURE 4.41: Equipartition magnetic fields, binned by de-projected distance from the "core".

Before the increase at ~ 5 pc, the field strength is ~ 0.3 G, but after this the field strength increases to between ~ 0.2 and 0.6 G at ~ 5 pc from the "core". Between 10 and 20 pc, there is an increase of magnetic field strength to between ~ 0.6 to 0.9 G. A possible physical interpretation could be that recollimation and shocks can lead to local enhancements of the magnetic field (e.g. Laing 1980), but could also be statistical noise due to the low sample size of six sources.

4.5.4.1 Distance to the Jet Base and B-field at Jet Base

Using the averages derived in Section 4.5.4 and a typical BH mass of $\sim 10^9$ solar masses, we can derive an estimate of the average distance from the VLBI "core" to the jet base and the average magnetic field at the jet base (see: Section 4.3.7 for more details). The degree that the magnetic field decreases with increasing "core" separation is relatively uncertain, therefore we investigate three possible scenarios. The magnetic field could decrease from 1.1 ± 0.2 G in the "core" to i) 0.3 ± 0.1 G at $R_{\text{de-proj}} \sim 3$ pc; ii) 0.4 ± 0.2 G at $R_{\text{de-proj}} \sim 5$ pc; and iii) 0.8 ± 0.4 G at $R_{\text{de-proj}} \sim 15$ pc. The results of this analysis are presented in Table 4.22.

Fuhrmann et al. (2014), found through the cross-correlation analysis of the total-intensity light curves of AGN within the FGAMMA program (see Section 4.2.4.1

Scenario	$r_{\text{apex}} (n=1)$	$r_{\text{apex}} (n=2)$	$B_{\text{apex}} (n=1)$	$B_{\text{apex}} (n=2)$
i	1.1 ± 0.4	0.2 ± 0.1	$5 \cdot 10^3 \pm 1 \cdot 10^3$	33.4 ± 4.1
ii	2.7 ± 1.3	0.7 ± 0.5	$15 \cdot 10^3 \pm 4 \cdot 10^3$	65.7 ± 10.4
iii	12.6 ± 15.4	4.1 ± 6.9	$66 \cdot 10^3 \pm 38 \cdot 10^3$	225.8 ± 74.6

TABLE 4.22: Estimated distance from the mm-wave “core” to the jet base. Three scenarios are investigated: i) 0.3 ± 0.1 G at $R_{\text{de-proj}} \sim 3$ pc; ii) 0.4 ± 0.2 G at $R_{\text{de-proj}} \sim 5$ pc; and iii) 0.8 ± 0.4 G at $R_{\text{de-proj}} \sim 15$ pc.

for more details), that the mm-wave “core” is ~ 2 -3 pc upstream of the jet base. This is consistent with scenario i and ii in Table 4.22. The power-law dependence derived in Section 4.5.4, is most consistent with scenario 1 (i). If either scenario i or ii are the case, and much of the γ -rays are produced in the “core” region or further downstream (see: Section 4.5.3), this suggests that γ -rays are being produced far outside the the broad line region (BLR) For a more detailed discussion, see Section 5.5.6.

If this is the case, this would suggest that the magnetic field at the jet base is ~ 5000 -18000 G with a toroidal magnetic field geometry and $B \sim 30$ -60 G under a poloidal geometry. If the dependence is $n \sim 0.3$ as suggested in Section 4.5.4, the magnetic field strength would be even higher, giving values of the order 10^4 G. A magnetic field strength of $\sim 5 \cdot 10^3 - 18 \cdot 10^4$ G would be too strong to be produced in a standard radiation dominated accretion disk (Ghosh & Abramowicz 1997; Nalewajko et al. 2014). The implications of this are discussed in greater detail in Section 5.5.5.

4.5.4.2 Apparant Brightness Temperature

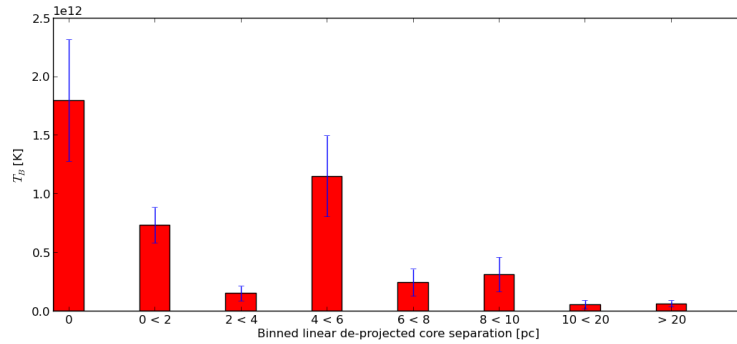


FIGURE 4.42: Binned intrinsic brightness temperatures as a function of distance from the “core”.

Brightness temperatures in the sources analysed show, on average, $T_B = 1.8 \times 10^{12}$ K in the “core” region, which is higher than the average of $\sim 10^{11}$ K found by [Pushkarev & Kovalev \(2012\)](#) over a sample of 360 AGN at 2.3 GHz and 8.6 GHz. Brightness temperatures are expected to be limited to $\sim 10^{12}$ K in the reference frame of the source, due to the inverse Compton limit ([Kellermann & Pauliny-Toth 1969](#)). At their highest, brightness temperatures can reach over 10^{13} K, suggesting strong Doppler boosting. The higher average in brightness temperature compared with other samples is not surprising, as the sources analysed here are particularly luminous, and expected to be amongst the most highly Doppler boosted sources.

In Fig. 4.42, the brightness temperatures have been binned in a similar fashion as was described in Section 4.5.4. As with the magnetic fields described in Section 4.5.4, they are maximised in the “core” region and exhibits elevated brightness temperatures at ~ 5 pc and 10-15 pc. This is perhaps consistent with the the location of compact downstream features, where the brightness temperature can be as high as or higher than in the “core”. or higher (e.g. Sections 4.4.3.2 and 4.4.4.2). Other studies have indicated that the brightness temperature drops off steadily from the “core”, following a power-law (e.g. [Kadler et al. 2004](#)). [Pushkarev & Kovalev \(2012\)](#) found that the power law dependence $T_B \propto r^{-k}$, was roughly the same at both 2.3 GHz and 8.6 GHz yielding $k = 2.2$. In Fig. 4.42, the brightness temperature clearly departs from a power-law behaviour. Fitting a power-law over all data yields $k = 0.75 \pm 0.2$. Fitting only for the inner 4 de-projected parsecs yields $k = 0.45 \pm 0.2$. Fitting to 43 GHz and 86 GHz brightness temperatures separately yields $k_{43} = 0.74 \pm 0.2$ and $k_{86} = 0.69 \pm 0.2$. We find no

statistically significant difference in the power law fitted to 43 GHz and 86 GHz data. The average brightness temperature is statistically significantly higher at 43 GHz with $T_{B,43} = 1.1(\pm 0.3) \times 10^{12}$ and $T_{B,86} = 4.8(\pm 1.1) \times 10^{11}$.

The much smaller value of k seen at high frequencies is easily explained by the fact that we are much closer to the jet base at higher frequencies. According to [Marscher \(1995\)](#), a smaller value of k , such as this, implies a slowly accelerating jet model. At larger distances from the jet base that would be observed at lower frequencies, the higher values of k imply a faster accelerating jet. The results suggest that the jet seen at mm wavelengths is more collimated, than the more freely expanding jets seen at lower frequencies. Indeed, the observed behaviour of the brightness temperature increasing at large “core” separations would imply collimation or even re-collimation.

4.5.5 Equipartition Doppler Factor

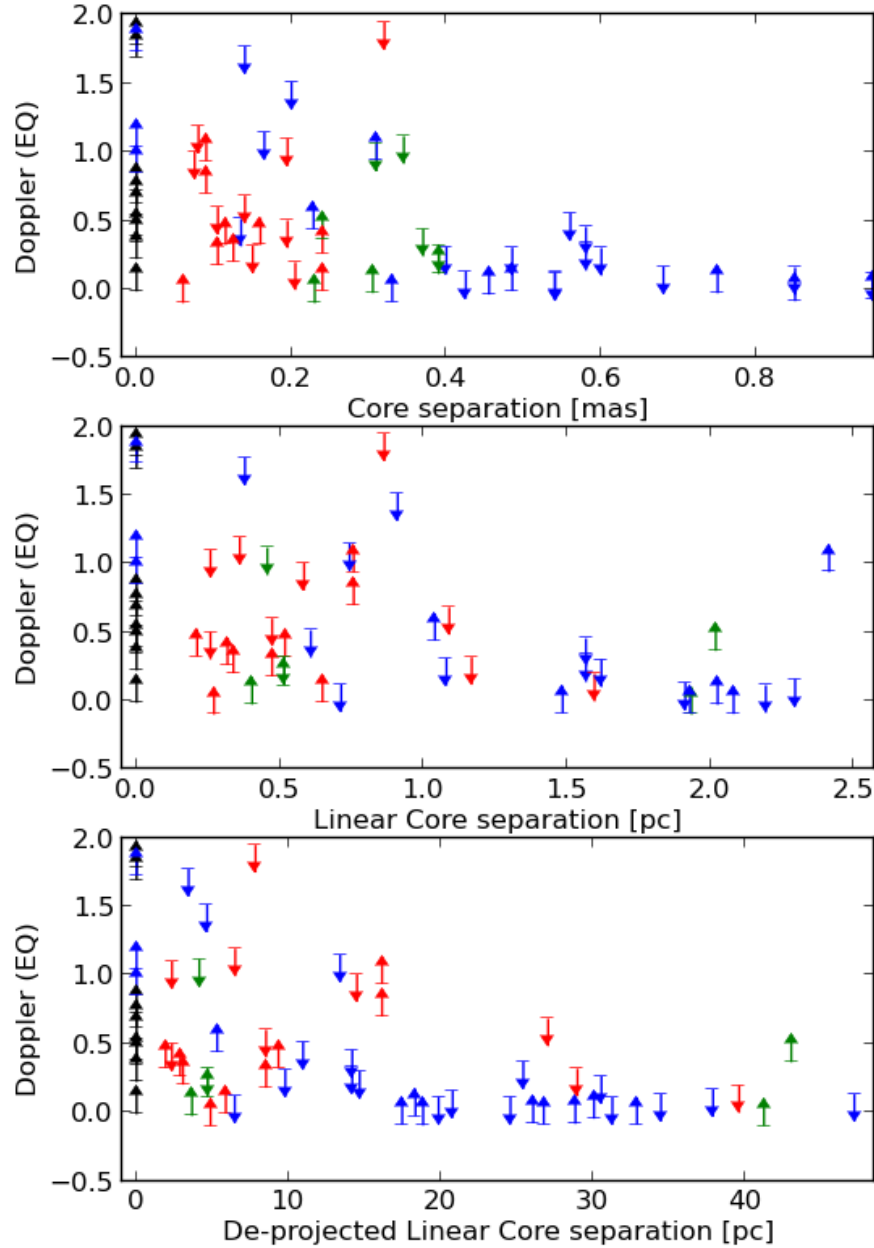


FIGURE 4.43: Equipartition brightness temperatures as distance from the “core”. From top to bottom, plots are (i) “core” separation in mas, (ii) projected “core” separation in parsecs and (iii) de-projected “core” separation in parsecs. Black symbols are C1, red symbols are other C components and blue symbols denote travelling components.

The equipartition Doppler factor (Fig. 4.43) is an independent method for determining the Doppler factor as described in Section 4.3.6.2. There is a clear trend of lowering equipartition Doppler factors. As the plot has all components from all sources plotted, changes in Doppler factor due to geometric jet bending

effects should be averaged out. Therefore, if the Doppler factor is decreasing, this suggests that the Lorentz factor, Γ , would be increasing, suggesting an accelerating jet, consistent with the results of Section 4.5.4.2. In Fig. 4.44, the equipartition Doppler factors are binned in a similar way to Fig. 4.41. Interestingly, it follows the same pattern of increasing at ~ 5 pc and ~ 10 pc “core” separation. If our interpretation regarding an accelerating jet with shocks is correct, this could perhaps suggest that the flow decelerates at the location of shocks, where the magnetic fields are also increased.

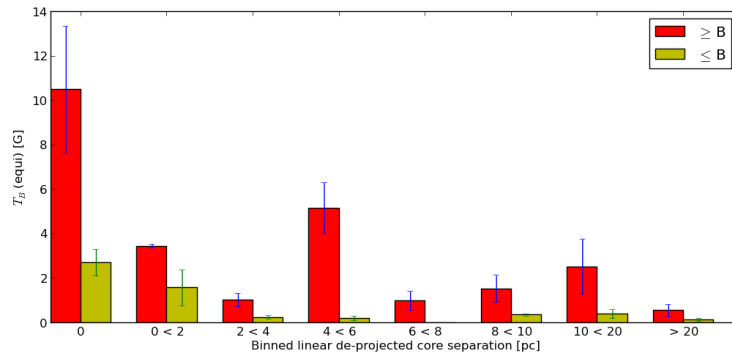


FIGURE 4.44: Binned equipartition Doppler factors as a function of distance from the “core”, similar to Fig. 4.41.

4.6 Summary

In this chapter, we have analysed in detail, from 2008 until 2012, a large number of 3 mm and 7 mm quasi-simultaneous VLBI maps to extract morphological, kinematic and spectral information at or near the turnover frequency for synchrotron self-absorption (SSA). Total-intensity radio and γ -ray light-curves were analysed for correlations with changes in morphology, kinematics and spectra over time. Using the data from spectral decompositions, magnetic fields were derived and spatially resolved at different locations along VLBI jets. Using the spatially resolved magnetic fields, we were then able to estimate the distance between the jet base and the mm-wave “core” and hence derive an estimate for the strength of the magnetic field at the jet base. Five sources in total (0716+714, 0836+710, 3C 273, OJ 287 and BL Lacertae) were analysed in this way. In addition, the raw data of the FSRQ 3C 454.3 was included in the analysis of brightness temperatures and magnetic fields. In summary, this analysis has found:

1. 3 mm VLBI maps with the GMVA exhibit broadly similar structure when compared to 7 mm maps with the VLBA, however 3 mm maps show finer structure that is not visible at 7 mm. All sources are partially resolved at 3 mm, as evidenced by the occasional detection of structure *upstream* of the VLBI “core” (Section 4.4.4.3). On average, the sources analysed are $21 \pm 3\%$ more resolved at 3 mm than at 7 mm (Section 4.4.1). All sources exhibit downstream quasi-stationary features downstream of the VLBI “core”, with some sources possibly exhibiting multiple downstream components. These downstream quasi-stationary features sometimes exhibit brightness temperatures in excess of those observed in the VLBI “core”.
2. Variability of $\sim 20\text{-}30\%$ is seen in the apparent speed of jet components, consistently seen at both 3 mm and 7 mm. There was no statistically significant difference in apparent jet speeds detected between the frequency bands. The time dependent variation of the jet kinematics could be explained by the variability of the point of ejection (Section 4.5.2) or by variations in pattern motions. This model is explored in greater detail in Chapter 5.
3. Component ejections correlate, at least in some cases, with radio flares, γ -ray flares and spectral changes within the “core” and downstream stationary components. In addition, structural changes such as position angle (PA) variations also appear to occur during flare periods. During flare periods, the “core” and downstream stationary features can exhibit optically thin spectra, consistent with travelling shocks. These bright shocks likely dominate the observed emission.
4. Using the 43-86 GHz spectrum, limits on the magnetic field strength can be computed for any component that is cross-identified between 3 mm and 7 mm. Two methods were used, including magnetic fields derived from synchrotron self-absorption and through equipartition. Due to the lack of good spectral coverage, the magnetic fields estimates from SSA were less reliable. On average the equipartition magnetic field strength in the entire jet is between ~ 0.5 and 0.6 G. The magnetic field strength in the “core” is on average between ~ 0.8 and 1.4 G, slightly stronger than in the jet.
5. The resolution of mm-VLBI allows us to spatially resolve changes down the jet in magnetic field strength. The magnetic field drops to ~ 0.3 G at a de-projected “core” separation of ~ 3 pc. We then see an increase in magnetic field strength at ~ 5 de-projected parsecs to between ~ 0.2 and

0.6 G. The magnetic field then decreases until ~ 10 pc where it once again increases to ~ 0.6 to 0.9 G.

6. Using the average decrease in magnetic field as a function of “core” separation, we were able to derive an average estimated distance to the jet base and an estimate magnetic field strength at the jet base, as described in Section 4.3.7. The magnetic field strength at the jet base and distance to it, depends on if a toroidal or poloidal magnetic field geometry is assumed. In Section 4.5.4.1, we find that on average, we find that the jet base is ~ 1 -3 pc upstream of the mm-wave “core” with toroidal geometry and ~ 0.2 -0.7 pc if a poloidal geometry is assumed. The magnetic field strength is ~ 5000 -15000 G at the jet base with toroidal geometry and ~ 30 -70 G with a poloidal geometry. Recent studies suggest toroidal geometries are more likely and a power-law fit to the equipartition magnetic field strengths yields a dependence of $n = 0.3 \pm 0.2$, consistent with a toroidal geometry. The magnetic field strength estimates are higher than theoretical predictions and simulation under the scenario of magnetically arrested discs (MAD), suggesting that either the theory is incorrect or that our assumptions about conically expanding jets and/or the magnetic field configuration close to the base of the jet are incorrect.
7. In Section 4.5.4.2, we find that the brightness temperature does not exhibit a smooth power-law decrease, as seen in other surveys at lower frequencies, with local increases in brightness temperatures seen at both ~ 5 pc and ~ 10 pc de-projected distance, similar to that seen in the magnetic field estimates. Nevertheless, fitting a power law ($T_B \propto r^{-k}$) to the data yields a value of $k = 0.75 \pm 0.2$ with no statistically significant difference between 3 mm and 7 mm. The low value suggests a slowly accelerating, collimating jet. The average brightness temperature is higher at 7 mm than at 3 mm, with $T_{B,43} = 1.1 \pm 0.3 \times 10^{12}$ and $T_{B,86} = 4.8 \pm 1.1 \times 10^{11}$.
8. In Section 4.5.5, the equipartition Doppler factor is seen to decrease with increased “core” separations, with increases at ~ 5 pc and ~ 10 pc, similar to that seen in magnetic field strengths and brightness temperatures. The decreasing equipartition Doppler factor suggests an increasing Lorentz factor, suggesting an accelerating jet. The downstream increases could be associated with shocks, where the jet flow locally decelerates.

In the future, more sources will be analysed. The interpretations presented here should be taken with some care, as the number of fully analysed sources is still

low. With the addition of all sources at more epochs, the statistics will be significantly improved and we will be able to further test the interpretations presented here. The addition of all sources may also allow us to discriminate differences between BL Lacs and FSRQs. In the next chapter, we take this analysis and add full 7 mm kinematics and near-in-time 15 GHz MOJAVE data to the BL Lac source OJ 287. The physical nature of stationary features and γ -ray flaring activity is also discussed in greater detail.

Chapter 5

OJ 287

In the previous chapter, we investigated the high-resolution morphological and spectral properties of four blazars. In this chapter, we add full 7 mm kinematics and near-in-time 15 GHz VLBI data from the MOJAVE program to perform an in-depth spectral and kinematic analysis of this blazar. The addition of 15 GHz MOJAVE VLBI data provides much improved spectral coverage, allowing for better estimates of magnetic field strengths. The addition of full 7 mm VLBI kinematics allows the connection between γ -ray flares, component ejections and spectral changes to be investigated.

5.1 Introduction

The BL Lac object OJ 287 ($z=0.306$, [Nilsson et al. 2010](#)) is a well studied blazar, harbouring a super-massive black hole (SMBH) with widely varying mass estimates of $4 \times 10^8 - 1.8 \times 10^{10} M_{\odot}$ and exhibiting quasi-periodic flaring that has been suggested as due to a binary black hole system (Valtonen et al. 2006, 2008; Liu & Wu 2002; Valtonen et al. 2012; Urry & Padovani 1995; Nilsson et al. 2010). The jet kinematics, light curves and polarisation properties of OJ 287 have been recently studied by Agudo et al. (2011, 2012), with the position angle (PA) of the jet axis appearing to change by $\approx 100^{\circ}$ between 2004 and 2006. Gamma-ray emission was suggested to be correlated with mm-radio flaring and placed at least 14 pc away from the central engine, largely in agreement with spectral energy distribution (SED) modelling by [Kushwaha et al. \(2013\)](#). Interestingly, while γ -rays have been detected in OJ 287, they have not been detected at TeV energies, unlike other similar sources such as BL Lacertae or 0716+714 ([Wang & Pan 2013](#)).

TABLE 5.1: Overview of VLBI observations

Epoch	Frequency (GHz)	Antennas	Beam (mas)	PA ($^{\circ}$)	Rec. rate (Mbit/s)	Pol.
2008.78	86.23	All	0.211 ; 0.047	-9.3	512	Dual
2009.35	86.23	All	0.219 ; 0.051	-2.5	512	Dual
2009.77	86.23	All	0.221 ; 0.045	-2.6	512	Dual
2010.35	86.23	All	0.269 ; 0.056	-2.7	512	Dual
2011.36	86.23	All	0.245 ; 0.047	-5.6	512	Dual
2011.78	86.23	All	0.255 ; 0.078	3.2	512	Dual
2012.38	86.23	All ²	0.230 ; 0.063	22.0	512	Dual
2007.45:2013.57	43.13	VLBA	0.351 ; 0.145 ¹	-2.9	512	Dual
2008.70:2012.39	15.36	VLBA	0.891 ; 0.379 ¹	-5.5	512	Dual

¹ Beam sizes are indicative only, ² Yebees participated.

In this chapter, we aim to determine further tests of the site of γ -ray emission, using recent 15, 43 GHz data and the semi-annual Global mm-VLBI Array (GMVA) observations at 86 GHz to derive magnetic field estimates in individual VLBI components and perform high-resolution kinematics. In Section 2, we present the data obtained and the methods to reduce and analyse the data. In Section 3, we present our methods of analysis. In section 4, we present an overview of the results obtained. In Section 5, we present the interpretation of these results and discuss them in the context of prevailing theories. In section 6, we present our conclusions and outlook for the future. Dates throughout the paper are presented in decimal years. A linear scale of 4.64 pc/mas and a luminosity distance D_L of 1.63 Gpc, at the source redshift of $z=0.306$ was adopted with standard cosmological constants of $\Omega_m = 0.302$, $\Omega_\lambda = 0.698$ and $H_0 = 68 \text{ km s}^{-1} \text{ Mpc}^{-1}$ (Spergel et al. 2013,0)

5.2 Observations and Data Analysis

5.2.1 GMVA Observations

Refer to Sections 4.2.2 and 4.2 for additional details. Scans of approximately 7 minutes every 15 minutes were recorded with pointing and calibration performed on European stations in the gaps between scans. A summary of observations is given in Table 5.1 and a summary of participating stations is given in Table 5.2. Between 2008.78 and 2012.38, observations were taken approximately every six months, except 2010.75. An examples of a typical map of this

TABLE 5.2: Overview of stations used in global 3 mm VLBI observations

Station	Country	Effective Diameter (m)	Typical SEFD (Jy)	Polarisation
Metsähovi	Finland	14	17500	Dual
Onsala	Sweden	20	5500	LCP
Effelsberg	Germany	80	1500	Dual
Plateau de Bure	France	34	500	Dual
Pico Veleta	Spain	30	700	Dual
Yebes	Spain	40	1700*	LCP
VLBA (x8)	United States	25	2000	Dual

* SEFD not yet optimum.

source using the GMVA is shown in Fig. 5.1. Calibration was performed on the brightest sources and scans within the experiment. Relative flux density accuracy of VLBI measurements as compared against F-GAMMA (section 2.3.2) and VLA/EVLA flux densities are within 5-10%.

5.2.2 VLBA Observations at 15 and 43 GHz

For additional details, refer to Section 4.2.3. In total, 72 observations of OJ287 were obtained approximately monthly as part of a BU-VLBA-BLAZAR 43 GHz VLBA monitoring program of γ -ray bright blazars (Marscher et al. 2008), with increased cadence during the flaring events of August 2007, October 2009 and November 2011. The data are publicly available from the BU-VLBA-BLAZAR program website and were re-imaged by us for this work. Data reduction and imaging was performed according to Jorstad et al. (2005). 15 GHz VLBI images were obtained as part of the MOJAVE monitoring program with data reduction and errors described in (Lister et al. 2009). 15 GHz MOJAVE data were primarily used to provide VLBI flux measurements at 15 GHz. For spectral index determination, we selected seven epochs of near-simultaneous MOJAVE VLBI and VLBA-BU data. Data for both the BU Blazar Monitoring Program and the MOJAVE program were correlated using DiFX at the National Radio Astronomy Observatory (NRAO) Array Operations Centre in Socorro, New Mexico. Examples of typical maps at these frequencies are shown in Fig. 5.1.

5.2.3 Long-term Total Intensity Lightcurves

Please refer to Section 4.2.4 for additional details. Long-term total intensity light-curves from late 2008 until 2014.1 were obtained from γ -ray to cm wavelengths at (i) 0.1-300 GeV, (ii) 350 GHz (0.87 mm), (iii) 225 GHz (1.3 mm), (iv) 86.24 GHz (3 mm) and (v) 43 GHz (7 mm). These light curves are presented in Fig. 5.4.

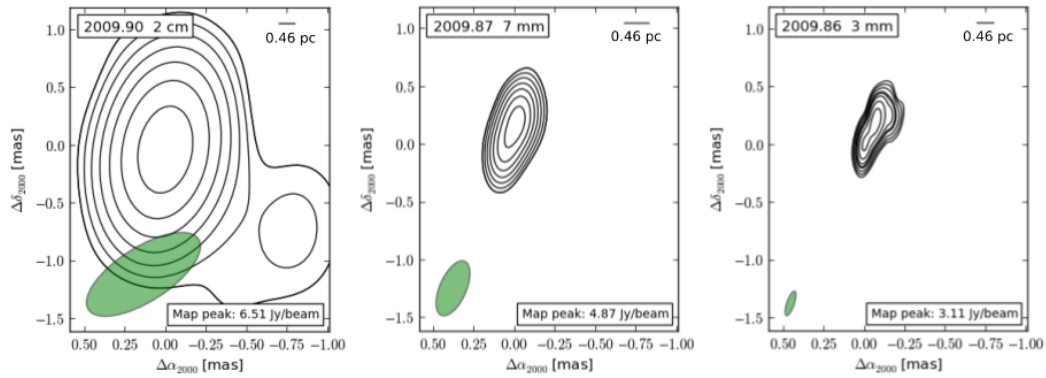


FIGURE 5.1: A comparison of VLBI maps of OJ287 at 15, 43 and 86 GHz. All maps are convolved with their natural beam. Contours: -1, 1, 2, 4, 8, 16, 32, 64%.

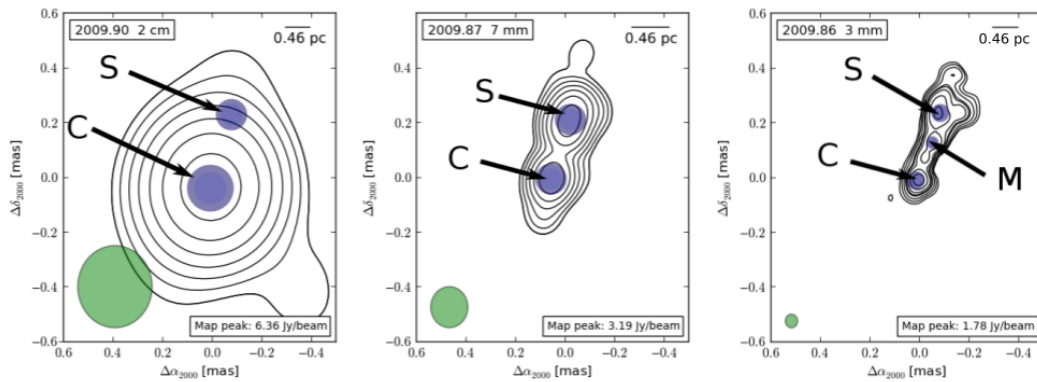


FIGURE 5.2: A comparison of super-resolved VLBI maps of OJ287 at 15, 43 and 86 GHz. 15, 43 and 86 GHz maps are convolved with 0.3 mas, 0.1 mas and 0.05 mas beams respectively. Contours: -1, 1, 2, 4, 8, 16, 32, 64%. Plots annotated with location of components C and S. Component M is located between C and S in the 3 mm map.

5.3 Results

5.3.1 Morphology

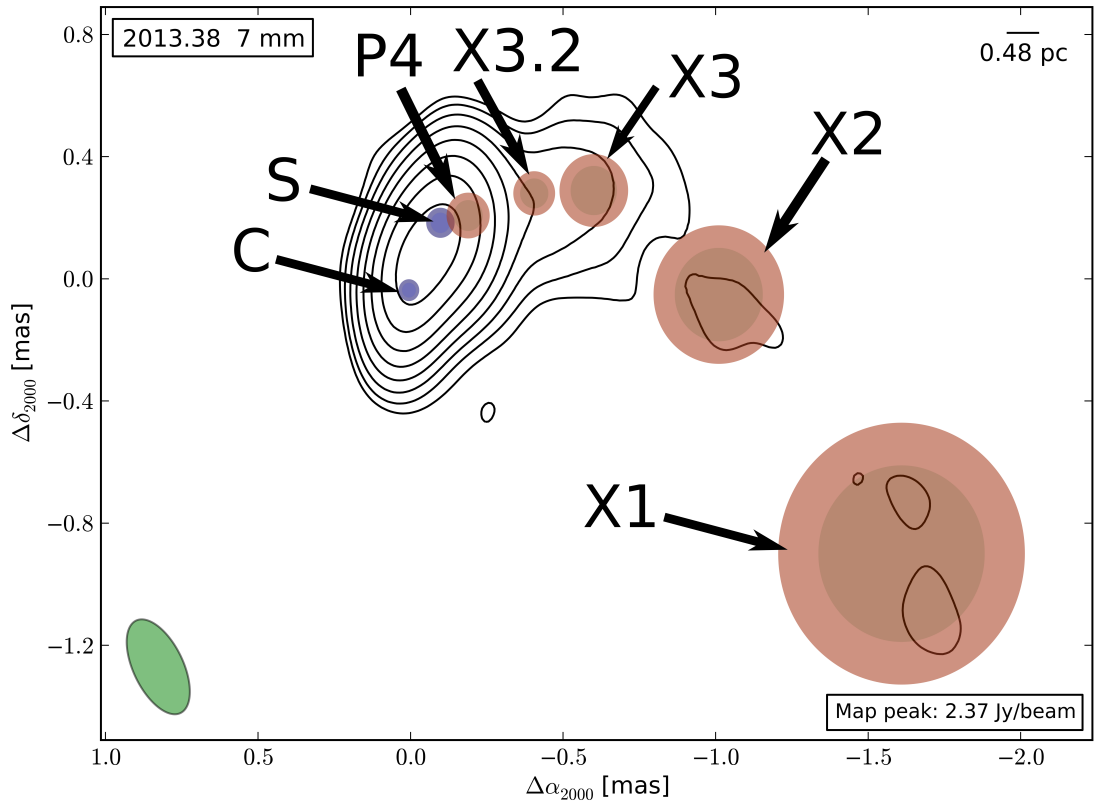


FIGURE 5.3: A recent example 7 mm map showing all fitted components and the shape of the jet. Contours: -1, -0.5, 0.5, 1, 2, 4, 8, 16, 32, 64%.

In Fig. 5.1, a comparison of natural beam VLBI maps of typical observations at 15, 43 and 86 GHz is presented. The 15 GHz map shows a bright unresolved feature and a fainter feature to the south-west. The 43 GHz map shows an elongation of the bright feature. The faint feature to the south-west is below the contour levels. At 3 mm, the bright feature is resolved into two bright features, approximately 0.2 mas from each other. A faint elongation is seen to the north and west of the northernmost component, which is not resolved at the lower frequencies. In Fig. 5.2, the same maps are now convolved with 0.3 mas, 0.1 mas and 0.05 mas beams respectively, offering a degree of super-resolution compared with the array's point spread function but similar to the resolution of the longest baselines. At 15 GHz, the brightest feature is unresolved, but at 43 GHz it becomes clearly resolved into two components, with faint emission to

the north of the northernmost component, which is also seen at 86 GHz. The 86 GHz map shows structure between these two bright components with additional faint emission to the west of the northernmost component, which is not apparent at 43 GHz.

3 mm CLEAN maps with a circular 0.05 mas beam are presented in Figs. 5.12-5.15. The morphology of the source is consistent with only minor differences between 3 mm and super-resolved 7 mm maps. In all epochs, two bright quasi stationary features are seen, labelled C and S, located approximately 0.2 mas from each other in an roughly north-south orientation. In 2010.35 and 2011.78, there appears to be an elongation of the southern component in the direction of the northern component. In epochs 2009.77 and 2011.36, there also appears to be a structure visible between the stationary components. In 2009.77, in addition to the structure visible between the two stationary features, there is also faint structure visible to the south-west of the northern stationary component, not apparent in 7 mm maps.

5.3.2 Stationary Features and “Core” Identification

To perform accurate kinematics, a common point of reference must be defined, typically taken to be the most upstream visible component or VLBI “core” (e.g. [Jorstad et al. 2005](#)). The “core” is typically identified on the basis of i) morphology, ii) a smaller size, higher flux densities and correspondingly higher brightness temperatures than downstream components, iii) an optically thick (inverted) spectrum, and iv) a stronger variability of the flux density. On average the southernmost feature (C) is smaller and brighter with a higher brightness temperature than the north-west component (S), although on some occasions the reverse situation is true (e.g. Fig. 5.12). Both components exhibit both negative and positive spectral indices at different times, with high degrees of variability. Travelling components are always first identified in the maps near the northern component (e.g. Fig. 5.14), moving away from the it. The structure between the northern and southern components seen in Fig. 5.12 and Fig. 5.13 cannot, however, be conclusively identified with newly ejected components. We cannot exclude the possibility that these components travel towards the southern component from the northern component, implying that the southern component could be a counter-jet. We consider this unlikely, since the source has historically exhibited highly superluminal motion and any counter-jet would be highly Doppler de-boosted ([Jorstad et al. 2005](#)). This leads us to identify the southern

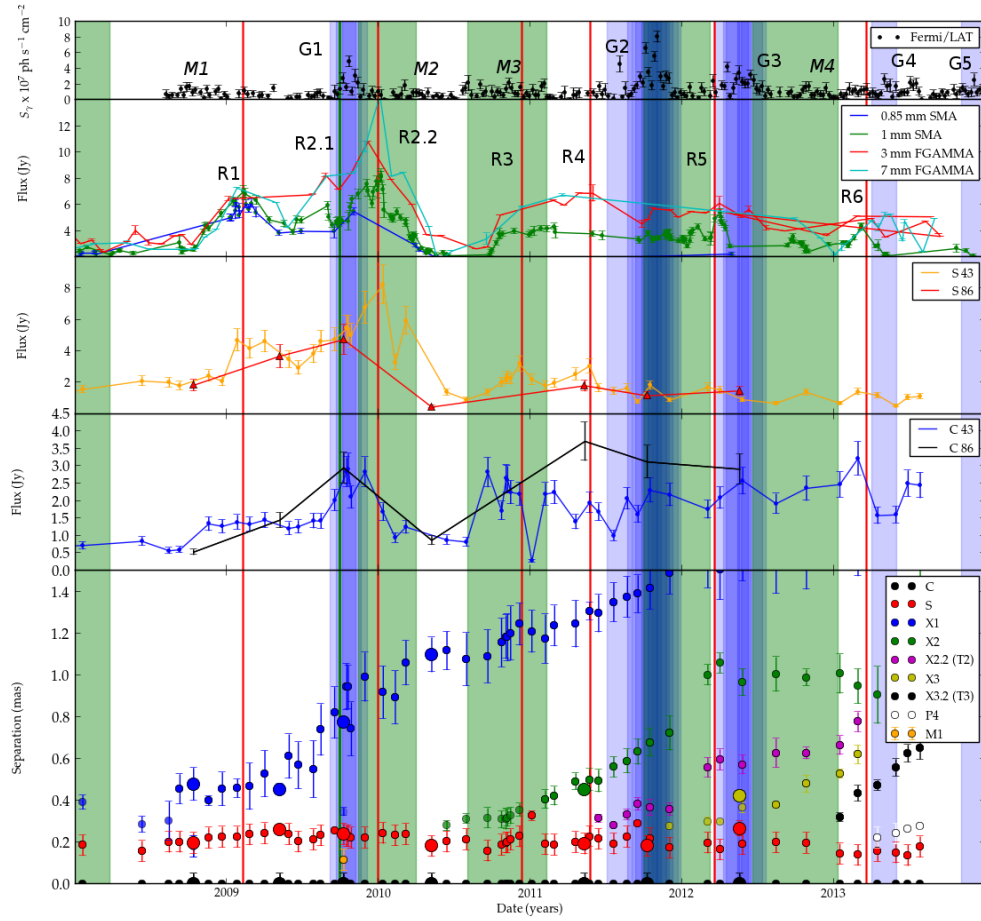


FIGURE 5.4: Multi-waveband light curves and kinematics from 2008.0 to 2014.0. From top to bottom: (i) γ -ray light curves, (ii) mm-wave total intensity light curves, (iii) VLBI flux-density light-curve of the stationary feature, (iv) VLBI flux-density light-curve of the “core” (dashed lines, 43 GHz; solid lines 86 GHz) and (v) kinematics (small circles 43 GHz, large circles 86 GHz). The scale is chosen to show the motions of the innermost parts, see Fig. 5.6 and Fig. 5.5 for larger “core” separations. Blue shaded areas indicate γ -ray flaring activity. Red lines indicate approximate peaks of radio flares. The green line indicates radio flare R2.1. Green shaded areas mark estimated t_0 dates of ejection from the “core” of travelling components.

component as the “core” (labelled C), consistent with the “core” identification of Agudo et al. (2011). We refer to the northern component as “the stationary feature” (labelled S). Component S can be seen as early as late 2004, but its current location ~ 0.2 mas from the core is not established until late 2008, after which it is persistent in all later epochs (see also: Agudo et al. 2012). A recent 7 mm map showing all fitted components is shown in Fig. 5.3.

5.3.3 Moving Component Identification and Kinematics

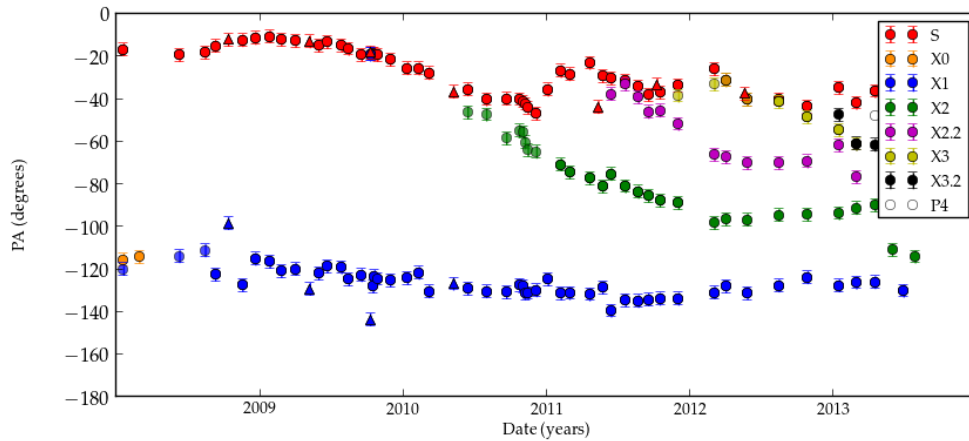


FIGURE 5.5: Evolution of the position angle (PA) of all components with time.

A summary of the kinematic properties of the moving components is given in Table 5.4 and a comparison with historical data from Agudo et al. (2011) in Table 5.5. Radial displacement from the “core” as a function of time is shown in the bottom panel of Fig. 5.4. Moving components are labelled ‘ X ’. There are “trailing” components (see: Agudo et al. 2001; Aloy et al. 2003; Jorstad et al. 2005) which are labelled ‘ $X_{n.2}$ ’ in Figures and Tables (e.g. $X_{2.2}$). If a component is separated by less than a beam-size from a stationary feature (≈ 0.15 mas at 7 mm and ≈ 0.07 mas at 3 mm), we label these ‘ P ’. Components located between C and S are labelled ‘ M ’. If a component is simultaneously labelled at 3 and 7 mm, a cross-identification between the frequencies is implied. Seven-mm model-fits use the previous epoch’s best model as a starting model for the current epoch, allowing for consistent component identifications. 7 mm model-fits aid the model-fitting and cross-identification of 3 mm maps. Discriminating between component denotations is based on positional and kinematic properties. It is possible that components have been occasionally mis-identified, although the effect on derived properties should be small.

Over the course of observations, there appears to have been three component ejections past the stationary feature, labelled X_1 , X_2 and X_3 , with two additional fainter ejections labelled $X_{2.2}$ and $X_{3.2}$, which can be seen in the bottom panel of Fig. 5.4. In 2009.77, the component located between C and S, labelled M_2 , could be associated with the component X_2 , seen in later epochs. There is possibly a new component ejection in the most recent data (≈ 2013.3), but we cannot conclusively identify this without more data. We tentatively identify it as

P4, although it could be a trailing component. Proper motion calculations are made only using epochs where the component is identified with an X feature.

5.3.4 Position Angle and Trajectories

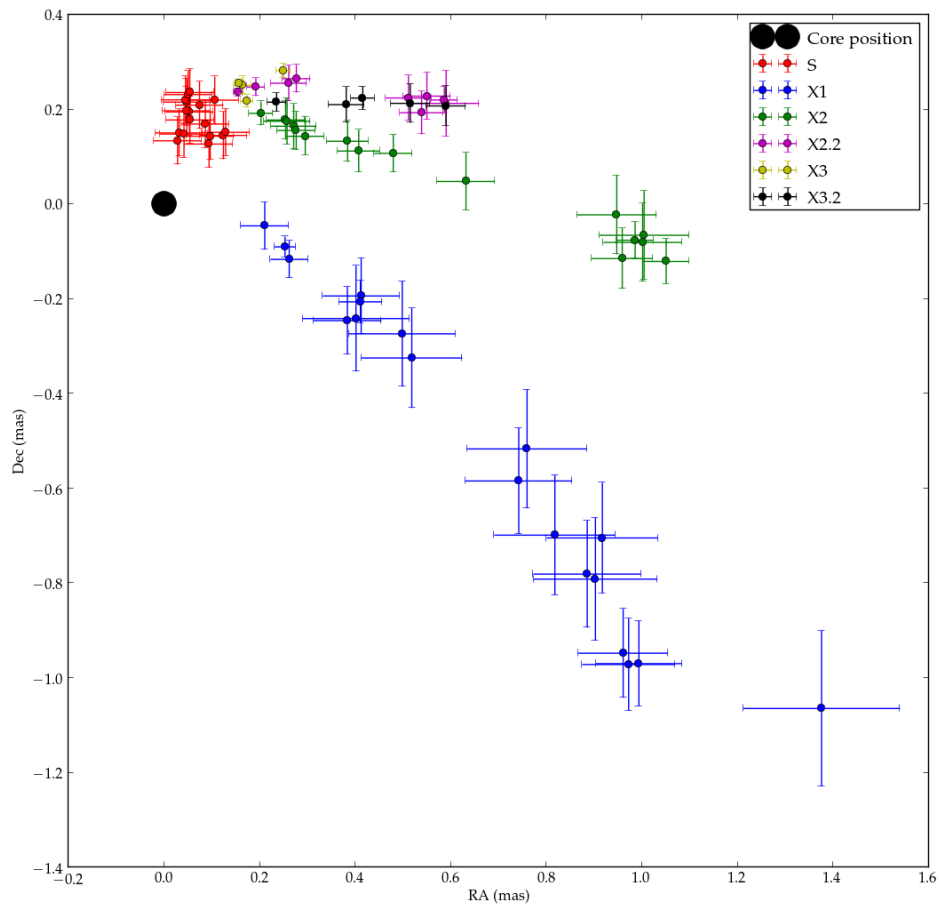


FIGURE 5.6: Component S and components X1-X3.2. Components X2 and later are travelling south-westerly from PA -40° to PA -100° . Component X1 travels south-westerly with a PA of approximately -120° .

Figure 5.5 shows the position angle (PA) between the “core” and all components for all images. Similarly, Figure 5.6 shows component trajectories relative to the “core” for all components and for all images. In Fig. 5.7, we observe the previous jet direction with a PA of $\sim 100^\circ$. Components X1 and X0 move

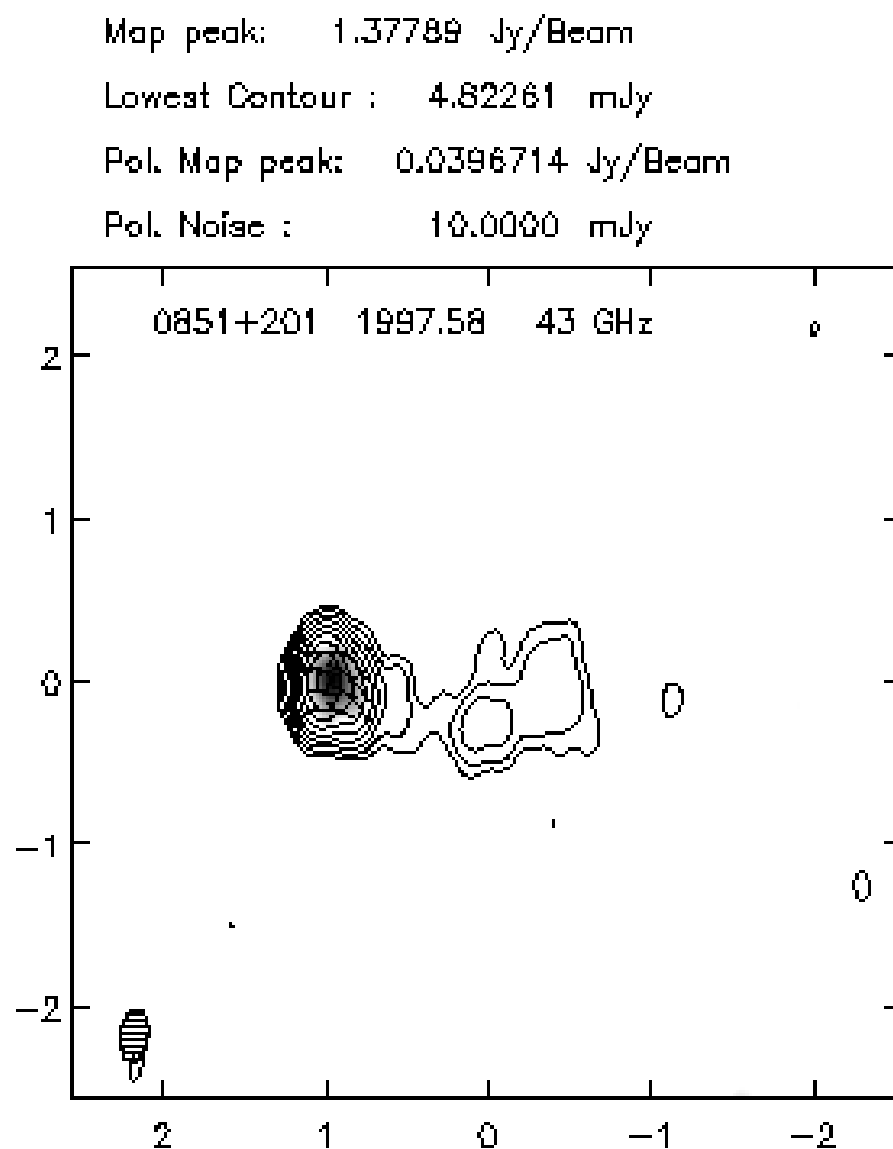


FIGURE 5.7: 7 mm map from 1997.58 showing the previous jet PA of $\sim -100^\circ$ ([Jorstad et al. 2001](#)).

with similar PAs of $\sim 110\text{--}120^\circ$. In comparison, components $X2$ and later travel along extremely different trajectories, with ejection PAs of $\sim 60^\circ$. After ejection, components $X2$ and later change PA to $\sim 90^\circ$, closer to the earlier jet PA. Components $X2$ and later are all co-spatial with S when ejected, but component $X1$ is not, having been ejected $\sim 100^\circ$ away from the stationary feature.

The PA of the stationary feature changes from $\sim -10^\circ$ in early 2009 to $\sim -40^\circ$ in mid 2010, coinciding with the ejection of component $X2$. The PA then fluctuates by approximately $\pm 20^\circ$ up to the most recent epochs. The 3 mm PA in S is consistent with 7 mm observations except in 2011.36 where a $\sim 20^\circ$ discrepancy is observed. Component S 's position relative to component C varies statistically significantly over time.

5.3.5 Light-Curves and Spectral Properties

5.3.5.1 Total Intensity Radio

Total intensity light-curves from 7 to 0.85 mm are presented in the second panel in Fig. 5.4. We identify five flares (R1-R6) denoted with red lines and listed in Table 5.3. Flares were identified by locating flux density maxima in the 7 mm VLBI data (see Section 5.3.5.2). Flare R2 is divided into two sub-flares R2.1 and R2.2 with R2.1 denoted with a green line. There appear to be two double peaked flares (R1/R2 and R3/R4) and two later flare in the most recent data (R5 and R6). Flare R1 has similar flux densities at different frequencies, suggesting a flat spectrum, similar with the quiescent periods of 2008. Flare R2.1 has higher flux densities at 3 and 7 mm, while flare R2.2 clearly has a peak frequency at 7 mm. Flares R3 and R4 appear flat between 3 and 7 mm, while for flare F5, the 1 mm flux density has risen to almost the level of the 7 and 3 mm light-curves. Flare R6 appears to show that the spectrum has returned to being mostly flat.

5.3.5.2 VLBI Component Flux Density Variability

The VLBI flux decomposition is shown in panels 2 and 3 of Fig. 5.4. We see that the total flux density S_{tot} is dominated by the “core” and stationary feature, with the sum of S_C and S_S nearly equal to the total flux density at almost all times. Prior to R3, the stationary feature is much brighter than the “core”, although

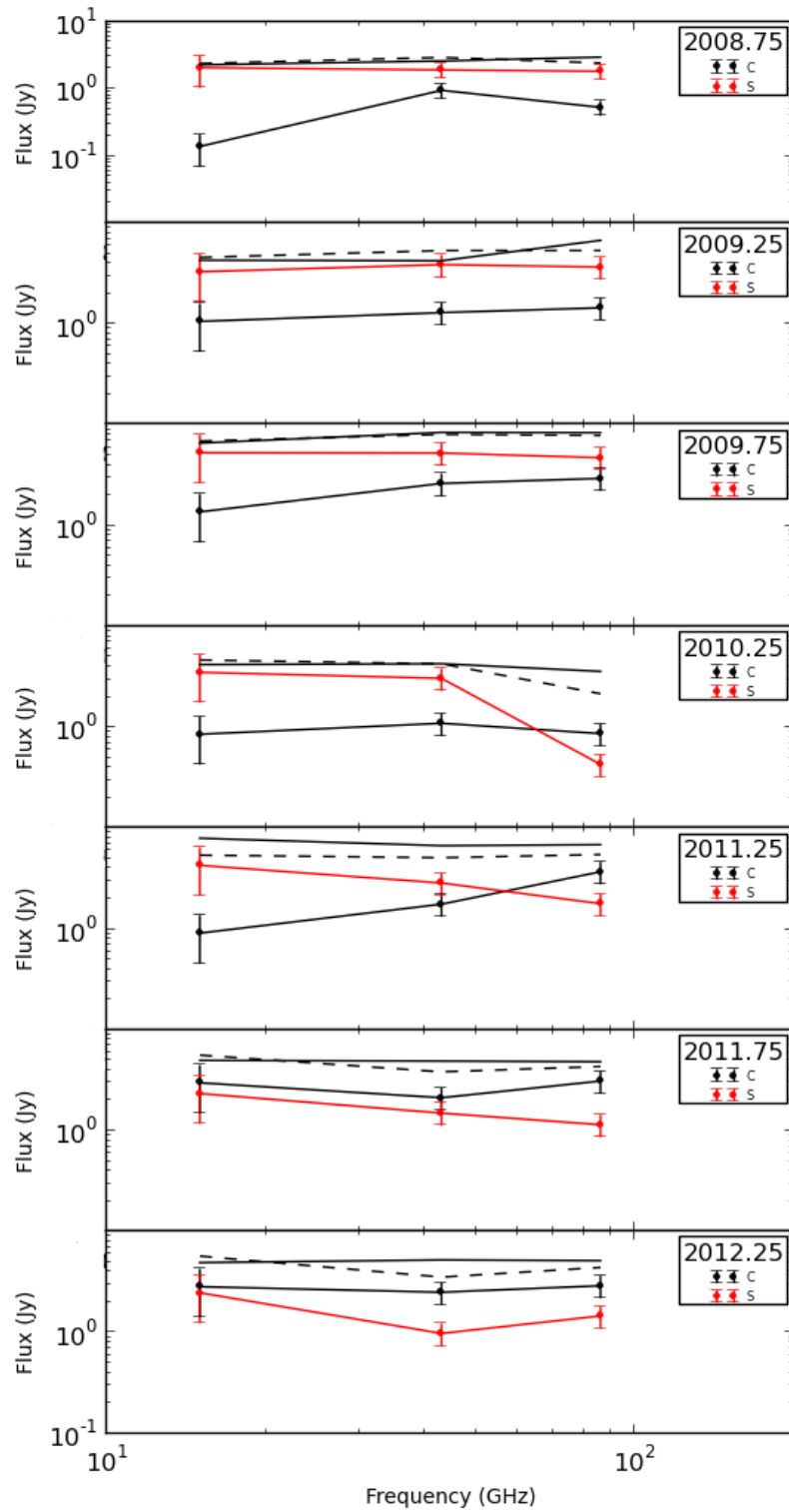


FIGURE 5.8: Spectral decomposition of OJ 287 for the “core” and standing feature from Gaussian model-fits of VLBI images. Errors on fluxes are 20 per-cent. When there the standing feature, S, is quiescent, the spectra are flat and inverted when non-quiescent. Solid black lines are total flux from VLBI and dashed black lines are total flux from the FGAMMA program.

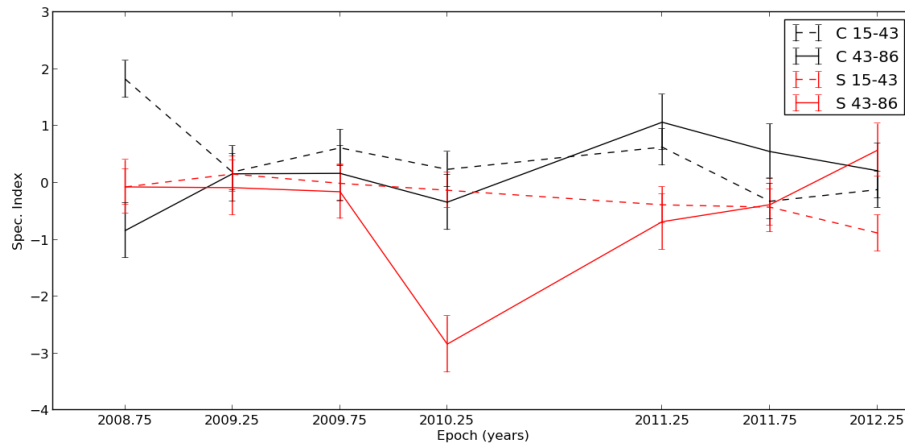


FIGURE 5.9: Evolution of spectral indices over time of “core” and stationary feature. .

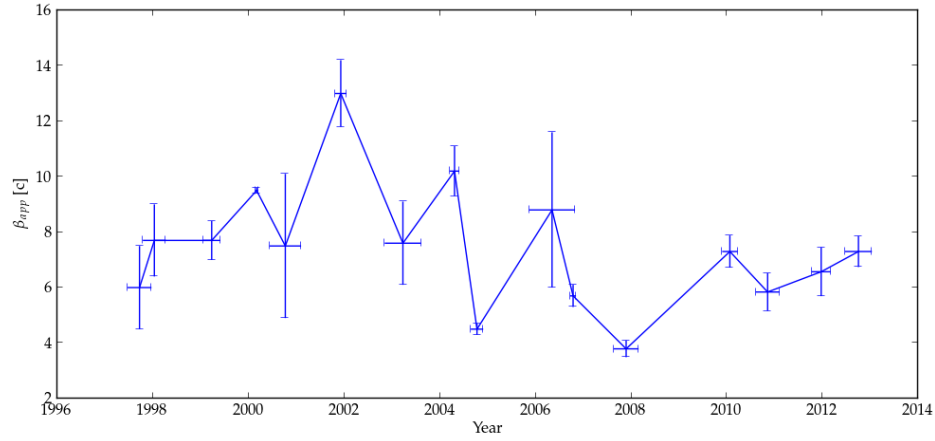


FIGURE 5.10: β_{app} as a function of estimated “core” ejection time (t_0), including data from (Agudo et al. 2011). There is a clear minimum in β_{app} in approximately 2008.0, but there is an increasing trend since then.

the shapes of their light-curves are very similar. Of particular interest is flare R2, which the decomposition shows is a superposition of two flares, with flare R2.1 peaking in the “core” (denoted with a green line) and the later, larger flare R2.2 peaking in the stationary feature. Flares R3 and R4 are also brighter in the stationary feature, before the flux density decreases to a quasi-steady value of 2 Jy post 2012. In the same period, the “core” flux rises much faster and drops rapidly very near-in-time to the peak in the stationary feature. It then rises again and stays elevated at above 2 Jy, rising to approximately 3 Jy in the most recent epochs, consistently exhibiting higher flux densities than the stationary feature over this period.

TABLE 5.3: Overview of radio and γ flares

Epoch	Type	S_{peak} ($\times 10^{-7}$ ph/cm $^{-2}$ s $^{-1}$)
2008.78 (M1)	Min. γ -ray	1.71 ± 0.04
2009.81 (G1)	Sig. γ -ray	4.94 ± 0.05
2010.17 (M2)	Min. γ -ray	1.88 ± 0.06
2010.59 (M3.1)	Min. γ -ray	2.16 ± 0.06
2011.09 (M3.2)	Min. γ -ray	2.04 ± 0.05
2011.83 (G2)	Sig. γ -ray	8.08 ± 0.07
2012.05 (M4.1)	Min. γ -ray	1.61 ± 0.06
2012.13 (M4.2)	Min. γ -ray	1.56 ± 0.06
2012.37 (G3)	Sig. γ -ray	3.46 ± 0.08
2013.33 (G4)	Sig. γ -ray	2.65 ± 0.06
2014.14 (G5)	Sig. γ -ray	3.29 ± 0.07
Epoch	Type	S_{peak} (Jy)
2009.11 (R1)	Radio	7.27 ± 0.02
2009.77 (R2.1)	Radio	8.26 ± 0.13
2010.01 (R2.2)	Radio	14.38 ± 0.04
2010.95 (R3)	Radio	3.6 ± 0.2
2011.41 (R4)	Radio	6.88 ± 0.30
2012.22 (R5)	Radio	5.37 ± 0.63
2013.22 (R6)	Radio	4.76 ± 0.28

* Significant γ -ray flares are taken as 5σ above the background and minor as being between 4 and 5σ .

5.3.5.3 Spectral Decomposition

In Figs. 5.8-5.9 and Table 5.6, we show the evolution of the spectral indices (α) between 15 GHz and 43 GHz and between 43 GHz and 86 GHz of the “core” (columns 2 and 3) and the stationary feature (columns 3 and 4). In our analysis, we use $S_\nu \propto \nu^\alpha$. Usually, the “core” is expected to have a flat to slightly inverted spectrum (flux density increasing with frequency), whilst travelling components are expected to have a steep spectrum (flux density decreasing with increasing frequency). In Fig. 5.9, we can see that the “core” (black lines) has a flat to inverted spectrum in most epochs, with the exception of 2008.78 and 2010.35. The stationary feature also exhibits flat-inverted spectra, although steeper on average than the “core”. The spectral indices move in correlated ways, giving us confidence in our component identification. Both the “core” and stationary feature have similar levels of spectral variability. In three epochs, the turnover frequency is measurable: 2008.25 and 2010.35 in the “core” and 2009.77 in the stationary feature. In 2010.35, the detection is rather tentative, but the fact

that the 3 mm flux density is higher than at 7 mm in the F-GAMMA and SMA total intensity light curves gives us confidence that the detection of the spectral turnover at 43 GHz is real. In epochs 2009.77 and earlier, the standing feature also exhibits a flat to steep 43–86 GHz spectrum. However, in epochs 2010.35 and later, the 15–43 GHz and 43–86 GHz spectral indices indicated an inverted spectrum, consistent with optically thick emission.

5.3.5.4 Gamma-Rays

The γ -ray light curve is plotted in the top panel of Fig. 5.4, with flare peaks listed in Table 5.3. To determine the significance of γ -ray flares, we estimate the quiescent level by removing any emission more than two standard deviations above the total mean flux and then recompute the mean and standard deviation. We define two forms of γ -ray activity: significant activity with ≥ 5 standard deviations above the quiescent level (labelled G) and minor activity, between 4 and 5 standard deviations above (labelled M). Significant γ -ray activity is highlighted in blue in Fig. 5.4. We find five periods of significant γ -ray activity from 2009.81 (G1) to 2014.14 (G5) and four periods of minor “flickering” activity (M1–M4), with M3 subdivided into M3.1 and M3.2 and M4 subdivided into M4.1 and M4.2. Minor flare M2 occurs soon after flare G1. We do not consider G4 and G5 in our analysis as we do not have recent enough VLBI data. Follow-up observations will be required to analyse these flares.

5.4 Analysis

5.4.1 Component Speeds and Doppler Factor

Based on setting the southernmost stationary component as the “core” and reference point, we can derive kinematics of components relative to component C. The kinematics are presented in Fig. 5.10 and Table 5.5 (see Section 5.4.1) and show a large drop in component speeds since 2004 (component d), although there may be a trend of increasing apparent component speeds in more recent data.

Please refer to Section 4.3 for additional details. The results of these computations are displayed in Table 5.4 and are shown in the bottom panel of Fig.

5.4. Component speeds were computed by first converting from radial coordinates into rectangular coordinates, computing the difference between points and smoothing the data. Speeds vary from $\beta_{\text{app}} \approx 3.8$ to 7.3 c. which is approximately half the apparent speed of previously reported speeds (Jorstad et al. 2001,0; Agudo et al. 2012). The previously reported values were $\theta_{\text{crit}} = 3.2^\circ \pm 0.9^\circ$ and Doppler factor $\delta = 18.9 \pm 6.4$ from (Jorstad et al. 2005). For the resulting calculations, we adopt the highest values from component X2, $\theta_{\text{crit}} = 7.8^\circ \pm 2.8^\circ$, Doppler factor $\delta = 7.9 \pm 2.7$ and minimum Lorentz factor $\Gamma_{\text{min}} = 7.4 \pm 0.3$.

TABLE 5.4: Table of fitted components and derived properties

	X1 ₄₃	X2 ₄₃	X2.2 ₄₃	X3 ₄₃	X3.2 ₄₃
μ (mas/yr)	0.27 ± 0.10	0.50 ± 0.24	0.40 ± 0.24	0.45 ± 0.13	0.50 ± 0.24
β_{app}	3.8 ± 1.5	7.3 ± 3.5	5.8 ± 3.5	6.6 ± 1.9	7.3 ± 3.5
Av. PA ($^\circ$)	-127.4 ± 0.1	-89.5 ± 0.5	-56.6 ± 1.1	-51.5 ± 1.8	-63.4 ± 1.4
θ_{crit} ($^\circ$)	15.2 ± 3.4	7.8 ± 2.8	9.8 ± 2.0	8.7 ± 2.5	7.9 ± 1.5
δ_{VLBI}	3.82 ± 0.4	7.9 ± 2.7	5.8 ± 0.7	7.4 ± 1.7	7.6 ± 2.5
Γ_{min}	3.9 ± 0.2	7.4 ± 0.2	5.9 ± 0.3	6.6 ± 1.7	7.4 ± 1.2
t_0 core	2007.93 ± 0.26	2009.89 ± 0.16	2010.69 ± 0.25	2011.85 ± 0.2	2012.74 ± 0.28
γ -peak	-	2009.81	-	2011.83	2012.37
$\Delta(t_0 - \gamma)$ (yr)	-	0.08 ± 0.16	-	0.02 ± 0.2	0.33 ± 0.28

5.4.2 Magnetic Fields

Please refer to Section 4.3.6.1 and Section 4.3.6.2 for additional details on the derivation of magnetic fields from synchrotron self-absorption (SSA) and equipartition respectively. When ν_m is above 86 GHz, we assume $\alpha = -0.7$ and compute a lower limit on the magnetic field strength. In epochs where ν_m is measured, an estimate of the magnetic field can be determined. As the turnover frequency is always somewhat uncertain, errors on the value of the turnover frequency are taken as ± 20 GHz. In other epochs, lower limits were computed when ν_m was above 86 GHz and upper limits when ν_m was below 15 GHz. The results of this analysis are given in Table 5.7 and discussed in Section 5.5.4. The values in this table are *uncorrected* by the Doppler factor.

Unfortunately, estimations of the turnover frequency could only be computed in three epochs, allowing only limits to be derived at other times. In epochs where it could be computed, the equipartition magnetic field is much stronger than from synchrotron self-absorption, possibly explained by Doppler factors or that the jet is not in equipartition. Limits on the magnetic field suggest that the value at the “core” is at least five times stronger than at the stationary feature.

TABLE 5.5: Current and historical component ejections.

Component	t_0 (yr)	β_{app} (c)
H*	1997.71 ± 0.25	6.0 ± 1.5
J*	1998.02 ± 0.24	7.7 ± 1.3
K*	1999.22 ± 0.18	7.7 ± 0.7
O*	2000.16 ± 0.03	9.5 ± 0.1
N*	2000.76 ± 0.33	7.5 ± 2.6
R*	2001.92 ± 0.12	13.0 ± 1.2
T*	2003.22 ± 0.38	7.6 ± 1.5
V*	2004.30 ± 0.10	10.2 ± 0.9
d*	2004.77 ± 0.13	4.5 ± 0.2
b*	2006.34 ± 0.48	8.8 ± 2.8
h*	2006.78 ± 0.06	5.7 ± 0.4
j*/X1	2007.93 ± 0.26	3.8 ± 0.3
X2	2009.89 ± 0.19	7.3 ± 0.6
X2.2	2010.69 ± 0.25	5.8 ± 0.7
X3	2011.85 ± 0.20	6.6 ± 0.9
X3.2	2012.37 ± 0.28	7.3 ± 0.6

* Historical data points from [Agudo et al. \(2011\)](#).

TABLE 5.6: Computed spectral indices for component C and S

Epoch	$\alpha_{C(15-43)}$	$\alpha_{C(43-86)}$	$\alpha_{S(15-43)}$	$\alpha_{S(43-86)}$
2008.78	1.82 ± 0.32	-0.84 ± 0.47	-0.07 ± 0.31	-0.07 ± -0.48
2009.35	0.19 ± 0.30	0.15 ± 0.48	0.15 ± 0.32	-0.07 ± -0.47
2009.77	0.61 ± 0.31	0.16 ± 0.46	-0.01 ± 0.30	-0.15 ± -0.47
2010.35	0.23 ± 0.31	-0.34 ± 0.46	-0.12 ± 0.31	-2.84 ± -0.46
2011.36	0.62 ± 0.31	1.06 ± 0.47	-0.38 ± 0.31	-0.68 ± -0.47
2011.78	-0.32 ± 0.31	0.55 ± 0.46	-0.42 ± 0.31	-0.38 ± -0.48
2012.38	-0.12 ± 0.31	0.21 ± 0.48	-0.88 ± 0.32	0.57 ± -0.49

Doppler factor limits derived from equipartition are consistent with values measured through other methods. In epochs where the turnover frequency was measured, 2008.78 (in C) and 2009.35 (in S) have equipartition Doppler factors higher than from other methods. In 2010.35 (in C) the Doppler factor is lower than measured through other methods. Averaged quantities are presented in Table 5.9.

TABLE 5.7: Table of derived values from SSA and equipartition

Component C									
Epoch	ν_m (GHz)	S_m (Jy)	θ_m (mas)	B_{SSA} (G)	T_{Bequi} ($\times 10^{11}$ K)	B_{equi} (G)	δ_{equi}	$\theta_{crit,eq}$ (mas)	
2008.78	43	0.59 ± 0.61	0.03 ± 0.03	0.08 ± 0.02	6.2 ± 3.7	0.98 ± 0.10	150 ± 16	0.8 ± 0.01	
2009.35	≥ 86	1.64 ± 1.30	0.04 ± 0.03	≥ 1.2	≥ 0.8	≥ 1.3	≥ 12.5	≥ 0.06	
2009.77	≥ 86	3.06 ± 2.56	0.06 ± 0.05	≥ 2.4	≥ 0.1	≥ 1.0	≥ 5.5	≥ 0.08	
2010.35	43	0.84 ± 0.90	0.10 ± 0.05	2.0 ± 0.5	7.8 ± 8.30	0.46 ± 0.23	5.6 ± 0.4	0.09 ± 0.02	
2011.36	≥ 86	3.20 ± 4.02	0.06 ± 0.05	≥ 3.1	≥ 0.2	≥ 0.9	≥ 4.1	≥ 0.09	
2011.78	≥ 86	3.18 ± 3.02	0.09 ± 0.1	≥ 9.4	≥ 0.1	≥ 0.7	≥ 1.4	≥ 0.09	
2012.38	≥ 86	2.46 ± 2.44	0.09 ± 0.12	≥ 14.6	≥ 0.2	≥ 0.7	≥ 0.9	≥ 0.08	
Component S									
Epoch	ν_m (GHz)	S_m (Jy)	θ_m (mas)	B_{SSA}/δ (G)	T_{Bequi} ($\times 10^{11}$ K)	B_{equi} (G)	δ_{equi}	$\theta_{crit,eq}$ (mas)	
2008.78	≤ 15	2.71 ± 2.76	0.13 ± 0.11	≤ 0.006	≤ 16.3	≤ 0.36	≤ 16.9	≤ 0.46	
2009.35	≤ 15	3.26 ± 3.48	0.13 ± 0.17	≤ 0.07	≤ 9.6	≤ 0.21	≤ 6.2	≤ 0.50	
2009.77	≤ 15	5.21 ± 4.64	0.06 ± 0.06	≤ 0.01	≤ 0.1	≤ 0.29	≤ 13.1	≤ 0.63	
2010.35	≤ 15	4.39 ± 3.84	0.20 ± 0.33	≤ 0.3	≤ 4.5	≤ 0.15	≤ 3.1	≤ 0.52	
2011.36	≤ 15	3.69 ± 4.81	0.20 ± 0.23	≤ 0.02	≤ 12.3	≤ 0.27	≤ 11.4	≤ 0.57	
2011.78	≤ 15	2.50 ± 2.73	0.32 ± 0.17	≤ 0.8	≤ 2.8	≤ 0.13	≤ 2.2	≤ 0.43	
2012.38	≤ 15	1.36 ± 1.33	0.04 ± 0.08	≤ 0.9	≤ 0.8	≤ 0.13	≤ 2.0	≤ 0.44	

* T_{Bequi} measured at ν_m

5.5 Discussion and Interpretation

The southern component (C) is identified as being further upstream than the stationary feature (S) and hence the “core”. The stationary feature (S) has very similar properties, exhibiting spectral and flux variability, suggesting that both are similar or related phenomena. In many epochs, additional structure is seen in maps between the “core” and stationary feature (e.g. Fig 5.13), which leads us to prefer the interpretation that components are emitted from the “core”, move towards the stationary feature and then bend to the north-east.

5.5.1 Jet opening angle

In Fig. 5.6, we can see two trajectories, with (1) X1 (and X0, not shown) travelling south-westerly with PA $\sim -120^\circ$ and (2) all later components travelling westerly with ejection PA $\sim -60^\circ$ changing to PA $\sim -100^\circ$ after ejection. This suggests that X0 and X1 were ejected before the stationary feature was established in its current position. Taken alone, the trajectories resemble the “fanning” of components reported in BL Lacertae (Cohen et al. 2014). Two interpretations of the jet opening angle are possible: (1) all components lie within the jet cone, which subtends an apparent opening angle of $\approx 85^\circ$ or (2) the projected opening angle is smaller ($\approx 30^\circ$) at any given time and the jet has changed direction by several degrees to give the appearance in projection of an extremely broad jet. We find in agreement with Agudo et al. (2011) that the second scenario is more likely, as the bends seen in the jet near the stationary feature would be hard to produce with large opening angles.

5.5.2 Gamma-Component Ejection Relations

The total-flux light curves are superpositions of emission from both the “core” and stationary feature, as seen in Fig. 5.4. We interpret the 2010 radio (R2) flare as a superposition of two flares (R2.1 and R2.2). R2.1 peaks in the “core” and flare R2.2 peaks in the stationary feature. The γ -ray flare G1 precedes flare R2.1 by 0.08 years and R2.2 by 0.20 years. However, the onsets of flares G1 and R2.1 are almost simultaneous. Similarly, a peak in “core” flux is seen closely coincident (within a few weeks) with γ -ray flare G2 and the estimated “core” ejection (t_0 time) of component X3. Gamma-ray flare G3 is difficult to interpret and could

be associated with the ejection of either component X3.2, P4, or the passage of component X3 through the stationary feature. Additional data would be required to resolve the issue. On average, γ -ray flares G1 and G2 precede their respective t_0 times by 18 ± 22 days. This is consistent with the results of [Fuhrmann et al. \(2014\)](#), who showed the γ -ray variations preceding the 3 mm “core” variations by 12 ± 8 days by analysing the total intensity light-curves of many blazars using the discrete correlation function (DCF). This would site the source of the γ -ray emission in the vicinity of the mm-wave “core.”

[Agudo et al. \(2011\)](#) analysed this flaring activity and concluded that γ -ray flare G1 originated in the stationary feature on the basis of electric vector position angle changes (EVPA) in the stationary feature at the time of the γ -ray flaring. Based on the addition of higher resolution 3 mm data reported here, we re-examine the time-coincidences of flares and ejections found by [Agudo et al. \(2011\)](#). In Fig. 5.2, we see structure both up and downstream of component S in an epoch near the peak of γ -ray flare G1. In particular, there is a component detected between C and S before the peak of the flare. Additionally, the onset of flare G1 and R2.2 are both near ~ 2009.8 , supporting the interpretation that γ -rays are emitted in component S. However, as the peak of flare R2.1 is also near in time to flare G1 and the ejection time of component X2, we cannot rule out the possibility that γ -ray emission originates in both component C and S. The lack of component ejection after flare G1 could be explained by the γ -ray flare reducing the energies of the electrons in the travelling component due to radiative losses.

5.5.2.1 Flaring Activity Within Stationary Feature

In Table 5.8, we summarise the estimate date at which travelling components passed the stationary feature and nearest-in-time peaks in γ -ray activity. The passing date is the first epoch at which a component was seen downstream of the stationary feature. Minor flare M2 appears to occur soon before the passing of component X2 through the stationary feature, *S*. The minor flare M3.1, however, occurs 0.24 yr after the passing of component X2. A rise in 7 mm flux coincides with the ejection of X2.2, with minor flare M3.2 occurring almost simultaneously with it. The passing of component X3 past the stationary feature either closely follows the peak of major flare G2 or precedes minor flare M4.1.

The passing of component X3.2 past the stationary feature is almost simultaneous with major flare *G*4. It is not possible to conclusively identify flaring activity within the stationary feature as there is often activity within the “core” at similar times. However, as there is γ -ray activity detected near-in-time to all components passing the stationary feature, we find it highly likely that γ -ray emission is being produced there. The stationary feature is over a parsec downstream of the “core” and hence the γ -rays must be produced outside of the BLR.

TABLE 5.8: Stationary feature γ -ray relations.

Component	‘S’ passing date (yr)	γ -ray flare (yr)
X2	2010.35	2010.17 (M2)/2010.59 (M3.1)
X2.2	2011.10	2011.09 (M3.2)
X3	2011.92	2011.83 (G2)/2012.05 (M4.1)
X3.2	2013.29	2013.33 (G4)

5.5.3 Physical Nature of the “Core” and Stationary Feature

Stationary features have been observed previously in this source and in many others (e.g. [Jorstad et al. 2005,0](#); [Fromm et al. 2013a](#); [Schinzel et al. 2012](#)), where they have typically been interpreted as recollimation shocks within a relativistic plasma flow. A stationary feature could also appear due to maximised Doppler factors in a bent jet (e.g. [Alberdi et al. 1993,9](#)), but [Jorstad et al. \(2001\)](#) suggest that stationary features within 2 mas of the “core” are likely hydrodynamical compressions, while further out, stationary features may be associated with maximised Doppler factors due to bends in jets. It is also unlikely that large radio or γ -ray flaring would occur for geometric reasons.

The high levels of polarisation, spectral variability and proximity to the “core” lead us to conclude that component *S* is probably a recollimation shock or an oblique shock associate with the bend in the jet. An oblique shock arises because the internal pressure of the jet decreases rapidly after being launched. When the jet pressure equalises with the ambient medium, the jets re-confine in order to adjust to the external pressure. These re-confinements occur repeatedly and move subluminally ([Meli & Biermann 2013](#); [Sanders 1983](#)). A recollimation shock then is a series of conically arranged oblique shocks. An oblique

shock would arise over a recollimation shock in the case of the jet was bent by a cloud or a wall (Marscher 2006). Hence, because the jet bends at the location of the stationary feature, that it is located so close to the “core” and that γ -ray flaring likely occurs within it, we conclude that the stationary feature, S , is likely an oblique shock.

In the sources examined in Chapter 4, the stationary features appear to be in relatively straight paths from the “core”, with the possible exception of component C2 in 0716+714 (see: Section 4.4.2.3). In that case, like in OJ287, the position of the stationary feature relative to the trajectories of travelling components suggests that it could be an oblique shock, rather than a recollimation shock. In the other sources, the downstream stationary features could be recollimation shocks, like the “core” or themselves oblique shocks.

The “core” could be associated with the $\tau = 1$ surface in a conical jet (e.g. Blandford & Königl 1979), although this is possibly not the case at mm wavelengths. The “core” and stationary feature have remarkably similar properties, with both exhibiting high levels of spectral and flux variability and possibly γ -ray activity. Additionally, we have detected optically thin emission in the “core” region on two occasions, consistent with an optically thin travelling feature passing through the “core”. This suggests that the “core” is a recollimation shock (e.g. Daly & Marscher 1988; Cawthorne 2006; Fromm et al. 2012; Marscher 2014). The stationary feature could itself be a recollimation shock or an oblique shock. A recollimation shock can be effected by disturbances passing through, resulting in fluctuations of its position, according to numerical simulations by Gómez et al. (1997). In Section 5.3.4 and Fig. 5.6, we showed that stationary feature changes position relative to the “core”, although the “core” itself may also shift position on the sky. Multi-epoch phase referencing would be needed to determine this.

5.5.4 Magnetic fields

In Sections 4.3.6.1-4.3.6.2, we derived estimates on the magnetic field strength at different positions along the jet via two methods; i) synchrotron self-absorbed spectra and ii) equipartition. Table 5.9 shows magnetic field estimates and limits

TABLE 5.9: Average properties in “Core” and stationary feature.

Property	“Core”	“Stationary Feature”
B_{SSA} (G)	≥ 1.6	≤ 0.4
B_{equi} (G)	≥ 1.2	≤ 0.3
δ_{equi}	≥ 8.7	≤ 9.9
T_{B} (K)	$\geq 1.4 \times 10^{11}$	$\leq 2.1 \times 10^{11}$

derived from averaged quantities. All values are consistent within an order-of-magnitude of each other. On average, there is a minimum $\sim 74\%$ decrease between B_{SSA} in the “core” and B_{SSA} in the stationary feature and a minimum $\sim 75\%$ decrease between B_{equi} in the “core” compared with the stationary feature. The values of the magnetic field strengths derived through both methods are broadly consistent, with the field strengths from SSA being $\sim 20\%$ higher than when computed from equipartition. Interestingly, the average size for the “core” (0.037 ± 0.01) is smaller than the equipartition critical size of ≥ 0.07 , suggesting particle dominance. The average size for the stationary feature (0.065 ± 0.01) is much smaller than the upper limit for the critical size of ≤ 0.5 , consistent with a jet in equipartition.

The results here show how important the 15 GHz spectral data point is in the calculation of magnetic fields through SSA. Although the derived field strengths are slightly stronger through SSA, the decrease in strength down the jet is very similar. As the SSA calculations do not depend on the assumption of equipartition, they could be more physical.

5.5.5 Magnetic field strength in the BLR and at the SMBH

We attempt to derive the distance to the jet base and the magnetic field strength at the jet base following the methods described in Section 4.3.7. Limits could only be computed, but because the total intensity flux density at 1 mm is much lower than at 3 mm, indicating a small optical depth, these lower limits may not deviate much from the true value. Assuming a toroidal configuration and using the magnetic field decrease from SSA calculations, we obtain $B_{0.05} \leq 600$ G at $r = 0.05$ pc. If we then assume a conservative black hole mass, $m_{\text{BH}} = 4 \times 10^8 M_{\odot}$, yielding a Schwarzschild Radius $R_s \approx 4 \times 10^{-5}$ pc, we compute a upper limit of $B_{\text{apex}} \leq 4200$ G at the jet apex (assumed to be at approximately $10 R_s$).

Assuming equipartition arguments yields values of $B_{0.05} \leq 500 \text{ G}$ and $B_{\text{apex}} \leq 3400 \text{ G}$. These computed values are very different, and could be due to the flaring activity in the stationary feature causing stronger than usual magnetic fields in the stationary feature over the period analysed. These values, however, are broadly consistent with those reported by [Silant'ev et al. \(2013\)](#). The presence of such strong magnetic fields at the jet apex would strongly favour the Blandford-Znajek process of jet formation dominating in OJ287 ([Blandford & Znajek 1977](#)).

Recent studies, have suggested that powerful jets could be produced via the mechanism of magnetically arrested disks (MAD), where a very strong magnetic field is produced by accreting gas being dragged in a poloidal magnetic field, causing gas to fall onto the black hole with a higher-than-free-fall velocity ([Narayan et al. 2003](#); [Bisnovatyi-Kogan & Ruzmaikin 1974](#)). The poloidal field generated is then twisted around the black hole, creating a toroidal ($n=1$) magnetic field ([Tchekhovskoy et al. 2011](#)). Recent results suggest that toroidal ($n=1$) magnetic fields are more important in sub-parsec to parsec scale jets (e.g. [Zamaninasab et al. 2014](#)), leading us to suggest our results also support this scenario, which has been further backed up with theory and simulations (e.g. [Tchekhovskoy et al. 2011](#); [McKinney et al. 2012,0](#)). An observational study by [Silant'ev et al. \(2013\)](#) also found magnetic fields of the order thousands of Gauss.

[Zamaninasab et al. \(2014\)](#) showed that $50(\dot{M}r_g^2)^{1/2} \propto L_{\text{acc}}^{1/2} M$, where \dot{M} is the mass accretion rate, r_g is the gravitational radius of the black hole, L_{acc} is the accretion disk luminosity and M is the central black hole mass. [Pihajoki et al. \(2013\)](#) estimates $L_{\text{acc}} \sim 2 \times 10^{46} \text{ erg/s}$ in OJ287, leading to a magnetic flux of $\phi_{\text{OJ287}} \sim 3 \times 10^{33} \text{ G cm}^2$, which yields an estimated magnetic field strength at the jet base, $B_{\text{apex}} \sim 2000 \text{ G}$, consistent with our predictions. For black-hole masses of $> 10^9$ solar masses and higher accretion disk luminosities, the magnetic field estimates can be $B_{\text{apex}} \sim 30000 \text{ G}$ or higher, consistent with the estimates derived in Chapter 4. However, if the magnetic field configuration is consistent with $n < 1$, this could make the estimated magnetic field strengths considerably stronger than expected from MAD, suggesting that our assumptions about the jet being conical or the magnetic field geometry may break down close to the base of the jet.

5.5.6 Location of γ -ray Emission

Figure 4.2 depicts a stylised sketch of a relativistic jet. The γ -ray emission region is located a distance r_{A-G} from the jet apex. This distance is the difference between the distance to the “core” from the jet apex, r_{apex} and the distance between the “core” and the γ -ray emission region, r_{G-C} . We found in Section 5.5.2 that the γ -ray emission region, r_{G-C} , lies in the region of the mm-wave “core” (or further upstream in the stationary feature).

In Section 4.3.7, we described a method to determine the distance from the “core” to the jet apex, r_{apex} , using the decrease of magnetic field strength down the jet. In the previous section (Section 5.5.4), we showed that the magnetic field is $\sim 75\%$ weaker in the stationary feature compared with the “core”. Recent work by McKinney & Blandford (2009); Gabuzda et al. (2014) and Zamaninasab et al. (2014) suggests that toroidal magnetic plays a more important role in AGN than assumed before. Therefore, if we assume $\Delta r_s = 0.2 \text{ mas}$, a toroidal magnetic field ($n=1$), this would place the jet apex $\leq 4.1 \text{ pc}$ upstream of the mm-wave “core” and γ -ray emitting regions. Using SSA calculations places the jet apex $\leq 6.0 \text{ pc}$ upstream of the mm-wave “core” and γ -ray emitting region. Sikora et al. (2008) analysed the blazar 3C 454.3 and also concluded that the blazar emission must be several parsecs downstream from the central engine. Our results here and those presented in Chapter 4 are consistent with this scenario.

We find it likely that the “core” is downstream of the jet base and hence BLR. Additionally, as it is likely that γ -rays are produced within the stationary feature (see: Section 5.5.2.1 and Agudo et al. 2011), it is located over a parsec downstream of the “core”. Even if the “core” were within the BLR, γ -ray emission from the stationary feature would be not be. Hence, if the γ -rays originate in either the “core” or stationary feature they are highly likely to be located outside of the BLR, which is considered to be less than a parsec in extent (Peterson et al. 2004; Bonnoli et al. 2011). This suggests that the synchrotron self-Compton (SSC) mechanism likely dominates γ -ray production in OJ287 (Bloom & Marscher 1996). If the interpretation of Agudo et al. (2011) is correct and γ -rays are produced in the stationary feature, the γ -ray emission region would be over 1 pc further downstream that presented here and would support the same interpretation. If our calculations are correct, this would place the γ -rays in a region consistent with where recollimation shocks would be expected to form,

(e.g. [Marscher et al. 2008](#)).

5.5.7 Apparent Speeds and "Jet-Wobbling"

In Fig. 5.6, we observe that the component S changes position relative to the "core" from epoch to epoch. We also see variability in apparent speeds, which is also seen in all other sources analysed in Chapter 4. We interpret its movement in a similar way to that proposed by [Molina et al. \(2014\)](#), in the blazar NRAO 150, where its emitting regions rotate relative to a reference point that is not a modelled jet feature. Simulations by [McKinney & Blandford \(2009\)](#) show that such rotations are likely naturally arising from time-variable twisting of magnetically driven jets. We propose that both the "core" and stationary feature have variable positions in this manner. Although the stationary feature's movement is measured relative to the "core", this may not necessarily be the case and both could be moving relative to some non-jet reference point. If this is the case, the stationary feature's (and "core's") line-of-sight would be changing from epoch to epoch. Therefore, a travelling component's apparent speed would depend on the line-of-sight to the stationary feature when the component passes through it. This interpretation could also explain the quasi-periodic variation in apparent speeds seen in Fig. 5.10 and Chapter 4. To test this model, over many years of high frequency observations, we would expect to see a correlation between β_{app} and ejections PA. This will be explored in the future.

5.5.7.1 Large PA changes

The large PA change of 2006-2008 was interpreted by [Agudo et al. \(2012\)](#) as being due to the jet passing through our line-of-sight. If the lower apparent speeds discussed in Section 5.4.1, compared to previous observations represent a change in the Doppler factor due to a change in the line-of-sight, this suggests that the highest apparent speeds seen must have been close to the critical angle θ_{crit} . If the jet had moved into our line-of-sight as [Agudo et al. \(2012\)](#) suggested, this would mean that we would observe lower apparent speeds but a much higher Doppler factor as the viewing angle would be higher than the critical angle. However, we consider this scenario unlikely as 1) if a higher (> 20) Doppler factor is adopted in the magnetic field calculations, the derived magnetic field strengths would be unrealistically large (e.g. > 50 G in the "core" on

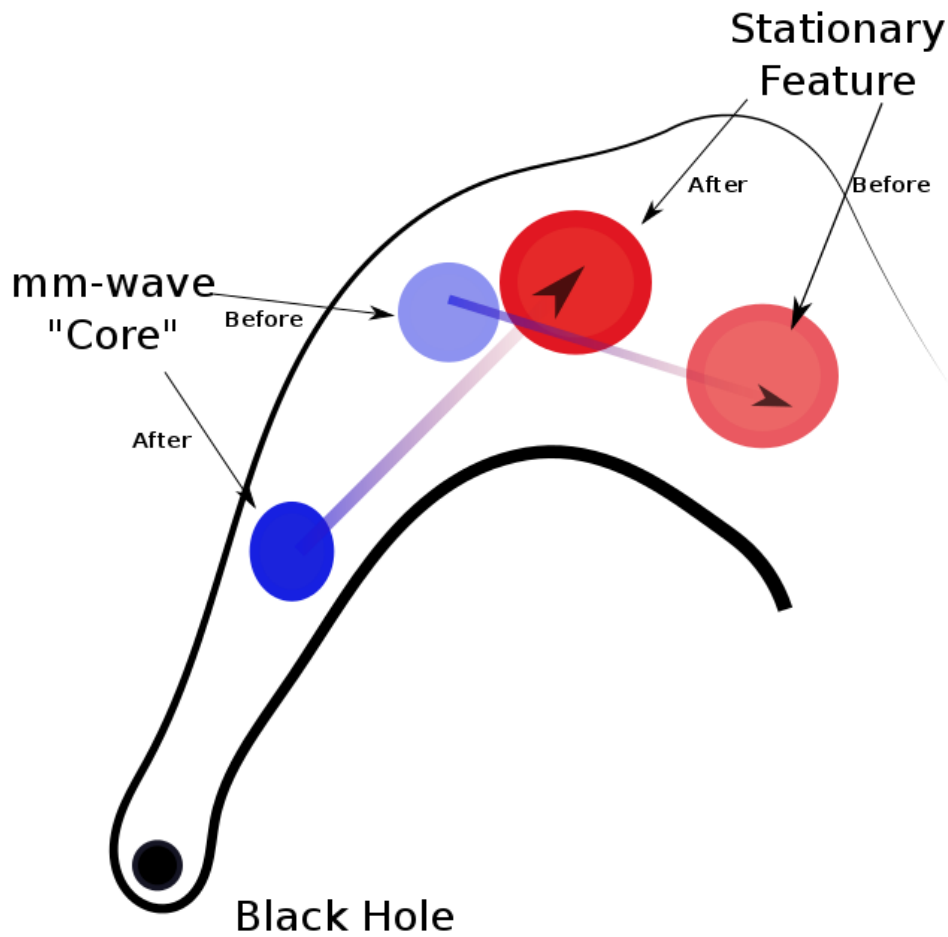


FIGURE 5.11: A sketch of the cause of the large PA change from 2006-2008. A large disturbance at the jet base causes a change in the pressure of the jet relative to the external medium, changing the location of recollimation shocks within the jet. This sketch shows the *de-projected* jet geometry. Effects such as this would be amplified observationally.

average) and 2) the equipartition Doppler factor is of the order ~ 10 . In this low angle solution, we find that the bulk flow Lorentz factor is $\Gamma = 35 \pm 4$, which is consistent with results in other sources (e.g. [Marscher 2006](#)). Hence, although the interpretation of [Agudo et al. \(2012\)](#) is plausible, we propose an alternative interpretation here.

If the jet is bent, and if the “core” position were to very suddenly change out of our line-of-sight by moving closer to the jet apex, we would observe an apparent large PA change and a coincident drop or increase in Doppler factor. Such a scenario could result from a change in the flow parameters injected at the jet base, perhaps a star falling into the SMBH, causing significant changes to the pressure ratio between the jet and external medium as shown in Fig. 5.11. This

occurring would shift the locations of the standing shocks up- or downstream. One could also speculate that if the pressure ratios return to their previous ratios in the future, the PA and Doppler factors would also return to their previous directions. While we cannot rule out a binary black hole in this model, it is not necessary to invoke it to explain the “wobbling”. Assuming a constant external medium and relativistic electron/positron plasma, the position (z_{recol}) of the first recollimation shock is given by (Daly & Marscher 1988):

$$z_{\text{recol}} \approx 3.3\Gamma_0 R_0 (\rho_0 / \rho_{\text{ext}}), \quad (5.1)$$

where Γ_0 is the Bulk Lorentz factor, R_0 is the jet opening angle ($\approx 30^\circ$), ρ_{ext} is the external pressure ($\approx 1.6 \times 10^{-24}$ Pa) and ρ_0 is the internal pressure varying from $1.0 \times 10^{-25} - 5 \times 10^{-28}$ Pa (approximate values from: Fromm 2014). The results indicate that doubling the internal pressure of the jet results in the z_{recol} of the first recollimation shock to be approximately twice as far out. This is necessarily very simplistic, but shows that such a scenario should be plausible. In OJ287, there appears to be a large drop in apparent speeds 2008. The derived viewing angle for OJ287 is now over 10° and the most recent ejection in MOJAVE data shows that the component is travelling much slower than previous ejections, consistent with this interpretation. If this interpretation is correct, we predict that β_{app} will increase to their previous levels and the jet will return to its original pre-2006 direction.

5.6 Summary

In this chapter, we have used multi-frequency VLBI data at 2 cm, 7 mm and 3 mm, total intensity radio data at 2 cm, 7 mm, 3 mm, 1 mm, 0.85 mm and γ -ray data from the *Fermi*/LAT space telescope to perform a detailed kinematic and spectral analysis of the highly variable BL Lac OJ287. We have used the 2 cm MOJAVE, 7 mm VLBA-BU and 3 mm GMVA data to determine the spectrum and hence estimates of the magnetic field at multiple locations down the jet. We combine this with kinematics derived from 3 mm and 7 mm data to determine the location of radio and γ -ray flaring events within the jet. We have found:

1. OJ 287 exhibits two stationary features, components C (“core”) and S (“stationary feature”), that have very similar properties, with the “core” exhibiting an optically thin spectrum at times. Both are interpreted as standing shocks. The stationary feature moves on the sky relative to other components and we postulate that the “core” could also.
2. The $\approx 100^\circ$ PA change reported by [Agudo et al. \(2011\)](#) resulted in a large drop in observed apparent speeds and radically different ejection position angles and trajectories. Recent data suggests that these values may be returning to their pre-2006 values. We suggest an alternate interpretation of this behaviour as due to a large disturbance at the jet base changing the jet pressure causing the location of downstream standing shocks to shift their locations in the jet and changing the viewing angle and hence the Doppler factor.
3. Radio flaring activity is found in both the “core” and stationary feature. A large mm-wave radio flare (R2) is found to be a superposition of flares in both the “core” and stationary feature. Gamma-ray flaring is found to likely originate in both the “core” and stationary feature, coinciding with the passage of components through both features.
4. The magnetic field, as derived from synchrotron self-absorption and from equipartition, decreases by ~ 75 between the “core” and stationary feature. This allows us to derive an estimate of the distance between the mm-wave “core” and the jet apex, r_{apex} . We find that r_{apex} is ≤ 6.0 pc upstream of the mm-wave “core” and the most upstream site of γ -ray emission.
5. We compute magnetic field strengths using synchrotron self absorption (SSA) and equipartition calculations and find consistent results to within $\sim 20\%$. We obtained $B_{\text{SSA}} \geq 1.6$ G and $B_{\text{equi}} \geq 1.2$ G in the “core”. In the stationary features, we obtain $B_{\text{SSA}} \leq 0.4$ G and $B_{\text{equi}} \leq 0.3$ G.
6. We also extrapolate estimates of the magnetic field strength to within the BLR and at the jet apex. Using SSA and assuming a toroidal magnetic field, this yields $B_{\text{BLR}} \lesssim 600$ G and $B_{\text{apex}} \lesssim 4000$ G. These results are broadly consistent with the estimates of the magnetic field strength at the jet base under scenario of magnetically arrested disks (MAD).

VLBI at 3 mm still currently lacks sensitivity and cadence, although the recently available 2 Gbps recording modes will improve the situation. Unfortunately with

only 6 month intervals, structural changes may be missed. In the future, it would be highly desirable to have monitoring at 3 mm (and 1 mm) at least as frequent as the ongoing 43 GHz monitoring. In a future paper, we will expand this analysis to other blazars observed at 3 mm to further investigate the physical conditions and dynamics of jets. We will also include polarisation observations, which may prove important in testing the location of γ -ray emission. In the next chapter, we investigate a novel approach to achieving microarcsecond scale resolution using lower resolution and lower frequency observations.

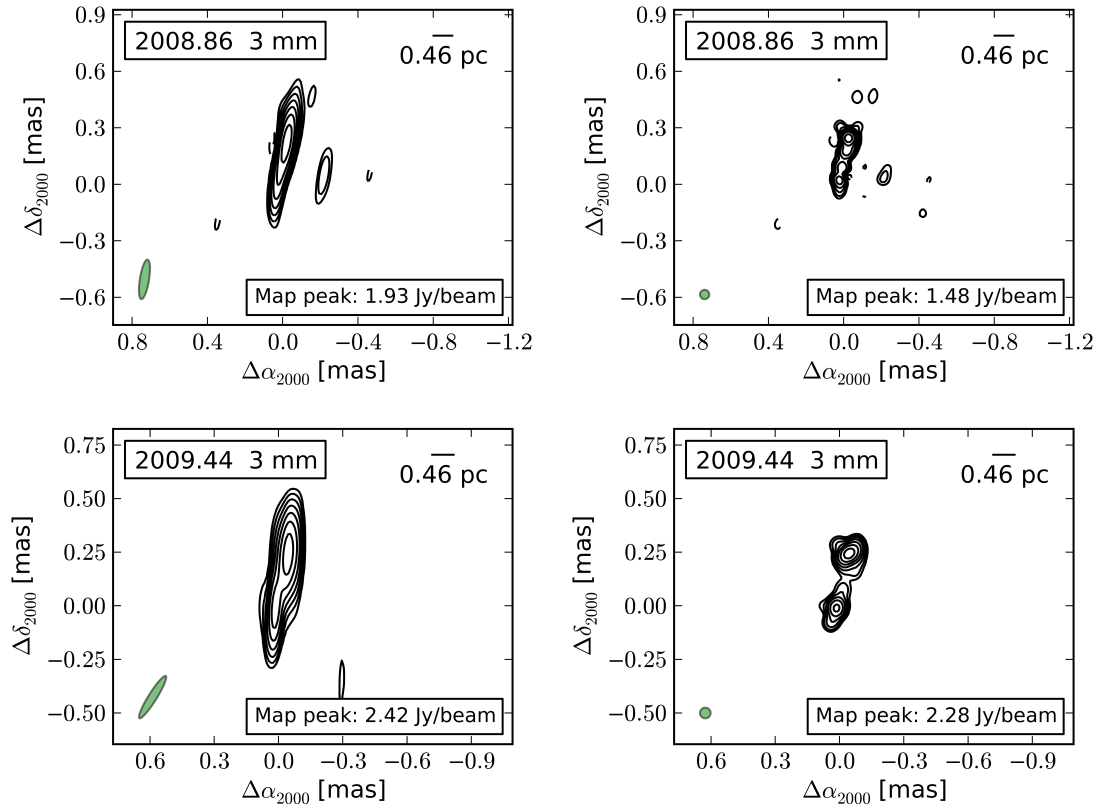


FIGURE 5.12: 3 mm maps of OJ287. Images to the left are convolved with the natural beam, images to the right are super-resolved with a 0.05 mas circular beam. Contours: -1, 1, 2, 4, 8, 16, 32, 64%.

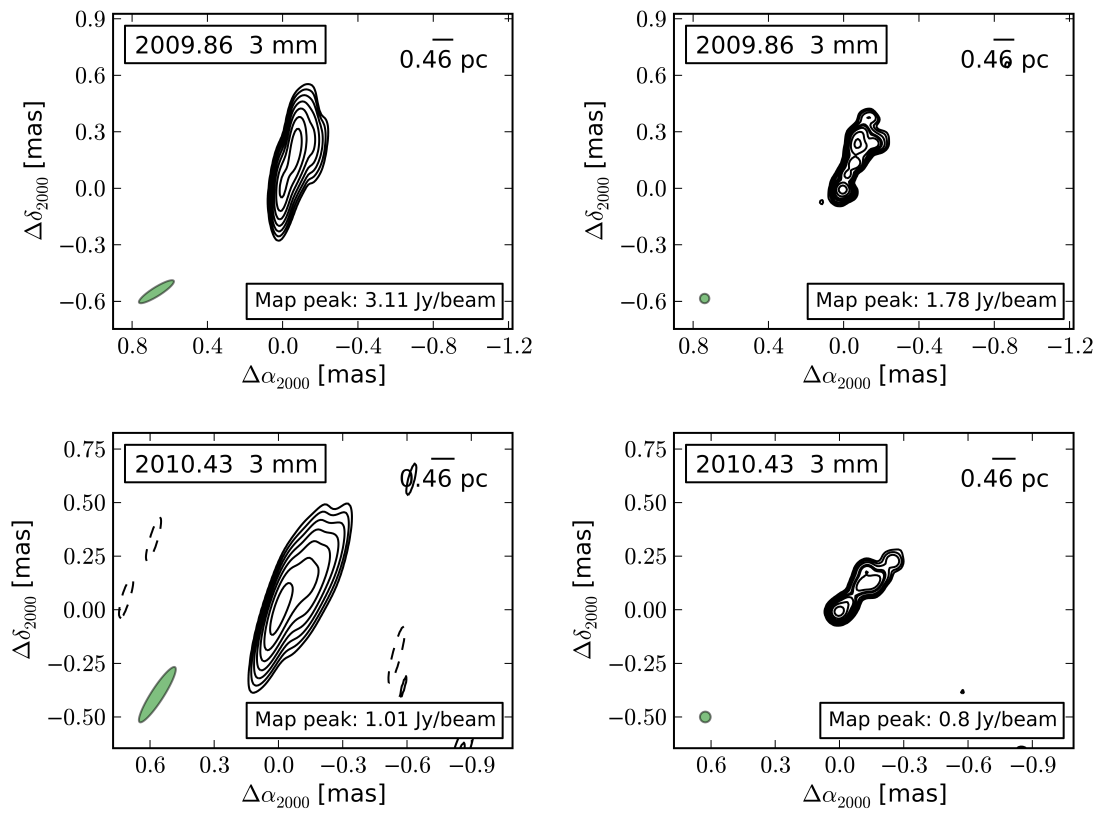


FIGURE 5.13: 3 mm maps of OJ287. Images to the left are convolved with the natural beam, images to the right are super-resolved with a 0.05 mas circular beam. Contours: -1, 1, 2, 4, 8, 16, 32, 64%.

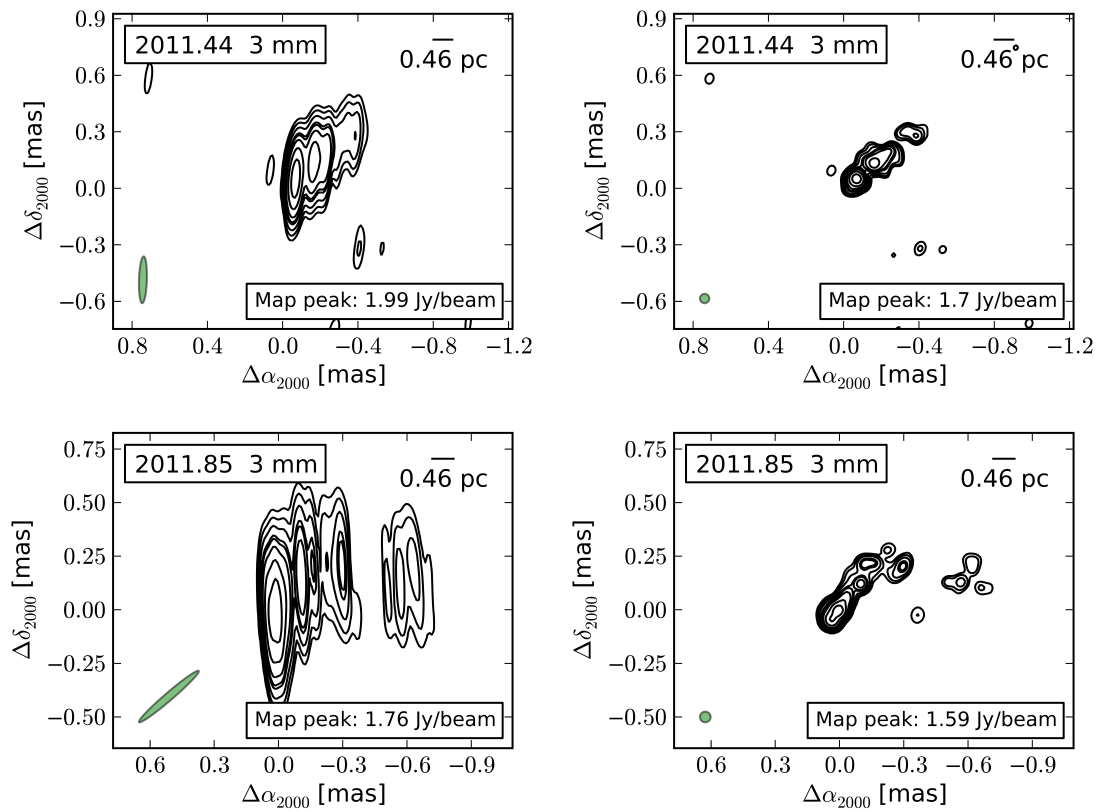


FIGURE 5.14: 3 mm maps of OJ287. Images to the left are convolved with the natural beam, images to the right are super-resolved with a 0.05 mas circular beam. Contours: -1, 1, 2, 4, 8, 16, 32, 64%.

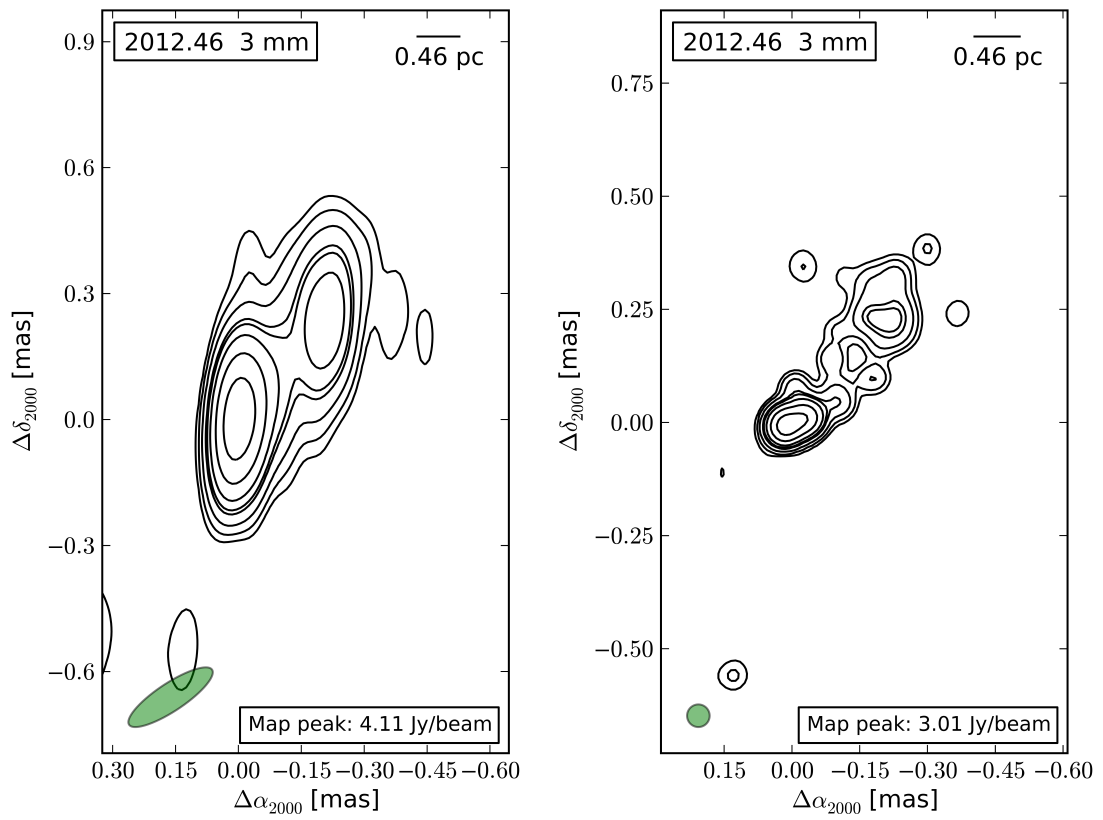


FIGURE 5.15: 3 mm maps of OJ287. Images to the left are convolved with the natural beam, images to the right are super-resolved with a 0.05 mas circular beam. Contours: -1, 1, 2, 4, 8, 16, 32, 64%.

Chapter 6

Conclusions and Future Perspectives

In this thesis, we have used the Global mm-VLBI Array (GMVA) at 3 mm to produce ultra-high resolution images of γ -ray blazars. Complimenting the use of the GMVA, we have used 7 mm maps as part of the BU-VLBA-BLAZAR monitoring program, 2 cm maps from the MOJAVE monitoring program, γ -ray data from the Fermi/LAT space telescope and radio total-intensity light curves from the FGAMMA and SMA blazar monitoring programs. Additionally, we have used data from the Australia Telescope Compact Array (ATCA) to observe the rapidly scintillating blazar PKS 1257-326, combined with VLBI observations from the TANAMI program and the Very Long Baseline Array (VLBA).

The study of these γ -ray bright blazars offers the astronomer a unique laboratory to investigate the physics of Active Galactic Nuclei (AGN) and how their jets are launched and collimated. Using mm-VLBI and scintillation imaging, we can probe these sources at sub-parsec scales. We can attempt to discriminate between jet launching models, find out if magnetic fields are important in jet launching, investigate the physical nature of common features observed in blazar jets at sub-parsec scales and explore the mechanisms required to produce high energy emission such as γ -rays.

In Chapter 1, we provided an overview of the history of astronomy, radio astronomy and VLBI studies, providing the broader context for this thesis. In Chapter 2, we produced a “back-to-front” description of the VLBI reduction and analysis process and in Chapter 3, we provided a thorough overview of the current state

of science relevant for the scientific work presented in this thesis.

The main objective of this thesis was to analyse an on-going 6 monthly monitoring program of γ -ray bright blazars using the GMVA. Data were observed between 2008 and 2012, with 26 sources observed at various times throughout this period. Five sources were fully analysed and presented, with 4 being presented in Chapter 4 and OJ 287 presented separately in Chapter 5.

In Chapter 4, we analysed in detail, from 2008 until 2012, a large number of 3 mm and 7 mm quasi-simultaneous VLBI maps to extract morphological, kinematic and spectral information at or near the turnover frequency for synchrotron self-absorption (SSA). Total-intensity radio and γ -ray light-curves were analysed for correlations with changes in morphology, kinematics and spectra over time. Using the data from spectral decompositions, magnetic field strengths were estimated and gradients found in the magnetic field strength at increasing “core” separations. Using the spatially resolved magnetic fields, we were then able to estimate the distance between the jet base and the mm-wave “core” and hence derive an estimate for the strength of the magnetic field at the jet base under the assumption of a conically expanding jet. Four sources in total (0716+714, 0836+710, 3C 273 and BL Lacertae) were analysed in this way.

The morphology of jets at 3 mm are broadly consistent with those seen at 7 mm and lower frequencies, but the sources analysed here consistently exhibit both moving and quasi-stationary features downstream of the VLBI “core” that can sometimes be more flux variable, more compact and exhibit higher brightness temperatures than the VLBI “core”. We find that component ejections appear to correlate in many cases with γ -rays likely being emitted from both the “core” region and these downstream stationary features. We interpret both the “core” and the downstream quasi-stationary features as being either recollimation or oblique shocks. Also often correlated with component ejections and γ -ray flaring is the exhibiting of optically thin (flux density decreasing with increasing frequency) in the “core” and stationary features. These features are normally expected to have optically thick (flux density not changing or increasing with increasing frequency) spectra. This behaviour is interpreted as optically thin travelling shocks interacting with either recollimation or oblique shocks, causing

both the flaring activity and the spectral changes due to blending of the stationary and travelling components.

The magnetic field structure of AGN jets and the role of magnetic fields near the black in their launching is another area of active research. Currently, observations and theory suggest that jets have a toroidal magnetic field ($B \propto r^{-(n)}$) where $n = 1$ or shallower ($n < 1$) magnetic field configuration. By computing the magnetic field strength at various distances from the “core” in the jets analysed and using their estimated viewing angles to de-project their linear separations, we find that the magnetic field decreases with increased de-projected separation from the VLBI “core” as $n = 0.3 \pm 0.2$. The strength of the magnetic field in the jet is, on average, $B \sim 0.6 - 0.9$ G.

If we assume that the jet is conically expanding and the jet has a toroidal magnetic field geometry of $n \leq 1$, we can estimate the distance from the mm-wave “core” to the base of the jet, and also estimate magnetic field strength there. On average, we find that the mm-wave “core” is ~ 1 -3 pc downstream of the base of the jet and the extrapolated magnetic field strength at the jet base ($R_{\text{jet}} = 10R_S$), is $B \sim 5 - 20 \times 10^3$ G. This would place γ -ray emission at least 1 pc downstream of the jet base and outside of the broad line region (BLR), suggesting the seed photons for γ -ray production come from within the jet. Recent observations and simulations expected strong magnetic fields near the base of the jet under the scenario of magnetically arrested accretion discs, and our estimates are consistent with this.

We find that the apparent brightness temperatures decrease with increased “core” separation, consistent with a slowly accelerating jet. Additionally, under the assumption of equipartition between magnetic field and relativistic particle energies, we can compute an equipartition Doppler factor, which we find to also be decreasing with increased “core” separation. The Doppler factor can be decreased with a higher viewing angle or higher Lorentz factor. By using several sources, viewing angle changes should be averaged out, suggesting an increase in Lorentz factor, consistent with the result of a slowly accelerating jet from brightness temperatures.

We analysed the source OJ287 in greater detail, using multi-frequency VLBI data at 2 cm, 7 mm and 3 mm, total intensity radio data at 2 cm, 7 mm, 3 mm,

1 mm, 0.85 mm and γ -ray data from the *Fermi*/LAT space telescope. We performed a detailed kinematic and spectral analysis using the multi-frequency VLBI data, we determined the spectrum and hence estimates of the magnetic field at multiple locations down the jet. We combine this with kinematics derived from 3 mm and 7 mm data to determine the location of radio and γ -ray flaring events within the jet.

We found that OJ287 exhibits two quasi-stationary features, components C (“core”) and S (“stationary feature”), that have very similar properties, with the “core” exhibiting an optically thin spectrum at times, consistent with the results in Chapter 4. Both are interpreted as either recollimation or oblique shocks. The northern quasi-stationary feature (S) appears to move on the sky relative to other components and we postulate that the “core” could also.

The $\approx 100^\circ$ PA change reported by [Agudo et al. \(2011\)](#) resulted in a large drop in observed apparent speeds and radically different ejection position angles and trajectories, which was interpreted as being due to the jet passing through our line-of-sight. Recent data suggests that these values may be returning to their pre-2006 values. We suggest an alternate interpretation of this behaviour as being caused large disturbance at the jet base changing the internal jet pressure, which in turn causes the location of downstream standing shocks to shift their locations. This therefore changes the viewing angle and hence the Doppler factor.

Radio flaring activity is found in both the “core” and stationary feature. A large mm-wave radio flare (R2) is found to be a superposition of flares in both the “core” and stationary feature. Gamma-ray flaring is found to likely originate in both the “core” and stationary feature, coinciding with the passage of components through both features.

The magnetic field, as derived from both synchrotron self-absorption and from equipartition, decreases by between $\sim 75\%$ between the “core” and stationary feature. This allows us to derive an estimate of the distance between the mm-wave “core” and the jet apex, r_{apex} . We find that r_{apex} is ≤ 6.0 pc upstream of the mm-wave “core” and the most upstream site of γ -ray emission. From SSA calculations, we find magnetic field strengths $B_{\text{SSA}} \geq 1.6$ G in the “core” and $B_{\text{SSA}} \leq 0.4$ G in the stationary feature. These values are $\sim 20\%$ higher than the

values from equipartition: $B_{\text{equi}} \geq 1.2 \text{ G}$ in the “core” and $B_{\text{SSA}} \leq 0.3 \text{ G}$ in the stationary feature. We extrapolated these estimates to within the BLR and at the jet apex. Using SSA and assuming a toroidal magnetic field, this yields $B_{\text{BLR}} \lesssim 600 \text{ G}$ and $B_{\text{apex}} \lesssim 4000 \text{ G}$. Under the model of magnetically arrested disks (MAD), we derived an estimate of $B_{\text{apex,MAD}} \sim 2000 \text{ G}$, which is consistent with our results.

The most significant findings of this thesis are the spectral changes correlated with component ejections and γ -ray flaring activity, the apparent decreases in magnetic field strength with increased “core” separation down the jet and the estimation of both the location of the mm-wave “core” from the jet base and the estimated magnetic field strengths close to the black hole.

The most significant limitations of these methods are the lack of cadence at 3 mm and the lack of high-frequency spectral coverage. Higher cadence at 3 mm (and possibly higher frequencies) could perhaps be achieved with ad-hoc observations using arrays such as the Korean VLBI Network (KVN) in conjunction with mm capable stations in Europe and (in the future) East Asia. In the future, the Event Horizon Telescope (EHT) will be able to provide even higher resolution maps with higher frequency spectral coverage, providing the scope to improve the spectral decompositions considerably. Additionally, imaging with the orbiting RadioAstron telescope provides high resolution imaging at 8 GHz and 22 GHz which would also provide additional spectral coverage with a matching observing beam.

With continued monitoring, work and effort, we will continue to investigate the mysteries of black holes and the jets that they produce.

Appendix A

Appendix A - Derived Magnetic Field Tables

ID	Epoch	ν (GHz)	S (Jy)	θ (mas)	α	B_{SSA}/δ (G)	B_{SSA} (G)	B_{equi} (G)	θ_{crit} (mas)	δ_{equi}
C1	2009.25	43	1.45 ± 0.14	0.044 ± 0.007	-0.72 ± 0.14	≤ 0.05	≤ 125.14	≤ 0.469	≤ 0.12	≤ 2.7
C2	2009.25	43	0.43 ± 0.04	0.066 ± 0.01	-0.9 ± 0.18	≤ 2.76	≤ 12217.53	≤ 0.234	≤ 0.068	≤ 0.5
C1	2009.75	43	1.60 ± 0.16	0.03 ± 0.004	-0.49 ± 0.1	≤ 0.01	≤ 11.44	≤ 0.668	≤ 0.125	≤ 5.7
C1	2010.25	43	2.22 ± 0.22	0.036 ± 0.005	-0.39 ± 0.08	≤ 0.01	≤ 9.3	≤ 0.628	≤ 0.146	≤ 5.4
C2	2010.25	86	0.67 ± 0.07	0.057 ± 0.009	0.34 ± 0.07	≥ 20.19	≥ 2467.37	≥ 0.366	≥ 0.042	≥ 0.3
C1	2011.25	86	2.11 ± 0.21	0.019 ± 0.003	0.4 ± 0.08	≥ 0.03	≥ 2.6	≥ 1.303	≥ 0.071	≥ 4.8
C2	2011.25	43	0.52 ± 0.05	0.046 ± 0.007	-0.66 ± 0.13	≤ 0.44	≤ 963.4	≤ 0.336	≤ 0.074	≤ 1.1
X6	2011.25	43	0.78 ± 0.08	0.057 ± 0.009	-1.48 ± 0.3	≤ 0.47	≤ 10878.38	≤ 0.315	≤ 0.089	≤ 1.0
C1	2011.75	43	3.14 ± 0.31	0.029 ± 0.004	-0.43 ± 0.09	≤ 0.0	≤ 2.19	≤ 0.833	≤ 0.172	≤ 10.5
C2	2011.75	86	0.59 ± 0.06	0.042 ± 0.006	0.71 ± 0.14	≥ 7.71	≥ 318.83	≥ 0.459	≥ 0.039	≥ 0.4
C1	2012.25	86	0.7 ± 0.07	0.036 ± 0.005	0.43 ± 0.09	≥ 2.97	≥ 279.15	≥ 0.551	≥ 0.043	≥ 0.6
X9	2012.25	43	0.28 ± 0.03	0.06 ± 0.009	-2.22 ± 0.44	≤ 4.44	≤ 891890.44	≤ 0.225	≤ 0.055	≤ 0.4
C1	AVER	43	1.755 ± 0.133	0.033 ± 0.001	-0.25 ± -0.05	≤ 0.011	≤ 0.181	≤ 0.619	≤ 0.007	≤ 4.698
C2	AVER	86	0.458 ± 0.032	0.028 ± 0.004	0.16 ± 0.03	≥ 2.511	≥ 42.691	≥ 0.606	≥ 0.087	≥ 0.646

TABLE A.1: An overview of B-fields in 0716+714.

ID	Epoch	ν (GHz)	S (Jy)	θ (mas)	α	B_{SSA}/δ (G)	B_{SSA} (G)	B_{equi} (G)	θ_{crit} (mas)	δ_{equi}
C1	2009.75	86	1.97 ± 0.2	0.3 ± 0.045	0.26 ± 0.05	≥ 728.82	≥ 147519.9	≥ 0.543	≥ 0.111	≥ 0.1
C2	2009.75	43	0.84 ± 0.08	0.03 ± 0.004	-2.3 ± 0.46	≤ 0.01	≤ 6581.12	≤ 2.5	≤ 0.148	≤ 7.6
C1	2010.25	43	3.37 ± 0.34	0.055 ± 0.008	-0.75 ± 0.15	≤ 0.01	≤ 39.26	≤ 2.205	≤ 0.285	≤ 8.3
C2	2010.25	86	0.3 ± 0.03	0.034 ± 0.005	0.66 ± 0.13	≥ 5.17	≥ 312.76	≥ 2.05	≥ 0.046	≥ 0.8
C1	2011.25	86	0.39 ± 0.04	0.041 ± 0.006	0.29 ± 0.06	≥ 6.43	≥ 1221.4	≥ 1.879	≥ 0.052	≥ 0.7
C2	2011.25	43	2.31 ± 0.23	0.052 ± 0.008	-1.34 ± 0.27	≤ 0.01	≤ 411.38	≤ 2.087	≤ 0.239	≤ 6.7
C1	2011.75	43	0.94 ± 0.09	0.062 ± 0.009	-1.91 ± 0.38	≤ 0.18	≤ 28704.96	≤ 1.376	≤ 0.156	≤ 2.4
C1	2012.25	43	0.37 ± 0.04	0.013 ± 0.002	-1.51 ± 0.3	≤ 0.0	≤ 104.69	≤ 4.053	≤ 0.101	≤ 16.8
C2	2012.25	86	0.82 ± 0.08	0.047 ± 0.007	0.31 ± 0.06	≥ 2.52	≥ 439.84	≥ 2.057	≥ 0.073	≥ 1.0
C1	AVER	43	1.328 ± 0.225	0.098 ± 0.024	-0.48 ± -0.1	≤ 0.547	≤ 11.656	≤ 0.995	≤ -0.021	≤ 1.321
C2	AVER	43	0.978 ± 0.142	0.048 ± 0.002	-0.98 ± -0.2	≤ 0.059	≤ 1.25	≤ 1.712	≤ -0.002	≤ 3.515
C3	AVER	43	0.393 ± 0.118	0.054 ± 0.014	-0.47 ± -0.09	≤ 0.569	≤ 12.127	≤ 1.199	≤ 0.026	≤ 1.385

TABLE A.2: An overview of B-fields in 0836+710

ID	Epoch	ν (GHz)	S (Jy)	θ (mas)	α	B_{SSA}/δ (G)	B_{SSA} (G)	B_{equi} (G)	θ_{crt} (mas)	δ_{equi}
C1	2008.75	86	6.14 ± 0.61	0.054 ± 0.008	0.65 ± 0.13	≥ 0.22	≥ 4.3	≥ 0.724	≥ 0.116	≥ 1.8
C2	2008.75	86	2.34 ± 0.23	0.096 ± 0.014	0.57 ± 0.11	≥ 14.96	≥ 352.14	≥ 0.335	≥ 0.074	≥ 0.3
X6	2008.75	43	1.61 ± 0.16	0.185 ± 0.028	-0.23 ± 0.05	≤ 13.73	≤ 1881.29	≤ 0.141	≤ 0.123	≤ 0.2
X5	2008.75	43	5.94 ± 0.59	0.425 ± 0.064	-0.29 ± 0.06	≤ 28.05	≤ 4324.3	≤ 0.1	≤ 0.228	≤ 0.2
C1	2009.25	86	2.92 ± 0.29	0.085 ± 0.013	0.9 ± 0.18	≥ 5.94	≥ 66.36	≥ 0.397	≥ 0.082	≥ 0.4
C2	2009.25	43	7.65 ± 0.77	0.08 ± 0.012	-0.49 ± 0.1	≤ 0.02	≤ 5.18	≤ 0.45	≤ 0.257	≤ 3.6
X7	2009.25	43	5.68 ± 0.57	0.075 ± 0.011	-0.25 ± 0.05	≤ 0.03	≤ 4.24	≤ 0.436	≤ 0.223	≤ 3.2
X6	2009.25	86	0.56 ± 0.06	0.112 ± 0.017	0.9 ± 0.18	≥ 484.66	≥ 5465.02	≥ 0.196	≥ 0.038	≥ 0.1
C1	2009.75	86	8.88 ± 0.89	0.039 ± 0.006	0.69 ± 0.14	≥ 0.03	≥ 0.51	≥ 1.067	≥ 0.138	≥ 4.3
C2	2009.75	86	2.94 ± 0.29	0.216 ± 0.032	0.15 ± 0.03	≥ 243.69	≥ 14364.09	≥ 0.179	≥ 0.082	≥ 0.1
X7	2009.75	43	4.48 ± 0.45	0.237 ± 0.036	-0.91 ± 0.18	≤ 4.81	≤ 2907.27	≤ 0.152	≤ 0.2	≤ 0.4
C1	2010.25	86	5.5 ± 0.55	0.109 ± 0.016	0.09 ± 0.02	≥ 4.53	≥ 301.34	≥ 0.384	≥ 0.11	≥ 0.5
C1x	2010.25	43	6.05 ± 0.6	0.112 ± 0.017	-1.83 ± 0.37	≤ 0.13	≤ 600.64	≤ 0.316	≤ 0.23	≤ 1.7
C2	2010.25	43	7.85 ± 0.78	0.108 ± 0.016	-0.64 ± 0.13	≤ 0.07	≤ 22.48	≤ 0.351	≤ 0.26	≤ 2.2
X6	2010.25	43	1.68 ± 0.17	0.175 ± 0.026	-0.03 ± 0.01	≤ 10.02	≤ 870.25	≤ 0.15	≤ 0.126	≤ 0.3
X4	2010.25	43	1.39 ± 0.14	0.338 ± 0.051	-0.31 ± 0.06	≤ 205.46	≤ 33473.52	≤ 0.081	≤ 0.115	≤ 0.1
C1	2011.25	86	4.42 ± 0.44	0.125 ± 0.019	0.61 ± 0.12	≥ 12.05	≥ 258.9	≥ 0.319	≥ 0.099	≥ 0.3
C2	2011.25	43	2.58 ± 0.26	0.067 ± 0.01	-0.45 ± 0.09	≤ 0.09	≤ 20.17	≤ 0.387	≤ 0.154	≤ 2.0
X9	2011.25	43	0.49 ± 0.05	0.113 ± 0.017	-0.61 ± 0.12	≤ 20.61	≤ 6549.29	≤ 0.153	≤ 0.071	≤ 0.2
X8	2011.25	43	0.84 ± 0.08	0.303 ± 0.045	-0.72 ± 0.14	≤ 361.18	≤ 144679.78	≤ 0.077	≤ 0.091	≤ 0.1
X7	2011.25	86	2.37 ± 0.24	0.264 ± 0.04	0.24 ± 0.05	≥ 835.42	≥ 40576.23	≥ 0.142	≥ 0.074	≥ 0.1
C1	2012.25	43	3.78 ± 0.38	0.03 ± 0.004	-0.71 ± 0.14	≤ 0.0	≤ 0.67	≤ 0.854	≤ 0.184	≤ 11.2
C2	2012.25	43	2.24 ± 0.22	0.066 ± 0.01	-1.83 ± 0.37	≤ 0.11	≤ 523.86	≤ 0.376	≤ 0.144	≤ 1.9
X10	2012.25	43	0.82 ± 0.08	0.148 ± 0.022	-1.71 ± 0.34	≤ 21.72	≤ 77706.11	≤ 0.141	≤ 0.09	≤ 0.2
C1	AVER	86	5.028 ± 0.363	0.078 ± 0.005	0.4 ± 0.08	≥ 1.404	≥ 12.636	≥ 0.525	≥ 0.168	≥ 0.783
C2	AVER	43	4.092 ± 0.435	0.091 ± 0.01	-0.43 ± -0.09	≤ 0.12	≤ 1.079	≤ 0.322	≤ 0.021	≤ 1.675

TABLE A.3: An overview of B-fields in 3C273

ID	Epoch	ν (GHz)	S (Jy)	θ (mas)	α	B_{SSA}/δ (G)	B_{SSA} (G)	B_{equi} (G)	θ_{crit} (mas)	δ_{equi}
C1	2009.25	86	1.32 ± 0.13	0.01 ± 0.002	0.28 ± 0.06	≥ 0.01	≥ 2.221	≥ 0.057	≥ 9.7	≥ 0.4
C2	2009.25	86	0.73 ± 0.07	0.046 ± 0.007	0.19 ± 0.04	≥ 8.84	≥ 476.94	≥ 0.508	≥ 0.043	≥ 1.0
C3	2009.25	43	0.92 ± 0.09	0.062 ± 0.009	-0.31 ± 0.06	≤ 0.57	≤ 93.5	≤ 0.344	≤ 0.096	≤ 10.6
C1	2009.75	43	1.78 ± 0.18	0.022 ± 0.003	-0.39 ± 0.08	≤ 0.0	≤ 0.46	≤ 1.009	≤ 0.13	≥ 2.7
C1a	2009.75	86	1.48 ± 0.15	0.022 ± 0.003	0.92 ± 0.18	≥ 0.11	≥ 1.19	≥ 1.168	≥ 0.06	≥ 0.4
C2	2009.75	86	0.52 ± 0.05	0.043 ± 0.006	0.18 ± 0.04	≥ 13.3	≥ 738.64	≥ 0.488	≥ 0.037	≥ 0.2
C3	2009.75	43	0.31 ± 0.03	0.089 ± 0.013	-1.25 ± 0.25	≤ 21.46	≤ 27869.71	≤ 0.185	≤ 0.057	≤ 30.1
C1	2010.25	43	2.11 ± 0.21	0.013 ± 0.002	-0.15 ± 0.03	≤ 0.0	≤ 0.02	≤ 1.662	≤ 0.141	≤ 3.3
C1a	2010.25	43	0.89 ± 0.09	0.031 ± 0.005	-0.48 ± 0.1	≤ 0.04	≤ 9.02	≤ 0.616	≤ 0.094	≤ 1.0
C2	2010.25	43	0.81 ± 0.08	0.059 ± 0.009	-0.13 ± 0.03	≤ 0.61	≤ 66.31	≤ 0.347	≤ 0.09	≤ 4.3
C1	2011.25	43	1.51 ± 0.15	0.034 ± 0.005	-0.04 ± 0.01	≤ 0.02	≤ 1.71	≤ 0.662	≤ 0.121	≤ 3.4
C1a	2011.25	43	1.14 ± 0.11	0.034 ± 0.005	-0.97 ± 0.19	≤ 0.03	≤ 23.64	≤ 0.608	≤ 0.106	≤ 0.4
C2	2011.25	43	0.78 ± 0.08	0.098 ± 0.015	-0.64 ± 0.13	≤ 4.94	≤ 1665.95	≤ 0.22	≤ 0.088	≤ 0.2
C3	2011.25	86	0.96 ± 0.1	0.078 ± 0.012	1.09 ± 0.22	≥ 42.06	≥ 310.23	≥ 0.35	≥ 0.049	≥ 0.8
C1	2012.25	86	3.19 ± 0.32	0.063 ± 0.009	0.07 ± 0.01	≥ 1.62	≥ 114.1	≥ 0.593	≥ 0.086	≥ 3.6
C2	2012.25	43	1.47 ± 0.15	0.037 ± 0.006	-1.71 ± 0.34	≤ 0.03	≤ 100.93	≤ 0.615	≤ 0.119	≥ 0.1
C3	2012.25	86	1.43 ± 0.14	0.174 ± 0.026	0.12 ± 0.02	≥ 474.28	≥ 30154.16	≥ 0.196	≥ 0.059	≤ 8.652
C1	AVER	43	1.906 ± 0.132	0.024 ± 0.001	-0.04 ± -0.01	≤ 0.003	≤ 0.021	≤ 0.929	≤ -0.014	≤ 1.863
C1a	AVER	43	0.937 ± 0.05	0.042 ± 0.004	-0.06 ± -0.01	≤ 0.115	≤ 0.803	≤ 0.473	≤ -0.087	≤ 0.738
C2	AVER	43	0.832 ± 0.068	0.068 ± 0.004	-0.5 ± -0.1	≤ 0.983	≤ 6.881	≤ 0.301	≤ -0.013	≥ 0.143
C3	AVER	86	0.815 ± 0.117	0.087 ± 0.014	0.12 ± 0.02	≥ 89.357	≥ 625.497	≥ 0.307	≥ 0.088	

TABLE A.4: An overview of B-fields in BL Lac

Appendix B

Appendix B - Modelfits

B.1 0716+714

TABLE B.1: Table of model-fit parameters

Epoch	ID	Flux (Jy)	FWHM (mas)	PA (°)	Core-sep. (mas)
2008.78					
2009.35	<i>C</i> ₁₄₃	1.45 ± 0.29	0.044 ± 0.06	0	0
	<i>C</i> ₁₈₆	0.88 ± 0.13	0.006 ± 0.02	0	0
	<i>C</i> ₂₄₃	0.43 ± 0.09	0.066 ± 0.06	40.8 ± 5	0.10 ± 0.03
	<i>C</i> ₂₈₆	0.23 ± 0.03	0.018 ± 0.02	34.6 ± 5	0.11 ± 0.01
	<i>X</i> ₁₈₆	0.01 ± 0.0	$0.0^* \pm 0.02$	34.8 ± 5	0.21 ± 0.01
	<i>E</i> ₁₄₃	0.07 ± 0.01	0.155 ± 0.06	2.2 ± 5	0.38 ± 0.03
	<i>E</i> _{1a86}	0.02 ± 0.01	$0.0^* \pm 0.02$	5.7 ± 5	0.35 ± 0.01
	<i>E</i> _{1b86}	0.12 ± 0.02	0.039 ± 0.02	1.0 ± 5	0.43 ± 0.01
	<i>E</i> ₂₄₃	0.07 ± 0.01	0.164 ± 0.06	7.9 ± 5	0.61 ± 0.03
	<i>E</i> ₂₈₆	0.02 ± 0.01	$0.0^* \pm 0.02$	11.2 ± 5	0.55 ± 0.01
	<i>E</i> ₃₄₃	0.02 ± 0.01	0.239 ± 0.06	4.8 ± 5	1.81 ± 0.03
	<i>E</i> ₃₈₆	0.09 ± 0.01	0.041 ± 0.02	22.0 ± 5	1.85 ± 0.01
2009.86	<i>C</i> ₁₄₃	1.60 ± 0.32	0.030 ± 0.06	0	0
	<i>C</i> ₁₈₆	1.08 ± 0.16	0.021 ± 0.02	0	0
	<i>C</i> ₂₈₆	0.06 ± 0.01	$0.0^* \pm 0.02$	67.8 ± 5	0.04 ± 0.01
	<i>C</i> ₂₄₃	0.47 ± 0.09	0.053 ± 0.06	51.0 ± 5	0.09 ± 0.03

Continues...

TABLE B.1: Table of model-fit parameters

Epoch	ID	Flux (Jy)	FWHM (mas)	PA (°)	Core-sep. (mas)
	X_{286}	0.15 ± 0.02	0.030 ± 0.02	40.3 ± 5	0.16 ± 0.01
	T_{143}	0.04 ± 0.01	0.164 ± 0.06	11.7 ± 5	0.5 ± 0.03
	X_{143}	0.05 ± 0.01	0.228 ± 0.06	13.7 ± 5	0.78 ± 0.03
	X_{1a86}	0.03 ± 0.01	$0.0^* \pm 0.02$	32.0 ± 5	0.72 ± 0.01
	X_{1b86}	0.02 ± 0.01	0.067 ± 0.02	30.4 ± 5	0.8 ± 0.01
	X_{1c86}	0.13 ± 0.02	0.162 ± 0.02	23.3 ± 5	0.91 ± 0.01
2010.36	C_{143}	2.22 ± 0.44	0.036 ± 0.06	0	0
	C_{186}	1.69 ± 0.25	0.010 ± 0.02	0	0
	C_{1x86}	0.38 ± 0.06	0.008 ± 0.02	65.4 ± 5	0.04 ± 0.01
	C_{243}	0.53 ± 0.11	0.055 ± 0.06	58.6 ± 5	0.11 ± 0.03
	C_{286}	0.67 ± 0.10	0.057 ± 0.02	73.5 ± 5	0.10 ± 0.01
	X_{343}	0.01 ± 0.01	0.0 ± 0.06	58.7 ± 5	0.25 ± 0.03
	X_{243}	0.05 ± 0.01	0.189 ± 0.06	11.8 ± 5	0.53 ± 0.03
	X_{2a86}	0.29 ± 0.04	0.046 ± 0.02	23.8 ± 5	0.27 ± 0.01
	X_{2b86}	0.10 ± 0.02	0.027 ± 0.02	42.7 ± 5	0.33 ± 0.01
	X_{2c86}	0.13 ± 0.02	0.02 ± 0.02	6.4 ± 5	0.38 ± 0.01
	X_{143}	0.02 ± 0.0	0.494 ± 0.06	14.7 ± 5	1.57 ± 0.03
	T_{186}	0.02 ± 0.0	0.0 ± 0.02	17.2 ± 5	1.18 ± 0.01
	X_{186}	0.06 ± 0.01	0.073 ± 0.02	15.4 ± 5	1.54 ± 0.01
2011.35	C_{143}	1.6 ± 0.32	0.026 ± 0.06	0	0
	C_{186}	2.11 ± 0.32	0.019 ± 0.02	0	0
	C_{243}	0.52 ± 0.10	0.046 ± 0.06	31.5 ± 5	0.08 ± 0.03
	C_{286}	0.33 ± 0.05	0.023 ± 0.02	16.9 ± 5	0.08 ± 0.01
	X_{643}	0.78 ± 0.16	0.057 ± 0.06	27.7 ± 5	0.17 ± 0.03
	X_{686}	0.28 ± 0.04	0.017 ± 0.02	49.3 ± 5	0.16 ± 0.01
	X_{543}	0.18 ± 0.04	0.290 ± 0.06	33.5 ± 5	0.32 ± 0.03
	X_{586}	0.53 ± 0.08	0.347 ± 0.02	41.4 ± 5	0.35 ± 0.01
	U_{143}	0.06 ± 0.01	0.230 ± 0.06	-39.0 ± 5	0.31 ± 0.03
	U_{186}	0.16 ± 0.02	$0.0^* \pm 0.02$	-3.9 ± 5	0.16 ± 0.01
	X_{443}	0.02 ± 0.01	0.126 ± 0.06	-3.2 ± 5	0.78 ± 0.03
	X_{486}	0.20 ± 0.03	0.278 ± 0.02	-11.9 ± 5	0.77 ± 0.01
	T_{386}	0.23 ± 0.03	0.185 ± 0.02	20.4 ± 5	0.91 ± 0.01

Continues...

TABLE B.1: Table of model-fit parameters

Epoch	ID	Flux (Jy)	FWHM (mas)	PA (°)	Core-sep. (mas)
	X_{343}	0.02 ± 0.01	0.289 ± 0.06	13.6 ± 5	1.39 ± 0.03
	X_{143}	0.02 ± 0.01	0.146 ± 0.06	13.1 ± 5	2.47 ± 0.03
	X_{186}	0.11 ± 0.02	0.039 ± 0.02	18.5 ± 5	2.43 ± 0.01
2011.75	C_{143}	3.14 ± 0.63	0.029 ± 0.06	0	0
	C_{186}	2.33 ± 0.35	0.029 ± 0.02	0	0
	C_{243}	0.36 ± 0.07	0.066 ± 0.06	37.0 ± 5	0.15 ± 0.03
	C_{286}	0.59 ± 0.09	0.042 ± 0.02	31.5 ± 5	0.08 ± 0.01
	X_{743}	0.09 ± 0.02	0.232 ± 0.06	34.1 ± 5	0.42 ± 0.03
	X_{786}	0.23 ± 0.03	0.058 ± 0.02	31.8 ± 5	0.23 ± 0.01
	X_{543}	0.06 ± 0.01	0.308 ± 0.06	27.7 ± 5	0.86 ± 0.03
	X_{586}	0.29 ± 0.04	0.217 ± 0.02	17.8 ± 5	0.84 ± 0.01
	X_{243}	0.03 ± 0.01	1.081 ± 0.06	3.3 ± 5	1.58 ± 0.03
2012.38	C_{143}	0.52 ± 0.10	0.036 ± 0.06	0	0
	C_{186}	0.70 ± 0.10	0.036 ± 0.02	0	0
	X_{943}	0.28 ± 0.06	0.060 ± 0.06	32.0 ± 5	0.10 ± 0.03
	X_{986}	0.06 ± 0.01	0.070 ± 0.02	22.8 ± 5	0.17 ± 0.01
	X_{843}	0.12 ± 0.02	0.176 ± 0.06	25.0 ± 5	0.40 ± 0.03
	X_{886}	0.10 ± 0.02	0.102 ± 0.02	23.0 ± 5	0.46 ± 0.01
	X_{743}	0.01 ± 0.01	0.146 ± 0.06	30.2 ± 5	0.69 ± 0.03
	X_{443}	0.03 ± 0.01	0.574 ± 0.06	23.0 ± 5	1.74 ± 0.03
	X_{486}	0.09 ± 0.01	0.379 ± 0.02	18.1 ± 5	1.58 ± 0.01

Continues...

B.2 0836+710

TABLE B.2: Table of model-fit parameters

Epoch	ID	Flux (Jy)	FWHM (mas)	PA (°)	Core-sep. (mas)
2008.78	-	-	-		
2009.35					
2009.86	<i>C</i> ₁₄₃	1.64 ± 0.33	0.028 ± 0.06	0	0
	<i>C</i> ₁₈₆	1.97 ± 0.30	0.034 ± 0.02	0	0
	<i>C</i> ₂₄₃	0.84 ± 0.17	0.030 ± 0.06	-128.6 ± 5	0.06 ± 0.03
	<i>C</i> ₂₈₆	0.67 ± 0.03	0.026 ± 0.02	-148.2 ± 5	0.14 ± 0.01
	<i>C</i> ₃₄₃	0.02 ± 0.01	$0.0^* \pm 0.06$	-128.3 ± 5	0.22 ± 0.03
	<i>C</i> ₃₈₆	0.07 ± 0.01	$0.0^* \pm 0.02$	-133.1 ± 5	0.24 ± 0.01
	<i>F</i> _{1a86}	0.06 ± 0.01	$0.0^* \pm 0.02$	-154.1 ± 5	0.46 ± 0.01
	<i>F</i> ₁₄₃	0.01 ± 0.01	0.096 ± 0.06	-131.3 ± 5	0.59 ± 0.03
	<i>F</i> _{1b86}	0.03 ± 0.01	0.020 ± 0.02	-136.3 ± 5	0.65 ± 0.01
	<i>F</i> ₂₄₃	0.01 ± 0.01	0.201 ± 0.06	-140.6 ± 5	1.34 ± 0.03
	<i>F</i> ₂₈₆	0.05 ± 0.01	0.029 ± 0.02	-132.7 ± 5	1.13 ± 0.01
	<i>E</i> ₁₄₃	0.05 ± 0.01	0.737 ± 0.06	-139.5 ± 5	2.3 ± 0.03
	<i>E</i> ₁₈₆	0.14 ± 0.02	0.200 ± 0.02	-133.9 ± 5	2.2 ± 0.01
	<i>E</i> ₂₄₃	0.01 ± 0.0	0.613 ± 0.06	-143.4 ± 5	3.29 ± 0.03
	<i>E</i> ₂₈₆	0.03 ± 0.0	0.028 ± 0.02	-140.8 ± 5	3.22 ± 0.01
2010.36	<i>C</i> ₁₄₃	3.37 ± 0.67	0.055 ± 0.06	0	0
	<i>C</i> ₁₈₆	2.01 ± 0.3	0.05 ± 0.02	0	0
	<i>C</i> ₂₄₃	0.19 ± 0.04	0.043 ± 0.06	-137.1 ± 5	0.09 ± 0.03
	<i>C</i> ₂₈₆	0.3 ± 0.04	0.034 ± 0.02	-140.3 ± 5	0.09 ± 0.01
	<i>X</i> ₁₈₆	0.21 ± 0.03	0.04 ± 0.02	-120.0 ± 5	0.22 ± 0.01
	<i>E</i> ₁₄₃	0.04 ± 0.01	0.505 ± 0.06	-142.4 ± 5	2.51 ± 0.03
	<i>E</i> ₁₈₆	0.24 ± 0.04	0.607 ± 0.02	-121.6 ± 5	2.29 ± 0.01
	<i>E</i> ₂₄₃	0.0 ± 0.0	0.387 ± 0.06	-145.5 ± 5	3.33 ± 0.03
	<i>E</i> ₂₈₆	0.14 ± 0.02	0.232 ± 0.02	-123.6 ± 5	3.61 ± 0.01
2011.35	<i>C</i> ₁₄₃	0.32 ± 0.06	0.028 ± 0.06	0	0
	<i>C</i> ₁₈₆	0.39 ± 0.06	0.041 ± 0.02	0	0
	<i>C</i> ₂₄₃	2.31 ± 0.46	0.052 ± 0.06	-139.1 ± 5	0.12 ± 0.03

Continues...

TABLE B.2: Table of model-fit parameters

Epoch	ID	Flux (Jy)	FWHM (mas)	PA (°)	Core-sep. (mas)
	<i>C2</i> ₈₆	0.91 ± 0.14	0.051 ± 0.02	-135.9 ± 5	0.12 ± 0.01
	<i>C3</i> ₄₃	0.29 ± 0.06	0.014 ± 0.06	-141.0 ± 5	0.21 ± 0.03
	<i>C3</i> ₈₆	0.35 ± 0.05	0.068 ± 0.02	-128.7 ± 5	0.27 ± 0.01
	<i>U</i> ₁₄₃	0.01 ± 0.0	$0.0^* \pm 0.06$	-136.1 ± 5	0.37 ± 0.03
	<i>X</i> ₁₈₆	0.03 ± 0.0	0.021 ± 0.02	-126.6 ± 5	0.60 ± 0.01
	<i>E</i> ₁₄₃	0.09 ± 0.02	1.317 ± 0.06	-142.4 ± 5	1.98 ± 0.03
	<i>E2</i> ₄₃	0.06 ± 0.01	0.154 ± 0.06	-139.6 ± 5	2.81 ± 0.03
2011.75	<i>C0</i> ₄₃	0.20 ± 0.04	0.051 ± 0.06	37.0 ± 5	0.13 ± 0.03
	<i>C0</i> ₈₆	0.03 ± 0.01	0.028 ± 0.02	37.4 ± 5	0.18 ± 0.01
	<i>C1</i> ₄₃	0.94 ± 0.19	0.062 ± 0.06	0.0 ± 5	0.0 ± 0.03
	<i>C1</i> ₈₆	0.65 ± 0.04	0.030 ± 0.02	0.0 ± 5	0.0 ± 0.01
	<i>C1x</i> ₈₆	0.75 ± 0.11	0.010 ± 0.02	-147.2 ± 5	0.04 ± 0.01
	<i>C2</i> ₄₃	0.89 ± 0.18	0.066 ± 0.06	-148.0 ± 5	0.09 ± 0.03
	<i>C2</i> ₈₆	0.58 ± 0.04	0.023 ± 0.02	-143.5 ± 5	0.08 ± 0.01
	<i>C3</i> ₄₃	0.04 ± 0.01	0.104 ± 0.06	-152.6 ± 5	0.28 ± 0.03
	<i>C3a</i> ₈₆	0.06 ± 0.01	0.006 ± 0.02	-149.7 ± 5	0.21 ± 0.01
	<i>C3b</i> ₈₆	0.15 ± 0.02	0.046 ± 0.02	-144.9 ± 5	0.26 ± 0.01
2012.38	<i>C1</i> ₄₃	0.37 ± 0.07	0.013 ± 0.06	0	0
	<i>C1</i> ₈₆	0.13 ± 0.02	0.059 ± 0.02	0	0
	<i>C2</i> ₄₃	0.66 ± 0.13	0.049 ± 0.06	-140.0 ± 5	0.08 ± 0.03
	<i>C2</i> ₈₆	0.82 ± 0.12	0.047 ± 0.02	-134.2 ± 5	0.10 ± 0.01
	<i>C3</i> ₄₃	0.87 ± 0.17	0.101 ± 0.06	-146.7 ± 5	0.29 ± 0.03
	<i>C3</i> ₈₆	0.43 ± 0.06	0.090 ± 0.02	-143.4 ± 5	0.33 ± 0.01
	<i>X1a</i> ₈₆	0.14 ± 0.02	0.302 ± 0.02	-146.0 ± 5	1.44 ± 0.01
	<i>X1b</i> ₈₆	0.06 ± 0.01	0.24 ± 0.02	-144.9 ± 5	1.78 ± 0.01
	<i>E1</i> ₄₃	0.02 ± 0.0	0.358 ± 0.06	-144.2 ± 5	2.07 ± 0.03
	<i>E2</i> ₄₃	0.09 ± 0.02	0.207 ± 0.06	-139.6 ± 5	2.83 ± 0.03
	<i>E2</i> ₈₆	0.02 ± 0.0	0.027 ± 0.02	-145.6 ± 5	2.82 ± 0.01
	<i>E3</i> ₈₆	0.08 ± 0.01	0.29 ± 0.02	-149.2 ± 5	3.25 ± 0.01

Continues...

B.3 3C 273

TABLE B.3: Table of model-fit parameters

Epoch	ID	Flux (Jy)	FWHM (mas)	PA (°)	Core-sep. (mas)
2008.78	<i>C</i> 1 ₄₃	3.91 ± 0.78	0.030 ± 0.06	0	0
	<i>C</i> 1 ₈₆	6.14 ± 0.92	0.054 ± 0.02	0	0
	<i>C</i> 2 ₄₃	1.58 ± 0.32	0.010 ± 0.06	-128.3 ± 5	0.11 ± 0.03
	<i>C</i> 2 ₈₆	2.34 ± 0.35	0.096 ± 0.02	-131.0 ± 5	0.14 ± 0.01
	<i>X</i> 6 ₄₃	1.61 ± 0.32	0.185 ± 0.06	-144.9 ± 5	0.61 ± 0.03
	<i>X</i> 6 ₈₆	1.37 ± 0.21	0.272 ± 0.02	-141.1 ± 5	0.56 ± 0.01
	<i>X</i> 5 ₄₃	5.94 ± 1.19	0.425 ± 0.06	-143.2 ± 5	1.26 ± 0.03
	<i>X</i> 5 ₈₆	4.87 ± 0.73	0.399 ± 0.02	-144.2 ± 5	1.23 ± 0.01
	<i>X</i> 4 ₄₃	1.20 ± 0.24	0.760 ± 0.06	-142.1 ± 5	2.67 ± 0.03
	<i>X</i> 4 ₈₆	0.26 ± 0.04	0.179 ± 0.02	-148.7 ± 5	2.62 ± 0.01
	<i>X</i> 3 ₄₃	0.67 ± 0.13	0.211 ± 0.06	-143.5 ± 5	3.78 ± 0.03
	<i>X</i> 3 ₈₆	0.14 ± 0.02	0.043 ± 0.02	-138.0 ± 5	3.30 ± 0.01
	<i>X</i> 2 ₄₃	0.61 ± 0.12	0.558 ± 0.06	-140.9 ± 5	4.34 ± 0.03
	<i>X</i> 2 ₈₆	0.61 ± 0.09	0.744 ± 0.02	-134.3 ± 5	4.47 ± 0.01
	<i>X</i> 1 ₄₃	0.94 ± 0.19	1.820 ± 0.06	-134.9 ± 5	6.55 ± 0.03
2009.35	<i>C</i> 1 ₄₃	1.56 ± 0.31	0.072 ± 0.06	0	0
	<i>C</i> 1 ₈₆	2.92 ± 0.44	0.085 ± 0.02	0	0
	<i>C</i> 2 ₄₃	7.65 ± 1.53	0.08 ± 0.06	-131.3 ± 5	0.17 ± 0.03
	<i>C</i> 2 ₈₆	5.43 ± 0.81	0.073 ± 0.02	-140.9 ± 5	0.18 ± 0.01
	<i>X</i> 7 ₄₃	5.68 ± 1.14	0.075 ± 0.06	-140.1 ± 5	0.35 ± 0.03
	<i>X</i> 7 ₈₆	4.78 ± 0.72	0.086 ± 0.02	-142.6 ± 5	0.33 ± 0.01
	<i>X</i> 6 ₄₃	0.3 ± 0.06	0.087 ± 0.06	-158.4 ± 5	0.86 ± 0.03
	<i>X</i> 6 ₈₆	0.56 ± 0.08	0.112 ± 0.02	-146.7 ± 5	0.69 ± 0.01
	<i>X</i> 5 ₄₃	4.92 ± 0.98	0.651 ± 0.06	-140.8 ± 5	1.61 ± 0.03
	<i>X</i> 5 ₈₆	4.01 ± 0.6	0.642 ± 0.02	-143.5 ± 5	1.50 ± 0.01
	<i>X</i> 4 ₄₃	1.61 ± 0.32	0.214 ± 0.06	-147.1 ± 5	3.12 ± 0.03
	<i>X</i> 4 ₈₆	0.73 ± 0.11	0.175 ± 0.02	-148.0 ± 5	3.13 ± 0.01
	<i>X</i> 4 _{a43}	0.49 ± 0.1	0.479 ± 0.06	-135.9 ± 5	3.26 ± 0.03
	<i>X</i> 3 ₄₃	0.52 ± 0.1	0.271 ± 0.06	-141.2 ± 5	4.10 ± 0.03
	<i>X</i> 3 ₄₃	0.51 ± 0.1	0.316 ± 0.06	-142.4 ± 5	4.57 ± 0.03
	<i>X</i> 2 ₄₃	0.35 ± 0.07	0.615 ± 0.06	-138.5 ± 5	5.63 ± 0.03

Continues...

TABLE B.3: Table of model-fit parameters

Epoch	ID	Flux (Jy)	FWHM (mas)	PA (°)	Core-sep. (mas)
	<i>X</i> 2 ₈₆	0.35 ± 0.05	0.397 ± 0.02	-139.3 ± 5	5.8 ± 0.01
	<i>X</i> 1 ₄₃	0.68 ± 0.14	1.697 ± 0.06	-131.7 ± 5	7.49 ± 0.03
2009.86	<i>C</i> 1 ₄₃	5.52 ± 1.1	0.115 ± 0.06	0	0
	<i>C</i> 1 ₈₆	8.88 ± 1.33	0.039 ± 0.02	0	0
	<i>C</i> 2 ₄₃	2.65 ± 0.53	0.214 ± 0.06	-139.7 ± 5	0.21 ± 0.03
	<i>C</i> 2 ₈₆	2.94 ± 0.44	0.216 ± 0.02	-139.2 ± 5	0.27 ± 0.01
	<i>X</i> 7 ₄₃	4.48 ± 0.9	0.237 ± 0.06	-143.6 ± 5	0.56 ± 0.03
	<i>X</i> 7 ₈₆	2.39 ± 0.36	0.068 ± 0.02	-144.7 ± 5	0.6 ± 0.01
	<i>X</i> 5 ₄₃	4.17 ± 0.83	0.784 ± 0.06	-141.7 ± 5	1.78 ± 0.03
	<i>X</i> 5 _{a86}	0.61 ± 0.09	0.078 ± 0.02	-146.0 ± 5	1.45 ± 0.01
	<i>X</i> 5 _{b86}	0.64 ± 0.1	0.058 ± 0.02	-133.5 ± 5	1.94 ± 0.01
	<i>X</i> 5 _{c86}	0.93 ± 0.14	0.252 ± 0.02	-140.2 ± 5	2.27 ± 0.01
	<i>X</i> 4 ₄₃	2.1 ± 0.42	0.305 ± 0.06	-145.6 ± 5	3.38 ± 0.03
	<i>X</i> 4 _{a86}	0.82 ± 0.12	0.049 ± 0.02	-147.1 ± 5	3.44 ± 0.01
	<i>X</i> 4 _{b86}	0.71 ± 0.11	0.033 ± 0.02	-148.2 ± 5	3.94 ± 0.01
	<i>X</i> 3 ₄₃	0.87 ± 0.17	0.793 ± 0.06	-139.3 ± 5	4.77 ± 0.03
	<i>X</i> 2 ₄₃	0.21 ± 0.04	0.328 ± 0.06	-135.4 ± 5	5.89 ± 0.03
	<i>X</i> 2 _{a86}	0.31 ± 0.05	0.272 ± 0.02	-114.1 ± 5	5.58 ± 0.01
	<i>X</i> 2 _{b86}	0.16 ± 0.02	0.039 ± 0.02	-132.4 ± 5	5.66 ± 0.01
2010.36	<i>C</i> 1 ₄₃	5.15 ± 1.03	0.106 ± 0.06	0	0
	<i>C</i> 1 ₈₆	5.5 ± 0.82	0.109 ± 0.02	0	0
	<i>C</i> 1 _{x43}	6.05 ± 1.21	0.112 ± 0.06	-140.4 ± 5	0.17 ± 0.03
	<i>C</i> 1 _{x86}	1.7 ± 0.26	0.05 ± 0.02	-135.4 ± 5	0.11 ± 0.01
	<i>C</i> 2 ₄₃	7.85 ± 1.57	0.108 ± 0.06	-142.3 ± 5	0.38 ± 0.03
	<i>C</i> 2 ₈₆	5.03 ± 0.75	0.087 ± 0.02	-137.2 ± 5	0.30 ± 0.01
	<i>X</i> 7 ₄₃	1.91 ± 0.38	0.258 ± 0.06	-145.2 ± 5	0.78 ± 0.03
	<i>X</i> 6 ₄₃	1.68 ± 0.34	0.175 ± 0.06	-138.2 ± 5	1.09 ± 0.03
	<i>X</i> 6 ₈₆	1.65 ± 0.25	0.198 ± 0.02	-140.9 ± 5	0.98 ± 0.01
	<i>X</i> 5 ₄₃	3.19 ± 0.64	0.806 ± 0.06	-143.7 ± 5	2.29 ± 0.03
	<i>X</i> 5 ₈₆	1.24 ± 0.19	0.28 ± 0.02	-142.9 ± 5	2.66 ± 0.01
	<i>X</i> 4 ₄₃	1.39 ± 0.28	0.338 ± 0.06	-144.0 ± 5	3.86 ± 0.03

Continues...

TABLE B.3: Table of model-fit parameters

Epoch	ID	Flux (Jy)	FWHM (mas)	PA (°)	Core-sep. (mas)
	X_{486}	1.12 ± 0.17	0.192 ± 0.02	-143.7 ± 5	3.79 ± 0.01
2011.35	C_{143}	2.9 ± 0.58	0.081 ± 0.06	0	0
	C_{186}	4.42 ± 0.66	0.125 ± 0.02	0	0
	C_{243}	2.58 ± 0.52	0.067 ± 0.06	-146.1 ± 5	0.15 ± 0.03
	C_{286}	1.89 ± 0.28	0.064 ± 0.02	-147.9 ± 5	0.18 ± 0.01
	X_{943}	0.49 ± 0.1	0.113 ± 0.06	-146.0 ± 5	0.36 ± 0.03
	X_{986}	0.32 ± 0.05	0.175 ± 0.02	-151.2 ± 5	0.46 ± 0.01
	X_{843}	0.84 ± 0.17	0.303 ± 0.06	-138.7 ± 5	0.88 ± 0.03
	X_{886}	0.51 ± 0.08	0.16 ± 0.02	-138.1 ± 5	0.81 ± 0.01
	X_{743}	2.01 ± 0.4	0.188 ± 0.06	-141.7 ± 5	1.25 ± 0.03
	X_{786}	2.37 ± 0.36	0.264 ± 0.02	-141.3 ± 5	1.2 ± 0.01
	X_{243}	0.79 ± 0.16	0.43 ± 0.06	-143.2 ± 5	1.96 ± 0.03
	X_{286}	0.49 ± 0.07	0.447 ± 0.02	-139.6 ± 5	1.89 ± 0.01
	X_{343}	1.2 ± 0.24	0.546 ± 0.06	-146.4 ± 5	3.23 ± 0.03
	X_{3a86}	0.3 ± 0.04	0.045 ± 0.02	-147.9 ± 5	3.33 ± 0.01
	X_{3b86}	0.47 ± 0.07	0.44 ± 0.02	-148.4 ± 5	3.02 ± 0.01
	X_{286}	0.53 ± 0.08	0.947 ± 0.02	-133.1 ± 5	4.76 ± 0.01
2011.75					
2012.38	C_{143}	3.78 ± 0.76	0.0 ± 0.06	0	0
	C_{186}	2.31 ± 0.35	0.054 ± 0.02	0	0
	C_{286}	1.98 ± 0.27	0.063 ± 0.02	-134.8 ± 5	0.13 ± 0.01
	C_{243}	2.24 ± 0.45	0.066 ± 0.06	-136.4 ± 5	0.27 ± 0.03
	X_{1186}	0.63 ± 0.09	0.124 ± 0.02	-138.3 ± 5	0.36 ± 0.01
	X_{1043}	0.82 ± 0.16	0.148 ± 0.06	-144.6 ± 5	0.62 ± 0.03
	X_{1086}	0.25 ± 0.04	0.07 ± 0.02	-144.0 ± 5	0.58 ± 0.01
	X_{943}	0.32 ± 0.06	0.088 ± 0.06	-140.9 ± 5	1.13 ± 0.03
	X_{986}	0.89 ± 0.13	0.325 ± 0.02	-132.9 ± 5	1.22 ± 0.01
	X_{743}	1.63 ± 0.33	0.58 ± 0.06	-141.4 ± 5	2.5 ± 0.03
	X_{786}	0.36 ± 0.05	0.312 ± 0.02	-143.2 ± 5	1.94 ± 0.01
	X_{686}	0.54 ± 0.08	0.294 ± 0.02	-147.7 ± 5	3.42 ± 0.01
	U_{143}	1.56 ± 0.31	0.489 ± 0.06	-145.6 ± 5	4.18 ± 0.03
	U_{1a86}	0.66 ± 0.10	0.288 ± 0.02	-146.3 ± 5	4.27 ± 0.01

Continues...

TABLE B.3: Table of model-fit parameters

Epoch	ID	Flux (Jy)	FWHM (mas)	PA (°)	Core-sep. (mas)
	$U1b_{86}$	0.40 ± 0.06	0.181 ± 0.02	-139.9 ± 5	4.71 ± 0.01

Continues...

B.4 BL Lac

TABLE B.4: Table of model-fit parameters

Epoch	ID	Flux (Jy)	FWHM (mas)	PA (°)	Core-sep. (mas)
2008.78	-	-	-		
2009.35	$C1_{43}$	1.09 ± 0.15	0.025 ± 0.06	0	0
	$C1_{86}$	1.32 ± 0.26	0.010 ± 0.02	0	0
	$C1a_{86}$	0.85 ± 0.17	0.023 ± 0.02	-178.6 ± 5	0.06 ± 0.01
	$C2_{43}$	0.64 ± 0.10	0.057 ± 0.06	-174.3 ± 5	0.15 ± 0.03
	$C2_{86}$	0.73 ± 0.15	0.046 ± 0.02	-172.5 ± 5	0.17 ± 0.01
	$C3_{43}$	0.92 ± 0.14	0.062 ± 0.06	-168.6 ± 5	0.34 ± 0.03
	$C3_{86}$	0.74 ± 0.15	0.069 ± 0.02	-165.8 ± 5	0.35 ± 0.01
	$X5_{43}$	0.16 ± 0.03	0.055 ± 0.06	-165.5 ± 5	0.44 ± 0.03
	$X4_{43}$	0.05 ± 0.01	0.34 ± 0.06	-165.0 ± 5	1.15 ± 0.03
	$X4_{86}$	0.09 ± 0.03	0.06 ± 0.06	-148.9 ± 5	1.09 ± 0.03
	$X3_{43}$	0.10 ± 0.02	0.27 ± 0.06	-165.5 ± 5	1.51 ± 0.03
	$X3_{86}$	0.20 ± 0.02	0.23 ± 0.02	-170.5 ± 5	1.41 ± 0.03
	$X2_{43}$	0.15 ± 0.03	0.48 ± 0.06	-167.6 ± 5	1.87 ± 0.03
	$X1_{43}$	0.07 ± 0.01	1.09 ± 0.06	-173.6 ± 5	2.95 ± 0.03
	$X1_{86}$	0.08 ± 0.02	0.07 ± 0.02	-170.1 ± 5	2.72 ± 0.03
2009.86	$C1_{43}$	1.78 ± 0.26	0.022 ± 0.06	0	0
	$C1_{86}$	1.36 ± 0.27	0.008 ± 0.02	0	0
	$C2_{43}$	0.78 ± 0.12	0.061 ± 0.06	-179.1 ± 5	0.11 ± 0.03
	$C2_{86}$	1.48 ± 0.29	0.022 ± 0.02	-173.3 ± 5	0.06 ± 0.01
	$C3_{43}$	0.46 ± 0.07	0.088 ± 0.06	-172.2 ± 5	0.29 ± 0.03
	$C3_{86}$	0.52 ± 0.11	0.043 ± 0.02	-176.4 ± 5	0.19 ± 0.01
	$X5_{43}$	0.31 ± 0.05	0.089 ± 0.06	-172.1 ± 5	0.41 ± 0.03
	$X5_{86}$	0.13 ± 0.03	0.026 ± 0.02	-175.2 ± 5	0.37 ± 0.01
	$X4_{43}$	0.29 ± 0.04	0.35 ± 0.06	-164.6 ± 5	1.58 ± 0.03
	$X4_{86}$	0.26 ± 0.05	0.14 ± 0.02	-154.8 ± 5	1.48 ± 0.01
	$X3_{43}$	0.47 ± 0.03	0.58 ± 0.06	-165.4 ± 5	2.13 ± 0.03
	$X3_{86}$	0.46 ± 0.09	0.12 ± 0.02	-167.7 ± 5	1.98 ± 0.01
2010.36	$C1_{43}$	2.11 ± 0.31	0.013 ± 0.06	0	0
Continues...					

TABLE B.4: Table of model-fit parameters

Epoch	ID	Flux (Jy)	FWHM (mas)	PA (°)	Core-sep. (mas)
	$C1_{86}$	1.90 ± 0.38	0.008 ± 0.02	0	0
	$C1a_{43}$	0.89 ± 0.13	0.031 ± 0.06	-160.7 ± 5	0.09 ± 0.03
	$C1a_{86}$	0.64 ± 0.13	0.023 ± 0.02	-152.5 ± 5	0.05 ± 0.01
	$C2_{43}$	0.81 ± 0.12	0.059 ± 0.06	-174.7 ± 5	0.22 ± 0.03
	$C2_{86}$	0.74 ± 0.15	0.046 ± 0.02	-172.5 ± 5	0.17 ± 0.01
	$C3_{43}$	0.48 ± 0.07	0.100 ± 0.06	-172.2 ± 5	0.32 ± 0.03
	$C3_{86}$	0.48 ± 0.09	0.08 ± 0.02	-171.5 ± 5	0.32 ± 0.01
	$X5_{86}$	0.25 ± 0.05	0.27 ± 0.06	-177.9 ± 5	1.49 ± 0.03
	$X5_{43}$	0.28 ± 0.04	0.43 ± 0.06	-170.9 ± 5	1.66 ± 0.03
	$X4_{43}$	0.54 ± 0.08	0.79 ± 0.06	-168.2 ± 5	2.61 ± 0.03
	$X4_{86}$	0.12 ± 0.02	0.14 ± 0.02	-164.9 ± 5	2.62 ± 0.03
2011.35	$C1_{43}$	1.51 ± 0.30	0.034 ± 0.06	0	0
	$C1_{86}$	1.47 ± 0.22	0.018 ± 0.02	0	0
	$C1a_{43}$	1.14 ± 0.23	0.034 ± 0.06	-171.5 ± 5	0.09 ± 0.03
	$C1a_{86}$	0.58 ± 0.09	0.010 ± 0.02	176.8 ± 5	0.06 ± 0.01
	$C2_{43}$	0.78 ± 0.16	0.098 ± 0.06	-171.1 ± 5	0.25 ± 0.03
	$C2_{86}$	0.50 ± 0.08	0.023 ± 0.02	-164.3 ± 5	0.14 ± 0.01
	$C3_{43}$	0.45 ± 0.09	0.076 ± 0.06	-172.1 ± 5	0.42 ± 0.03
	$C3_{86}$	0.96 ± 0.14	0.078 ± 0.02	-167.0 ± 5	0.36 ± 0.01
	$X7_{86}$	0.26 ± 0.01	0.028 ± 0.02	-164.9 ± 5	0.44 ± 0.01
	$X6_{43}$	0.13 ± 0.03	0.393 ± 0.06	-167.9 ± 5	1.69 ± 0.03
	$X6_{86}$	0.26 ± 0.04	0.144 ± 0.02	-162.6 ± 5	1.83 ± 0.01
	$X5_{43}$	0.17 ± 0.03	0.396 ± 0.06	-171.0 ± 5	2.39 ± 0.03
	$X5_{86}$	0.12 ± 0.02	0.342 ± 0.02	-174.3 ± 5	2.18 ± 0.01
	$X4_{43}$	0.21 ± 0.04	1.013 ± 0.06	-168.6 ± 5	3.09 ± 0.03
2011.75	$C1_{43}$	2.97 ± 0.59	0.028 ± 0.06	0	0
	$C1_{86}$	1.7 ± 0.26	0.023 ± 0.02	0	0
	$C2_{43}$	1.51 ± 0.3	0.06 ± 0.06	-175.1 ± 5	0.12 ± 0.03
	$C2_{86}$	1.85 ± 0.28	0.048 ± 0.02	164.6 ± 5	0.07 ± 0.01
	$C3_{43}$	0.71 ± 0.14	0.085 ± 0.06	-170.5 ± 5	0.3 ± 0.03
	$C3_{86}$	1.42 ± 0.21	0.019 ± 0.02	176.9 ± 5	0.19 ± 0.01
	$E1_{43}$	0.09 ± 0.02	0.146 ± 0.06	-168.4 ± 5	0.46 ± 0.03

Continues...

TABLE B.4: Table of model-fit parameters

Epoch	ID	Flux (Jy)	FWHM (mas)	PA (°)	Core-sep. (mas)
	$E1_{86}$	1.54 ± 0.23	0.074 ± 0.02	-176.3 ± 5	0.41 ± 0.01
	$E2_{43}$	0.14 ± 0.03	0.42 ± 0.06	-169.8 ± 5	1.76 ± 0.03
	$E3_{43}$	0.28 ± 0.06	0.42 ± 0.06	-171.3 ± 5	2.34 ± 0.03
	$E4_{43}$	0.16 ± 0.03	0.962 ± 0.06	-169.6 ± 5	3.34 ± 0.03
2012.38	$C1_{43}$	3.04 ± 0.45	0.027 ± 0.06	0	0
	$C1_{86}$	3.19 ± 0.64	0.063 ± 0.02	0	0
	$C2_{43}$	1.47 ± 0.22	0.037 ± 0.06	-174.5 ± 5	0.12 ± 0.03
	$C2_{86}$	0.95 ± 0.01	0.058 ± 0.02	-178.3 ± 5	0.17 ± 0.01
	$C3_{43}$	1.32 ± 0.19	0.097 ± 0.06	-169.6 ± 5	0.31 ± 0.03
	$C3_{86}$	1.43 ± 0.29	0.174 ± 0.02	-160.4 ± 5	0.30 ± 0.01
	$X7_{43}$	0.13 ± 0.02	0.308 ± 0.06	-170.7 ± 5	1.70 ± 0.03
	$X7_{86}$	0.12 ± 0.03	0.112 ± 0.02	-173.0 ± 5	1.58 ± 0.01
	$T6_{43}$	0.16 ± 0.02	0.421 ± 0.06	-167.3 ± 5	2.17 ± 0.03
	$T6_{86}$	0.29 ± 0.06	0.171 ± 0.02	-171.9 ± 5	2.19 ± 0.01
	$X6_{43}$	0.32 ± 0.05	0.586 ± 0.02	-168.4 ± 5	2.66 ± 0.01
	$X6_{86}$	0.46 ± 0.02	0.317 ± 0.06	-172.3 ± 5	2.84 ± 0.03

Continues...

Appendix C

Appendix C - OJ 287 Modelfits

TABLE C.1: Table of model-fit parameters

Epoch	Freq (GHz)	Flux (Jy)	Core sep (mas)	PA (°)	FWHM (mas)	ID
2007.45	43.2	0.49±0.05	0±0	0±0	0.04±0.03	C
2007.45	43.2	0.55±0.06	0.13±0.02	-11.7±5	0.016±0.03	S
2007.45	43.2	0.13±0.01	1.00±0.15	-125.9±5	0.48±0.09	X0
2007.45	43.2	0.09±0.01	0.21±0.03	-102.2±5	0.09±0.01	P1
2007.66	43.2	0.52±0.05	0±0	0±0	0.02±0.03	C
2007.66	43.2	0.79±0.08	0.15±0.02	-11.5±5	0.02±0.03	S
2007.66	43.2	0.12±0.01	1.01±0.15	-119.6±5	0.52±0.10	X0
2007.66	43.2	0.17±0.01	0.26±0.04	-109.5±5	0.10±0.02	P1
2007.74	43.2	0.68±0.07	0±0	0±0	0.02±0.03	C
2007.74	43.2	0.93±0.10	0.15±0.02	-15.4±5	0.003±0.03	S
2007.74	43.2	0.12±0.01	1.04±0.15	-119.6±5	0.47±0.09	X0
2007.74	43.2	0.16±0.02	0.30±0.04	-109.5±5	0.13±0.02	P1'
2008.05	43.2	0.72±0.07	0±0	0±0	0.03±0.03	C
2008.05	43.2	1.55±0.17	0.18±0.02	-16.7±5	0.02±0.03	S
2008.05	43.2	0.06±0.01	1.12±0.16	-115.5±5	0.38±0.07	X0
2008.05	43.2	0.06±0.01	0.39±0.05	-119.9±5	0.17±0.03	P1
2008.44	43.2	0.84±0.09	0±0	0±0	0.02±0.03	C
2008.44	43.2	2.09±0.22	0.15±0.02	-19.3±5	0.049±0.03	S
2008.44	43.2	0.11±0.01	0.28±0.04	-113.9±5	0.19±0.03	P1

Continues...

TABLE C.1: Table of model-fit parameters

Epoch	Freq (GHz)	Flux (Jy)	Core sep (mas)	PA (°)	FWHM (mas)	ID
2008.62	43.2	0.57±0.06	0±0	0±0	0.04±0.03	C
2008.62	43.2	1.99±0.21	0.20±0.03	-18.1±5	0.07±0.03	S
2008.62	43.2	0.20±0.02	0.30±0.04	-111.2±5	0.47±0.03	P1
2008.69	43.2	0.60±0.06	0±0	0±0	0.05±0.05	C
2008.69	43.2	1.79±0.19	0.20±0.03	-15.0±5	0.02±0.03	S
2008.69	43.2	0.10±0.01	0.45±0.06	-122.6±5	0.35±0.07	X1
2008.78	86.2	0.53±0.05	0±0	0±0	0.01±0.01	C
2008.78	86.2	1.82±0.20	0.19±0.02	-12.2±5	0.01±0.01	S
2008.78	86.2	0.13±0.01	0.17±0.02	-59.4±5	0.11±0.02	T1
2008.78	86.2	0.42±0.04	0.33±0.04	-10.8±5	0.05±0.01	N1
2008.78	86.2	0.07±0.01	0.47±0.07	-98.4±5	0.39±0.07	X1
2008.88	43.2	1.34±0.14	0±0	0±0	0.02±0.03	C
2008.88	43.2	2.42±0.26	0.22±0.03	-12.4±5	0.02±0.03	S
2008.88	43.2	0.11±0.01	0.39±0.05	-127.5±5	0.11±0.02	X1
2008.97	43.2	1.27±0.13	0±0	0±0	0.04±0.03	C
2008.97	43.2	2.08±0.22	0.22±0.03	-11.3±5	0.04±0.03	S
2008.97	43.2	0.13±0.01	0.45±0.06	-115.1±5	0.40±0.08	X1
2009.07	43.2	1.39±0.15	0±0	0±0	0.028±0.03	C
2009.07	43.2	4.70±0.51	0.22±0.03	-10.6±5	0.03±0.03	S
2009.07	43.2	0.10±0.01	0.45±0.06	-116.6±5	0.22±0.04	X1
2009.15	43.2	1.33±0.14	0±0	0±0	0.042±0.03	C
2009.15	43.2	4.17±0.45	0.23±0.03	-12.1±5	0.04±0.03	S
2009.15	43.2	0.18±0.02	0.46±0.07	-121.0±5	0.55±0.11	X1
2009.35	86.2	1.45±0.15	0±0	0±0	0.021±0.014	C
2009.35	86.2	3.68±0.40	0.26±0.03	-13.0±5	0.04±0.014	S
2009.35	86.2	0.24±0.02	0.45±0.06	-129.3±5	0.13±0.026	X1
2009.41	43.2	1.21±0.13	0±0	0±0	0.035±0.03	C
2009.41	43.2	3.46±0.38	0.23±0.03	-15.0±5	0.04±0.03	S
2009.41	43.2	0.18±0.02	0.61±0.09	-122.0±5	0.52±0.10	X1
2009.47	43.2	1.26±0.13	0±0	0±0	0.033±0.03	C
2009.47	43.2	2.94±0.32	0.20±0.03	-13.3±5	0.04±0.03	S

Continues...

TABLE C.1: Table of model-fit parameters

Epoch	Freq (GHz)	Flux (Jy)	Core sep (mas)	PA (°)	FWHM (mas)	ID
2009.47	43.2	0.19±0.02	0.56±0.08	-118.7±5	0.55±0.11	X1
2009.57	43.2	1.43±0.15	0±0	0±0	0.031±0.03	C
2009.57	43.2	3.81±0.41	0.21±0.03	-14.8±5	0.03±0.03	S
2009.57	43.2	0.18±0.01	0.55±0.08	-119.1±5	0.68±0.13	X1
2009.62	43.2	1.42±0.15	0±0	0±0	0.032±0.03	C
2009.62	43.2	4.62±0.50	0.23±0.03	-16.4±5	0.03±0.03	S
2009.62	43.2	0.16±0.01	0.73±0.11	-124.8±5	0.61±0.12	X1
2009.71	43.2	2.02±0.22	0±0	0±0	0.003±0.0006	C*
2009.71	43.2	4.73±0.52	0.25±0.03	-19.3±5	0.04±0.03	S
2009.71	43.2	0.19±0.02	0.82±0.12	-122.8±5	0.61±0.12	X1
2009.77	86.2	2.95±0.32	0±0	0±0	0.036±0.03	C
2009.77	86.2	0.51±0.05	0.11±0.02	-19.0±5	0.02±0.01	M
2009.77	86.2	4.73±0.52	0.23±0.03	-18.1±5	0.04±0.03	S
2009.77	86.2	0.81±0.08	0.34±0.05	-32.2±5	0.09±0.03	T1
2009.77	86.2	0.13±0.01	0.77±0.11	-143.7±5	0.06±0.01	X1
2009.79	43.2	2.83±0.31	0±0	0±0	0.014±0.03	C
2009.79	43.2	5.44±0.59	0.23±0.03	-18.6±5	0.03±0.03	S
2009.79	43.2	0.17±0.01	0.94±0.14	-128.2±5	0.55±0.11	X1
2009.80	43.2	2.92±0.32	0±0	0±0	0.004±0.03	C*
2009.80	43.2	5.42±0.59	0.23±0.03	-18.9±5	0.03±0.03	S
2009.80	43.2	0.18±0.02	0.94±0.14	-123.3±5	0.51±0.10	X1
2009.82	43.2	2.11±0.23	0±0	0±0	0.042±0.03	C
2009.82	43.2	4.99±0.54	0.22±0.03	-19.3±5	0.03±0.03	S
2009.82	43.2	0.25±0.02	0.74±0.11	-124.6±5	0.64±0.12	X1
2009.91	43.2	2.83±0.31	0±0	0±0	0.066±0.03	C
2009.91	43.2	6.78±0.74	0.22±0.03	-21.6±5	0.05±0.03	S
2009.91	43.2	0.15±0.01	0.99±0.14	-125.2±5	0.58±0.11	X1
2010.03	43.2	1.68±0.18	0±0	0±0	0.039±0.03	C
2010.03	43.2	8.24±0.90	0.24±0.03	-25.6±5	0.06±0.03	S
2010.03	43.2	0.17±0.01	0.91±0.13	-124.2±5	0.62±0.12	X1

Continues...

TABLE C.1: Table of model-fit parameters

Epoch	Freq (GHz)	Flux (Jy)	Core sep (mas)	PA (°)	FWHM (mas)	ID
2010.11	43.2	0.94±0.10	0±0	0±0	0.044±0.03	C
2010.11	43.2	3.27±0.35	0.23±0.03	-25.7±5	0.06±0.03	S
2010.11	43.2	0.13±0.01	0.89±0.13	-121.7±5	0.63±0.12	X1
2010.18	43.2	1.25±0.13	0±0	0±0	0.059±0.03	C
2010.18	43.2	5.94±0.65	0.23±0.03	-27.8±5	0.06±0.03	S
2010.18	43.2	0.18±0.02	1.05±0.15	-130.5±5	0.53±0.10	X1
2010.35	86.2	0.87±0.09	0±0	0±0	0.023±0.014	C
2010.35	86.2	0.43±0.04	0.18±0.02	-36.6±5	0.03±0.01	S
2010.35	86.2	0.84±0.09	0.23±0.03	-43.9±5	0.08±0.01	P2
2010.35	86.2	0.07±0.01	1.09±0.16	-126.8±5	0.41±0.08	X1
2010.45	43.2	0.88±0.09	0±0	0±0	0.04±0.03	C
2010.45	43.2	1.38±0.15	0.20±0.03	-35.5±5	0.04±0.03	S
2010.45	43.2	0.57±0.06	0.27±0.04	-46.4±5	0.12±0.02	P2
2010.45	43.2	0.13±0.01	1.11±0.16	-129.1±5	0.46±0.09	X1
2010.58	43.2	0.82±0.09	0±0	0±0	0.036±0.03	C
2010.58	43.2	0.90±0.09	0.21±0.03	-40.1±5	0.05±0.03	S
2010.58	43.2	0.85±0.09	0.31±0.04	-47.3±5	0.11±0.02	P2
2010.58	43.2	0.17±0.02	1.07±0.16	-130.5±5	0.63±0.12	X1
2010.72	43.2	2.82±0.31	0±0	0±0	0.038±0.03	C
2010.72	43.2	1.37±0.15	0.15±0.02	-39.9±5	0.08±0.03	S
2010.72	43.2	0.89±0.09	0.31±0.04	-58.6±5	0.23±0.04	P2
2010.72	43.2	0.33±0.03	1.09±0.16	-130.9±5	0.63±0.12	X1
2010.81	43.2	1.72±0.18	0±0	0±0	0.023±0.03	C
2010.81	43.2	2.02±0.22	0.18±0.02	-40.1±5	0.06±0.03	S
2010.81	43.2	0.43±0.04	0.31±0.04	-54.9±5	0.19±0.03	P2
2010.81	43.2	0.14±0.01	1.15±0.17	-127.5±5	0.58±0.11	X1
2010.84	43.2	2.64±0.29	0±0	0±0	0.035±0.03	C
2010.84	43.2	2.21±0.24	0.19±0.02	-41.2±5	0.09±0.03	S
2010.84	43.2	0.62±0.06	0.31±0.04	-55.6±5	0.24±0.04	P2
2010.84	43.2	0.16±0.01	1.18±0.17	-128.0±5	0.52±0.10	X1
2010.85	43.2	2.61±0.28	0±0	0±0	0.035±0.03	C
2010.85	43.2	2.36±0.25	0.19±0.02	-42.4±5	0.08±0.03	S

Continues...

TABLE C.1: Table of model-fit parameters

Epoch	Freq (GHz)	Flux (Jy)	Core sep (mas)	PA (°)	FWHM (mas)	ID
2010.85	43.2	0.59±0.06	0.31±0.04	-60.5±5	0.20±0.04	P2
2010.85	43.2	0.19±0.02	1.18±0.17	-131.4±5	0.56±0.11	X1
2010.87	43.2	2.25±0.24	0±0	0±0	0.012±0.03	C
2010.87	43.2	2.22±0.24	0.21±0.03	-44.0±5	0.07±0.03	S
2010.87	43.2	0.52±0.05	0.32±0.04	-64.0±5	0.20±0.04	P2
2010.87	43.2	0.15±0.01	1.20±0.18	-131.2±5	0.64±0.12	X1
2010.93	43.2	2.20±0.24	0±0	0±0	0.04±0.03	C
2010.93	43.2	3.19±0.35	0.22±0.03	-46.9±5	0.10±0.03	S
2010.93	43.2	0.42±0.04	0.35±0.05	-64.8±5	0.15±0.03	P2
2010.93	43.2	0.13±0.01	1.24±0.18	-130.0±5	0.50±0.10	X1
2011.01	43.2	0.27±0.03	0±0	0±0	0.00006±0.000012	C*
2011.01	43.2	2.09±0.22	0.12±0.01	-22.0±5	0.01±0.03	U
2011.01	43.2	2.19±0.24	0.32±0.04	-35.6±5	0.11±0.03	S
2011.01	43.2	1.07±0.11	0.43±0.06	-54.4±5	0.17±0.03	P2
2011.01	43.2	0.14±0.01	1.20±0.18	-124.8±5	0.50±0.10	X1
2011.10	43.2	2.19±0.24	0±0	0±0	0.036±0.03	C
2011.10	43.2	1.79±0.19	0.19±0.02	-26.8±5	0.05±0.03	S
2011.10	43.2	1.40±0.15	0.27±0.04	-41.6±5	0.12±0.02	T2
2011.10	43.2	0.92±0.10	0.40±0.06	-70.8±5	0.21±0.04	X2
2011.10	43.2	0.17±0.02	1.17±0.17	-131.4±5	0.58±0.11	X1
2011.16	43.2	2.25±0.24	0±0	0±0	0.014±0.03	C
2011.16	43.2	1.97±0.21	0.18±0.02	-28.4±5	0.04±0.03	S
2011.16	43.2	0.94±0.10	0.28±0.04	-39.0±5	0.12±0.02	T2
2011.16	43.2	0.79±0.08	0.42±0.06	-74.5±5	0.22±0.04	X2
2011.16	43.2	0.14±0.01	1.23±0.18	-131.3±5	0.48±0.09	X1
2011.30	43.2	1.40±0.15	0±0	0±0	0.035±0.03	C
2011.30	43.2	2.52±0.27	0.20±0.03	-23.0±5	0.04±0.03	S
2011.30	43.2	1.48±0.16	0.26±0.04	-33.9±5	0.08±0.03	T2
2011.30	43.2	0.34±0.03	0.34±0.05	-50.3±5	0.09±0.03	U
2011.30	43.2	0.49±0.05	0.49±0.07	-77.3±5	0.19±0.03	X2
2011.30	43.2	0.18±0.02	1.24±0.18	-131.8±5	0.56±0.11	X1
2011.36	86.2	3.71±0.40	0±0	0±0	0.043±0.014	C
2011.36	86.2	1.79±0.19	0.19±0.02	-43.8±5	0.11±0.01	S

Continues...

TABLE C.1: Table of model-fit parameters

Epoch	Freq (GHz)	Flux (Jy)	Core sep (mas)	PA (°)	FWHM (mas)	ID
2011.36	86.2	0.74±0.08	0.45±0.06	-66.0±5	0.15±0.03	X2
2011.39	43.2	1.95±0.21	0±0	0±0	0.053±0.03	C
2011.39	43.2	3.05±0.33	0.22±0.03	-29.3±5	0.05±0.03	S
2011.39	43.2	2.55±0.28	0.28±0.04	-38.6±5	0.16±0.03	T2
2011.39	43.2	0.73±0.08	0.49±0.07	-81.2±5	0.26±0.05	X2
2011.39	43.2	0.15±0.01	1.30±0.19	-128.7±5	0.21±0.04	X1
2011.45	43.2	1.68±0.18	0±0	0±0	0.016±0.03	C
2011.45	43.2	1.65±0.18	0.21±0.03	-30.3±5	0.03±0.03	S
2011.45	43.2	1.61±0.17	0.31±0.04	-37.7±5	0.09±0.01	T2
2011.45	43.2	0.68±0.07	0.49±0.07	-75.3±5	0.26±0.05	X2
2011.45	43.2	0.18±0.02	1.29±0.19	-139.5±5	0.44±0.08	X1
2011.55	43.2	1.00±0.11	0±0	0±0	0.019±0.03	C
2011.55	43.2	1.45±0.15	0.19±0.02	-31.5±5	0.03±0.03	S
2011.55	43.2	1.24±0.13	0.28±0.04	-33.1±5	0.04±0.01	T2
2011.55	43.2	0.40±0.04	0.36±0.05	-45.2±5	0.14±0.02	U
2011.55	43.2	0.48±0.05	0.56±0.08	-81.0±5	0.24±0.04	X2
2011.55	43.2	0.17±0.02	1.34±0.20	-134.6±5	0.46±0.09	X1
2011.64	43.2	2.07±0.22	0±0	0±0	0.084±0.03	C
2011.64	43.2	1.64±0.18	0.22±0.03	-34.3±5	0.05±0.03	S
2011.64	43.2	1.10±0.12	0.33±0.04	-39.1±5	0.12±0.02	T2
2011.64	43.2	0.46±0.05	0.58±0.08	-83.7±5	0.28±0.05	X2
2011.64	43.2	0.19±0.02	1.37±0.20	-135.0±5	0.48±0.09	X1
2011.71	43.2	1.62±0.17	0±0	0±0	0.017±0.03	C
2011.71	43.2	0.55±0.06	0.13±0.02	-32.2±5	0.02±0.03	U
2011.71	43.2	0.78±0.08	0.28±0.04	-38.0±5	0.05±0.03	S
2011.71	43.2	0.36±0.03	0.38±0.05	-46.1±5	0.14±0.02	T2
2011.71	43.2	0.28±0.03	0.63±0.09	-85.6±5	0.30±0.06	X2
2011.71	43.2	0.16±0.01	1.38±0.20	-134.3±5	0.45±0.09	X1
2011.77	86.2	3.12±0.34	0±0	0±0	0.052±0.03	C
2011.77	86.2	1.15±0.12	0.18±0.02	-33.2±5	0.05±0.03	S
2011.77	86.2	0.29±0.03	0.46±0.06	-74.4±5	0.06±0.01	T2
2011.79	43.2	2.30±0.25	0±0	0±0	0.029±0.03	C
2011.79	43.2	0.78±0.08	0.09±0.01	-28.9±5	0.05±0.03	U

Continues...

TABLE C.1: Table of model-fit parameters

Epoch	Freq (GHz)	Flux (Jy)	Core sep (mas)	PA (°)	FWHM (mas)	ID
2011.79	43.2	1.82±0.20	0.21±0.03	-37.0±5	0.06±0.03	S
2011.79	43.2	0.48±0.05	0.36±0.05	-45.5±5	0.18±0.03	T2
2011.79	43.2	0.26±0.02	0.67±0.10	-87.8±5	0.33±0.06	X2
2011.79	43.2	0.21±0.02	1.41±0.21	-133.9±5	0.50±0.10	X1
2011.92	43.2	2.18±0.23	0±0	0±0	0.019±0.03	C
2011.92	43.2	0.87±0.09	0.17±0.02	-33.7±5	0.04±0.03	S
2011.92	43.2	1.21±0.13	0.27±0.04	-38.4±5	0.06±0.03	P3
2011.92	43.2	0.59±0.06	0.35±0.05	-51.7±5	0.14±0.02	T2
2011.92	43.2	0.18±0.02	0.72±0.10	-88.9±5	0.41±0.08	X2
2011.92	43.2	0.17±0.02	1.48±0.22	-133.9±5	0.50±0.10	X1
2012.17	43.2	1.76±0.19	0±0	0±0	0.036±0.03	C
2012.17	43.2	1.68±0.18	0.19±0.02	-26.0±5	0.01±0.03	S
2012.17	43.2	0.97±0.10	0.30±0.04	-33.1±5	0.09±0.03	P3
2012.17	43.2	0.42±0.04	0.41±0.06	-48.4±5	0.12±0.02	U
2012.17	43.2	0.28±0.03	0.55±0.08	-66.2±5	0.23±0.04	T2
2012.17	43.2	0.11±0.01	1.00±0.15	-98.3±5	0.24±0.04	L2
2012.17	43.2	0.17±0.02	1.52±0.22	-131.0±5	0.56±0.11	X1
2012.25	43.2	2.09±0.22	0±0	0±0	0.013±0.03	C
2012.25	43.2	1.52±0.16	0.16±0.02	-31.1±5	0.04±0.03	S
2012.25	43.2	1.87±0.20	0.30±0.04	-31.2±5	0.03±0.03	P3
2012.25	43.2	0.79±0.08	0.43±0.06	-42.6±5	0.17±0.03	U
2012.25	43.2	0.27±0.02	0.59±0.08	-67.4±5	0.24±0.04	T2
2012.25	43.2	0.12±0.01	1.05±0.15	-96.5±5	0.23±0.04	L2
2012.25	43.2	0.23±0.03	1.50±0.22	-128.1±5	0.71±0.14	X1
2012.38	86.2	2.91±0.32	0±0	0±0	0.057±0.014	C
2012.38	86.2	1.46±0.16	0.26±0.03	-37.6±5	0.05±0.014	S
2012.38	86.2	0.28±0.03	0.42±0.06	-61.3±5	0.19±0.038	X3
2012.38	86.2	0.48±0.05	0.62±0.09	-64.6±5	0.24±0.048	T2
2012.40	43.2	2.58±0.28	0±0	0±0	0.034±0.03	C
2012.40	43.2	0.90±0.09	0.19±0.02	-40.3±5	0.04±0.03	S
2012.40	43.2	1.30±0.14	0.36±0.05	-40.2±5	0.13±0.02	P3
2012.40	43.2	0.26±0.02	0.57±0.08	-70.2±5	0.22±0.04	T2
2012.40	43.2	0.12±0.01	0.96±0.14	-96.8±5	0.32±0.06	L2
2012.40	43.2	0.22±0.02	1.58±0.23	-131.3±5	0.68±0.13	X1

Continues...

TABLE C.1: Table of model-fit parameters

Epoch	Freq (GHz)	Flux (Jy)	Core sep (mas)	PA (°)	FWHM (mas)	ID
2012.62	43.2	1.92±0.21	0±0	0±0	0.02±0.03	C
2012.62	43.2	0.67±0.07	0.19±0.02	-40.1±5	0.05±0.03	S
2012.62	43.2	0.45±0.04	0.37±0.05	-41.4±5	0.07±0.03	X3
2012.62	43.2	0.26±0.02	0.46±0.06	-51.7±5	0.13±0.02	U
2012.62	43.2	0.12±0.01	0.62±0.09	-70.1±5	0.34±0.06	T2
2012.62	43.2	0.09±0.00	1.00±0.15	-94.5±5	0.41±0.08	L2
2012.62	43.2	0.14±0.01	1.53±0.23	-127.7±5	0.72±0.14	X1
2012.82	43.2	2.36±0.25	0±0	0±0	0.049±0.03	C
2012.82	43.2	1.37±0.15	0.19±0.02	-43.5±5	0.09±0.03	S
2012.82	43.2	0.88±0.09	0.47±0.07	-48.6±5	0.20±0.04	X3
2012.82	43.2	0.09±0.01	0.62±0.09	-69.3±5	0.13±0.02	T2
2012.82	43.2	0.07±0.01	0.98±0.14	-94.4±5	0.19±0.03	L2
2012.82	43.2	0.20±0.02	1.58±0.23	-123.9±5	0.87±0.17	X1
2013.04	43.2	2.47±0.27	0±0	0±0	0.007±0.03	C
2013.04	43.2	0.68±0.07	0.14±0.02	-34.7±5	0.05±0.03	S
2013.04	43.2	0.20±0.02	0.31±0.04	-47.4±5	0.09±0.03	T3
2013.04	43.2	0.14±0.01	0.52±0.07	-54.6±5	0.10±0.02	X3
2013.04	43.2	0.14±0.01	0.66±0.09	-61.7±5	0.22±0.04	T2
2013.04	43.2	0.09±0.01	1.00±0.15	-93.7±5	0.46±0.09	L2
2013.04	43.2	0.11±0.01	1.73±0.26	-127.7±5	0.82±0.16	X1
2013.16	43.2	3.22±0.35	0±0	0±0	0.05±0.03	C
2013.16	43.2	1.41±0.15	0.13±0.02	-41.8±5	0.12±0.03	S
2013.16	43.2	0.12±0.01	0.43±0.06	-61.0±5	0.18±0.03	T3
2013.16	43.2	0.15±0.01	0.62±0.09	-61.1±5	0.22±0.04	X3
2013.16	43.2	0.04±0.01	0.77±0.11	-76.6±5	0.23±0.04	T2
2013.16	43.2	0.08±0.01	0.94±0.14	-91.3±5	0.41±0.08	L2
2013.16	43.2	0.12±0.01	1.66±0.25	-126.3±5	0.91±0.19	X1
2013.29	43.2	1.58±0.17	0±0	0±0	0.02±0.03	C
2013.29	43.2	1.18±0.12	0.15±0.02	-36.3±5	0.04±0.03	S
2013.29	43.2	0.99±0.10	0.22±0.03	-48.1±5	0.12±0.02	P4
2013.29	43.2	0.08±0.01	0.47±0.07	-61.6±5	0.12±0.02	T3
2013.29	43.2	0.11±0.01	0.63±0.09	-65.6±5	0.22±0.04	L3
2013.29	43.2	0.08±0.01	0.90±0.13	-89.9±5	0.68±0.13	L2
2013.29	43.2	0.10±0.01	1.72±0.25	-126.1±5	0.87±0.17	X1
2013.41	43.2	1.60±0.17	0±0	0±0	0.015±0.03	C

Continues...

TABLE C.1: Table of model-fit parameters

Epoch	Freq (GHz)	Flux (Jy)	Core sep (mas)	PA (°)	FWHM (mas)	ID
2013.41	43.2	0.50±0.05	0.15±0.02	-39.6±5	0.06±0.03	S
2013.41	43.2	0.60±0.06	0.24±0.03	-43.3±5	0.11±0.02	P4
2013.41	43.2	0.22±0.02	0.55±0.08	-67.4±5	0.20±0.04	T3
2013.41	43.2	0.13±0.01	1.11±0.16	-110.9±5	1.00±0.20	L2
2013.49	43.2	2.50±0.27	0±0	0±0	0.024±0.03	C
2013.49	43.2	1.05±0.11	0.13±0.02	-42.1±5	0.05±0.03	S
2013.49	43.2	0.44±0.04	0.26±0.03	-48.5±5	0.12±0.02	P4
2013.49	43.2	0.19±0.02	0.62±0.09	-70.5±5	0.20±0.04	L3
2013.49	43.2	0.07±0.01	1.02±0.15	-91.4±5	0.61±0.12	L2
2013.49	43.2	0.05±0.01	1.88±0.28	-130.1±5	0.86±0.17	X1
2013.57	43.2	2.45±0.26	0±0	0±0	0.029±0.03	C
2013.57	43.2	1.11±0.12	0.17±0.02	-48.8±5	0.05±0.03	S
2013.57	43.2	0.51±0.05	0.27±0.04	-49.8±5	0.10±0.02	P4
2013.57	43.2	0.17±0.02	0.65±0.09	-72.0±5	0.27±0.05	L3
2013.57	43.2	0.10±0.01	1.27±0.19	-114.1±5	1.26±0.25	L2

Continues...

References

- Abdo, A. A., Ackermann, M., Agudo, I., et al. 2010, *ApJ*, 716, 30
- Abdo, A. A., Ackermann, M., Ajello, M., et al. 2011, *ApJ*, 726, 43
- Acadamy, K. 2014, Introduction to the convolution, available at:
<https://www.khanacademy.org/math/differential-equations/laplace-transform/convolution-integral/v/introduction-to-the-convolution>
- Agudo, I., Bach, U., Krichbaum, T. P., et al. 2007a, *A&A*, 476, L17
- Agudo, I., Bach, U., Krichbaum, T. P., et al. 2007b, *A&A*, 476, L17
- Agudo, I., Gómez, J.-L., Martí, J.-M., et al. 2001, *ApJ*, 549, L183
- Agudo, I., Jorstad, S. G., Marscher, A. P., et al. 2011, *ApJ*, 726, L13
- Agudo, I., Krichbaum, T. P., Bach, U., et al. 2007c, The Innermost Regions of AGN with Future mm-VLBI, ed. A. P. Lobanov, J. A. Zensus, C. Cesarsky, & P. J. Diamond (Springer-Verlag), 179
- Agudo, I., Marscher, A. P., Jorstad, S. G., et al. 2012, *ApJ*, 747, 63
- Ahmed, M., Mangus, D., & Burch, P. 2001, in *ESA Special Publication*, Vol. 473, *Space Debris*, ed. H. Sawaya-Lacoste, 495–500
- Alberdi, A., Krichbaum, T. P., Graham, D. A., et al. 1997, *A&A*, 327, 513
- Alberdi, A., Krichbaum, T. P., Marcaide, J. M., et al. 1993, *A&A*, 271, 93
- Alef, W., Krichbaum, T. P., Roy, A. L., et al. 2003, in *Astronomical Society of the Pacific Conference Series*, Vol. 306, *New technologies in VLBI*, ed. Y. C. Minh, 75
- Alfvén, H. & Herlofson, N. 1950, *Physical Review*, 78, 616
- Aloy, M.-Á., Martí, J.-M., Gómez, J.-L., et al. 2003, *ApJ*, 585, L109
- Alpher, R. A., Follin, J. W., & Herman, R. C. 1953, *Physical Review*, 92, 1347

- Antoniadis, J., Freire, P. C. C., Wex, N., et al. 2013, *Science*, 340, 448
- Antonucci, R. R. J., Hickson, P., Olszewski, E. W., & Miller, J. S. 1986, *AJ*, 92, 1
- Arshakian, T. G., Ros, E., & Zensus, J. A. 2006, *A&A*, 458, 397
- Asada, K., Inoue, M., Uchida, Y., et al. 2002, *PASJ*, 54, L39
- Attridge, J. M., Wardle, J. F. C., & Homan, D. C. 2005, *ApJ*, 633, L85
- Atwood, W. B., Abdo, A. A., Ackermann, M., et al. 2009, *ApJ*, 697, 1071
- Azad, K. 2012, An interactive guide to the Fourier Transform, available at:
<http://betterexplained.com/articles/an-interactive-guide-to-the-fourier-transform/>
- Baade, W. & Minkowski, R. 1954, *ApJ*, 119, 206
- Baath, L. B. 1994, in *Astronomical Society of the Pacific Conference Series*, Vol. 59, IAU Colloq. 140: Astronomy with Millimeter and Submillimeter Wave Interferometry, ed. M. Ishiguro & J. Welch, 44
- Baath, L. B. & Booth, R. S. 1991, in *Astronomical Society of the Pacific Conference Series*, Vol. 19, IAU Colloq. 131: Radio Interferometry. Theory, Techniques, and Applications, ed. T. J. Cornwell & R. A. Perley, 326–329
- Baath, L. B., Padin, S., Woody, D., et al. 1991, *A&A*, 241, L1
- Baath, L. B., Rogers, A. E. E., Inoue, M., et al. 1992, *A&A*, 257, 31
- Bach, U., Krichbaum, T. P., Ros, E., et al. 2005, 433, 815
- Backer, D. C. 1984, in *IAU Symposium*, Vol. 110, VLBI and Compact Radio Sources, ed. R. Fanti, K. I. Kellermann, & G. Setti, 31
- Backer, D. C., Wright, M. C. H., Plambeck, R. L., et al. 1987, *ApJ*, 322, 74
- Bardeen, J. M., Press, W. H., & Teukolsky, S. A. 1972, *ApJ*, 178, 347
- Bare, C., Clark, B. G., Kellermann, K. I., Cohen, M. H., & Jauncey, D. L. 1967, *Science*, 157, 189
- Bartel, N. 2003, in *Astronomy in Latin America*, ed. R. Teixeira, N. V. Leister, V. A. F. Martin, & P. Benevides-Soares, 35–42
- Bartel, N., Dhawan, V., Krichbaum, T., Graham, D. A., & Pauliny-Toth, I. I. K. 1988, *Nature*, 334, 131

- Beasley, A. J., Dhawan, V., Doeleman, S., & Phillips, R. B. 1997, in *Millimeter-VLBI Science Workshop*, ed. R. Barvainis & R. B. Phillips, 53
- Begelman, M. C., Blandford, R. D., & Rees, M. J. 1984, *Reviews of Modern Physics*, 56, 255
- BICEP2 Collaboration, Ade, P. A. R., Aikin, R. W., et al. 2014, *ArXiv e-prints*
- Bignami, G. F., Boella, G., Burger, J. J., et al. 1975a, *Space Science Instrumentation*, 1, 245
- Bignami, G. F., Fichtel, C. E., Kniffen, D. A., & Thompson, D. J. 1975b, *ApJ*, 199, 54
- Bisnovatyi-Kogan, G. S. & Ruzmaikin, A. A. 1974, *Ap&SS*, 28, 45
- Blackett, P. M. S. & Lovell, A. C. B. 1941, *Royal Society of London Proceedings Series A*, 177, 183
- Blandford, R. D. & Königl, A. 1979, *ApJ*, 232, 34
- Blandford, R. D., McKee, C. F., & Rees, M. J. 1977, *Nature*, 267, 211
- Blandford, R. D. & Rees, M. J. 1971, in *Bulletin of the American Astronomical Society*, Vol. 3, *Bulletin of the American Astronomical Society*, 472–+
- Blandford, R. D. & Rees, M. J. 1978, *Phys. Scr*, 17, 265
- Blandford, R. D. & Znajek, R. L. 1977, *MNRAS*, 179, 433
- Bloom, S. D. & Marscher, A. P. 1996, *ApJ*, 461, 657
- Boeck, M., . 2012, PhD thesis, Universität Urlangen
- Bogovalov, S. & Tsinganos, K. 2005, *MNRAS*, 357, 918
- Bonnoli, G., Ghisellini, G., Foschini, L., Tavecchio, F., & Ghirlanda, G. 2011, *MNRAS*, 410, 368
- Böttcher, M. & Bloom, S. D. 2000, *AJ*, 119, 469
- Böttcher, M., Reimer, A., Sweeney, K., & Prakash, A. 2013, *ApJ*, 768, 54
- Bridle, A. H., Fomalont, E. B., & Cornwell, T. J. 1981, *AJ*, 86, 1294
- Broten, N. W., Locke, J. L., Legg, T. H., McLeish, C. W., & Richards, R. S. 1967, *Nature*, 215, 38
- Cao, X. & Bai, J. M. 2008, *ApJ*, 673, L131
- Caproni, A., Abraham, Z., & Monteiro, H. 2013, *MNRAS*, 428, 280

- Cawthorne, T. V. 2006, *MNRAS*, 367, 851
- Clark, B. G. 2003, in *Astronomical Society of the Pacific Conference Series*, Vol. 300, *Radio Astronomy at the Fringe*, ed. J. A. Zensus, M. H. Cohen, & E. Ros, 1–58381
- Clausen-Brown, E., Savolainen, T., Pushkarev, A. B., Kovalev, Y. Y., & Zensus, J. A. 2013, *A&A*, 558, A144
- Cohen, M. H., Linfield, R. P., Moffet, A. T., et al. 1977, *Nature*, 268, 405
- Cohen, M. H., Meier, D. L., Arshakian, T. G., et al. 2014, *ApJ*, 787, 151
- Colomer, F., Bujarrabal, V., Ruiz, R. S., et al. 2009, in *Astronomical Society of the Pacific Conference Series*, Vol. 402, *Approaching Micro-Arcsecond Resolution with VSOP-2: Astrophysics and Technologies*, ed. Y. Hagiwara, E. Fomalont, M. Tsuboi, & M. Yasuhiro, 404
- Compton, A. H. 1923, *Physical Review*, 21, 483
- Condon, J. J., Cotton, W. D., Greisen, E. W., et al. 1998, *AJ*, 115, 1693
- Conway, J. E. & Murphy, D. W. 1993, *ApJ*, 411, 89
- Cornwell, T. & Fomalont, E. B. 1999, in *Astronomical Society of the Pacific Conference Series*, Vol. 180, *Synthesis Imaging in Radio Astronomy II*, ed. G. B. Taylor, C. L. Carilli, & R. A. Perley, 187
- Cotton, W. D. 1979, *AJ*, 84, 1122
- Curtis, H. D. 1918, *Publications of Lick Observatory*, 13, 9
- Daly, R. A. & Marscher, A. P. 1988, *ApJ*, 334, 539
- Darling, D. 2012, *Encyclopedia of Science, Blazars*, available at:
<http://www.daviddarling.info/encyclopedia/B/blazar.html>
- Deller, A. T., Briske, W. F., Phillips, C. J., et al. 2011, *PASP*, 123, 275
- Dermer, C. D. & Schlickeiser, R. 1993, *ApJ*, 416, 458
- Dexter, J., McKinney, J. C., & Agol, E. 2012, *MNRAS*, 421, 1517
- Dhawan, V., Burke, B., Bartel, N., et al. 1986, in *Bulletin of the American Astronomical Society*, Vol. 18, *Bulletin of the American Astronomical Society*, 970

- Díaz Trigo, M., Miller-Jones, J. C. A., Migliari, S., Broderick, J. W., & Tzioumis, T. 2013, *Nature*, 504, 260
- Dickel, J. R. 1969, *Astrophys. Lett.*, 4, 109
- Doeleman, S., Rogers, A. E. E., Bower, G. C., Wright, M. C. H., & Backer, D. C. 1995, in *Bulletin of the American Astronomical Society*, Vol. 27, American Astronomical Society Meeting Abstracts, 1300
- Doeleman, S. S., Fish, V. L., Schenck, D. E., et al. 2012, *Science*, 338, 355
- Doeleman, S. S., Weintroub, J., Rogers, A. E. E., et al. 2008, *Nature*, 455, 78
- Dolence, J. C., Gammie, C. F., Shiokawa, H., & Noble, S. C. 2012, *ApJ*, 746, L10
- Donea, A.-C. & Biermann, P. L. 2002, *PASA*, 19, 125
- Einstein, A. 1905, *Annalen der Physik*, 322, 891
- Einstein, A. 1916, *Annalen der Physik*, 354, 769
- ESO. 2009, Centaurus A, available at:
<http://www.eso.org/public/images/eso0903a/>
- Ewen, H. I. & Purcell, E. M. 1951, *Nature*, 168, 356
- Fanaroff, B. L. & Riley, J. M. 1974, *MNRAS*, 167, 31P
- Fath, E. A. 1909, *Lick Observatory Bulletin*, 5, 71
- Fichtel, C. E., Bertsch, D. L., Hartman, R. C., et al. 1993, *A&AS*, 97, 13
- Fomalont, E. B. 1999, in *Astronomical Society of the Pacific Conference Series*, Vol. 180, *Synthesis Imaging in Radio Astronomy II*, ed. G. B. Taylor, C. L. Carilli, & R. A. Perley, 301
- Frater, R. H. 1984, *Proceedings of the Astronomical Society of Australia*, 5, 440
- Fromm, C. 2014, *Spectral Evolution in Blazars: The Case of CTA 102*, Springer Theses (Springer International Publishing)
- Fromm, C. M., Perucho, M., Ros, E., et al. 2012, *International Journal of Modern Physics Conference Series*, 8, 323
- Fromm, C. M., Ros, E., Perucho, M., et al. 2013a, *A&A*, 551, A32
- Fromm, C. M., Ros, E., Perucho, M., et al. 2013b, *A&A*, 557, A105
- Fuhrmann, L., Krichbaum, T. P., Witzel, A., et al. 2008, *A&A*, 490, 1019

- Fuhrmann, L., Larsson, S., Chiang, J., et al. 2014, *MNRAS*, 441, 1899
- Gabuzda, D. C., Cantwell, T. M., & Cawthorne, T. V. 2014, *MNRAS*, 438, L1
- Gao, X.-Y., Wang, J.-C., & Zhou, M. 2011, *Research in Astronomy and Astrophysics*, 11, 902
- Gardner, E. & Done, C. 2014, *MNRAS*, 438, 779
- Georganopoulos, M. & Kazanas, D. 2003, *ApJ*, 594, L27
- George, I. M., Nandra, K., Turner, T. J., & Celotti, A. 1994, *ApJ*, 436, L59
- Ghisellini, G., Celotti, A., Fossati, G., Maraschi, L., & Comastri, A. 1998, *MNRAS*, 301, 451
- Ghisellini, G. & Madau, P. 1996, *MNRAS*, 280, 67
- Ghosh, P. & Abramowicz, M. A. 1997, *MNRAS*, 292, 887
- Giroletti, M., Giovannini, G., Cotton, W. D., et al. 2008, *A&A*, 488, 905
- Gómez, J. L., Martí, J. M., Marscher, A. P., Ibáñez, J. M., & Alberdi, A. 1997, *ApJ*, 482, L33
- Graham, D. A. & Matveenko, L. I. 1984, in *IAU Symposium*, Vol. 110, *VLBI and Compact Radio Sources*, ed. R. Fanti, K. I. Kellermann, & G. Setti, 43
- Grandi, P., Urry, C. M., Maraschi, L., et al. 1996, *ApJ*, 459, 73
- Guijosa, A. & Daly, R. A. 1996, *ApJ*, 461, 600
- Gurwell, M. A., Peck, A. B., Hostler, S. R., Darrah, M. R., & Katz, C. A. 2007, in *Astronomical Society of the Pacific Conference Series*, Vol. 375, *From Z-Machines to ALMA: (Sub)Millimeter Spectroscopy of Galaxies*, ed. A. J. Baker, J. Glenn, A. I. Harris, J. G. Mangum, & M. S. Yun, 234
- Hanbury Brown, R. & Hazard, C. 1952, *Nature*, 170, 364
- Hardee, P. E. 2003, *ApJ*, 597, 798
- Hartigan, P., Edwards, S., & Ghandour, L. 1995, *ApJ*, 452, 736
- Hartman, R. C., Bertsch, D. L., Dingus, B. L., et al. 1993, *ApJ*, 407, L41
- Hartman, R. C., Bertsch, D. L., Fichtel, C. E., et al. 1992, *ApJ*, 385, L1
- Hartman, R. C., Böttcher, M., Aldering, G., et al. 2001, *ApJ*, 553, 683
- Healey, S. E., Romani, R. W., Cotter, G., et al. 2008, *ApJS*, 175, 97

- Hertz, H. 1894, *Die Prinzipien Der Mechanik In Neuem Zusammenhange Dargestellt* (1894) (German Edition) (Kessinger Publ)
- Hewish, A., Bell, S. J., Pilkington, J. D. H., Scott, P. F., & Collins, R. A. 1968, *Nature*, 217, 709
- Hewitt, A. & Burbidge, G. 1991, *ApJS*, 75, 297
- Hey, J. S. 1946, *Nature*, 157, 47
- Hey, J. S. 1973, *The evolution of radio astronomy*, by J. S. Hey (Elek London), x, 214 p.
- Hirabayashi, H. 1998, in *Astronomical Society of the Pacific Conference Series*, Vol. 144, IAU Colloq. 164: Radio Emission from Galactic and Extragalactic Compact Sources, ed. J. A. Zensus, G. B. Taylor, & J. M. Wrobel, 11
- Hobbs, G. 2011, in *High-Energy Emission from Pulsars and their Systems*, ed. D. F. Torres & N. Rea, 229
- Hodgson, J. A., Krichbaum, T. P., Marscher, A. P., et al. 2014, *ArXiv e-prints*
- Högbom, J. A. 1974, *A&AS*, 15, 417
- Homan, D. C. & Lister, M. L. 2006, *AJ*, 131, 1262
- Hovatta, T., Aller, M. F., Aller, H. D., et al. 2014, *AJ*, 147, 143
- Hujeirat, A., Livio, M., Camenzind, M., & Burkert, A. 2003, *A&A*, 408, 415
- Hunter, S. D., Bertsch, D. L., Dingus, B. L., et al. 1993a, *ApJ*, 409, 134
- Hunter, S. D., Bertsch, D. L., Dingus, B. L., et al. 1993b, *A&A*, 272, 59
- Jansky, Jr., C. M. 1979, *Cosmic Search*, 1, 12
- Jennison, R. C. 1958, *MNRAS*, 118, 276
- Jorstad, S., Marscher, A., Larionov, V., et al. 2013a, in *European Physical Journal Web of Conferences*, Vol. 61, *European Physical Journal Web of Conferences*, 4003
- Jorstad, S. G., Marscher, A. P., Lister, M. L., et al. 2005, *AJ*, 130, 1418
- Jorstad, S. G., Marscher, A. P., Mattox, J. R., et al. 2001, *ApJ*, 556, 738
- Jorstad, S. G., Marscher, A. P., Smith, P. S., et al. 2013b, *ApJ*, 773, 147
- Jorstad, S. G., Marscher, A. P., Stevens, J. A., et al. 2007, *AJ*, 134, 799

- Jung, T., Sohn, B. W., Byun, D.-Y., & KVN Group. 2012, *Mem. Soc. Astron. Italiana*, 83, 978
- Kadler, M., Ros, E., Lobanov, A. P., Falcke, H., & Zensus, J. A. 2004, *A&A*, 426, 481
- Kanbach, G., Bennett, K., Bignami, G. F., et al. 1977, in *ESA Special Publication*, Vol. 124, *Recent Advances in Gamma-Ray Astronomy*, ed. R. D. Wills & B. Battrick, 21–32
- Kanbach, G., Bertsch, D. L., Fichtel, C. E., et al. 1988, *Space Sci. Rev.*, 49, 69
- Kardashev, N. S. 1962, *Soviet Ast.*, 6, 317
- Kardashev, N. S., Khartov, V. V., Abramov, V. V., et al. 2013, *Astronomy Reports*, 57, 153
- Kawaguchi, N., Sasao, T., & Manabe, S. 2000, in *Society of Photo-Optical Instrumentation Engineers (SPIE) Conference Series*, Vol. 4015, *Radio Telescopes*, ed. H. R. Butcher, 544–551
- Kellermann, K. I. 1966, *ApJ*, 146, 621
- Kellermann, K. I. & Cohen, M. H. 1988, *JRASC*, 82, 248
- Kellermann, K. I. & Moran, J. M. 2001, *ARA&A*, 39, 457
- Kellermann, K. I. & Pauliny-Toth, I. I. K. 1969, *ApJ*, 155, L71+
- Kerr, R. P. 1963, *Physical Review Letters*, 11, 237
- Kniffen, D. A., Fichtel, C. E., & Hartman, R. C. 1973, *NASA Special Publication*, 339, 139
- Koide, S. 2004, *ApJ*, 606, L45
- Koide, S., Shibata, K., Kudoh, T., & Meier, D. L. 2002, *Science*, 295, 1688
- Konigl, A. 1981, *ApJ*, 243, 700
- Kovalev, Y. Y., Kellermann, K. I., Lister, M. L., et al. 2005, *AJ*, 130, 2473
- Krawczynski, H., Coppi, P. S., & Aharonian, F. 2002, *MNRAS*, 336, 721
- Krichbaum, T. P. 1996, *ArXiv Astrophysics e-prints*
- Krichbaum, T. P., Graham, D. A., Witzel, A., et al. 1998, *A&A*, 335, L106
- Krichbaum, T. P., Graham, D. A., Witzel, A., et al. 2001, in *Astronomical Society of the Pacific Conference Series*, Vol. 250, *Particles and Fields in Radio Galaxies Conference*, ed. R. A. Laing & K. M. Blundell, 184

- Krichbaum, T. P., Hummel, C. A., Quirrenbach, A., et al. 1990, *A&A*, 230, 271
- Krichbaum, T. P., Witzel, A., & Zensus, J. A. 1999, *ArXiv Astrophysics e-prints*
- Kushwaha, P., Sahayanathan, S., & Singh, K. P. 2013, *Monthly Notices of the Royal Astronomical Society*, 433, 2380
- Laing, R. A. 1980, *MNRAS*, 193, 439
- Lau, M. M. & Young, E. C. M. 1985, *International Cosmic Ray Conference*, 1, 285
- Lee, S. . 2007, PhD thesis, Universität Bonn
- Lee, S.-S., Lobanov, A. P., Krichbaum, T. P., et al. 2008, *AJ*, 136, 159
- Lerner, M. S., Baath, L. B., Inoue, M., et al. 1993, *A&A*, 280, 117
- Lichti, G. G., Balonek, T., Courvoisier, T. J.-L., et al. 1995, *A&A*, 298, 711
- Lin, Y. C., Bertsch, D. L., Chiang, J., et al. 1992, *ApJ*, 401, L61
- Linfield, R. P., Levy, G. S., Edwards, C. D., et al. 1990, *ApJ*, 358, 350
- Linford, J. D., Taylor, G. B., Romani, R. W., et al. 2012, *ApJ*, 744, 177
- Lister, M. L., Aller, M., Aller, H., et al. 2011, *ApJ*, 742, 27
- Lister, M. L., Aller, M. F., Aller, H. D., et al. 2013, *AJ*, 146, 120
- Lister, M. L., Cohen, M. H., Homan, D. C., et al. 2009, *AJ*, 138, 1874
- Lister, M. L. & Homan, D. C. 2005, *AJ*, 130, 1389
- Liu, H. T., Bai, J. M., & Ma, L. 2008, *ApJ*, 688, 148
- Lobanov, A. P. 2005, *ArXiv Astrophysics e-prints*
- Lobanov, A. P., Krichbaum, T. P., Graham, D. A., et al. 2000, *A&A*, 364, 391
- Lobanov, A. P. & Zensus, J. A. 1999, *ApJ*, 521, 509
- Lobanov, A. P. & Zensus, J. A. 2001, *Science*, 294, 128
- Lodge, O. 1900, *Signalling Across Space Without Wires*.
- Lonsdale, C. J., Doeleman, S. S., & Phillips, R. B. 1998, *AJ*, 116, 8
- Lovell, B. 1968, *The story of Jodrell Bank* (by) Bernard Lovell (Oxford U.P London), xvi, 265 p.
- Lyubarsky, Y. & Eichler, D. 2001, *ApJ*, 562, 494

- MacFadyen, A. I. & Woosley, S. E. 1999, *ApJ*, 524, 262
- Macomb, D. J., Akerlof, C. W., Aller, H. D., et al. 1995, *ApJ*, 449, L99
- Maraschi, L., Grandi, P., Urry, C. M., et al. 1994, *ApJ*, 435, L91
- Marcaide, J. M., Pauliny-Toth, I. I. K., Graham, D. A., Ronnang, B., & Booth, R. S. 1985, in *European Southern Observatory Conference and Workshop Proceedings*, Vol. 22, *European Southern Observatory Conference and Workshop Proceedings*, ed. P. A. Shaver & K. Kjar, 157–167
- Marscher, A. P. 1977, *ApJ*, 216, 244
- Marscher, A. P. 1983, *ApJ*, 264, 296
- Marscher, A. P. 1995, *Proceedings of the National Academy of Science*, 92, 11439
- Marscher, A. P. 1999, *Astroparticle Physics*, 11, 19
- Marscher, A. P. 2006, in *American Institute of Physics Conference Series*, Vol. 856, *Relativistic Jets: The Common Physics of AGN, Microquasars, and Gamma-Ray Bursts*, ed. P. A. Hughes & J. N. Bregman, 1–22
- Marscher, A. P. 2014, *ApJ*, 780, 87
- Marscher, A. P. & Gear, W. K. 1985, *ApJ*, 298, 114
- Marscher, A. P., Gear, W. K., & Travis, J. P. 1992, in *Variability of Blazars*, ed. E. Valtaoja & M. Valtonen, 85
- Marscher, A. P., Jorstad, S. G., D’Arcangelo, F. D., et al. 2008, *Nature*, 452, 966
- Marscher, A. P. & Travis, J. P. 1996, *A&AS*, 120, C537
- Marfí-Vidal, I., Krichbaum, T. P., Marscher, A., et al. 2012, *A&A*, 542, A107
- Matsumoto, J. & Masada, Y. 2013a, in *European Physical Journal Web of Conferences*, Vol. 61, *European Physical Journal Web of Conferences*, 2005
- Matsumoto, J. & Masada, Y. 2013b, *ApJ*, 772, L1
- Mattox, J. R., Bertsch, D. L., Chiang, J., et al. 1996, *ApJ*, 461, 396
- Mattox, J. R., Bertsch, D. L., Chiang, J., et al. 1993, *ApJ*, 410, 609
- Maxwell, J. C. 1865, *Philosophical Transactions of the Royal Society of London*, 155, 459

- McKinney, J. C. 2005, *ApJ*, 630, L5
- McKinney, J. C. 2006, *MNRAS*, 368, 1561
- McKinney, J. C. & Blandford, R. D. 2009, *MNRAS*, 394, L126
- McKinney, J. C. & Gammie, C. F. 2004, *ApJ*, 611, 977
- McKinney, J. C., Tchekhovskoy, A., & Blandford, R. D. 2012, *MNRAS*, 423, 3083
- McKinney, J. C., Tchekhovskoy, A., Sadowski, A., & Narayan, R. 2014, *MNRAS*, 441, 3177
- Meegan, C., Bhat, N., Connaughton, V., et al. 2007, in *American Institute of Physics Conference Series*, Vol. 921, *The First GLAST Symposium*, ed. S. Ritz, P. Michelson, & C. A. Meegan, 13–18
- Meli, A. & Biermann, P. L. 2013, *A&A*, 556, A88
- Mizuta, A., Yamada, S., & Takabe, H. 2004, *ApJ*, 606, 804
- Moffat, A. F. J., Schlickeiser, R., Shara, M. M., et al. 1983, *ApJ*, 271, L45
- Molina, S. N., Agudo, I., Gómez, J. L., et al. 2014, *ArXiv e-prints*
- Mukherjee, R. 2001, in *American Institute of Physics Conference Series*, Vol. 558, *American Institute of Physics Conference Series*, ed. F. A. Aharonian & H. J. Völk, 324–337
- Mukherjee, R., Böttcher, M., Hartman, R. C., et al. 1999, *ApJ*, 527, 132
- Muller, C. A. & Oort, J. H. 1951, *Nature*, 168, 357
- Mutel, R. L. & Denn, G. R. 2005, *ApJ*, 623, 79
- Nalewajko, K., Sikora, M., & Begelman, M. C. 2014, *ApJ*, 796, L5
- Napier, P. J., Bagri, D. S., Clark, B. G., et al. 1994, *IEEE Proceedings*, 82, 658
- Narayan, R., Igumenshchev, I. V., & Abramowicz, M. A. 2003, *PASJ*, 55, L69
- Nilsson, K., Takalo, L. O., Lehto, H. J., & Sillanpää, A. 2010, *A&A*, 516, A60
- Nolan, P. L., Abdo, A. A., Ackermann, M., et al. 2012, *ApJS*, 199, 31
- Norman, M. L., Winkler, K.-H. A., Smarr, L., & Smith, M. D. 1982, *A&A*, 113, 285
- Ojha, R., Kadler, M., Böck, M., et al. 2010, *A&A*, 519, A45

- Oort, J. H. & Muller, C. A. 1952, *Monthly Notes of the Astronomical Society of South Africa*, 11, 65
- Orr, M. J. L. & Browne, I. W. A. 1982, *MNRAS*, 200, 1067
- O'Sullivan, S. P. & Gabuzda, D. C. 2009, *MNRAS*, 400, 26
- Padin, S., Woody, D. P., Hodges, M. W., et al. 1990, *ApJ*, 360, L11
- Pawsey, J. L. 1957a, in *IAU Symposium, Vol. 4, Radio astronomy*, ed. H. C. van de Hulst, 123
- Pawsey, J. L. 1957b, in *IAU Symposium, Vol. 4, Radio astronomy*, ed. H. C. van de Hulst, 228
- Pawsey, J. L. 1958, *PASP*, 70, 133
- Pearson, T. J., Unwin, S. C., Cohen, M. H., et al. 1981, *Nature*, 290, 365
- Penzias, A. A. & Wilson, R. W. 1965, *ApJ*, 142, 419
- Perucho, M. 2013, in *European Physical Journal Web of Conferences, Vol. 61, European Physical Journal Web of Conferences*, 2002
- Perucho, M., Kovalev, Y. Y., Lobanov, A. P., Hardee, P. E., & Agudo, I. 2012, *ApJ*, 749, 55
- Peterson, B. M., Ferrarese, L., Gilbert, K. M., et al. 2004, *ApJ*, 613, 682
- Petry, D., Böttcher, M., Connaughton, V., et al. 2000, *ApJ*, 536, 742
- Pihajoki, P., Valtonen, M., Zola, S., et al. 2013, *ApJ*, 764, 5
- Pogrebenko, S. V., Gurvits, L. I., Campbell, R. M., et al. 2004, in *ESA Special Publication, Vol. 544, Planetary Probe Atmospheric Entry and Descent Trajectory Analysis and Science*, ed. A. Wilson, 197–204
- Punch, M., Akerlof, C. W., Cawley, M. F., et al. 1992, *Nature*, 358, 477
- Pushkarev, A. B., Hovatta, T., Kovalev, Y. Y., et al. 2012, *A&A*, 545, A113
- Pushkarev, A. B. & Kovalev, Y. Y. 2012, *A&A*, 544, A34
- Pushkarev, A. B., Kovalev, Y. Y., Lister, M. L., & Savolainen, T. 2009, *A&A*, 507, L33
- Rani, B., Krichbaum, T. P., Fuhrmann, L., et al. 2013, *A&A*, 552, A11
- Rani, B., Krichbaum, T. P., Marscher, A. P., et al. 2014, *A&A*, 571, L2
- Rantakyro, F. T., Baath, L. B., Backer, D. C., et al. 1998, *A&AS*, 131, 451

- Readhead, A. C. S., Mason, C. R., Mofett, A. T., et al. 1983, *Nature*, 303, 504
- Readhead, A. C. S., Walker, R. C., Pearson, T. J., & Cohen, M. H. 1980, *Nature*, 285, 137
- Reber, G. 1944, *ApJ*, 100, 279
- Robertson, P. 2010, 40 Years of The Dish, available at:
<http://http://www.abc.net.au/science/articles/2010/02/09/2814525.htm>
- Rogers, A. E. E., Phillips, R. B., & Lonsdale, C. J. 1995, in *Bulletin of the American Astronomical Society*, Vol. 27, American Astronomical Society Meeting Abstracts, 1300
- Ros, E. 2005, in *Astronomical Society of the Pacific Conference Series*, Vol. 340, *Future Directions in High Resolution Astronomy*, ed. J. Romney & M. Reid, 482
- Rushton, A., Spencer, R. E., Strong, M., et al. 2007, in *IAU Symposium*, Vol. 238, *IAU Symposium*, ed. V. Karas & G. Matt, 437–438
- Rybicki, G. B. & Lightman, A. P. 1979, *Radiative processes in astrophysics*
- Ryle, M. & Scheuer, P. A. G. 1955, *Royal Society of London Proceedings Series A*, 230, 448
- Ryle, M. & Vonberg, D. D. 1946, *Nature*, 158, 339
- Sanders, R. H. 1983, *ApJ*, 266, 73
- Savolainen, T., Wiik, K., Valtaoja, E., et al. 2006, *ApJ*, 647, 172
- Schinzel, F. . 2011, PhD thesis, Universität zu Köln
- Schinzel, F. K., Lobanov, A. P., Taylor, G. B., et al. 2012, *A&A*, 537, A70
- Schmidt, M. 1963, *Nature*, 197, 1040
- Schuh, H. & Behrend, D. 2012, *Journal of Geodynamics*, 61, 68
- Schulz, R., Kadler, M., Ros, E., et al. 2013, *ArXiv e-prints*
- Schwab, F. R. & Cotton, W. D. 1983, *AJ*, 88, 688
- Schwarzschild, K. 1916, *Abh. Konigl. Preuss. Akad. Wissenschaften Jahre 1906,92, Berlin,1907, 1916*, 189
- Schwinger, J. 1949, *Physical Review*, 75, 1912
- Scott, M. A. & Readhead, A. C. S. 1977, *MNRAS*, 180, 539

- Shepherd, M. C., Pearson, T. J., & Taylor, G. B. 1994, in *Bulletin of the American Astronomical Society*, Vol. 26, *Bulletin of the American Astronomical Society*, 987–989
- Sikora, M., Begelman, M. C., Madejski, G. M., & Lasota, J.-P. 2005, *ApJ*, 625, 72
- Sikora, M., Begelman, M. C., & Rees, M. J. 1994, *ApJ*, 421, 153
- Sikora, M., Moderski, R., & Madejski, G. M. 2008, *ApJ*, 675, 71
- Silant'ev, N. A., Gnedin, Y. N., Buliga, S. D., Piotrovich, M. Y., & Natsvlshvili, T. M. 2013, *Astrophysical Bulletin*, 68, 14
- Smart, L. L., Norman, M. L., & Winkler, K.-H. A. 1984, *Physica D Nonlinear Phenomena*, 12, 83
- Smith, A. G., Lebo, G. R., Six, Jr., N. F., et al. 1965, *ApJ*, 141, 457
- Spergel, D., Flauger, R., & Hlozek, R. 2013, *ArXiv e-prints*
- Spergel, D. N., Bean, R., Doré, O., et al. 2007, *ApJS*, 170, 377
- Stecker, F. W. 1977, *ApJ*, 212, 60
- Stecker, F. W., Puget, J. L., Strong, A. W., & Bredekamp, J. H. 1974, *ApJ*, 188, L59
- Stirling, A. M., Cawthorne, T. V., Stevens, J. A., et al. 2003, *MNRAS*, 341, 405
- Swanenburg, B. N., Hermsen, W., Bennett, K., et al. 1978, *Nature*, 275, 298
- Taylor, G., Carilli, C., Perley, R., & (U.S.), N. R. A. O. 2008, *Synthesis imaging in radio astronomy II: a collection of lectures from the Sixth NRAO/NMIMT Synthesis Imaging Summer School, held at Socorro, New Mexico, USA, 17-23 June, 1998, Astronomical Society of the Pacific conference series No. v. 2 (Astronomical Society of the Pacific)*
- Taylor, J. H. & Weisberg, J. M. 1989, *ApJ*, 345, 434
- Tchekhovskoy, A., Narayan, R., & McKinney, J. C. 2011, *MNRAS*, 418, L79
- Thompson, D. J. 2008, *Reports on Progress in Physics*, 71, 116901
- Thompson, D. J., Bertsch, D. L., Dingus, B. L., et al. 1993, *ApJ*, 415, L13
- Thompson, D. J., Fichtel, C. E., Kniffen, D. A., & Ogelman, H. B. 1975, *ApJ*, 200, L79

- Tsuboi, M. 2008, in Society of Photo-Optical Instrumentation Engineers (SPIE) Conference Series, Vol. 7010, Society of Photo-Optical Instrumentation Engineers (SPIE) Conference Series
- Türler, M. 2011, *Mem. Soc. Astron. Italiana*, 82, 104
- Urry, C. M. & Padovani, P. 1995, *PASP*, 107, 803
- Valtaoja, E. & Terasranta, H. 1995, *A&A*, 297, L13
- van de Hulst, H. C. 1946, PhD thesis, *Recherches Astronomiques de l'Observatoire d'Utrecht*, vol. 11, pp.1.i-1.87
- van de Hulst, H. C., Muller, C. A., & Oort, J. H. 1954, *Bull. Astron. Inst. Netherlands*, 12, 117
- Villata, M., Raiteri, C. M., Larionov, V. M., et al. 2008, *A&A*, 481, L79
- Wagner, S. J., Witzel, A., Heidt, J., et al. 1996, *AJ*, 111, 2187
- Wang, H.-t. & Pan, Y.-p. 2013, *Chinese Astron. Astrophys.*, 37, 8
- Wardle, J. F. C., Homan, D. C., Ojha, R., & Roberts, D. H. 1998, *Nature*, 395, 457
- Wilms, J., Reynolds, C. S., Begelman, M. C., et al. 2001, *MNRAS*, 328, L27
- Wilsing, J. & Scheiner, J. 1896, *Annalen der Physik*, 295, 782
- Woltjer, L. 1964, *Nature*, 201, 803
- Xie, W., Lei, W.-H., Zou, Y.-C., et al. 2012, *Research in Astronomy and Astrophysics*, 12, 817
- Young, E. C. M. & Yu, K. N. 1988, *Vistas in Astronomy*, 31, 579
- Zamaninasab, M., Clausen-Brown, E., Savolainen, T., & Tchekhovskoy, A. 2014, *Nature*, 510, 126
- Zensus, J. A., Krichbaum, T. P., & Lobanov, A. P. 1995, *Proceedings of the National Academy of Science*, 92, 11348
- Zhang, S., Collmar, W., & Schönfelder, V. 2005, *A&A*, 444, 767

Erklärung

Ich versichere, dass ich die von mir vorgelegte Dissertation selbständig angefertigt, die benutzten Quellen und Hilfsmittel vollständig angegeben und die Stellen der Arbeit, einschließlich Tabellen, Karten und Abbildungen, die anderen Werken im Wortlaut oder dem Sinn nach entnommen sind, in jedem Einzelfall als Entlehnung kenntlich gemacht habe; dass diese Dissertation noch keiner anderen Fakultät oder Universität zur Prüfung vorgelegen hat; dass sie, abgesehen von unten angegebenen Teilpublikationen – noch nicht veröffentlicht worden ist sowie, dass ich eine solche Veröffentlichung vor Abschluss des Promotionsverfahrens nicht vornehmen werde. Die Bestimmungen der Promotionsordnung sind mir bekannt. Die von mir vorgelegte Dissertation ist von Prof. Dr. J. Anton Zensus und Prof. Dr. Andreas Eckart betreut worden.

Köln, den 13.12.2014

Lebenslauf

Akademischer Lebenslauf



Jeffrey Adam Hodgson
22 Nov 1986, Melbourne, Australien/ Britisch

jhodgson@mpifr-bonn.mpg.de
+49 177 669 6856

Aktueller Dienstadresse

Max-Planck-Institut für Radioastronomie
Bonn, 53121, Deutschland

Akademischer Werdegang

Max-Planck-Institut für Radioastronomie, Universität zu Köln (University of Cologne), Bonn & Cologne, Germany

Ph.D. — 2011- expected defense, Jan 2015

Projekte: Ultra-high resolution observations of selected blazars

Curtin University, Perth, Australia

Honours — 2009 - 2010

Projekte: Microarcsecond scale structure in blazar PKS 1257-326

Curtin University, Perth, Australia

Bachelors — 2005-2009

Akademischer Publikationen

Rani, B.; Krichbaum, T. P.; Marscher, A. P.; Jorstad, S. G.; **Hodgson, J. A.**; Fuhrmann, L.; Zensus, J. A. *Jet outflow and gamma-ray emission correlations in SS 0716+714*, 2014, Astronomy and Astrophysics Letters (accepted)

Tilanus, R. P. J.; Krichbaum, T. P.; Zensus, J. A.; Baudry, A.; Bremer, M.; Falcke, H.; Giovannini, G.; Laing, R.; van Langevelde, H. J.; Vlemmings, W.; Abraham, Z.; Afonso, J.; Agudo, I.; Alberdi, A.; Alcolea, J.; Altamirano, D.; Asadi, S.; Assaf, K.; Augusto, P.; Bacsko, A.-K.; Boeck, M.; Boller, T.; Bondi, M.; Boone, F.; Bourda, G.; Brajsa, R.; Brand, J.; Britzen, S.; Bujarrabal, V.; Cales, S.; Casadio, C.; Casasola, V.; Castangia, P.; Cernicharo, J.; Charlot, P.; Chemin, L.; Clenet, Y.; Colomer, F.; Combes, F.; Cordes, J.; Coriat, M.; Cross, N.; D'Ammando, F.; Dallacasa, D.; Desmurs, J.-F.; Eatough, R.; Eckart, A.; Eisenacher, D.; Etoka, S.; Felix, M.; Fender, R.; Ferreira, M.; Freeland, E.; Frey, S.; Fromm, C.; Fuhrmann, L.; Gabanyi, K.; Galvan-Madrid, R.; Giroletti, M.; Goddi, C.; Gomez, J.;ourgoulhon, E.; Gray, M.; di Gregorio, I.; Greimel, R.; Grosso, N.; Guirado, J.; Hada, K.; Hanslmeier, A.; Henkel, C.; Herpin, F.; Hess, P.; **Hodgson, J.**; Horns, D.; Humphreys, E.; Hutawarakorn, B.; Ilyushin, V.; Impellizzeri, V.; Ivanov, V.; Julião, M.; Kadler, M.; Kerins, E.; Klaassen, P.; van 't Klooster, K.; Kording, E.; Kozlov, M.; Kramer, M.; Kreikenbohm, A.; Kurtanidze, O.; Lazio, J.; Leite, A.; Leitzinger, M.; Lepine, J.; Levshakov, S.; Lico, R.; Lindqvist, M.; Liuzzo, E.; Lobanov, A.; Lucas, P.; Mannheim, K.; Marcaide, J.; Markoff, S.; Martí-Vidal, I.; Martins, C.; Masetti, N.; Massardi, M.; Menten, K.; Messias, H.; Migliari, S.; Mignano, A.; Miller-Jones, J.; Minniti, D.; Molaro, P.; Molina, S.; Monteiro, A.; Moscadelli, L.; Mueller, C.; Müller, A.; Muller, S.; Niederhofer, F.; Odert, P.; Olofsson, H.; Orienti, M.; Paladino, R.; Panessa, F.; Paragi, Z.; Paumard, T.; Pedrosa, P.; Pérez-Torres, M.; Perrin, G.; Perucho, M.; Porquet, D.; Prandoni, I.; Ransom, S.; Reimers, D.; Rejkuba, M.; Rezzolla, L.; Richards, A.; Ros, E.; Roy, A.; Rushton, A.; Savolainen, T.; Schulz, R.; Silva, M.; Sivakoff, G.; Soria-Ruiz, R.; Soria, R.; Spaans, M.; Spencer, R.; Stappers, B.; Surcis, G.; Tarchi, A.; Temmer, M.; Thompson, M.; Torrelles, J.; Truemstedt, J.; Tudose, V.; Venturi, T.; Verbiest, J.; Vieira, J.; Vielzeuf, P.; Vincent, F.; Wex, N.; Wiik, K.; Wiklind, T.; Wilms, J.; Zackrisson, E.; Zechlin, H. *Future mmVLBI Research with ALMA: A European vision*, 2014, arXiv: 1406.4650

Rani, B.; Marscher, A. P.; Jorstad, S.; **Hodgson, J. A.**; Krichbaum, T. P.; Fuhrmann, L.; Zensus, J. A.; *Probing the jet acceleration region - SS 0716+714 - a case study*, 2014, 40th COSPAR Scientific Assembly

Macquart, J.-P.; Godfrey, L. E. H.; Bignall, H. E.; **Hodgson, J. A.**, *The Microarcsecond Structure of an Active Galactic Nucleus Jet via Interstellar Scintillation*, 2013, The Astrophysical Journal, Volume 765, Issue 2, p142

Hodgson J. A.; Krichbaum, T. P.; Marscher, A. P.; Jorstad, S. G.; Martí-Vidal, I.; Bremer, M.; Lindqvist, M.; de Vicente, P.; Zensus, J. A.; *The latest results from the Global mm-VLBI Array*, 2013, Proceedings of the 11th EVN Symposium

Krichbaum, T. P.; Roy, A.; Wagner, J.; Rottmann, H.; **Hodgson, J. A.**; Bertarini, A.; Alef, W.; Zensus, J. A.; Marscher, A. P.; Jorstad, S. G.; Freund, R.; Marrone, D.; Strittmatter, P.; Ziurys, L.; Blundell, R.; Weintraub, J.; Young, K.; Fish, V.; Doeleman, S.; Bremer, M.; Sanchez, S.; Fuhrmann, L.; Angelakis, E.; Karamanavis, V.; *Zooming towards the Event Horizon - mm-VLBI today and tomorrow*, 2013, Proceedings of the 11th EVN Symposium

Bignall, H. E., **Hodgson, J. A.**; *On Rapid Interstellar Scintillation of Quasars: PKS 1257-326 Revisited*, 2012, International Astronomical Union